UNIVERSITÀ DEGLI STUDI DI MILANO

Dipartimento di Fisica

Scuola di Dottorato di Ricerca in
Fisica, Astrofisica e Fisica Applicata

Ciclo XXXIV

Astrometry techniques for the calibration of the ASTRI telescope with the Variance method

Supervisor:
Marco Potenza

Co-supervisors:
Giorgia Sironi
Giovanni Pareschi

Candidate:
Simone Iovenitti
Matricola R 12 351

Anno Accademico 2020–2021

Commission of the final examination:

External Referees:
Prof. Michele Doro
Dr. Roberta Zanin

External Members:
Prof. Roberto Ragazzoni (president)
Prof. Riccardo Paoletti
Prof. Valter Maggi

Internal Members:
-

Final thesis defense:

22 marzo 2022

Università degli Studi di Milano,
Dipartimento di Fisica,
Milano – Italy.

Cover image:
E. Giro
Illustrations:
C. Righi
Document design:
S. Iovenitti

PACS code:
95.55.-n

MIUR subjects:
FIS/05 - Astronomy and astrophysics

`simone.iovenitti@unimi.it`

Tesi di Dottorato

Astrometry techniques for the calibration of the ASTRI telescope with the Variance method

Scuola di Dottorato in Fisica, Astrofisica e Fisica Applicata
Università degli Studi di Milano, dipartimento di Fisica
Milano, 22 marzo 2022.

Relatore:
Marco Potenza

Candidato:
Simone Iovenitti

Correlatori:
Giorgia Sironi
Giovanni Pareschi

Abstract

In the study of Very High-Energy (VHE) astrophysical phenomena the next generation of Imaging Atmospheric Cherenkov Telescopes (IACT) will play a key role thanks to specific ground-based astronomical observations. In this context, the ASTRI project developed a novel instrument endowed with a Schwarzschild-Couder dual-mirror optical configuration (that has never been adopted before in gamma-ray astronomy) and a dedicated Cherenkov camera entirely designed by the Istituto Nazionale di Astrofisica (INAF) based on SiPM sensors. The prototype telescope *ASTRI–Horn* is located in Italy and carried out successfully in 2019 the technology validation phase, paving the way for the realization of the *MiniArray*: 9 identical telescopes working in stereoscopic mode to be installed in Tenerife (Canary Islands) within the next three years. However, several issues related to the pointing performances emerged during operations with ASTRI–Horn. Actually the pointing calibration is in general a critical aspect for Cherenkov telescopes, as their cameras are designed for the detection of nanosecond atmospheric flashes rather than for imaging the star field and, consequently, it is impossible to use the standard astrometry of the focal plane. Furthermore, in the case of ASTRI the compactness of the mechanical structure prevents from installing an auxiliary monitoring camera sharing the same optical system of the telescope. Despite these difficulties, the optimization of the pointing performances is crucial for ensuring the scientific accuracy of the whole system.

The present PhD thesis aims at the development and validation of new astrometric techniques for the pointing calibration of the ASTRI telescope exploiting the so-called *Variance method*, a statistical algorithm implemented in the Cherenkov camera electronic board. Thanks to the Variance, the ASTRI telescope is endowed with an ancillary output owning the potentiality to image the stellar component of the night sky background in the Field of View (FoV), with a quite coarse angular resolution ($\sim 11'$, corresponding to the pixel size of the Cherenkov camera), but a relatively good sensitivity for an IACT (visual magnitude limit ~ 7). As we discuss in this document the Variance constitutes a unique opportunity for enhancing the pointing performances of the telescope, and we demonstrate that our procedures offer a chance to reach the critical accuracy level required for achieving the scientific objectives of the ASTRI project.

Unfortunately, in this period the COVID-19 pandemic and other accidental events, heavily delayed the maintenance operations on the ASTRI–Horn telescope, and up to now it is still impossible to make new observations dedicated to the validation of our procedures, hence only data taken in previous months were used. As in any other experimental activity, new data taken on purpose would have considerably facilitated our work, but due to the present situation we focused our attention to Variance data available in the ASTRI archive that has never been explored before. The resulting work represents the first complete and detailed analysis of the Variance method together with its numerous unexplored applications. Our custom astrometry techniques allowed us to reveal that ASTRI–Horn was affected by two kind of systematic errors, that we characterized and measured for the first time. The experience gained with archive data allowed us to understand how to apply our routines for calibrating the incoming ASTRI MiniArray, indicating an effective strategy to match the crucial requirement for the pointing accuracy. The resulting procedure has already been inserted into the calibration plan of the MiniArray and its Online Observation Quality System (OOQS).

The structure of the present document is articulated in eight chapters and three appendices, whose content can be summarized as follows.
Chapter 1 presents the status of the art in VHE astrophysics, focusing on the observational features of cosmic rays and gamma rays, together with a description of the main open questions in this research field.
Chapter 2 is dedicated to IACTs, presenting their history and operating principles, and introducing the major examples of instruments currently in activity worldwide.
Chapter 3 focuses on the ASTRI project, presenting both the prototype telescope ASTRI–Horn and the incoming observatory of the MiniArray. In particular, it is reported a detailed description of the most relevant subsystems for this thesis: the camera, the optical scheme and the pointing strategy.
Chapter 4 goes into the details of the Variance method. A technical description of its functioning at electronic level is provided at first, while the core of the chapter is dedicated to our routines for the production of sky images and their calibration.
Chapter 5 reports specific tools and procedures that we developed for the analysis of Variance images: the astometric calibration, the de-convolution of the star signal and the transformation function to correct the artifacts introduced by the geometric arrangement of the pixels.
Chapter 6 describes the algorithm to assess the alignment of the Cherenkov

camera to the optical axis of the telescope exploiting the apparent rotation of the FoV during long observing run in tracking mode.
Chapter 7 shows a custom procedure for the star identification developed on purpose for Variance images (as it is impossible to adopt the standard astrometry software for their analysis) allowing to monitor in real time the actual pointing direction of the telescope.
Chapter 8 contains the concluding remarks. It summarizes the main results achieved in this thesis, highlighting their importance but also some limitations and suggesting further improvements. Future perspectives of this work are briefly presented at last, with particular attention to its implementation on the incoming ASTRI MiniArray.
At the end of this document three appendices reports additional/complementary material concerning respectively metrological techniques for the inspection of shape and reflectivity of primary mirror segments (A), more details about the software developed for this thesis and the access to it (B), and the massive activity of outreach and education carried out during the doctoral period in the field of Cherenkov astronomy (C).

Contents

List of Symbols

Although a complete list of acronyms and abbreviations is given at the end of this document, it is useful to clarify immediately the most important terminology adopted. In particular, “ASTRI–Horn” indicates the prototype telescope in Italy, “MiniArray” the incoming observatory in Tenerife, while “ASTRI” refers indifferently to either the first or the second. Moreover, we choose the following convention for relevant astronomical quantities (whose explanation is provided in the document, when necessary).

α	right ascension
δ	delicnation
ξ	horizontal std. coord.
ψ	vertical std. coord.
Az	azimuth
El	elevation
φ	latitude
λ	longitude
β	position angle
d	great circle distance
h	hour angle
η	parallactic angle
ζ	zenith angle
θ	planar polar angle
r	planar radial coordinate

1

The sky at the highest energies

In the current era of multi-messanger astronomy we are used to believing that the Universe is not like it looks to our eyes. Today this is evident for gravitational waves or neutrino observatories, but it was in the electromagnetic spectrum that we first discovered this peculiar characteristic of the cosmos: different eyes take different pictures. In particular, nowadays we think that the most energetic part of the electromagnetic spectrum contains the key to unveil some of the most intriguing astrophysics phenomena that we still don't understand. This is the reason why this introductory chapter is focused on the Gamma-ray component of the cosmic radiation, which is ultimately the true gray eminence of the whole thesis.

We have known for a little over a century that space outside the Earth atmosphere is filled with energetic radiation. Using balloon flights, Victor Hess in 1912 first revealed the presence of this cosmic flow investing our planet, when he found out that the amount of ionized particles increases with altitude [1]. The physicist R. Millikan introduced the name of Cosmic Rays (CRs) [2] for indicating this mysterious energetic radiation coming from extra-terrestrial sources. Today we know tha CRs are composed of energetic particles: protons and alpha particles ($99\,\%$), heavy nuclei, electrons, positrons and neutrinos. In some cases, their energy level can exceed the impressive value of $10^{20}\,\mathrm{eV}$ [3] and we know that their origin is non-thermal, but their production processes are not completely well understood yet. Moreover, it is extremely difficult to locate the position of

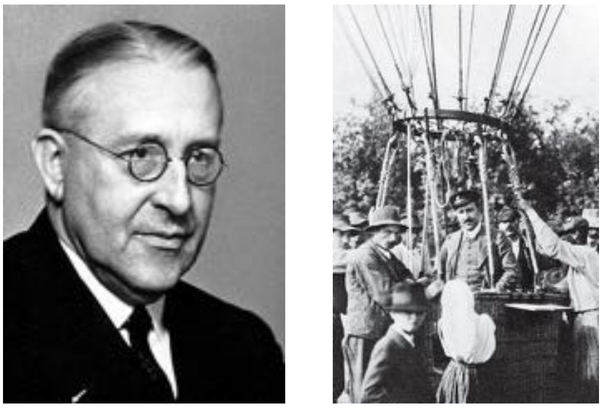

Fig. 1.1: Picture of Victor Hess (*left*) after one of the successful balloon flights in which the increase in ionisation with altitude through the atmosphere was discovered (*right*, Sekido and Elliot, 1985).

their cosmic sources: charged particles are deviated by galactic magnetic fields during their travel towards the Earth [4], and hence we observe that the distribution of CRs is isotropic around our planet, having lost the information of their direction of origin [5]. As a consequence, we can study the spectrum and the composition of CRs but to trace their origin we need a proxy, a neutral component generated in the same process of creation and acceleration of CRs: neutrinos and gamma rays (GRs).
The following sections will focus on the science of CRs (section 1.1) and GRs (section 1.2), before of a brief overview of the general scientific perspectives of this specific flourishing discipline carrying the name of Very High Energy astrophysics.

1.1 Cosmic rays

The term CRs generally refers to the flow of energetic massive particles that invests our planet from the outer space. They are composed for more than $99\,\%$ of protons and Helium nuclei, while electrons, positrons, neutrons and heavier nuclei constitute the remaining part. Scientists from different areas makes a slightly different usage of this term: sometimes CRs are identified with hadrons only, while in other occasions also GRs and neutrinos are included. In any case, the energy range of CRs is very wide, spanning between $10^{8}\,\mathrm{eV}$ to $10^{21}\,\mathrm{eV}$, and they can originate from a large variety of celestial sources: the Sun, other stars, energetic phenomena as Novae or Supernovae, or again remote objects like quasars. Depending on their energy also the instrumentation for the detection is very different:

up to $10^{14}\,\mathrm{eV}$ they can be measured with balloon experiments or satellites, while at higher energies the only chance is to use ground-based instruments sensible to the interaction of CRs with matter (see section 1.2.4).
The study of CRs led to important discoveries, such as the existence of the positron (e+) or pions. However, many question lack for an answer yet, as e.g. which are the sources responsible for the CRs production?.

1.1.1 Spectrum

CRs appears to be distributed isotropically around the Earth and their energy spectrum has a very characteristic shape, as it is measured by several experiments, with remarkable agreement [6]. The energy range spans more than 10 decades, from $10^8\,\mathrm{eV}$ to $10^{21}\,\mathrm{eV}$, and its shape clearly accounts for non-thermal phenomena, as particle populations at thermal equilibrium should follow different, less dispersed distributions (i.e. the usual Maxwell-Boltzmann law [7]). The plot of the CRs flux is reported in figure 1.2 and can be described in the following way. The CR spectrum is well defined by a broken power law,

$$\frac{dN}{dE} \propto E^{-\Gamma} \,, \tag{1.1}$$

where N is the number of particle and E their kinetic energy, with three different photon indices Γ. The first region is in the energy range between $\sim 1\,\mathrm{GeV}$ and $\sim 5\,\mathrm{PeV}$, where the slope of the measured distribution is reproduced with $\Gamma \sim 2.7$. The upper limit of this region is the so-called *knee* of the CR spectrum: the point where the index of the power law becomes $\Gamma \sim 3$. This second region extends from $\sim 5\,\mathrm{PeV}$ to $\sim 3 \times 10^3\,\mathrm{PeV}$, where there is another changing in the power index: the *ankle* of the distribution. In the third part, above $\sim 3 \times 10^3\,\mathrm{PeV}$ the value of Γ is about 2.6.
To explain the morphology of the all-particle CR spectrum the scientific community does not agree on a unique interpretation yet, but there is a large consensus on some general aspects. The external regions are associated to particles with different origins: below the knee the particles are accelerated inside our galaxy (see section 1.1.3), while above the ankle the source must be extra-galactic. In the intermediate part, between the knee and the ankle, the origin of the particles is not clear, and the reason of the steepening of the spectrum is not understood yet. There are some evidence that the knee is related to chemical composition changes [8], but there are conflicting views on the details of the transition: some observations suggest that the knee is generated by a cutoff of light elements [9], while others find that light elements disappear at lower energies and the

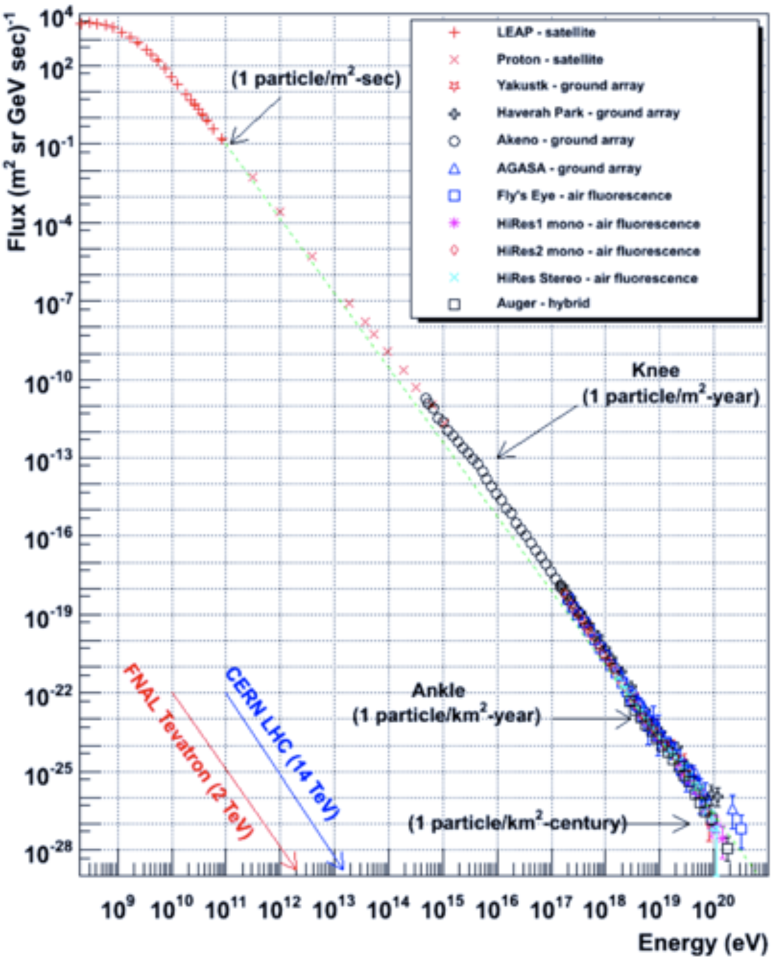

Fig. 1.2: Spectrum of CRs with data from different experiments: a broken power law [*link* 281].

knee is produced by elements with intermediate mass [10]. Also different explanations have been proposed, connected to CR propagation or to changes in the production mechanism, as e.g. a two-step acceleration in Supernova Remnants (SNRs) [11].

At the edge of its extension, the CR spectrum presents two peculiar features. On the low energy side the distribution seems to flatten and this behavior is related again to the different origin of those particles. In fact, below $\sim 1\,\mathrm{GeV}$ CRs from outside the Solar System are blocked by the wind of the Sun, and hence the only particles we observe in this energy band come from the emissions of our star itself. On the other hand, at the high energy side, the spectrum collapses into an evident cutoff at $\sim 10^{20}\,\mathrm{eV}$ (see

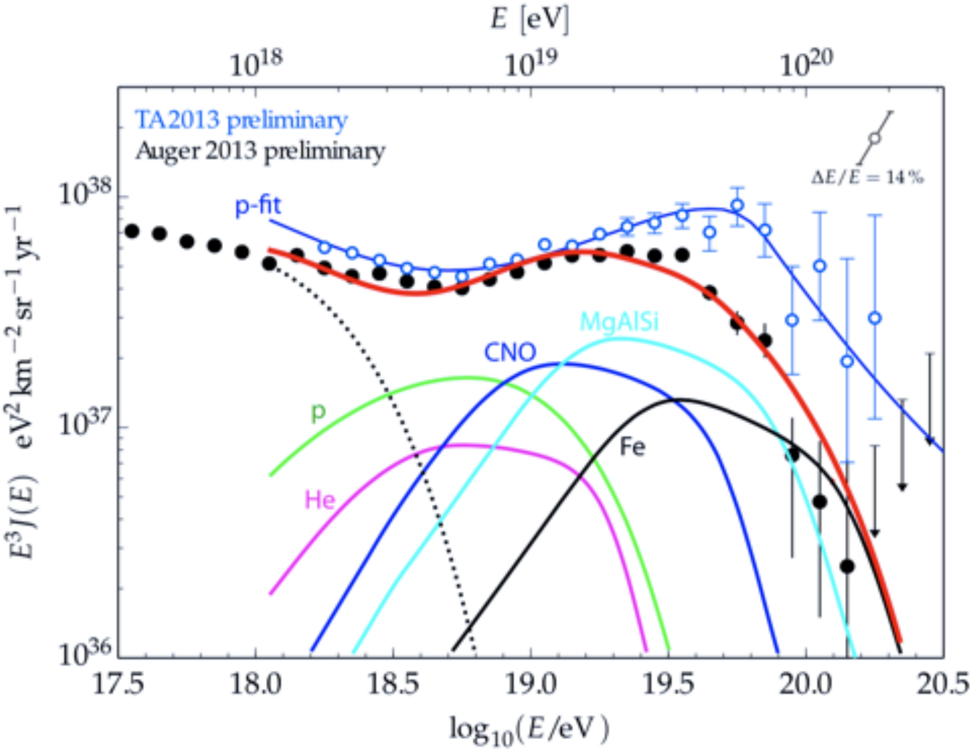

Fig. 1.3: The spectrum of CRs presents a cutoff at energies $\sim 10^{21}$ eV, as it is evident from this plot by Auger and Telescope Array (TA) Collaboration (taken from [12]).

figure 1.3 of this region). At this energy value the protons of CRs are expected to interact with the photons of the Cosmic Microwave Background (CMB, $\sim 10^{-3}$ eV), reducing their energy as a consequence of the hadrons production in the Δ resonance:

$$p + \gamma_{CMB} \rightarrow \Delta^{+} \rightarrow p + \pi^{0} \ , \tag{1.2}$$

$$p + \gamma_{CMB} \rightarrow \Delta^{+} \rightarrow n + \pi^{+} \ , \tag{1.3}$$

where Δ is the Delta barion and $\pi^{0/+}$ are pions. This process is known as Greisen-Zatsepin-Kuzmin (GZK) effect and it determines the upper limit of the CR spectrum [13] [14]. However, it is interesting to notice that in recent years particles with higher energies have been recorded (as the famous *Oh-My-God Particle* [3]), opening the intriguing perspectives that either some fundamental physics laws can be broken in certain conditions (see section 1.3) or CR accelerators may be nearby the Solar System: considering the mean free path of the interactions 1.2 and 1.3, a particle with energy greater than 10^{20} eV can travel maximum ~ 50 Mpc (GZK horizon).

To CR accelerators and the acceleration mechanism is dedicated the next section.

1.1.2 Acceleration

The problem of acceleration of CRs is condensed in the following question: how is it possible to accelerate non-thermal particles to the observed high energies? As the CRs are charged particles the solution should lie in the interaction with the interstellar magnetic field within the galaxies, but how can a particle *gain* energy if the magnetic field conserves energy? The solution is absolutely not trivial and it was first proposed by the physicist E. Fermi [15]. Magnetic fields are not static in the interstellar medium, as they are inserted in an environment of moving magnetized gas clouds: Fermi suggested that non-thermal particles can be accelerated by undergoing multiple reflections over the magnetic inhomogeneities of the medium. It is important to notice that in this scenarios particles are moving faster than the dynamic magnetic field, and hence they will experience also the presence of an electric field, as a consequence of the Lorentz transformations: the electric field in the particles reference frame is truly responsible for the acceleration.

Depending on the relative motion between the particle and the magnetized gas cloud, we can distinguish between two detailed mechanisms to produce acceleration: they are the so-called First and Second Order Fermi acceleration, briefly reported hereafter.

1.1.2.1 Second-order Fermi acceleration

This is the original argument proposed by Fermi in 1949. Within the environment of moving magnetized gas clouds, a travelling relativistic particle can interact with one of those “magnetic reflectors”, whose mass is much greater than the particle’s one, and hence their collision can be considered fully elastic. With these assumptions, Fermi demonstrated that, on average, the energy gain of the particle $\langle \Delta E/E \rangle$ after the interaction with the cloud, is proportional to the second power of V/c, where V is the relative velocity between the cloud and the particle. For this reason, this process is called a *second-order Fermi acceleration*, and actually it is not very efficient: even around supernovae, V/c is always much less than unity [7, pp.196]. The problem is that the first term of the expansion in the small parameter V/c vanishes, essentially because it contains the dependence on the direction ($\cos\theta$) that on average is zero if the direction of the collision is randomly distributed.

1.1.2.2 Diffusive shock acceleration

For many years, the second-order mechanism was considered the only possible one, until physicists (e.g. [16]) determined that there is a situation in which the first-order mechanism can exists: around shock waves. This phenomenon is known as "Diffusive shock acceleration" and it is though to be the responsible of the particle acceleration up to tev and pev ranges. In a plasma presenting shock waves (blobs of material moving at supersonic velocities) there are typically moving magnetic inhomogeneities both preceding and following the discontinuities. If we consider a particle traveling across the shock wave, it will encounter a moving change in the magnetic field in the other side and hence it will be reflected back through the shock again, but with increased energy. This process can give rise to multiple reflection, greatly increasing the particles' energy, even because at each step the energy gain $\langle \Delta E/E \rangle$ is proportional to V/c, where V is the relative velocity between the shock and the particle, as in this case the direction is normal to the wave front and not randomly distributed. The resulting energy spectrum of many particles undergoing this process turns out to be a power law [7], $dN/dE \propto E^{-p}$, similar to the CRs spectrum that we presented in section 1.1.1.
The Diffusive shock acceleration is a process much more efficient than the Second-order Fermi mechanism, but it presents an interesting problem: the so-called paradox of injection. In the environment of a shock, only particles with energies that exceed the thermal energy by much (a factor of a few at least) can cross the shock and "enter the game" of acceleration. What process causes the particles to initially have energies sufficiently high to do so, hence differentiating non-thermal particles from the background, is still unclear nowadays [17, pp.362].

1.1.3 Sources candidates

The CRs acceleration process sets an important constraint on the properties of the accelerators, helping us to identify some classes of possible sources. The charged particle must remain inside the magnetized area in order to gain energy, but its trajectory is determined by the intensity and the direction of the local magnetic field: it can happen that the particle is driven outside the acceleration region before having reached a considerable energy. As a consequence, only the objects with an adequate relation between the representative size R_S and the magnetic field B_S can be sources of CRs. For simplicity, considering the presence of a uniform magnetic field, the maximum deviation of a charged particle is given by a circular trajectory with radius R_L, the *Larmor radius*,

$$R_L = \frac{E}{ZeB_S} \; , \tag{1.4}$$

where Z is the atomic number of the particle, and E its energy [18]. If R_L exceeds the size R_S of the magnetized cloud, the particle will escape the acceleration region: using equation 1.4, the condition $R_L \leq R_S$ provides an estimate of the maximum energy $E_{MAX} = ZeB_SR_S$ that a particle can reach within a source characterized by R_S and B_S. This is a simple geometrical constraint known as the *Hillas criterion* for all types of CR sources and it is useful in selecting potential acceleration sites [19]. In figure 1.4 are reported possible classes of CR sources, distributed according to their size

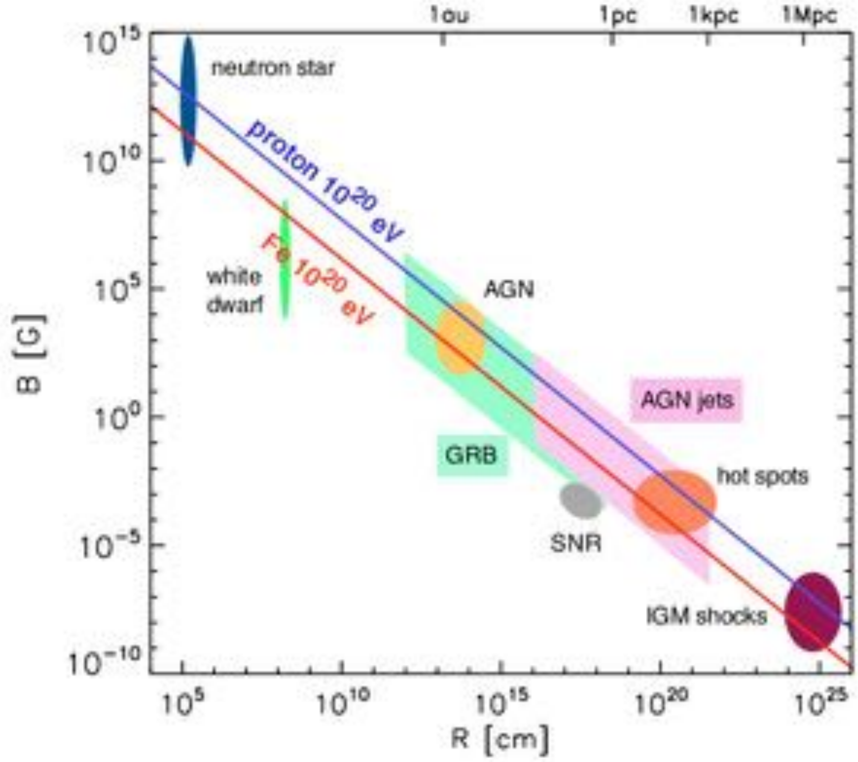

Fig. 1.4: Possible CR sources as a function of their size and magnetic field strenght (*Hillas plot*). Above the blue (red) line protons (iron nuclei) can be accelerated to a maximum energy of $E_{MAX} = 10^{20}$ eV. Objects below each line cannot accelerate those particles up to the indicated energy (taken from [20], adapted from [21]).

and magnetic field strenght. In particular, there are neutron stars (NS), White dwarfs (WD), Gamma Ray Bursts (GRB), Active Galactic Nuclei (AGN) with their cores and jets, Supernova Remnants (SNR) and Intergalactic Medium (IGM) shocks; also the galactic disk and halo, clusters, and colliding galaxies are possible sources, while the theory of "hot spots" (sky regions presenting an excess in the CR flux, [22]) has been discarded by physicists in recent years. A detailed analysis of these sources is reported in section 1.2.3.

Lastly, it is interesting to notice that using the typical values of interstellar magnetic fields, one could verify with equation 1.4 that protons below $\sim 10^{18}\,\mathrm{eV}$ are *confined* within the galactic disk. This is the reason why the CR spectrum component below the *knee* is though to be generated by galactic sources (see section 1.1.1). However, at higher energies, the trapping by magnetic field would be inefficient, and so the CRs can travel from a galaxy to another [23].

1.2 Gamma rays

As previously mentioned in the introduction, CRs do not point sources because their directions are randomized by the magnetic fields, and hence they don't have memory of the position where they come from. As a consequence, to trace the CR sources and study their properties, we need to make use of the observation of neutral particles associated to CRs: the gamma rays (GRs).

The origin of GRs is intimately connected with the production of CRs: energetic photons are produced in the acceleration of CRs and during their interaction with the surrounding environment. In sections 1.2.1 and 1.2.2 we will discuss different phenomena responsible respectively for the production and absorption of GRs, analyzing different processes of interaction between matter, magnetic fields, and photon fields. Depending on the source observed, the dominant mechanism will be different and hence the shape of the energy spectrum will be modified as well. In general, the energy range spans from $\sim 1\,\mathrm{MeV}$, the energy associated to electron/positron annihilation ($2 \times m_e = 2 \times 0.511\,\mathrm{MeV}$, where m_e is the mass of the electron), up to the highest energies achievable. Traditionally, the whole GR energy range is divided into the domains reported in table 1.1. Up to now, the highest GR emission ever detected was recorded by the LHAASO[1] collaboration in 2021 [24], together with the discovery of an impressive $1.4\,\mathrm{PeV}$

---

[1] The Large High Altitude Air Shower Observatory [*link* 257].

signal from the Crab Nebula, the standard candle of gamma ray astronomy. This detection challenges many pre-existing theoretical models of this source's emission, and paves the way for the hunt of other objects able to produce such energetic photons in the Universe, the so-called *Pevatrons*. Actually, given that the CR spectrum extends up to 10^{20} eV and beyond, it is reasonable that the lack of GR signals at higher energy is due to limitations of our detection techniques. A brief description of the methods and instrumentation adopted today will be presented in section 1.2.4.

Domain (abbreviation)	Energy range
Low energy (LE)	1 MeV – 30 MeV
High energy (HE)	30 MeV – 50 GeV
Very-high energy (VHE)	50 GeV - 100 TeV
Ultra-high energy (UHE)	100 TeV - 100 PeV
Extremely-high energy (EHE)	> 100 PeV

Table 1.1: Traditional energy domains of gamma ray astronomy.

1.2.1 Production

From a certain point of view, the presence of non-thermal electromagnetic radiation is exactly what allows us to carry out observations: if the whole Universe were in thermal equilibrium, and at the same temperature, it would be impossible to distinguish the sources from the background. This section contains a very brief overview of the main radiative processes responsible for the production of GRs in the cosmic sources. Our aim is provide a schematic summary of the fundamental results, without presenting the whole formal derivation: more details can be found in the beautiful and very complete book by Rybicki and Lightman (1979) [25], or in the more recent work, focused on cosmic gamma radiation, by Aharonian (2004) [26].

1.2.1.1 Bremsstrahlung

When a charged particle is deflected by the electromagnetic field of another one, the moving particle loses kinetic energy and emits "braking radiation" or *bremsstrahlung* according to the law of energy conservation. This process is more efficient when the difference in mass between the two particles involved in the collision is higher: the typical situation is represented by an electron scattering off an atomic nucleus, as it is shown in figure 1.5a. In this case, since the relative accelerations are inversely proportional to the masses, it is permissible to treat the electron as moving in a fixed Coulomb field of the ion. In this scenario, the mean bremsstrahlung energy loss as a function of the distance traveled by the electron in the medium is given by

$$-\frac{dE}{dx}\bigg|_{Brem} = \frac{E_p}{\chi_0}\,, \tag{1.5}$$

where E_p is the kinetic energy of the moving charged particle, and χ_0 is the *radiation length*, i.e. the average distance over which E_p decreases to $1/e$ times its original value because of bremsstrahlung. The value of χ_0 depends on the environment: low/high density medium will allow larger/smaller radiation length, and hence in rarefied clouds there is a poor bremsstrahlung emission.

The spectrum of the GRs produced with this process presents the same distribution as the charged particles, as a consequence of the direct proportionality in equation 1.5 between the energy loss and the energy of the particles. The energy range of VHE gamma rays can be achieved through bremsstrahlung of Ultra-High-Energy (UHE) charges.

1.2.1.2 Electron–positron annihilation

We know that matter dominates the Universe, but particles of anti-matter can originate from different processes. For example, positrons could come from the decay of long-lived radioactive isotopes produced in the Supernova nucleosynthesis, or from the decay of positive pions

$$\pi^+ \longrightarrow \mu^+ + \nu_\mu \qquad \text{and} \qquad \mu^+ \longrightarrow e^+ + \overline{\nu}_\mu + \nu_e\,, \tag{1.6}$$

but also from the pair-production process that will be discussed in section 1.2.2. As a consequence, a certain amount of anti-matter is available in the Universe and hence energetic photons can originate from annihilation processes. At the low energy side of the cosmic GR domain, the annihilation between an electron and a positron with negligible speed, shown in figure 1.5c, constitutes an important mechanism for the GR production, as it releases two photons at $511\,\mathrm{keV}$ (the mass energy of those leptons), with the reaction

$$e^- + e^+ \rightarrow \gamma + \gamma\,. \tag{1.7}$$

If one or both charged particles carry a larger amount of kinetic energy, the emitted GR will be more energetic (up to $\sim$$10\,\mathrm{MeV}$ and beyond) and also various other heavy particles can be produced. Furthermore, in the presence of a third charged particle absorbing th excess of momentum, also the annihilation of an electron–positron pair into a single photon can occur: this is the inverse process of the *pair production* that will be discussed in section 1.2.2.

1.2.1.3 Pion decay

Pions are the lightest mesons (particles made of a quark and an anti-quark) and in general the lightest hadrons [27]. They can be charged (π^+, π^-) or neutral (π^0), they are all instable and decay into muons and neutrinos (equation 1.6) or gamma-rays (equation 1.8) after very short mean lifetimes ($\sim 10^{-8}\,\mathrm{s}$ for charged ones and $\sim 10^{-17}\,\mathrm{s}$ for π^0). Pions are not produced in radioactive decay, but they commonly come from high-energy collisions between hadrons: we detect their production in Earth's atmosphere after the interaction with high energy CR protons, but also in Supernovae explosions through the observation of characteristic secondary gamma-ray photons. Actually, the pion decay is the dominant mechanism for GR production, in particular because π^0 decays into two gamma rays $99\,\%$ of the time, following the reaction

$$\pi^0 \longrightarrow \gamma + \gamma \,. \tag{1.8}$$

As the rest energy of π^0 is $\sim 135\,\mathrm{MeV/c^2}$ [28] then the resulting GRs have a minimum energy of $67.5\,\mathrm{MeV}$, but they can be much more energetic if the neutral pion is moving fast (the final energy spectrum has a typical power-law shape with index $\Gamma \sim 2.5$).

1.2.1.4 Synchrotron

When a charged particle is subject to an acceleration perpendicular to its velocity, due for example to the Lorentz force generated by the transverse component of a magnetic field, there is a typical emission of electromagnetic waves which is called *synchrotron radiation* (or *cyclotron* radiation in the non-relativistic case). The energy spectrum of the radiation from this process is continuous and very broad, from microwaves to gamma-rays, associated with a strong and characteristic polarization[2]. As represented in figure 1.5e, when a uniform flow of electrons with energy E_e enters a region with a perpendicular magnetic field B, then the particles will begin to spiral around the lines, emitting a synchrotron radiation peaked at [30, pp. 212]

$$E_{peak} \sim \frac{e}{2\pi c^4 m_e^3} B E_e^2 \,. \tag{1.9}$$

---

[2] Also in the case of astrophysical GR sources, as for example in the Crab Nebula [29].

Normally the synchrotron GR emission does not reach the VHE regime, unless the charged particles are trapped into the magnetic fields of extreme environments, as in the case of pulsar wind nebulae, reaching outstanding values of kinetic energy E_e [31]. However, there is another peculiar process taking the synchrotron radiation up to the VHE regime: in certain conditions the electron population has enough kinetic energy to up-scatter the GR photons they have just emitted by synchrotron radiation. This process is called Synchrotron Self Compton (SSC) scattering, and it is a specific case of Inverse Compton (IC) scattering, which is described in the next paragraph.

1.2.1.5 Inverse Compton

The Compton effect is the scattering of a photon on a free charged particle[3], usually an electron. In this process part of the energy of the photon is transferred to the recoiling electron, and hence the wave length of the scattered light is increased. However, also the inverse process can happen, when relativistic electrons up-scatter low-energy photons. This mechanism is known as *Inverse Compton* and it is the most effective process for the production of VHE gamma rays. The conceptual scheme of Inverse Compton is very simple and it is represented in figure 1.5d, but the cross section of the interaction can be very different depending on the energy regime. In the non-relativistic approximation, that holds until the energy of the electron and the photon satisfy the relation $E_e E_\gamma \ll m_e^2 c^4$, the cross section is constant and given by $\sigma_T = \frac{8}{3}\pi r_e^2$, where r_e is the classic radius of the electron: this approximation is known as *Thomson scattering*. On the other hand, if $E_e E_\gamma \gtrapprox m_e^2 c^4$, we are in the so-called *Klein-Nishima regime* (KN) and the cross section will strongly depend on the energy of the incident photon E_γ. In particular, when $E_e E_\gamma \gg m_e^2 c^4$ the cross section is approximately given by the formula $\sigma_{KN} \sim \pi r_e^2 [\ln(\frac{2E_\gamma}{m_e c^2}) + \frac{1}{2}] \frac{m_e c^2}{E_\gamma}$.
If the population of electrons have a power low distribution of energy with index Γ_e, then the spectrum of the up-scattered GRs will follow a power-law function as well. In the Thomson regime the resulting GR index will be $\Gamma_\gamma = \Gamma_e + 1/2$ [32], while in the KN domain the spectrum will be steeper, with $\Gamma_\gamma = \Gamma_e + 1$.

---

[3] If the particle is bound into an atom or a molecule the scattering of a low energy photon (without ionization) is known as *Rayleigh scattering*.

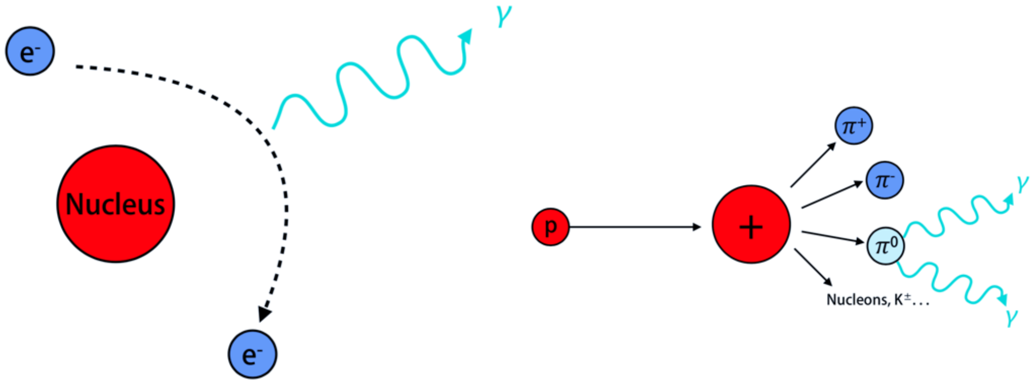

(a) Bremsstrahlung. **(b)** Pion decay.

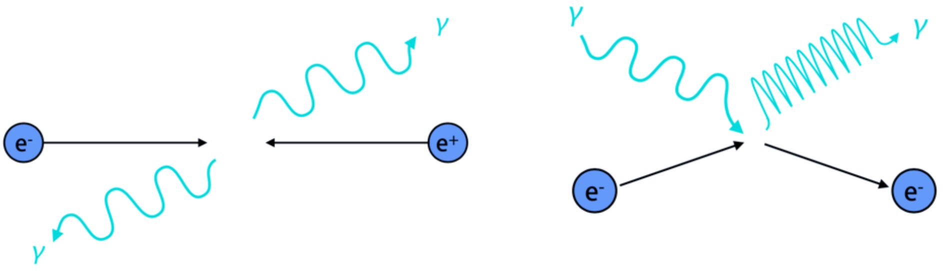

(c) Electron/positron annihilation. **(d)** Inverse Compton.

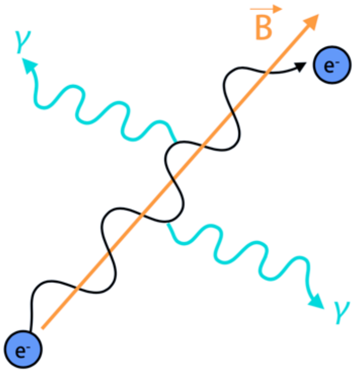

(e) Synchrotron.

Fig. 1.5: Cosmic gamma radiation production processes (adapted from [33].

1.2.2 Absorption

The original flux of GRs produced by cosmic sources can be attenuated during its propagation towards the Earth. In fact, a certain fraction of GR photons will be involved in an absorption mechanism based on the production of an electron/positron pair. It is the inverse process of the annihilation presented in section 1.2.1.2, and it is commonly referred to as *pair production*.

Classic pair production In presence of electric field, e.g. close to the nuclei of a medium, a HE photon can be transformed into an electron/positron pair following the reaction

$$\gamma \longrightarrow e^- + e^+ \,. \tag{1.10}$$

In free space, without a nucleus receiving some recoil, this reaction is prohibited as the conservation of energy and momentum would not be satisfied. Pair production is responsible for the absorption of cosmic GRs in the Earth atmosphere, and in particular for the production of the cascades of secondary particles (*Extended Air Shower*, EAS) that will be described in chapter 2. In figure 1.6 is reported an image showing the pair production in a bubble chamber. The probability of pair production in photon–matter interactions increases with photon energy (pair production is the dominant mode pf photon interaction at MeV scale and above), and the resulting particles will have a crescent kinetic energy in accordance with the law of energy conservation.

Photon–photon annihilation In this process the reaction is very similar to the previous one, but the HE photon interacts with another real photon (at low-energy) instead of with a virtual particle,

$$\gamma + \gamma \longrightarrow e^- + e^+ \,. \tag{1.11}$$

The cross section of this process, for a VHE photon of $\sim 100\,\mathrm{GeV}$, peaks between the infrared and ultraviolet bands: for this reason the photon-photon annihilation is responsible for the attenuation of VHE gamma radiation by the diffuse Extragalactic Background Light (EBL) [34].

1.2.3 Sources

In section 1.2.1 we introduced several mechanisms responsible for the production of cosmic GRs up to the highest energy domains. We now present

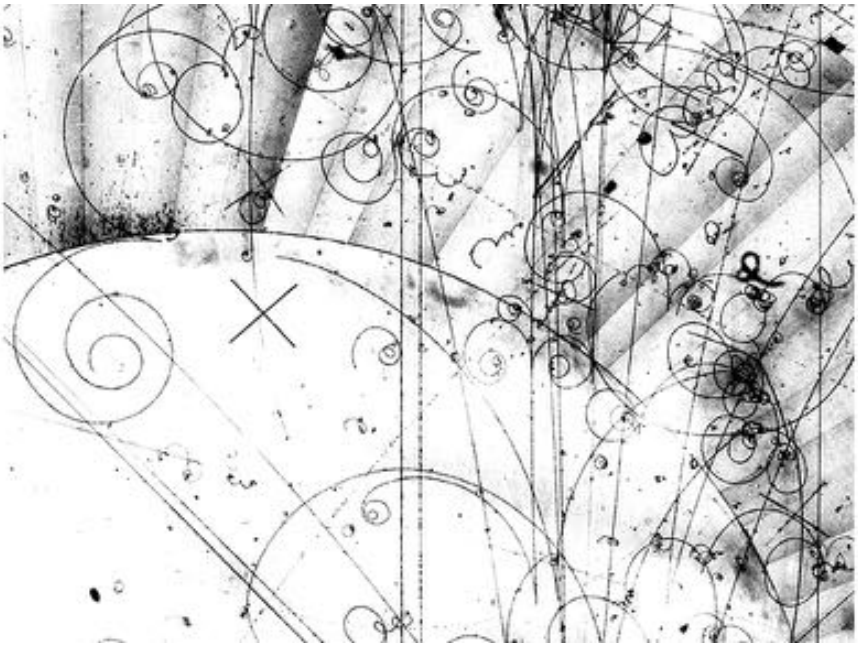

Fig. 1.6: Pair production in the Fermilab 15-foot bubble chamber [*link* 234]: electrons and positrons spiral in opposite direction after they are created with the pair-production process [35].

a brief overview of the main environment where those processes take place, describing the main well-established GR sources, both galactic and extragalactic.

1.2.3.1 Galactic sources

The Milky Way (MW) is undoubtedly the best studied galaxy. The sources in the MW can be observed with higher spatial resolution, due to their small distance from us (less then $\sim 46\,\mathrm{kpc}$, about $150\,000\,\mathrm{ly}$), and also the signal propagation can be modeled with better accuracy as the structure of our galaxy is known in detail. However, for certain classes of observation it is preferable to point sources in other galaxies in order to avoid the strong attenuation due to cosmic dust along the line of sight. In the following paragraphs there is a brief presentation of the main types of galactic GR sources.

Supernova Remnants (SNRs) Structures resulting from the explosion of a star in a Supernova, characterized by ejecta at highly supersonic speed, thus forming a strong shock wave expanding from the center and sweeping up the Interstellar Medium (ISM). The production of CRs will happen through the diffusive shock acceleration process presented in section 1.1.2, while energetic GRs will be released after their interaction with the ISM [36]. Figure 1.7 reports an image of a very famous SNR in the Cassiopeia constellation. SNRs are considered the major source of galactic CRs, up to the VHE regime [37]. Recently, a PeV emission from the Crab Nebula (a SNR in the Taurus constellation) has been detected [38].

Pulsars This term is the acronym of *Pulsating Radio sources* and it indicates a highly magnetized rotating neutron stars (NS) emitting beams of electromagnetic radiation out of its magnetic poles, at different frequencies. As the rotation axis is not usually aligned with the magnetic one, the narrow cones of emission illuminate the Earth only when they point in our direction, resulting in an apparently pulsating signal. The extreme magnetic environment of pulsars is suitable for producing gamma-ray photons, in fact the pulsating signal from the Crab Pulsar [31] has been recently detected also in the TeV energy band [39].

Pulsar Wind Nebulae (PWNe) There are different classes of SNRs: if the central region is composed of a nebula powered by the stellar wind of a pulsar, then it will constitute a PWN, or *plerion*. In this case, the VHE emission is mostly generated through IC scattering of ambient photons by the electrons of the pulsar wind, a particle flow accelerated to relativistic velocities by the rotating and powerful magnetic fields of the central spinning NS [40]. The Crab Nebula is the archetype of this class of objects: it constitutes a SNR with a central PWN powered by a pulsar [41].

Gamma-Ray Binaries Binary systems are an ideal place for the production of the most energetic cosmic radiation, because of the large amount of gravitational energy that can be released from those objects in several ways. In particular, GR binaries are a subclass of high-mass binary systems whose energy spectrum extends up to $\sim$100 GeV and beyond. They are composed by a massive star and a compact object, and their emission is explained by two models: the pulsar wind scenario and microquasars. In the first model, the compact object is a pulsar and the VHE emission is produced by the interaction of the pulsar wind with the stellar material. In the microquasar scenario, the compact object is a stellar-mass black hole, accreting material from his extended companion and presenting two relativistic jets where particles are accelerated. The GR emission is due to the IC interaction with the stellar wind [*link* 241]. Only few GR binaries are

Fig. 1.7: X-ray image from Chandra of the supernova remnant Cassiopeia A (Cas A) in 2007. The glowing in X-rays is produced by synchrotron emission in the diffusive shock acceleration process 1.1.2 Credit: NASA/Chandra [*link* 232].

known so far and none of them belong to the microquasar scenario [42].

1.2.3.2 Extragalactic sources

Extragalactic objects are extremely further than galactic ones. The Local Group of galaxies to which we belong is approximately $3\,\mathrm{Mpc}$ in diameter (about $10^7\,\mathrm{ly}$), but we currently monitor also sources in other galaxy clusters. Very often we detect the emission of whole galaxies, but sometimes we resolve the component of single stellar objects involved in catastrophic events, thus emitting extreme amounts of energy.

Active Galactic Nucleus (AGN) An AGN is a region at the center of a galaxy whose luminosity is too high to be produced by stars only. Such anomalous emission is due to the accretion process of matter by a supermassive black hole at the center of its host galaxy, that will be referred to as an "active galaxy". AGN present two relativistic jets perpendicular to the accretion disk, where the GR emission is formed as a consequence of

Fig. 1.8: The Antennae Galaxies are an example of a starburst galaxy occurring from the collision of NGC 4038/NGC 4039. Brilliant star-forming regions (blue dotted) are surrounded by glowing hydrogen gas (pink), while dense dust appears brown in this image. Credit: HST NASA/ESA.

the charged particles acceleration in those regions. Numerous subclasses of AGN have been defined based on their observed characteristics: *quasars* are the most powerful AGN, while *blazars* are the AGN with a jet pointed toward the Earth. The first two TeV blazars to be discovered were Markarian 421 and Markarian 501 (both at distances around $120\,\mathrm{Mpc}$, and both "BL Lac objects"), usually seen at TeV energies below the intensity of the Crab emission, but often presenting *flare states* with enhancement up to a factor 10 [5]. The production of GRs in these BL Lac blazars is interpreted through TeV electrons radiating synchrotron photons and up-scattering the latter to TeV energy (Klein-Nishima regime).

Starburst galaxies On average, the rate of star formation is a few $M_\odot/\mathrm{yr}$ in common galaxies, but there are some cases where this value is higher by more than a factor ten: the starburst galaxies [43]. The inside of those objects is quite an extreme environment. In order to form stars there must be a large supply of gas available, and hence very massive stars are usually formed (OB type). These stars burn very bright and very fast, and are quite likely to explode at the end of their lives as Supernovae. As a consequence, starburst galaxies usually present a large rate of SN explosions, giving rise to a high CR density, as in the case of the galaxy NGC253 [44] or the galaxy M82 [45], in the constellation Ursa Major, which hosted the closest Type Ia SN in the last decades, SN 2014J.

Gamma-Ray Burst (GRB) GRBs are sudden and intense energetic explosions observed in distant galaxies: the brightest electromagnetic events known to occur in the Universe. They are thought to be associated to the biggest Supernovae, when high-mass stars implode to form neutron stars or black holes[46]. A subclass of GRBs (the "short" bursts) appear to originate from the merger of binary neutron stars [47]. Recently, thanks to the improvement of IACT ground-based observatories (see chapter 2), GRBs have been observed also at TeV energies by the MAGIC [48] and HESS telescopes [49].

1.2.4 Detection techniques

There are several difficulties related to the detection of cosmic GR sources. The first one is that gamma radiation cannot be focused using neither normal incidence nor a grazing scheme as in the case of X-ray optics [50]. Moreover, gamma photons are comparatively rare, and hence even the brightest sources require long exposures to be detected (tens of minutes) and also a large collecting area. Lastly, the isotropic background of CRs requires in general an effective strategy to distinguish energetic photons from energetic particles. Different detection techniques are required to work in different bands of the broad gamma-ray spectrum. Roughly they can be divided in two categories: *direct observations*, adopting satellites above the Earth atmosphere, and *indirect observations* at ground level, exploiting the interaction of GRs with air or water. Hereafter there is a brief overview of the most important detection techniques, reporting a summary of their characteristics in terms of angular resolution, energy resolution, and gamma/hadron separation.

1.2.4.1 Satellites

Direct observations of cosmic GRs are carried out with the usage of dedicated satellite missions, up to a few hundred GeV. They have a duty cycle

Fig. 1.9: The Fermi satellite before launch. The box on the top is the LAT instrument, composed of 4×4 towers of silicon detectors to measure the direction of the incoming GR photons, with a calorimeter at the bottom measuring the energy of the electron/positron pairs. Credit: NASA/Kim Shiflett.

of $\sim 100\,\%$ and they usually provide an excellent gamma/hadron separation, with a very good energy resolution thanks to the calibration on ground before launch (which is not possible for IACTs, see the next section). On the other hand, their angular resolution is modest and their energy range is limited by the reduced collection area that detectors on-board satellites have. The Large Area Telescope (LAT) instrument, onboard the NASA's Fermi mission, is the only one reaching energies above the GeV, exploiting the pair production process to recover the frequency and the direction of incoming GR photons [51]. LAT covers an energy range from $20\,\mathrm{MeV}$ up to more than $300\,\mathrm{GeV}$ and has a field of view of $\sim 2.4\,\mathrm{sr}$.

1.2.4.2 Imaging Atmospheric Cherenkov Telescopes (IACTs)

Indirect detections of cosmic GRs can be carried out with ground-based optical telescopes observing the peculiar interaction of such energetic photons in the Earth atmosphere. In fact, the primary gamma-ray originates a cascade of charged particles moving faster than light in the air, hence producing a bright flash due to Cherenkov effect. Considering the properties of the light flash all the characteristic of the original GR photon can be retrieved, for incoming radiation above $\sim 30\,\mathrm{GeV}$. This technique provides a good gamma/hadron separation and excellent angular resolution. Moreover, the energy range is considerably larger compared to the one covered by satellites, thanks to the usage of arrays of telescopes increasing the collecting area up to several km^2. Chapter 2 is entirely dedicated to this technique and the major examples of IACTs.

1.2.4.3 Water Cherenkov arrays

Another technique to study the cosmic GR radiation is to consider the Cherenkov effect produced by secondary particle not in the air, but in water tanks, in a Water Cherenkov Array. In this case, the energy of the incoming GR photon must be higher (above $\sim 100\,\mathrm{GeV}$) because the charged secondary particles must be so energetic to reach the ground. For this same reason, such observatories are located in places at high altitudes, in order to reduce the thickness of the overlying atmosphere. They are characterized by very poor angular and energy resolutions compared to IACTs, but they have full duty cycles, since daytime observations are possible, and thanks to their very large collecting areas they can reach higher energies [24]. An example is the High Altitude Water Cherenkov Experiment (HAWC) [*link* 245], built at an elevation of $4100\,\mathrm{m}$ above sea level in Mexico, composed of an array of 300 water Cherenkov detectors for CRs and GRs. Another more recent facility is the Large High Altitude Air Shower Observatory (LHAASO) [*link* 257], in China, also studying both GRs and CRs with a very complex apparatus composed of 20 wide field-of-view air Cherenkov telescopes, a surface water Cherenkov detector facility, an array of 1171 underground water Cherenkov tanks for muon detection and $1\,\mathrm{km}^2$ array of electromagnetic particle detectors [52]. With its impressive extension, the LHAASO experiment sheds light on the UHE domain of cosmic GRs, observing for the first time the PeV emission from several sources, the *PeVatrons* [38].

Fig. 1.10: Bird view of the High Altitude Water Cherenkov Experiment (HAWC), in 2014, Mexico. The full extension of 300 water tanks was completed in spring of 2015.

1.3 Open questions for UHE astrophysics

The very recent discovery by LHAASO of the PeV emission from several cosmic sources has opened a new and intriguing era for the research in astrophysics: thanks to technological progress, humans have just been gifted with new eyes to observe the Universe, with the capability to detect UHE photons that have never been accessible before. There are several open questions that may have an answer in this energy domain, and new observations could lead us to change our models for many exotic astronomical objects, or to review the innermost structure of fundamental physics to cope with unexpected behaviors of Nature. This perspectives justify the efforts of the scientific community for developing new techniques and facilities to study the GR cosmic radiation. In this section we will present a brief overview of some key topics in UHE gamma-ray astronomy, in tight connection with cosmic-ray astrophysics, following the clear and schematic layout of the white paper of the largest incoming experiment devoted to this research: the Cherenkov Telescope Array (CTA) [53].

1.3.1 Origin and role of relativistic cosmic particles

A major goal of UHE astrophysics is to understand the origin of relativistic cosmic particle and to establish their role in the Universe. To this end, it is necessary to shed light on the processes of acceleration, transport and interaction of the cosmic radiation, also through future observations with the incoming generation of telescopes, carrying out a census of particle accelerators in the Universe and studying in detail archetypal sources with precise measurements. With this strategy, it will be possible to understand how and where particles are accelerated in the Universe, but also to clarify what role these particles play in the evolution of their host objects and how they travel out to large distances.

Accelerators Nowadays the primary goals of CR astrophysics is to understand in which cosmic objects the particle acceleration takes place and to identify the sources of the dominant contribution to the locally measured CRs. More specifically, the following questions are still unanswered: where and how in our galaxy are particles accelerated beyond PeV energies[4]? What are the sources of the UHE CRs? Are SNRs the only major contributor to the Galactic CRs? Are they *PeVatrons* or not? Up to now, several accelerators have been already identified and strong evidences of hadron acceleration in a handful of sources have been detected (see section 1.2.3.1). However, there is still a huge potential for the exciting discovery of new classes of accelerators, as for example the possible emission from clusters of galaxies, and others.

Effects of accelerated particles Accelerated cosmic particles appear to be an important ingredient of a wide range of astrophysical systems, from PWNe and SNRs to active galactic nuclei and clusters of galaxies. Moreover, it is thought that they can impact on the star-formation process and the evolution of galaxies. However, the details of their contribution is very poorly understood yet: even inside the interstellar medium of our own galaxy, the interaction between CRs with the environment has never been modeled with accuracy, due to a lack of high quality data. Anyway, we know that UHE CRs impact upon their environments in a number of ways: as a dynamical constituent of the medium, through generation/amplification of magnetic fields, through ionization and subsequent impact on the chemical evolution of, for example, dense cloud cores. All

---

[4] The Fermi processes presented in section 1.1.2 cannot produce particles above PeV energies, and also the injection problem still has to be solved.

these effects are relevant for the interstellar medium of our own Galaxy and they are likely to be important in star-forming systems on all scales.

1.3.2 Probing Extreme environments

Extreme environments are typically associated with the particle acceleration up to the UHE range and beyond. For this reason, the gamma emission from these particles can be a probe of the exotic environments where they are originated: neutron stars, black holes, relativistic outflows or explosions. The gamma radiation provides an insight to time and distance scales which are inaccessible in other wavebands, and it is independent on magnetic fields.

Black holes and jets The strong gravity of black holes works as a central engine for the production of relativistic outflows and collimated jets out of the extreme environments where they are hosted. This mechanism takes place both around stellar-mass black holes, for example in binary systems, and in the core of AGNs, where super-massive black holes (SMBH) dominate the dynamics of the whole galaxy. The process of emission from these objects is still poorly-understood: the particle acceleration may occur extremely close to the SMBH but also up to the Mpc scale, at the end of the largest relativistic jets. VHE observations are key to disentangling different scenarios, measuring the jet power and dynamics, probing magnetic fields and identifying the leptonic or hadronic contribution to the CR production and emission. Among the main goals there is to investigate the relationship between the central source and the diffuse emission of nearby objects (as for the case of Sgr A*) and to carry out a comparison between SMBH and stellar-mass systems, studying their high-energy non-thermal emissions (e.g. observing Cyg X-1).

Neutron stars and gravitational wave events Neutron stars constitute a very interesting subject of gamma-ray astronomy, as they are involved in several systems that need to be investigated through their VHE/UHE emissions. First, binary systems including a pulsar: they provide a unique opportunity to study a relativistic outflow under changing physical conditions as the orbit progresses. Second, merging events including neutron stars: they are sources of gravitational waves (GW) and short GRBs, but they have never been observed in the energy range of $\gtrsim 100\,\mathrm{TeV}$. With a rapid response to GW alert triggers, there is a chance to perform such observation and hence to study the highest energy processes associated with

NS mergers. In particular, as $\sim$100 TeV photons are produced by $\sim$PeV protons, such measurements would confirm or not the nature of NS mergers as *PeVatrons*.

Cosmic voids VHE photons from distant objects can be used as a probe of the intervening space. In particular, they can be used to investigate the properties of extremely under-dense regions, known as *cosmic voids*, constituting much of the Universe. Firstly, the interaction of VHE photons in cosmic voids (pair production) allow us to measure the extremely weak magnetic fields thought to exist in these regions. Secondly, thanks to GR photons we can probe the diffuse radiation field known as Extragalactic Background Light (EBL): the integrated emission from stars and galaxies of all types throughout the evolution of the Universe. The EBL is an important tool for cosmology, but it is extremely difficult to measure directly, due to very strong foregrounds from the Solar System and the Milky Way. However, the EBL leaves an imprint on the measured spectra of gamma-ray sources behind cosmic voids, via the process of photon-photon pair production. Lastly, if VHE photons actually heat the remaining gas in cosmic voids, this would suppress the formation of dwarf satellite galaxies, resolving a very old open question about these objects in cosmology.

1.3.3 New frontiers in physics

The most exciting research topic in astrophysics of cosmic radiation is probably the search for possible new frontiers in fundamental physics. Actually, there are several theoretical models that need to be supported or discarded by dedicated observations in GR astronomy. For many cases, also a negative result in the detection would be very helpful, providing a clue to constraint the parameters of models with upper/lower limits: experimental results would guide the work of theoretical physicists. Among the most intriguing topics, there are Dark Matter, Lorentz Invariance Violation, and Axions-Like Particles: they are briefly presented hereafter.

Dark Matter Modern cosmology relies on the existence of Dark Matter (DM): a massive ingredient of the Universe which is completely invisible to our telescopes. Up to now, we don’t have any clue on its particle nature, but the most popular scenarios suggests that DM is made of Weakly Interacting Massive Particles (WIMPs): a large class of new elementary particles, potentially not part of the Standard Model, with a mass typically between few tens of GeV and a few TeV, and a self-annihilation cross-section of the order of the weak interaction. There are many models for DM including WIMP candidates: their success relies on the fact that such particles are expected to have been produced in the early Universe and their self-annihilation cross-section implies their residual abundance to be close to the currently observed value [54]. The annihilation of WIMPs in the Galaxy results in the production of GRs in the VHE range, hence a deep investigation of this radiation will significantly impact on the WIMP paradigm, both through a signature detection or non-detection.

Lorentz Invariance Violation A Lorentz Invariance Violation (LIV) is any possible deviation or exception from the *Lorentz Invariance* or *symmetry*: a set of fundamental frameworks at the heart of physics, and modern science in general. In particular, LIVs concern the fundamental predictions of *CPT symmetry* and *Special Relativity*, such as the constancy of the speed of light in all inertial frames of reference, time dilation, but also the predictions of the Standard Model of particle physics. The existence of LIVs is predicted by some variations of quantum gravity, string theory, and alternative theories to General Relativity.
Several studies are trying to detect observational evidences of LIVs, but no signatures have been measured so far [55]. However, it is possible that the cosmic gamma radiation constitutes the key to unveil this mystery. In fact, the long travel times of GRs from extra-galactic sources combined with their short wavelength make them a sensitive probe for energy-dependent variation of the speed of light due to quantum-gravity induced fluctuations of the spacetime metric[5]. As a consequence, with the improvement of VHE astronomy it is possible to probe the existence of LIVs through high statistics measurements of GRs from extra-galactic sources, as GRBs or blazars, over a wide energy range.

Axion Like Particles Axion-Like Particles (ALPs) are a generic prediction of many extensions of the Standard Model of particle physics: a new class of light particles with characteristics similar to those of Axions[6]. The possible existence of ALPs could have a signature in astrophysical settings, as they are expected to convert into photons (and vice versa) as they traverse cosmic magnetic fields [57]. As a consequence, relative to very bright

---

[5] This effect is similar to a non-trivial refractive index of the vacuum, introducing time delays between photons with different energies traveling over large distances.

[6] Hypothetical elementary particles whose existence was postulated to resolve the strong CP problem in quantum chromo-dynamics [56].

and distant sources, the ALP–photon coupling can result in a detectable enhancement of the TeV photon flux, introducing a spectral modulation dependent on the ALP mass [58]. Moreover, such ALP–photon oscillations effectively make the Universe more transparent to gamma rays (competing with the absorption on the EBL) [59]. For these reasons, photons in the highest range of GRs from distant cosmic sources can provide a powerful tool to search for possible new physics beyond the Standard Model.

2

Imaging Atmospheric Cherenkov Telescopes

In the last century, detectors flown in spacecraft seemed to be the obvious route for detecting the gamma radiation from cosmic sources, as the incoming photon flux is rapidly attenuated by the Earth atmosphere at such high energies. However, the genetic relationship with cosmic-ray particles causes the flux of cosmic gamma rays to decrease rapidly with increasing energy (remember equation 1.1), and hence a very large detector area is required to have a good statistics in the VHE domain and beyond. For this reason, ground based telescopes with big collecting areas are actually the only instruments adequate for an effective study of the cosmic gamma radiation so far, given a good strategy to reject signals due to hadronic cosmic rays based on *image analysis*[1]. Of course, as the gamma photons do not reach the ground level, such telescopes provide only an *indirect* detection, nevertheless it is possible to obtain VHE spectra and VHE sky imaging, as the energy and direction of the primary photons can be reconstructed anyway. These instruments record the Cherenkov effect produced in the atmosphere by the incoming cosmic radiation and hence they are called *Imaging Atmospheric Cherenkov Telescopes* (IACTs). This chapter is dedicated to their characteristics and their operating principles (section 2.1), but also

---

[1] Onboard satellites this rejection is made through anti-coincidence counters.

on the phenomena of Cherenkov light (section 2.1.3) and the production of Extended Air Showers (EASs, section 2.1.2). Finally, the key features of IACTs and some major examples of instruments (section 2.3) will be presented and discussed.

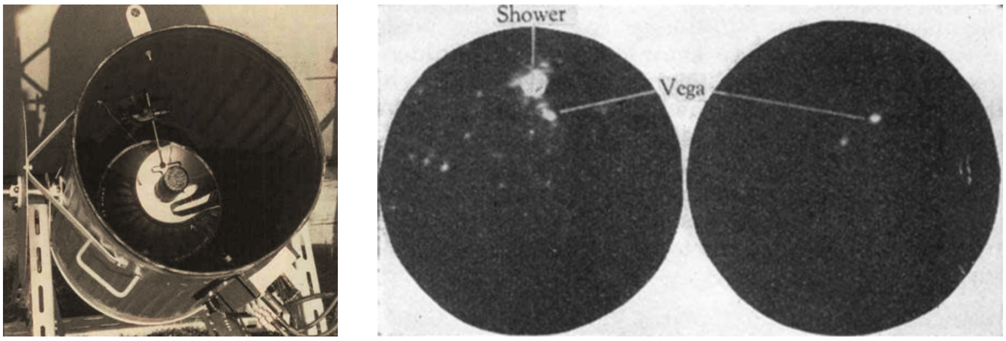

Fig. 2.1: Original setup *(left)* for the discovery of Cherenkov light pulses from extensive air showers *(right)*: a garbage can, a 60 cm diameter mirror in it, and a PMT in its focus (used by Galbraith and Jelly, in 1952).

2.1 Introduction

The electromagnetic spectrum extends for more than 20 energy decades (or orders of magnitude), between radio and gamma rays. Every energy band experiences a different behavior of the Earth atmosphere, depending on the frequency of the incoming photons: for example, cosmic GRs are completely absorbed in interactions with atoms and hence they cannot reach the ground level of our planet. Therefore, Earth atmosphere is not transparent for GR photons, but their interaction gives rise to a peculiar phenomenon (a Cherenkov flash) that can be recorded by IACTs, and hence the arrival of a cosmic GR can be successfully detected anyway. In particular, when a VHE particle (not only photons, but leptons and hadrons too) interacts with the atmosphere, it produces an Extended Air Shower (EAS), or a cascade of secondary particles (section 2.1.2). As long as these products are charged and so energetic to be faster than light in the air, they radiate near-UV and optical photons in a narrow cone around their flight direction, due to the Cherenkov effect (section 2.1.3), originating a rapid ($\sim 10^{-9}$ s) flash of light. Through an appropriate sampling frequency, IACTs can record these signals over the Night Sky Background

Fig. 2.2: Jelley's "light receiver" in 1961, Harwell (UK): three 1 m f/0.5 mirrors mounted equatorially for drift scans [60]. In following years the light collecting area would be increased using a cluster of small mirrors with a common focus.

(NSB) and retrieve the origin and the energy of the primary cosmic GR. Basically, IACTs exploit the atmosphere as a giant calorimeter, where the telescope is the actual sensitive device, hence taking advantage of a huge effective collection area, much bigger than the real size of the instrument. The idea of such instruments dates back to the beginning of the second half of the last century, as it is briefly reported in the next section.

2.1.1 Brief history

Historically, Pierre Auger first reported of the charged particles of an EAS in his work about cosmic rays in 1939 [61]. Afterwards, the idea that such particles could emit Cherenkov radiation in air was first conceived by Blackett in 1948 [62], who estimated also that 10^{-4} of the light of the night sky would arise from this process. Already in 1952, Galbraith and Jelley revealed the presence of light-pulses of short duration correlated with cosmic radiation using a photomultiplier and a very raw optical apparatus [63] (see figure 2.1, and its evolution shown in figure 2.2). Despite this exciting early result, the development of IACTs was quite slow in this

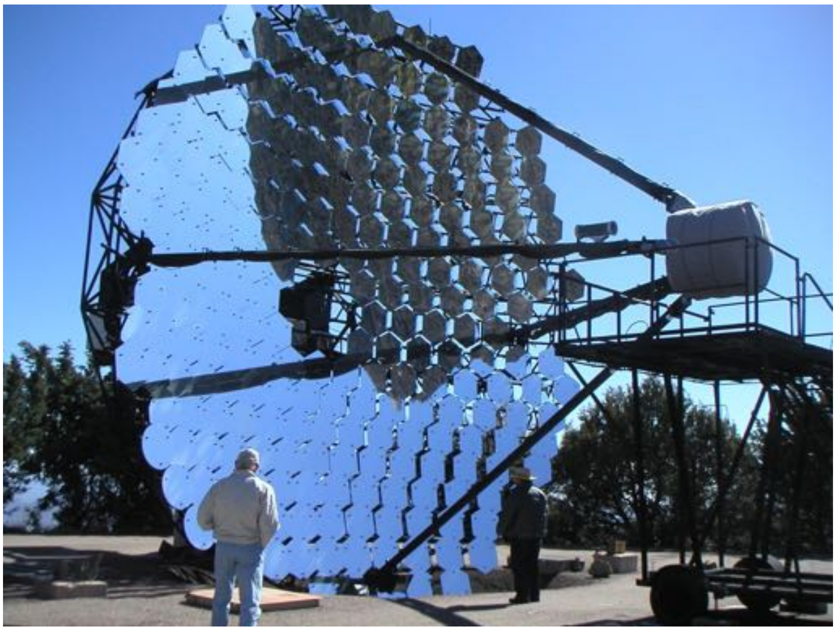

Fig. 2.3: The Whipple 10 m telescope, on Mt. Hopkins (USA).

period: the next generation[2] of instruments came out only in 1967, with the hard work of Trevor Weekes on the Whipple telescope [65], shown in figure 2.3, that was awarded at the end with the first detection of the Crab pulsar at TeV energies [66], after more than twenty years. The main difficulty was related to the rejection of hadronic showers [5]: the signal from any gamma point source was completely overwhelmed by flashes from EASs produced by ordinary charged cosmic rays, spread evenly over the sky. Nowadays the hadron rejection is performed effectively by examining the shape of the Cherenkov images, using the so-called *Hillas parameters* presented in section 2.2.1.2. However, before jumping to image analysis, it is necessary to consider some characteristics of EASs and the Cherenkov light production in the next sections.

2.1.2 Extended Air shower

The interaction of a High Energy cosmic particle with the atoms of the Earth atmosphere produces a large cascade of secondary particles, known as Extended Air Shower (EAS). This process is triggered both by pho-

---

[2] Historicaly, this is the *second* generation of Cherenkov telescopes, while the third is the one characterized by stereoscopic view, i.e. Veritas, Cangaroo III [64], H.E.S.S. and MAGIC (see section 2.3 for details).

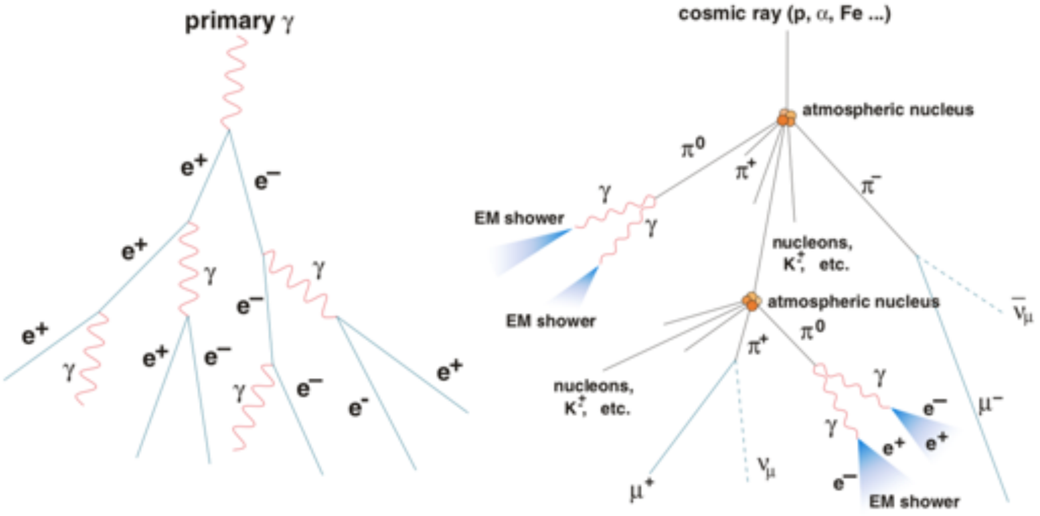

Fig. 2.4: Schematic description of extended air showers: EM shower *(left)* and hadronic shower *(right)* [68].

tons and hadrons, but the respective EASs will present different characteristics. In fact, GRs' interaction is electromagnetic: they produce electron/positron pairs, giving rise in turn to other photons again. On the other hand, the interaction of hadrons is driven by the strong nuclear force and it presents a wider spectrum of particles, including π mesons. Both electromagnetic and hadronic cascades will produce Cherenkov flashes (see section 2.1.3), but their morphological structure will be different, due to their specific development. This aspect plays a key role in order to distinguish EASs of the two kinds. This discrimination is crucial, as charged particles arrive on the Earth after a curved path due to cosmic magnetic fields, while IACTs perform VHE imaging of the sky relying on the straightness of the path that the photons follow from the source to our planet. For this reason, we are interested in photon induced events, while hadronic showers constitute an undesired background in this context. The discrimination is based on the shape of the consequent Cherenkov flash, so the better we know the characteristics of both types of showers, the better we can get rid of hadronic background in GR observations. The problem is that hadronic cascades are much more numerous, by a factor of about 10^3, even for strong gamma-ray sources as the Crab Nebula [67]. For this reason, a deep analysis of both hadronic and gamma cascades is mandatory.

2.1.2.1 Electromagnetic cascades

Electromagnetic cascades are initiated by photons or $e^{\pm}$ entering the Earth atmosphere. They are based on two processes driven by electromagnetic interactions: bremsstrahlung emission and pair production (described in sections 1.2.1 and 1.2.2). In particular, the energy threshold for a gamma photon to initiate a particle cascade through the pair production process on air nuclei is $\sim 20\,\mathrm{MeV}$. The newly-born charged particles will emit in turn other gamma rays via bremsstrahlung, and hence a loop is started and a cascade is originated. The shower extinguishes when the energy of the final products falls below the critical energy E_C, that in air is $\sim 83\,\mathrm{MeV}$ [30]. Below this energy value, ionization losses dominate over the bremsstrahlung for electrons, while the photoelectric absorption and Compton scattering start competing with the pair production for photons.
An important characteristic of electromagnetic cascades is that the *radiation length* for the pair production in the ultra-relativistic limit and for the bremsstrahlung process are very similar, $\epsilon_{pp} \approx \epsilon_{br}$ [30, pp.271], where ϵ represents the *radiation length* χ_0 introduced in equation 1.5 on page 11 conveniently expressed in terms of the number of kilograms per metre squared traversed by the particle [30, pp.175]: $\epsilon_0 = \rho\chi_0$, indicating with ρ the density of the medium[3]. This similarity is not a surprise, as both processes involve a photon and an electron and hence they are basically the same interaction in terms of quantum electrodynamics [69]. As a consequence, after a common typical distance in air χ_0, a photon produces a pair, and a lepton radiates about half of its energy by means of bremsstrahlung: this balance produces a shower quite symmetric, as it is shown in figure 2.5, *left*. Moreover, for the same reason, on average, after any typical length the number of particles in the shower is doubled, and their energy is halved, therefore after a distance $n\chi_0$ the cascade contains 2^n particles of average energy $E_0/2^n$, where E_0 represents the energy of the primary gamma.
Regarding the vertical extension of the EAS, the cross-section for pair production is weakly dependent on the photon energy and hence the height of the shower ignition is similar for different GR energies: $\sim 20\,\mathrm{km}$ to $30\,\mathrm{km}$ above sea level. The EAS is disrupted when the average energy per particle is E_C, that will be coincident with the moment when the number of particles is maximum. The altitude H_{MAX} at which this condition is fulfilled is inversely proportional to the logarithm of the primary gamma-ray energy, $H_{MAX} \propto 1/\ln(E_0)$ [70]. In conclusion, the peculiar properties of electromagnetic cascades are: (i) only photons and $e^{\pm}$ are produced; (ii)

---

[3] For $\sim 1\,\mathrm{TeV}$ gamma ray, $\epsilon \sim 33\,\mathrm{g/cm^2}$ [30].

the initial growth of the cascades is exponential; (iii) the shower depth increases logarithmically with the energy; (iv) beyond the maximum, the electron flux drops due to ionization losses and the shower is rapidly extinguished.

2.1.2.2 Hadronic cascades

Hadronic cascades are much different from electromagnetic ones. They originate from the interaction between atmospheric nuclei and cosmic rays. In these cases, normally the EAS is started by protons, as they are the most abundant components of cosmic rays. About the $90\,\%$ of the products of their collisions is constituted of pions, approximately in the same proportion of π^+, π^- and π^0, but also kaons and secondary heavy nuclei can be originated, as it is shown in figure 2.4. Afterwards, both barions and pions undergo other interactions and decays, continuing to multiply in successive generations of nuclear collisions, hence generating the EAS.
The interactions happening inside hadronic cascades are numerous. The neutral π^0 decays in energetic photons, originating $e^{\pm}$ couples and subsequent electromagnetic showers, while charged pions decay in muons and neutrinos. The low energy muons in turn decay weakly into positrons, electrons and neutrinos (see eqation 1.6 on page 11) starting other secondary electromagnetic showers, while the muons produced by very high energy pions, in the uppermost atmosphere, are very penetrating and reach the ground[4] without taking part in other nuclear interactions, but radiating part of their energy by ionization. Also secondary protons lose energy by ionization, and the cascade stops when their energy falls below $\sim$1 GeV, the threshold for pion production. In general, the shape of the hadronic EAS is more articulated and large, with respect to the electromagnetic one. In fact, nuclei and mesons are heavy particles and hence the transferred transverse momentum in their collision is larger, therefore the resulting EAS will be wider. Furthermore, hadronic cascades presents more subshowers, as they contain several components (hadronic, muonic, electromagnetic) leading to a not only wider but also more asymmetric EAS. Figure 2.5, presents a simulations of electromagnetic *(left)* and hadronic *(right)* cascades, and the differences in their shapes are evident. Another gap between electromagnetic and hadronic cascades is represented by their *time length*: the former develops in less than $3\,\mathrm{ns}$ so it is faster compared to the $10\,\mathrm{ns}$ taken in hadronic cascades.

---

[4] Despite their short lifetime, the ground is reached as a consequence of the time dilation due to their high speed [71].

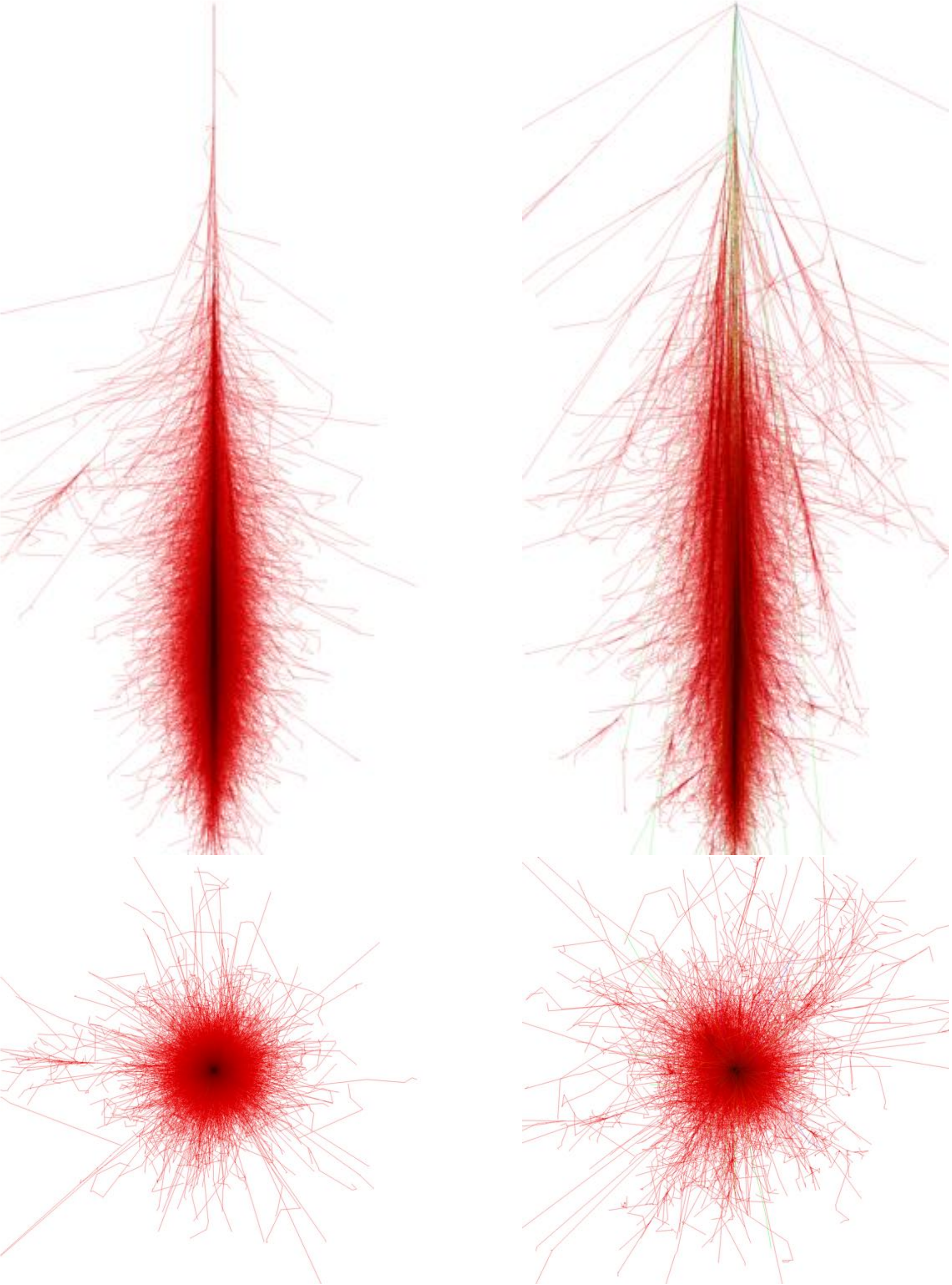

Fig. 2.5: The different character of gamma showers (left) and hadronic showers (right), for a 1 TeV particle. Color scheme: $e^{\pm}$ red, $\mu^{\pm}$ green, and hadrons in blue. The gamma shower is slender and to lowest approximation axially symmetric about the direction of the primary. The hadronic shower is irregular and may contain electromagnetic sub-showers as a result of the large transverse momenta generated in hadronic interactions (simulations made with `CORSIKA` [*link* 235]).

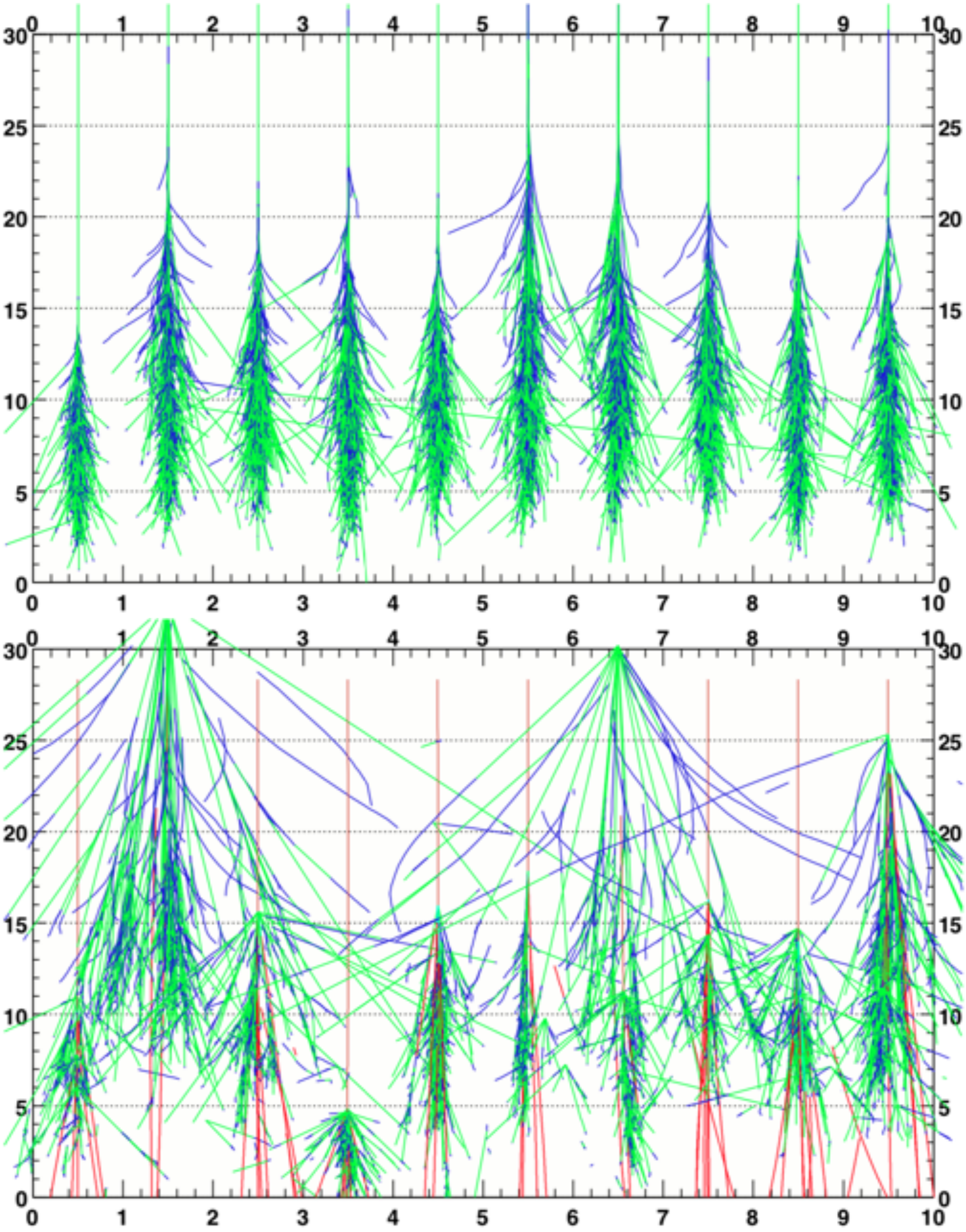

Fig. 2.6: Illustration of the intrinsic variability of shower development. Top: Simulation of 10 showers, each initiated by a gamma ray of 300 GeV. Bottom: Simulation of 10 showers initiated by a proton of the same energy. Due to larger transverse momentum transfers, hadronic showers show larger fluctuations [72].

2.1.3 Cherenkov Light

When a charged particle travels faster than light in a medium, there is a reaction by the molecules producing a kind of shock wavefront in the electromagnetic field, radiating energy mostly in the wavelength ranges between 300 and $500\,\mathrm{nm}$, detectable as a light flash. This phenomenon is known as *Cherenkov effect*[5], after the name of the Soviet physicist Pavel Alekseyevich Cherenkov [74] who received the Nobel prize in 1958 for this discovery, together with Ilya Frank and Igor Tamm [75]. Actually, charged particles involved in EASs are so energetic to exceed the speed of light in the Earth atmosphere, and hence they will emit Cherenkov light. As a consequence, a very short bluish flash is produced by both hadronic and electromagnetic cascades, allowing us to observe them with adequate telescopes. From a microscopical point of view, the Cherenkov effect arises from the Coulomb interaction. When a charged particle travels through the air, it polarizes the molecules in the neighborhoods of its trajectory: these behave in first approximation as electrical dipoles, so they will change their orientation following the charged particle. Given that c is the speed of light in vacuum and n is the refraction index of the medium, if the particle velocity is low ($v < c/n$) then the polarization pattern is symmetrical (figure 2.7, *left*) and hence the overall electromagnetic field remains zero. On the other hand, if the particle velocity is greater than the speed of light ($v > c/n$) then it travels faster than its electric field

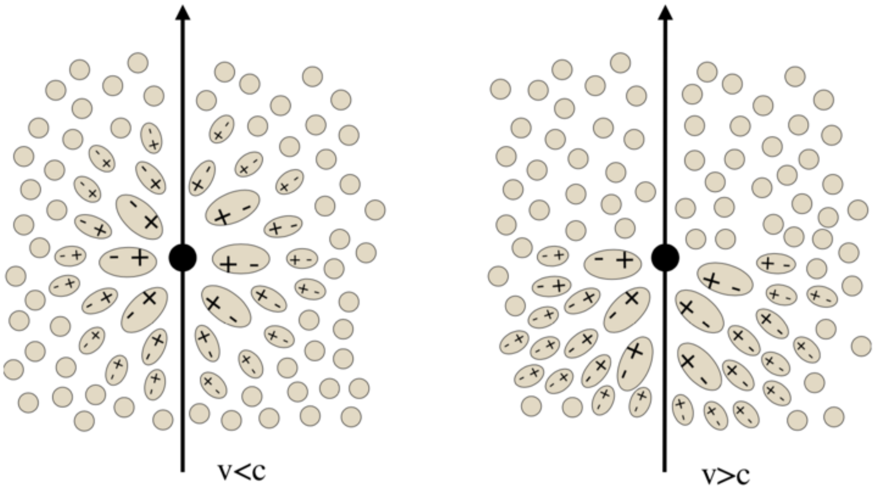

Fig. 2.7: Polarization of a medium when a charged particle travels slower (left) or faster (right) than the speed of light in it (taken from [72]).

---

[5] For more details and an historical review, refer to [73].

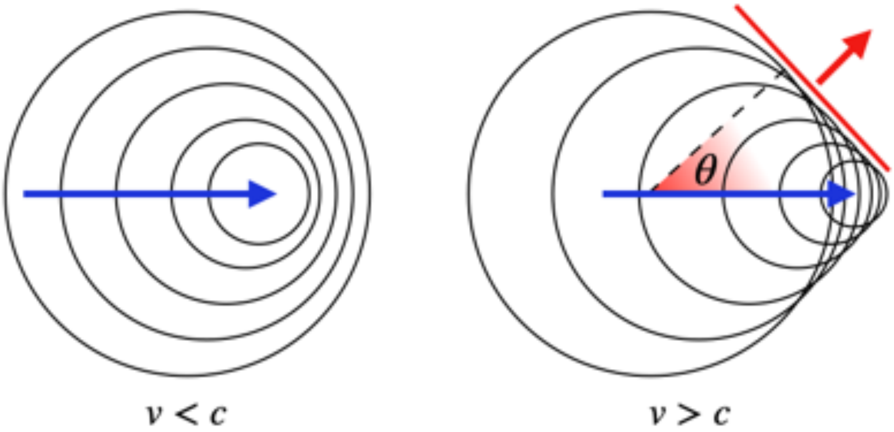

Fig. 2.8: Cherenkov radiation geometrical scheme.

leaving behind a non-symmetric perturbation (figure 2.7, *right*). In this case, Cherenkov radiation is emitted in association to the coherent depolarization of the molecules returning to the equilibrium configuration [72]. The emission of the Cherenkov light flash, or the formation of the shock wavefront in the electromagnetic field, can be easily illustrated by means of the Huygens Principle, as it is shown in figure 2.8. In this scheme, at each point along the particle's trajectory a spherical wave expanding with speed c/n is produced. As long as the particle speed is $v < c/n$, wavefronts generated at different points and times do not intersect, but as soon as $v \geq c/n$, wavefronts sum constructively along a conical surface. The aperture angle θ of the cone around the track of the charged particle is known as the *Cherenkov angle* and it can be expressed as

$$\cos\theta = \frac{c/n \cdot t}{\beta c \cdot t} = \frac{1}{\beta n}, \tag{2.1}$$

where $\beta = v/c$ is the adimensional speed of the particle, n the dielectric refraction index and t a generic time interval considered in the geometrical construction. For every given refraction index n the Cherenkov angle is constrained in the range $[0, \arccos\frac{1}{n})$, and increases with the growth of the particle speed. The value of n is related to the dielectric constant ϵ dependent on the wavelength λ but also on the density of the atmosphere[6]. On average, its value is near to unity (e.g. at sea level $\Delta n = n - 1 = 2.76 \times 10^{-4}$ [30]) and hence the aperture of the cone is narrow (for Cherenkov wavelengths the mean value of θ in air is $\sim 1°$). It is interesting to notice that the

---

[6] For details refer to [72, pp. 5].

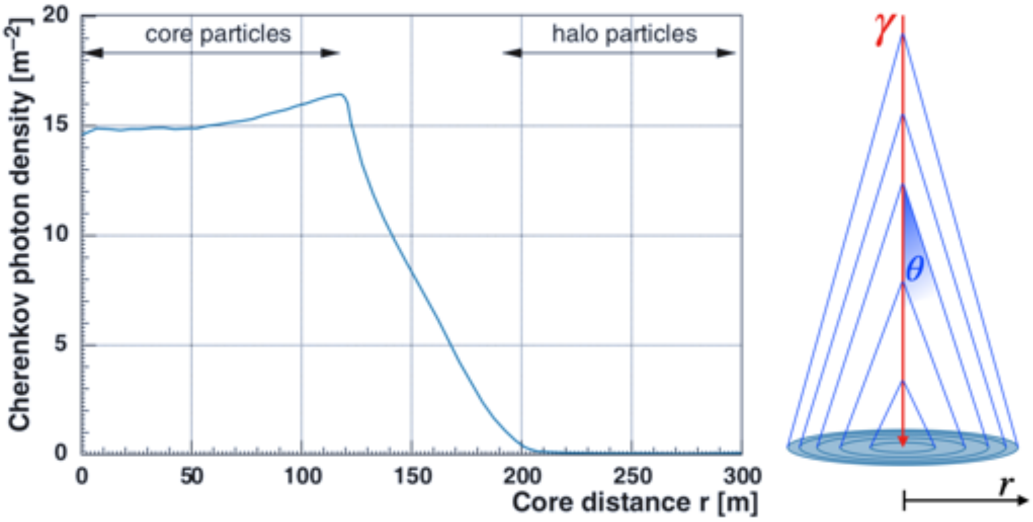

Fig. 2.9: Lateral Cherenkov photon density distribution of a 100 GeV gammaray-initiated shower at an altitude of 2200 m a.s.l. for vertical incidence. Up to 120 m distance the dominant contribution is from the shower core, while light produced by halo particles contributes to the region $r > 120\,\mathrm{m}$ [68] (for a similar plot in the case of hadrons refer to [76], while for energy dependence see [77, 78]).

threshold speed for the Cherenkov effect v_t can be easily converted into a minimum Lorentz factor,

$$\frac{v_t}{c} = \frac{1}{n} \longrightarrow \sqrt{(1-\beta^2)} = \sqrt{(1-\frac{1}{n^2})} \approx \sqrt{(2\Delta n)}\,. \tag{2.2}$$

Using the value of Δn at ground level we obtain $\gamma \approx 40$, therefore the energy threshold ($E = m\gamma c^2$) for the production of Cherenkov radiation is 20 MeV in the case of electrons.

Cherenkov light pool As a consequence of the Cherenkov light emission scheme, an ultra-relativistic particle propagating vertically through the atmosphere creates an annulus of Cherenkov light on the ground, but the sum of the contributions of all the particles involved in the EAS leads to a full circle, the so-called Cherenkov light pool (figure 2.9, *right*). The shape of the light pool is circular for vertical showers, while it results an ellipse if the cascade propagates with some inclination. Considering the typical Cherenkov angle $\theta \sim 1°$ and an average altitude for half of the shower (e.g. 10 km), one obtains that the radius of the light pool is ~170 m, but the photon density is not uniform all over the illuminated area, and hence the

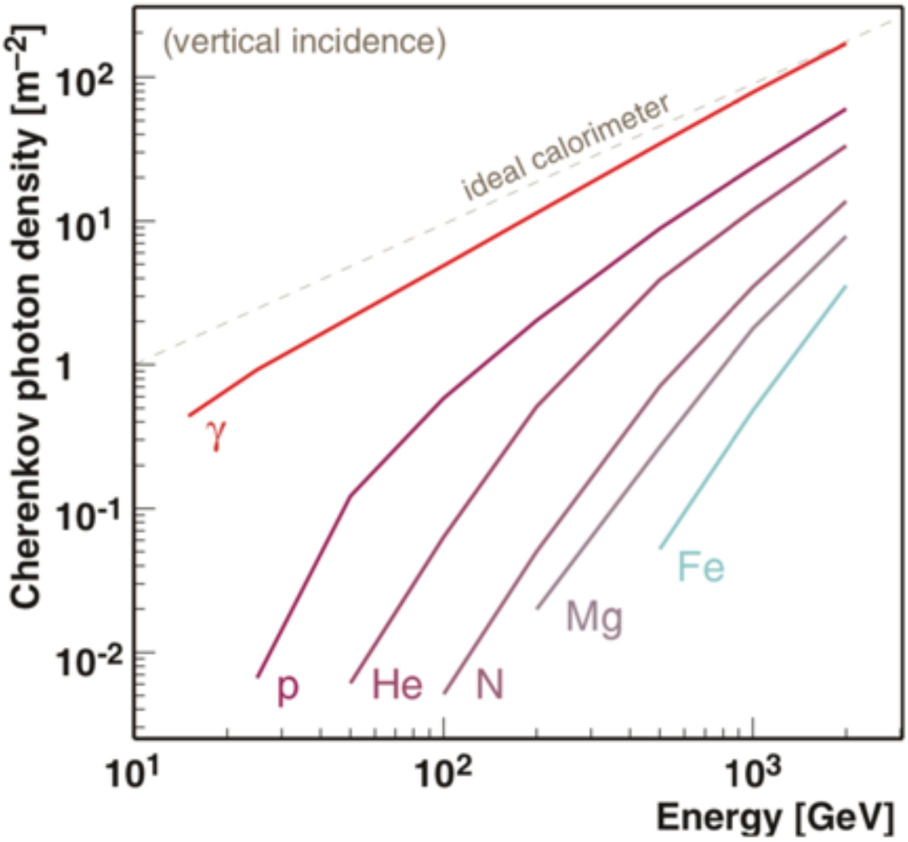

Fig. 2.10: The plot shows the mean Cherenkov photon density within $125\,\mathrm{m}$ of the cascade core for vertically incident showers. For GR initiated air showers, the atmosphere behaves almost like an ideal calorimeter (adapted from [79]).

characteristic radius is usually considered $R_{pool} \sim 170\,\mathrm{m}$, as it is explained hereafter.

In the case of a vertical EAS initiated by a gamma ray, the Cherenkov photons density peaks at a distance of $\sim R_{pool}$ from the core of the cascade, as it is reported in figure 2.9, *left*. This peak is known as the *hump*, and its origin arises from an increase in the opening angle θ due to changes in the refraction index n with the altitude[7]. Inside the hump the photon density is quite uniform, while outside it fades rapidly. For this reason, the radius of the hump is considered the typical radius of the whole light pool.

Only the telescopes inside the light pool can see the EAS, as it will be discussed in section 2.2.2.1. This $\sim 240\,\mathrm{m}$ (diameter) disc on the ground represents the effective *collecting area* of the gamma-ray detector.

---

[7] For a more detailed and accurate description refer to [72].

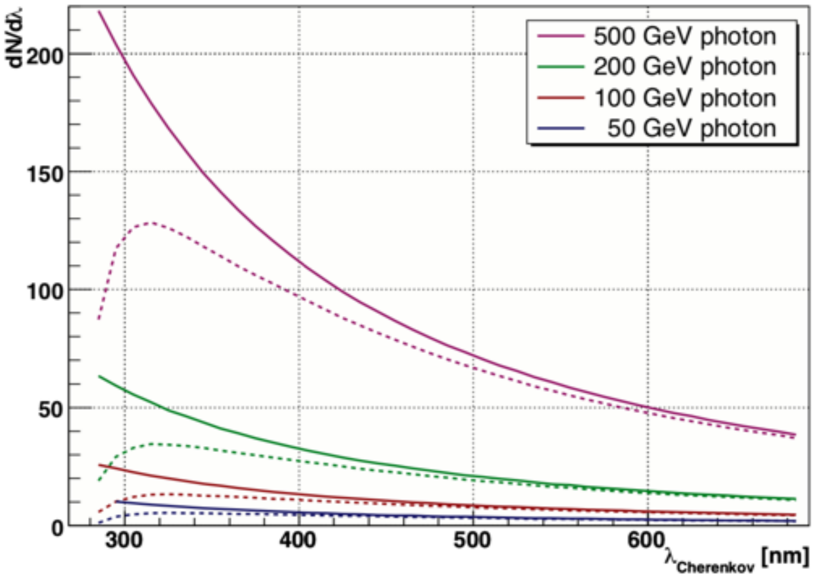

Fig. 2.11: Spectra of Cherenkov radiation produced by vertical EAS initiated by gamma rays at different energies. The solid lines corresponds to the unabsorbed spectra at $10\,\mathrm{km}$ altitude, while the dashed line are the observed spectra attenuated by Rayleigh and Mie scattering as detected at $2200\,\mathrm{m}$ a.s.l. [68].

Cherenkov light spectrum The properties of the photons at the ground level in the Cherenkov light pool depends on both the type of EAS and the characteristics of the atmosphere. The mean photon density inside the pool is related to the energy and the species of the particle originating the EAS. In the case of gamma rays, the photon density is almost proportional to the energy of the primary particle, as reported in figure 2.10, hence it can be used to estimate the energy of the incident cosmic photon. This chance is no more valid in case of different incident particles, like protons or heavy nuclei: in this case the general equation for the number of photons emitted per unit track length dz and per unit wavelength $d\lambda$ is

$$\frac{d^2N_{ph}}{dzd\lambda} = 2\pi\alpha Z^2 \frac{\sin^2\theta}{\lambda^2}\,, \tag{2.3}$$

where α is the fine-structure constant [72]. Integrating this equation in dz, it appears that the flux distribution of Cherenkov photons is inversely proportional to the squared wavelength $dN/d\lambda \sim \lambda^{-2}$. However, there are several attenuation effects in the atmosphere that modify the actual shape of the observed Cherenkov light spectrum. The most important transmission loss in atmosphere is due to Rayleigh scattering off air molecules ($d < \lambda$), with a typical wavelength dependency $\sim \lambda^{-4}$. This phenomenon affects mostly the UV/blue part of the spectrum and it is the dominant contribution during good atmospheric conditions. Another important effect is the Mie scattering[8] off aerosols, dust and water droplets ($d \gtrsim \lambda$), without any strong dependence on the photon wavelength ($\sim \lambda^{-(1 \text{ to } 1.5)}$). Above $\sim$800 nm the strong infrared attenuation is caused by H_2O and CO_2 molecules. Below $\sim$280 nm ozone molecules O_3 are responsible for the absorption of hard UV photons. Since ozone is present at altitudes above 10 km, this introduces a zenith angle dependence on the lower wavelength cutoff of the spectrum, and hence at larger zenith ranges the peak of the Cherenkov radiation spectrum shifts to larger wavelengths. In general, for showers at high zenith angles all the attenuation effects presented above are more intense:cascades develop in the highest layers of the atmosphere and hence particles need to travel a longer path. As a consequence, only EASs initiated by particles at the highest energies are significantly detected by the telescopes at high zenith distance ranges.

Figure 2.11 reports the shape of the Cherenkov spectrum for the case of vertical showers initiated by gamma rays at different energy. The effects of the attenuation processes described above can be recognized in the shape of the spectrum, comparing the observed flux at 2200 m a.s.l with the unabsorbed spectra at 10 km altitude. In particular, it is evident the peculiar characteristic of the peak at $\sim$320 nm, in the UV band, for the spectrum of observed Cherenkov flashes.

2.2 Operating principles

Ultra-relativistic charged particles originated in the EASs travel faster than the speed of light in the air and hence they emit Cherenkov radiation in a very rapid light flash. If an IACT is located inside the light pool of the shower, pointing in its direction, part of the Cherenkov light will be reflected in the telescope's mirrors and collected in the detection camera. The resulting image constitutes a projection of the light emitted by the EAS, and hence through the analysis of its morphological characteristics it is possible to retrieve the properties of the primary particle (energy and direction) that originated the shower. Sections 2.2.1 reports the fundamental concepts of this EAS image analysis, while in figure 2.12 is shown a schematic drawing of the operating principle of IACTs, as it is just been described. Differently from the most of objects that telescopes

---

[8] The scattering of an electromagnetic plane wave λ by a homogeneous sphere of diameter d. It reduces to the Rayleigh scattering when $d \ll \lambda$ [80].

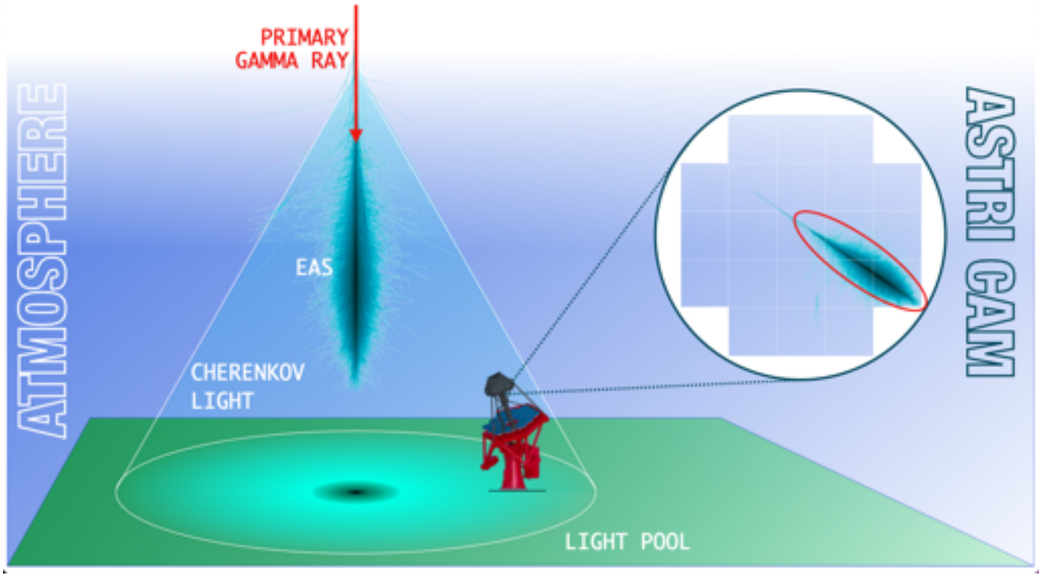

Fig. 2.12: Sketch of the imaging atmospheric technique. The Cherenkov light from the cascade is reflected in the mirrors and collected in the camera.

usually observe, the Cherenkov flashes have two peculiar characteristics: (i) they happen in the atmosphere, and hence IACTs are normally focused at $\sim 10\,\mathrm{km}$; (ii) they have an extremely short lifetime. The typical duration of this phenomenon can vary with the energy of the progenitor, but it is generally about $3\,\mathrm{ns}$ to $9\,\mathrm{ns}$. This fact has important implications on the optical design of IACTs (see section 2.2.3), but also on electronics and detectors, that must be very fast. Nowadays, the most common sensors utilized for the pixels of the IACTs cameras are Photo Multiplier Tubes (PMT, [81]), very efficient and fast ($\sim 3\,\mathrm{ns}$) detectors. However, in recent years the advent of Silicon Photo-Multipliers (SiPMs, [82]) sensors have provided successful results as well and their small size, compared to cumbersome PMTs, has allowed to exploit new and effective optical configurations, such as the dual mirror Schwarzschild-Couder design implemented in the ASTRI telescope (chapter 3).

2.2.1 Imaging analysis of EASs

The image of an EAS on the focal plane of IACTs is a diffuse light spot covering several pixels. The analysis of its topology provides information on the properties of the shower and its progenitor, allowing first of all the discrimination between hadronic and electromagnetic showers. In

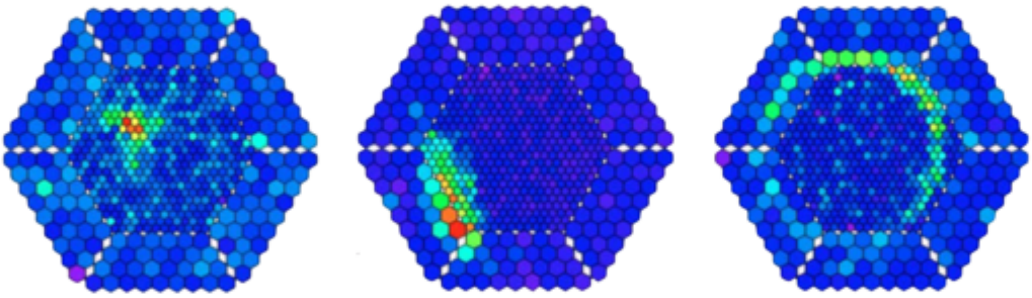

Fig. 2.13: Images recorded by the MAGIC telescopes of the Cherenkov radiation induced by hadron *(left)*, gamma ray *(middle)* and muon *(right)* [adapted from [70]].

fact, as mentioned before, the hadronic shower are much more numerous and they constitute an irreducible background for the gamma-ray observations. Fortunately, the rejection of hadronic events is made effectively with the gamma/hadron separation procedure presented in section 2.2.1.1. However, there are other sources of background, such as muons or cosmic $e^{\pm}$: while the former can be easily rejected because of their typical ring-like images on the camera plane (see figure 2.13), the latter produce electromagnetic cascades identical to those produce by gamma rays and hence they are impossible to be distinguished. Moreover, the diffuse gamma radiation coming from the galactic plane [83] can be also a noise source for specific galactic observations. Lastly, besides the background from the EASs, photons isotropically distributed on the sky can affect the observations as well: this is the so-called Night Sky Background (NSB) that is formed by the stars' light, airglow, polar and zodiacal light, and artificial lights.

2.2.1.1 Gamma–hadron separation

The discrimination between different progenitors is successfully operated through the analysis of the topology of the showers. In general, the diffuse light spot produced by the EAS in the focal plane can be roughly fitted with an ellipse, whose parameters can be effectively used to perform the separation between hadron and electromagnetic signals. Figure 2.13 qualitatively illustrates how in principle this rejection of background can be performed.

Showers initiated by gamma rays tend to be compact and narrow: their shape tends to be roughly elliptical and with rather clean edges. The major axis of the elongated light spot is the projection on the focal plane of the shower axis, therefore pointing to the position of the apparent source direction in the camera coordinate system. Among researchers, these images are nicely called "goldfishes" (figure 2.13, *center*). Inversely, hadronic showers tend to produce wider images, more fragmented and irregular, reflecting the characteristics of their cascades, and are not aligned in general with the supposed source at the center of the field of view, because cosmic rays arrive isotropically (figure 2.13, *left*). Lastly, muons traveling towards the telescope produce characteristic ring–shaped images (figure 2.13, *right*), due to their isolated Cherenkov cone[9]. In the case where the muon impact parameter is large (i.e. the distance between the telescope and the point where the ray hits the ground) the figure will be incomplete and a characteristic light arc will appear in the image.

A refinement of the basic concepts presented here provides an effective procedure for the rejection of the background showers initiated by charged particles. This operation is made with the usage of the so-called Hillas parameters [84], presented in the next section.

2.2.1.2 Hillas parameters

Knowing the brightness of each pixel, the raw image can be adequately described by the position of the centroid and second moments (RMS width and length) of the (noise-cleaned) light distribution. In practice, the possibly complicated image shape of an EAS is reduced to an equivalent ellipse, with length and width as semi-major and semi-minor axes of the light pattern. With this parameterization, it is possible to distinguish very effectively between background hadronic showers and gamma ray showers from a point source. More in details, considering the image recorded and its main axis (the direction best interpolating the signals), the full set of *Hillas parameters* [84] can be defined as follows:

- **length**, the RMS of light in direction parallel to the axis;
- **width**, the RMS of light in direction perpendicular to the axis;
- **frac**, fraction of the total light collected which is contained in the two brightest pixels (i.e. the "concentration" of the image);
- **miss**, the perpendicular distance of the source from the image axis;
- **azwidth**, (or azimuthal-width) the RMS width relative to the axis joining the source with the centroid of the image;

---

[9] Muons are originated in hadronic showers but they can have very large emission angles because of their light weight compared to hadrons.

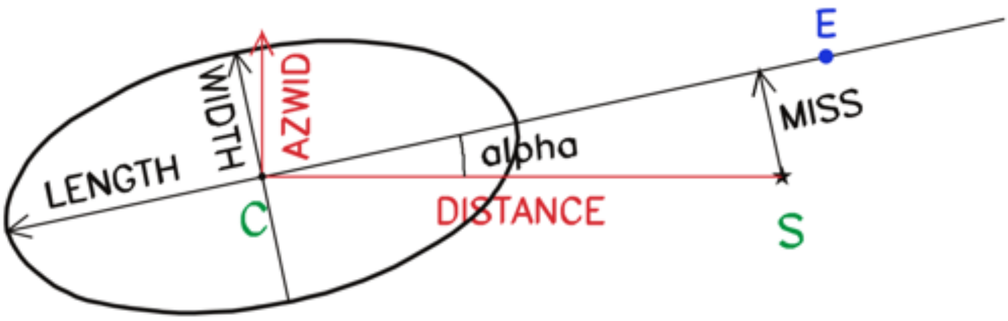

Fig. 2.14: Hillas parameters used in the description of Cherenkov shower images. C represents the signal centroid, while S is the supposed source (center of the field of view). The E point is the source position expected from data, see section 2.2.2 (adapted from[5]).

- **distance**, the distance of the centroid from source.

Figure 2.14 presents these parameters with a conceptual drawing. With 3D Monte-Carlo calculation, simulating both hadronic and electromagnetic showers, it is possible to demonstrate that for each parameter there is a boundary marking off the "gamma domain", containing most gamma images but not many hadrons [84]. In particular, the most effective single parameter is azwidth leading to rejection of over 98 % of hadronic images. The *miss* parameter was subsequently replaced by **alpha** [85], the angle between the image axis and the direction of the (supposed) source. This new parameter presented superior properties to *miss* and soon became an important tool also to announce the detection of a gamma point source with the so-called *alpha-plot*, which is presented in the next section.

2.2.2 Sky sources view

IACTs are peculiar telescopes: they do not record the radiation from the cosmos but from the atmosphere, and hence in their cameras ther is not the formation of images from celestial sources. The way an IACTs actually *sees* a source is through the excess of gamma photons from a specific sky region.

Alpha-plot The detection is carried out comparing the data taken pointing towards the supposed position of the source ("ON" mode) and pointing an empty sky region ("OFF" mode). In case of detection, the histogram

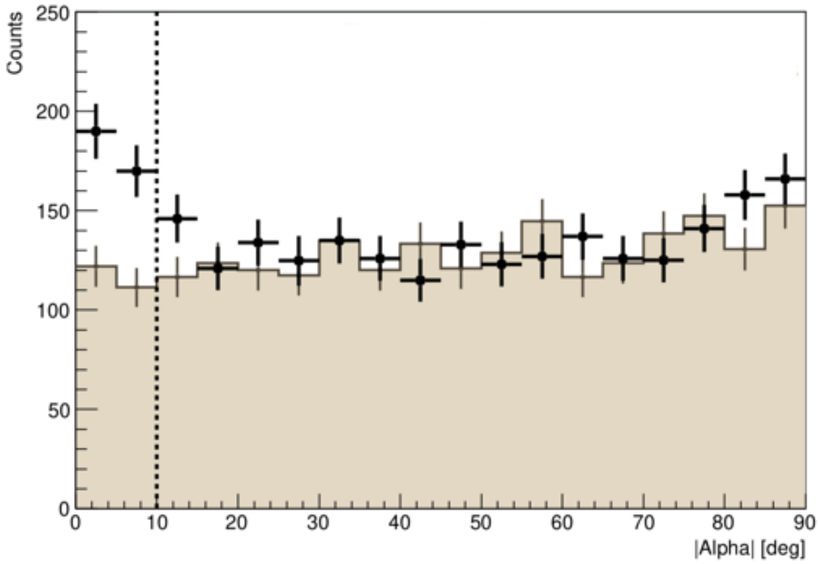

Fig. 2.15: Alpha-plot of the Crab detection with the ASTRI–Horn telescope. with a total of 12.4 h ON-source and 5.4 σ significance [86].

of the alpha parameter will present a peak in 0° for events on-source, with respect to those off-source showing a nearly random distribution. This means that the EASs are mostly oriented to the center of the field of view when the telescope is pointing the position of the supposed source, which is a strong evidence for the actual presence of a gamma ray emitter. Image 2.15 reports the alpha-plot of the first detection of the Crab Nebula with the telescope ASTRI–Horn, and similar plots can be found in the papers of the first detections from other telescopes [86, 87, 88, 5].

False source plot The alpha-plot is a useful tool to present the detection of a point-like source and estimate its flux, but normally it has only a coarse angular resolution and does not provide the possibility to figure out a sky map of the source in case of extended emission regions. To this end, it is necessary to estimate the direction of origin of the photons without assuming that the source is concentrated in the center of the field of view as in the alpha-plot method. Actually, with the analysis of Hillas parameters, it is possible to extract the source position relying only on the observed light ellipse (see the E point in figure 2.14), and hence to obtain for each shower a celestial coordinate associated to the primary gamma ray photon. The cumulative 2D distribution of the photons will provide a representation of the morphology of the source, showing the regions with

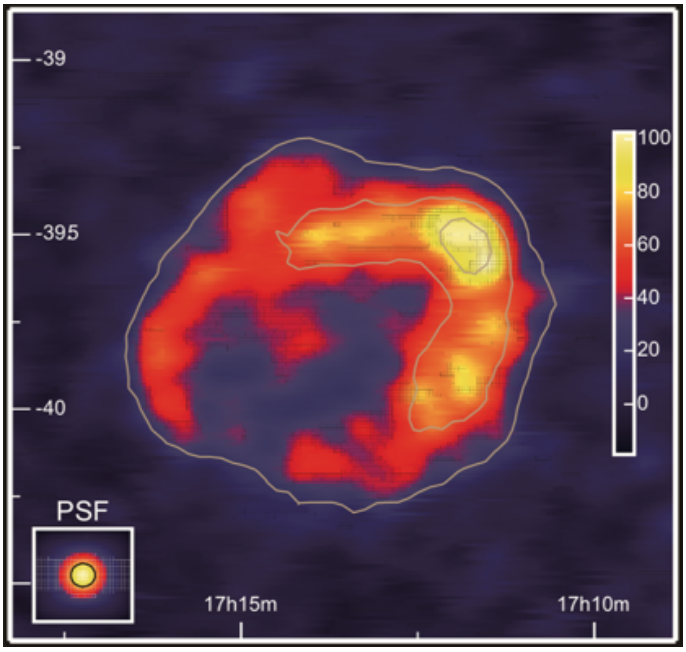

Fig. 2.16: Sky map (false method plot) of an extended gamma ray source with the HESS telescope (see section 2.3.1) [89]. The object is a shell-type SNR (`RX J1713.7-3946` [*link* 273]) while the plot is smoothed with a $\sigma 2'$ Gaussian, which is denoted as black circle in the inset. See also [90] for observations with increased angular resolution.

the most intense emission. This technique is often referred to as *false-source plot* (or false-method) and an example[10] is reported in figure 2.16. The angular resolution of such images is much better than the typical bin width of alpha-plots, and it doesn't correspond to the optical point spread function of the instrument nor the field of view of each pixel, as the telescope is observing the atmosphere, not the sky sources. The actual sky angular resolution of an IACT can be estimated through the so called *theta-squared plot*, which is presented in the next section together with a powerful technique to increase the angular resolution: the stereoscopic vision.

2.2.2.1 Stereoscopic vision

Estimating the source position E through the analysis of the hillas parameters, it is possible to compute the angular distance θ by which the apparent arrival direction of any gamma-like shower differs from the direction

---

[10] The process of creation of a false plot is described in an illuminating animation available online [*link* 236].

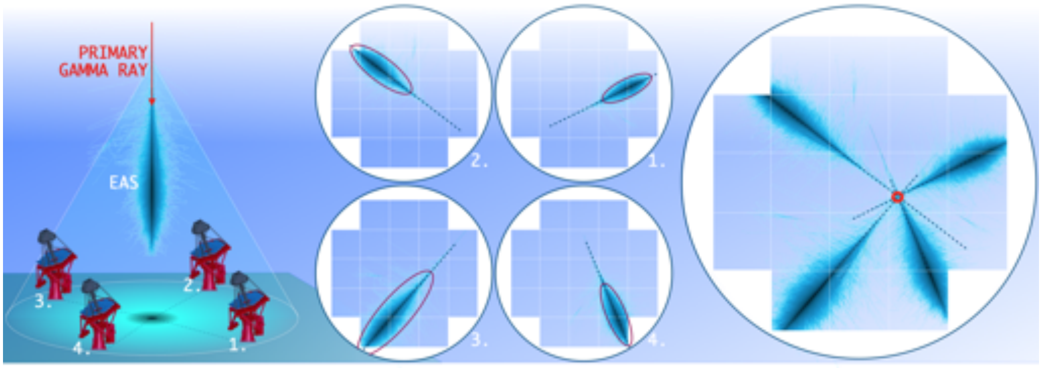

Fig. 2.17: Conceptual drawing representing the stereoscopic view strategy. The Cherenkov light produced by the EAS initiated by a gamma ray (*left*) is recorded by four ASTRI telescopes (*center*): the stereoscopic analysis (*right*) provides an accurate reconstruction of the original gamma-ray photon direction of origin.

of some supposed source S. Considering an histogram, similarly to the alpha-plot, for background events there should be a uniform distribution in θ^2, while for a true source there should be an excess[11] of events at very small θ^2. It is important to note that α is the angle subtended by the segment $\overline{ES}$ in the camera coordinate system, while θ is the conversion of the distance $\overline{ES}$ in angular units using the plate scale of the telescope (see section 2.2.3). Consequently, *theta-square plots* allow to define the true angular resolution of the IACT, defined as the angular radius θ_{68} containing the $68\,\%$ of the "on-source" excess signal, with the threshold energy adopted for the selection of the events [5].

Especially at low energy scales where the cosmic flux is more abundant, a good angular resolution is fundamental both to separate the contribution from different sources and to retrieve the shape of extended emission regions. For this reason, in modern IACTs observatories, the estimation of the source position is improved with a powerful technique: *the stereoscopic view*. With two or more telescopes several meters apart, pointing in the same direction, the light from every shower is recorded under different perspectives, creating different images whose main axis intersect in correspondence of the source. This method provides an improvement of the angular resolution[12] of the IACT technique and traditionally its imple-

---

[11] The same argument applies also to the θ distribution, but θ^2 allow a better visualization of the narrow peak.

[12] Actually, when the impact parameter is very large, and hence the intersection angle is very small, the average of the positions E extracted with the Hillas parameters could be a better approximation (see [5, fig.14] for more details).

mentation marks the beginning of the “third generation” of instruments: arrays of imaging telescopes operating stereoscopically. Figure 2.17 reports a graphic representation of the stereoscopic technique.

2.2.3 Optics

Unlike other astronomical telescopes, to study the cosmic radiation IACTs observe atmospheric phenomena: fast, faint and diffuse Cherenkov flashes. For this reason, the characteristics of their optical design have to cope with peculiar requirements.
First, to avoid contamination of the shower images with night sky background photons, the exposure must be matched to the intrinsic duration of the Cherenkov light pulse from atmospheric cascades, less then $10\,\mathrm{ns}$. Therefore, unlike in conventional optical astronomy, the image cannot be improved integrating for long exposures. This motivates the development of optical systems with very large primary mirrors, having diameters in the range of $10\,\mathrm{m}$ to $30\,\mathrm{m}$, to collect as much light as possible. In addition, the optical systems of IACTs must be composed of the minimal number of elements, typically one, to circumvent light loss. Lastly, the time spread of the optics must be very small, as also the temporal evolution of the Cherenkov shower is an important element for scientific analysis.

Notation Before focusing on the considerations of the next sections, it is important to spend a few lines to clarify the notation of the present thesis. The very basic elements of optics to describe the configuration of an IACT (as for every other telescope) are the focal length f, the primary mirror raw aperture D, the focal ratio $f_{/} = f/D$ and the plate-scale P_S of the instrument. In particular, the plate-scale connects the angular extension of an object θ with the linear dimension s of its image at the focal plane [91],

$$P_S = \theta/s = 1/f\,, \tag{2.4}$$

and it is usually measured in $'/\mathrm{mm}$ or equivalently $'/\mathrm{px}$.

2.2.3.1 Davies–Cotton design

The Davies-Cotton (DC) design is the most common optical configuration among IACTs. It consists in spherical panels of focal length $2f$ on a sphere of radius f, equal to the focal length of the system [72]. With this configuration, free of spherical aberration, even for inclined rays some facets

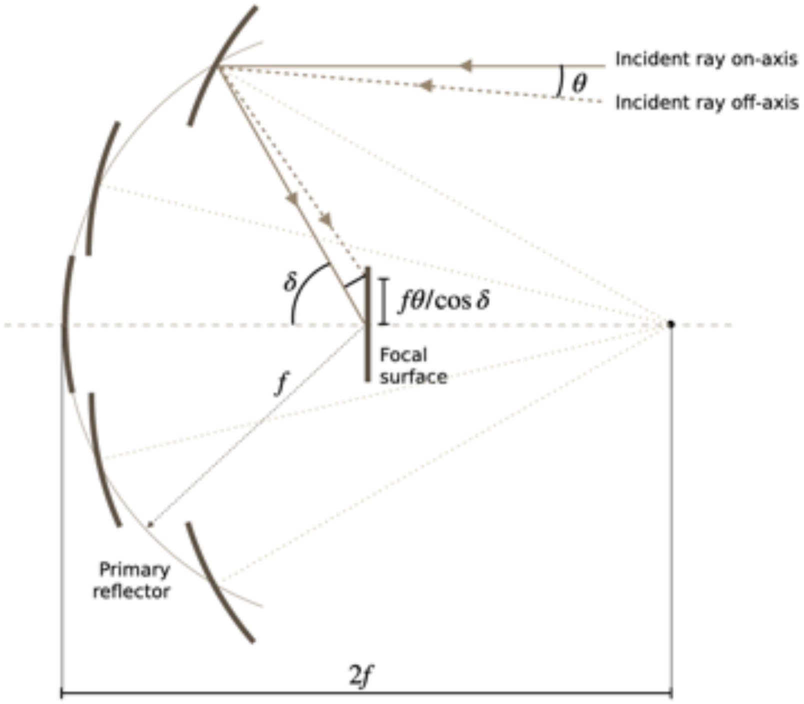

Fig. 2.18: Scheme of the Davies–Cotton optical design (adapted from [96]).

are on-axis, thus reducing the coma aberration, which remains anyway the most important limit of this optical design.A very common modified version of this optical configuration is obtained by arranging the spherical facets, with increasing focal length, along the surface of a parabola, in order to reduce the time spread and obtain an isochronous telescope [92].
In origin, the DC configuration was not conceived for astronomical purposes, but it was developed for solar concentrators [93]: facilities where the solar light is focused for producing energy. However, nowadays the DC is widely spread among IACTs ([92, 94, 95], and [76, Appendix A]) because of the following features: first, it is inexpensive to build, as all the facets are identical; second, the alignment is trivial, as the facets are spherical; third, the performance at large field angles is better than that of a single spherical or parabolic reflector [65].
The most important limit of this optical design is that the coma aberration cannot be removed in such a single mirror system, because in general n reflecting surfaces at least are necessary to correct n aberrations[13] [97].

---

[13] This very general result is sometimes referred to as the *Schwarzschild theorem* of optics.

Moreover, in this configuration it is impossible to implement modern and efficient Silicon PhotoMultipliers (SiPMs, [98]) detectors on the focal plane, because their small dimension compared to PMTs would lead to a useless oversampling of the point spread function (PSF), making unacceptable the effort of maintaining a camera with an impressing high number of sensors [99, 92]. The only chance to implement miniaturized detectors would be to increase the plate-scale of the instrument, so reducing the focal length, which would have disastrous consequences on a DC telescope because of the primary aberrations which behave as negative powers of f. However, having an *aplanatic* telescope (i.e. free of coma and spherical aberrations) the possibility to shorten the focal length would become more interesting.

2.2.3.2 Schwarzschild–Couder design

In 1905 Karl Schwarzschild invented a new aplanatic optical configuration [100], composed of two reflecting surfaces, and in 1926 it was enhanced by André Couder [101], who introduced a curved focal plane to reduce the astigmatism aberration. At that time, it was impossible to manufacture a mirror surface with the correct geometry, and hence the Schwarzschild-Couder (SC) design was forgotten for almost a century. In 2002 Lynden-Bell, starting from this pioneering work, proposed a solution for exact optics in aplanatic telescopes [102], but it was only in 2007 that Vladimir Vassiliev proposed to recover that configuration, with adequate modern improvements, to develop a new optical design for IACT application [99]. The ultimate purpose is to extend the highest limit of the gamma ray observable range with IACTs. To this end, a wide FoV is mandatory, because the most energetic photons originate longer showers, visible even if they have an impact parameter of few kilometers, hence producing very elongates images on the focal plane. Moreover, a large FoV means a wider overlap for the stereoscopic analysis, and it allows in principle a larger displacement of the telescopes on the ground, hence increasing the collecting area. This leads to the requirement of a small f, but this in turn unavoidably implies that aberrations become dominant and the plate-scale gets larger, ruining the resolution of the instrument.

The advent of miniaturized SiPM sensors [82] to cover the focal plane of IACTs has permitted to find a balance between the competing requirements of adequate plate scale, tolerance to aberrations, large field of view and large telescope aperture, exploiting the possibility of new optical configuration such as the dual mirror SC design, with its enhanced optical

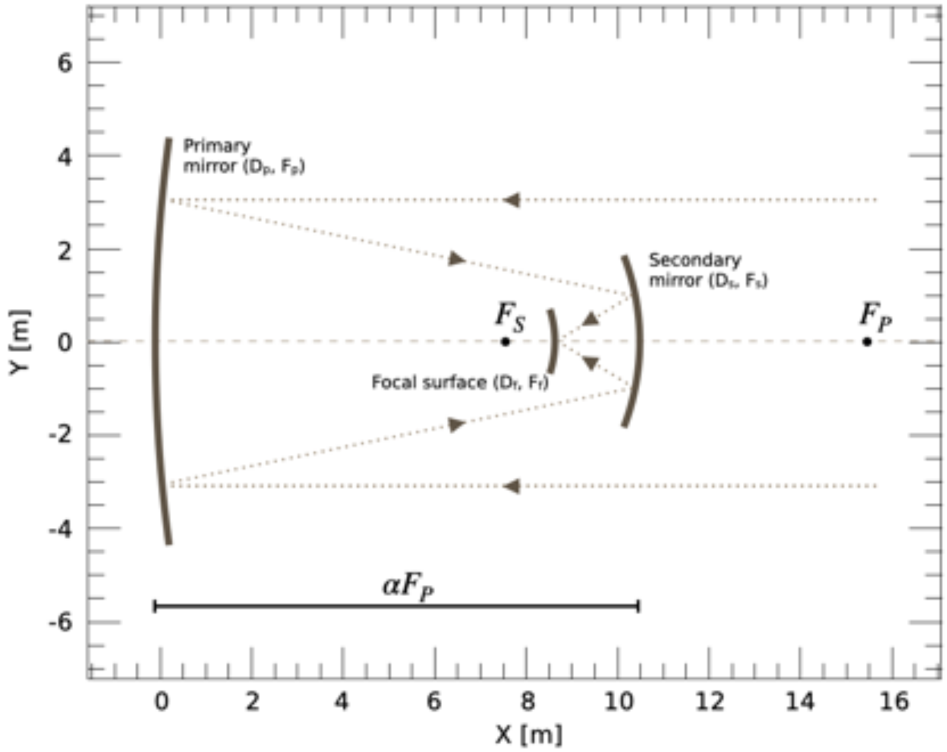

Fig. 2.19: Scheme of the Schwarzschild–Couder optical design (adapted from [99]).

properties[14].

The most important disadvantage of the SC configuration is that the double reflection reduces the effective area of the telescope, both for the shadow of the secondary mirror and for the reflectivity of the surfaces that is never equal to $100\,\%$. Moreover, the short focal length makes the system more difficult to be managed in general, as it will result very sensitive to little variations in the alignment and positioning of optical elements. Lastly, the light rays will arrive on the camera surface with high incidence angles, thus requiring a good behavior relative to refraction for the material of every possible filter or shield in front of the sensors. The SC configuration was implemented in the realization of two new types of telescopes: SCT [103**?**] described in section 2.3.4, and ASTRI [104], to which is specifically dedicated the chapter 3 but also the whole thesis.

---

[14] In optical astronomy a well-known example of aplanatic system in the Cassegrain configuration is the Ritchey-Chretien design (Hubble, Keck, VLT, WIYN etc.). In this case the second mirror increases the focal length while in the SC design it has the effect to shorten f.

2.3 Examples of IACTs

In this section we present a brief overview of the major IACTs currently in operation: HESS, VERITAS and MAGIC, whose main features are reported in table 2.1, together with the next-generation CTA Observatory that is in an advanced state of development at present. Traditionally, in the so-called *third generation* of IACTs [5] are included also the CANGAROO experiment [64], dismissed in 2011, and the HEGRA apparatus[15] [105, 106] dismantled in 2002. In very recent years, also twenty Cherenkov telescopes have been realized for the LHAASO experiment, already described in section 1.2.4.3.

Name	Telescopes	Energy range	FoV	Resolution
HESS	5	0.030–100 TeV	3.2° – 5.0°	0.08° – 0.14°
VERITAS	4	0.050–50 TeV	3.5°	0.1° – 0.14°
MAGIC	2	0.025–30 TeV	3.5°	0.08° – 0.17°

Table 2.1: Details of current Cherenkov telescopes.

2.3.1 H.E.S.S.

H.E.S.S. is a system of five IACTS located in Namibia, investigating cosmic gamma rays in the energy range from $30\,\mathrm{GeV}$ to $100\,\mathrm{TeV}$. The name H.E.S.S. stands for High Energy Stereoscopic System, and is also intended to pay homage to Victor Hess, for his discovery of cosmic radiation. The first four telescopes went into operation in December 2003 (H.E.S.S. I, [107]), while a much larger fifth telescope (H.E.S.S. II, [108]) is operational since July 2012, extending the energy coverage towards lower energies and further improving sensitivity. In particular, the H.E.S.S. II telescope has a parabolic reflector of $36\,\mathrm{m}$ focal length consisting of 850 individual mirrors, with a an impressing diameter of $28\,\mathrm{m}$ and a total mass of almost $600 \times 10^3\,\mathrm{kg}$. The four H.E.S.S. I telescopes present a spherical DC optical layout, with a focal distance f of $15\,\mathrm{m}$ combined with a characteristic dish size D of $13\,\mathrm{m}$. The camera is endowed with PMTs and supported by four arms. It presents a FoV of $5°$ diameter and a pixel size of $0.15°$, resulting in 960 pixels for each camera. In front of PMTs there are non-imaging light concentrators (in particular, Winston cones [109]) to reduce dead areas at

---

[15] Web page still available [*link* 246].

Fig. 2.20: Picture of the HESS telescope in Namibia (taken from [*link*247]).

the outer edges of PMTs due to their circular shape and the support structures, but also to limit the solid angle viewed by each PMT hence reducing noise due to stray light. A guide telescope mounted off-axis on the dish and equipped with a CCD camera provides arc-second pointing resolution for each of the five telescopes [92].

2.3.2 VERITAS

VERITAS (acronym of *Very Energetic Radiation Imaging Telescope Array System*) is a ground-based gamma-ray telescope operating at the Fred Lawrence Whipple Observatory (FLWO) in southern Arizona, USA. It is an array of four optical reflectors, optimized for the energy band between $50\,\mathrm{GeV}$ and $50\,\mathrm{TeV}$, with maximum sensitivity from $100\,\mathrm{GeV}$ and $10\,\mathrm{TeV}$. The optics of each VERITAS telescope follows the Davies–Cotton configuration, with a $12\,\mathrm{m}$ raw aperture equal to the focal length of the instrument ($f_/ = 1$), covered by 350 identical hexagonal spherical mirrors, of area $0.322\,\mathrm{m}^2$ and radius-of-curvature of approximately $24\,\mathrm{m}$, giving a total reflector area of $110\,\mathrm{m}^2$ [94]. The use of hexagonal facets allows the full area of the optical support structure to be exploited. The increased $f_/$ with respect to the Whipple telescope ($D = 10\,\mathrm{m}$, $f_/ = 0.7$) introduced a remarkable improvement in the optical quality of the telescopes, by reducing the effects of aberrations. This enhancement was fundamental as the displacement of the 499 PMTs on the focal surface ensured a better angular resolution: each PMT is $25\,\mathrm{mm}$ diameter, and the maximum distance between their centers

Fig. 2.21: Picture of the VERITAS telescope in Arizona (USA) (taken from [*link* 278]).

equals to $0.15°$. In front of the camera there is an array of 499 light cones, funnels with a hybrid of the Winston light concentrator design, optimizing the efficiency of the VERITAS camera made of circular PMTs arranged in a hexagonal pattern [110]. An auxiliary optical telescope is adopted for the pointing.

2.3.3 MAGIC

MAGIC (acronym of *Major Atmospheric Gamma Imaging Cherenkov Telescopes* [*link* 258]) is an instrument composed of two telescopes located at the Observatorio del Roque de los Muchachos, on the Canary island of La Palma (Spain). The observatory is located at the top of an extinct volcano, with the MAGIC telescopes at an altitude of $2200\,\mathrm{m}$ above sea level, in a site among the best locations for optical astronomy all over the world, due to the favorable weather conditions and the low artificial light pollution. The construction of the first telescope (MAGIC-I) was completed in 2004 and it was operated in standalone mode (monoscopic observations) until 2009, when the second telescope (MAGIC-II) was completed, $83\,\mathrm{m}$ apart along the SW–NE axis. The energy range of MAGIC ranges between $25\,\mathrm{GeV}$ and $30\,\mathrm{TeV}$, and it was originally conceived in 1998 [76] with the main goal of being the IACT with the lowest possible gamma energy threshold so to cover the energy gap between space-based instrument (e.g. EGRET onboard the CGRO satellite) and the previous generation of ground-based telescopes [88].
The two telescopes have a diameter of $17\,\mathrm{m}$, equal to the focal length ($f_/ = 1$), and a total reflecting surface of $236\,\mathrm{m}^2$. They present a parabolic shape

Fig. 2.22: Picture of the MAGIC telescope in LA Palma, at Canary Islands, Spain (Credit: G.Ceribella [*link* 259]).

($z = r^2/(4f)$), to ensure the isochrony of the reflected light, while the number of spherical mirrors is different (964 facets for MAGIC-I and 247 $1\,\mathrm{m}^2$ mirrors for MAGIC-II) and their focal length varies with the distance from the optical axis. The orientation of each mirror is adjusted several times during the observations by software-controlled actuators [111], maintaining the ideal configuration to keep the telescope focused to about $10\,\mathrm{km}$, the typical distance of the EAS maxima for the energies at which MAGIC operates [112].

The MAGIC camera has $1.5\,\mathrm{m}$ diameter, $450\,\mathrm{kg}$ weight and $3.5°$ FoV. The inner hexagonal area is composed by 397 $0.1°$ FoV hemispherical PMTs of $25\,\mathrm{mm}$ diameter, surrounded by 180 $0.2°$ FoV PMTs of $39\,\mathrm{mm}$ diameter [81]. The PSF on-axis[16] is about half a pixel ($\sim 10\,\mathrm{mm}$), corresponding to an angular size of $\sim 2'$. Winston cones light guides are adopted to concentrate the incoming radiation into the PMTs increasing the efficiency of the camera [113]. A close-up view of the light cones is reported in figure 2.23.

---

[16] In this optical design the PSF off-axis has larger dimension (see section 3.2 for comparisons).

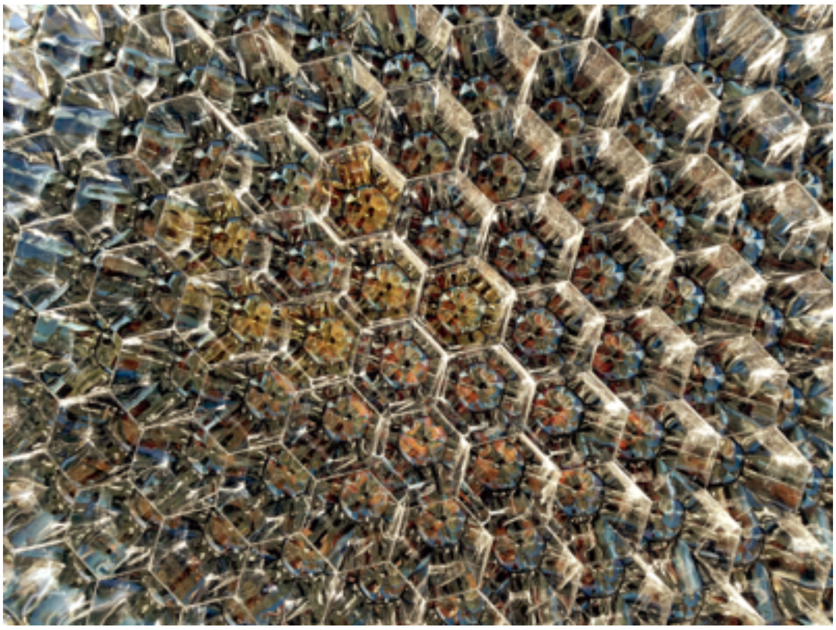

Fig. 2.23: Close-up view of the MAGIC camera light guides (photo credit: C.Righi). This picture was presented in the scientific photography exhibition reported in appendix C.

2.3.4 CTA

CTA stands for *Cherenkov Telescope Array* and it is the future generation of ground-base observatory to study the VHE gamma rays. It is planned to have 118 IACTs in total, distributed between two sites: the Northern array will be located in La Palma, at El Roque de los Muchachos along with the MAGIC telescopes; the Southern site will be placed in the Paranal Observatory (Chile). The full energy range of CTA will be between $20\,\mathrm{GeV}$ and $300\,\mathrm{TeV}$, and three classes of telescope types will be adopted to cover such a wide energy band. Eight Large-Sized Telescopes (LSTs), four per each site, will work in the energy range below $100\,\mathrm{GeV}$. Seventy Small-Sized Telescopes (SSTs) will be located at the Southern site to study the

Specification	LST	MST	SST
Mirror diameter	$23\,\mathrm{m}$	$12\,\mathrm{m}$	$4\,\mathrm{m}$
Energy range	10–500 GeV	0.1–10 TeV	1–300 TeV
Telescopes	8	40	70

Table 2.2: Specifications of the three classes of CTA telescopes (see [*link* 237] for more details).

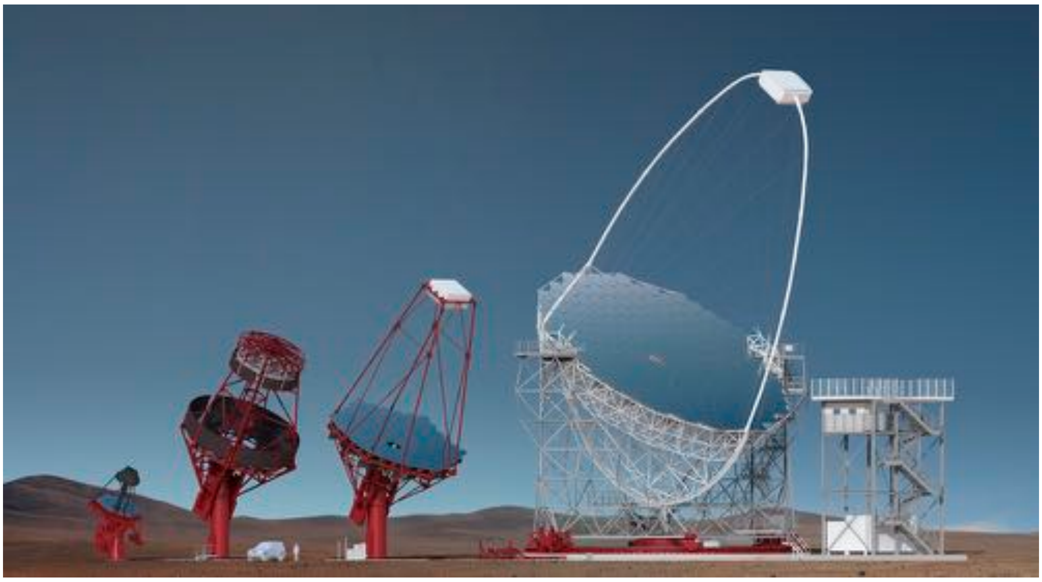

Fig. 2.24: Rendering of telescopes for CTA. LST on the right, ASTRI on the left, while two prototypes for the medium size telescopes (SCT and MST) are in the middle (taken from [*link* 237]).

energy range above $10\,\mathrm{TeV}$. Lastly, for the core energy range ($100\,\mathrm{GeV}$ to $10\,\mathrm{TeV}$), CTA is planning forty Medium-Sized Telescopes (MSTs), 15 in the Northern site and 25 in Chile. Each of the three classes of telescopes correspond to different working sub-groups within the Collaboration. Figure 2.24 shows a rendering of the prototype telescopes, while table 2.2 provides a summary of these three classes, whose main characteristics will be discussed in the following paragraphs.

2.3.4.1 Large-Sized Telescope (LST)

The LST telescope is designed to work in the low energy range, down to $20\,\mathrm{GeV}$, where gamma rays photons produce a small amount of Cherenkov light, and hence a very large mirror is required to capture their image. For this reason, LST is an alt-azimuth telescope with a $23\,\mathrm{m}$ raw aperture for a total reflective surface of $\sim 370\,\mathrm{m}^2$ [114]. The optical design is based on a parabolic configuration with a $28\,\mathrm{m}$ focal length, accommodating 198 spherical segmented mirrors with hexagonal shape of $1.51\,\mathrm{m}$ side-by-side size [115]. The whole telescope is supported by a tubular structure made of reinforced carbon fibre and steel tubes: although it stands $45\,\mathrm{m}$ tall and weighs around $100 \times 10^3\,\mathrm{kg}$, LST is extremely nimble and is able to reposition within $20\,\mathrm{s}$, allowing very fast transient sources follow up.

Fig. 2.25: Picture of the LST-1 prototype telescope in La Palma (photo credit: C.Righi). This photograph was presented in the scientific exhibition reported in appendix C.

The camera weights about $2 \times 10^3\,\mathrm{kg}$ and it is composed by 1855 $0.1°$ FoV PMTs, equipped with light concentrators, providing a total FoV of $4.5°$ [116]. Recently, an interesting study was carried out about the possibility to replace the PMTs with more efficient SiPM [117], but initial design is not changed so far.

The construction of the LST prototype, LST-1, was completed in October 2018 in La Palma, Canary Islands (Spain), on the site of the Observatorio del Roque de los Muchachos. The prototype is foreseen to become the first LST telescope of CTA, and actually it is the first telescope on a CTA site, to be operated directly by the CTA Observatory (CTAO). Figure 2.25 shows a beautiful picture of the LST-1 prototype.

2.3.4.2 Medium-Sized Telescope (MST)

CTA will host 40 MST to cover the core energy range between $100\,\mathrm{GeV}$ and $10\,\mathrm{TeV}$. Currently, there are two alternative types of medium-sized telescopes available for CTA, named MST and SCT, that are briefly presented below.

MST The first prototype is called MST, acronym of *Medium Size Telescope*[17], a single-mirror instrument with an alt-azimuth mount. The optics is arranged as a modified Davies–Cotton design: a tradeoff to optimise the PSF over a large fraction of the Cherenkov camera's FoV and to improve the isochronocity of the reflector. The mirror is tessellated and consists of 86 hexagonally-shaped segments with $1.2\,\mathrm{m}$ flat-to-flat side length. The mirrors are mounted on a sphere of $19.2\,\mathrm{m}$ radius. The distance between the imaginary central mirror and the focal plane of the camera is $f = 16.0\,\mathrm{m}$, while the spherical mirror segments themselves have a radius of curvature of $32.14\,\mathrm{m}$, i.e. approximately twice the focal length, and are aligned to reflect rays parallel to the optical axis into the focal point. The diameter of the aperture is $12\,\mathrm{m}$ [118]. The structure of the telescope is made out of steel, to ensure sufficient stiffness under varying elevation angles, without the need of active mirror alignment during the observation. In the phase of initial telescope assembly, a set of actuators are used to align the individual mirrors forming a homogenous reflector, collecting the light on the focal plane where the Cherenkov camera is located. In particular, up to now there are two alternative pixelized Cherenkov cameras designed for the MST, both endowed with PMT sensors: NectarCAM and FlashCAM [119]. The pointing calibration for MST makes use of a single, wide FoV CCD camera installed in the dish center, aligned to the optical axis of the telescope and facing the Cherenkov camera. The FoV of this camera is chosen sufficiently large to observe both the star field (to determine the direction of the optical axis) and the pointing LEDs mounted on the Cherenkov camera body (to determine its orientation w.r.t. the optical axis) [120]. A prototype was built in 2013 in Adlershof, Berlin, for tests and serial production preparation of mainly the optical and mechanical systems [121].

SCT The second prototype is **SCT**, acronym of *Schwarzschild–Couder Telescope*, which is a dual-mirror instrument and the only one in the world with a pure SC optical design. The first mirror aperture is $9.7\,\mathrm{m}$ in diameter, while the secondary mirror is $5.4\,\mathrm{m}$, and the focal length of the system is $f = 5.6\,\mathrm{m}$. Both the reflectors are segmented and endowed with an active alignment system [122]. The large plate scale of the optical system allows densely packed miniaturized SiPM to be used for the Cherenkov camera, which will present $\sim 7.6°$ FoV and $11\,328$ pixels in total (resolution

---

[17] The prototype telescope shares the same name with the CTA class of telescopes.

Fig. 2.26: The prototype telescope pSCT.

$0.067°$). Up to now, a prototype telescope (pSCT, see figure 2.26) has been constructed at the Fred Lawrence Whipple Observatory in Arizona (USA), with the main goals to demonstrate the performance of the optical system and gain experience with the optical alignment and operation of the SiPM camera. It presents a reduced configuration of only 1600 pixels covering a FoV of $2.7°$ [123]. It was officially inaugurated on 17 January 2019, and within the first year of operation it carried out the detection of the Crab Nebula with a statistical significance of 8.6 σ [87].

2.3.4.3 Small-Sized Telescope (SST)

The Small-Sized Telescopes (SSTs) will outnumber all the other telescopes with 70 instruments planned to be spread out over several square kilometers in the Southern hemisphere array only. SSTs are designed to work in the highest energy range, where gamma-ray showers produce a large amount of Cherenkov light over a large area, and hence their primary aperture is smaller compared to MSTs and LSTs, while their FoV is wider and their arrangement is larger on the ground. Originally, there were three different SST prototypes proposed for CTA: ASTRI [124], GCT [125] and SST-1M [126]. After a long harmonization process the CTAO decided that the CTA-SST design should be based on the ASTRI design, taking

Fig. 2.27: Picture of the prototype CHEC Cherenkov camera (Credit: C.Foehr/MPIK).

into account the experience gained from all others. A rendering of the current proposed SST design is reported in figure 2.28. The mechanical structure is identical to the one implemented in the ASTRI MiniArray, as well as the optical design, described in detail in chapter 3. It is based on a dual-mirror modified[18] Schwarzschild-Couder aplanatic configuration, with a $4.3\,\mathrm{m}$ primary mirror segmented into hexagonal facets and $1.8\,\mathrm{m}$ monolithic secondary mirror. However, the SST Cherenkov camera is different from the MiniArray: SSTs will be endowed with the CHEC SiPM Cherenkov camera, consisting of 2048 silicon photo-multiplier pixels forming approximately a $9° \times 9°$ field of view [127] (figure 2.27.

---

[18] See section 3.2 for details.

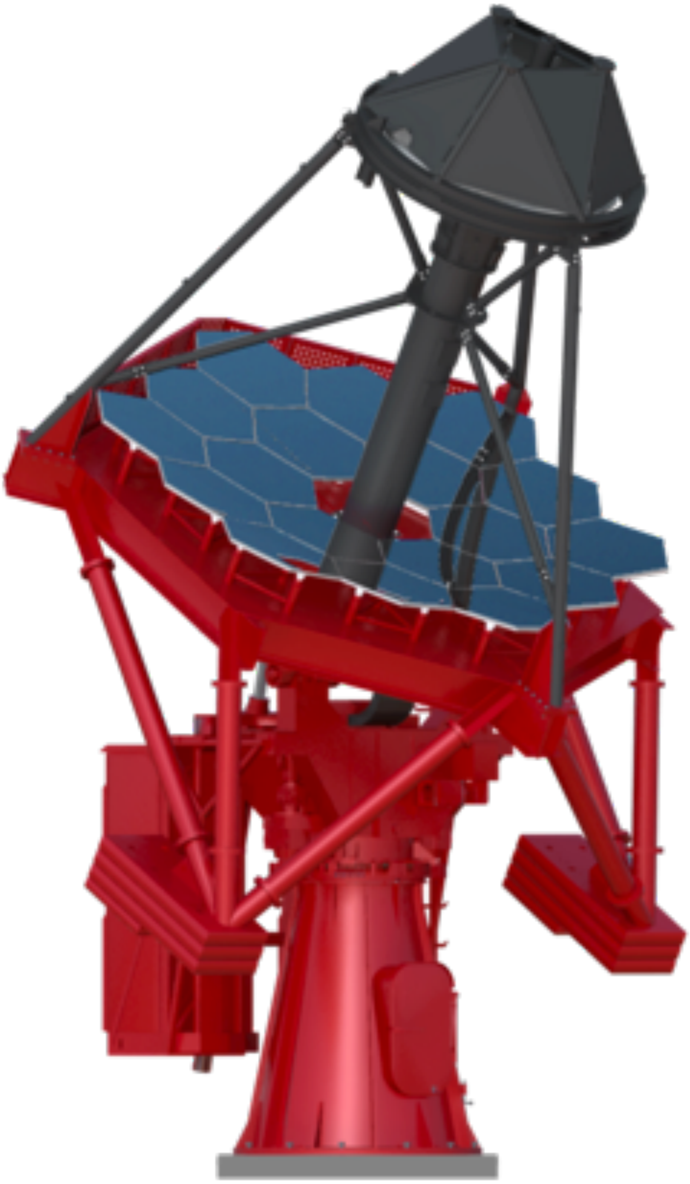

Fig. 2.28: Rendering of the current ASTRI design for the CTA's SST telescopes (taken from [*link* 237]). This mechanical structure is optimized with respect to the first version adopted for the prototype ASTRI–Horn. Together with the CHEC camera (figure 2.27), 70 identical telescopes with this design will be implemented in the incoming observatory CTA.

3

The ASTRI project

ASTRI is a project aiming at the study of VHE cosmic radiation thanks to the end-to-end development of a new class of IACT, presenting several technological novelties in both the optical design and the acquisition chain [*link* 225]. The name ASTRI is the acronym of *Astrofisica con Specchi a Tecnologia Replicante Italiana* (astrophysics with Italian replicant technology mirrors) with explicit reference to the process for the realization of the mirrors developed by INAF, which is applied today also to the reflectors of other instruments [128]. The ASTRI telescopes were originally conceived as SSTs for CTA (see section 2.3.4.3), but today the project is more ambitious and articulated: after the success of the prototype telescope ASTRI–Horn in Italy, it is currently under development the realization of an array of nine ASTRI telescopes, to be installed in the Canary Islands as a pathfinder for CTA: the ASTRI MiniArray. The whole project is supported by the Italian Ministry of Education, University, and Research (MIUR) with funds specifically assigned to the Italian National Institute for Astrophysics (INAF, [*link* 255]), to lead a collaboration of different institutions, such as the Universidade de Sao Paulo (Brazil), the North-West University (South Africa) and the National Institute for Nuclear Physics (Italy) and the Istituto de Astrofisica de Canarias (Spain).

This chapter is dedicated to the presentation of the peculiar features of the ASTRI telescopes: the optical configuration is explained in section 3.2,

Fig. 3.1: The ASTRI–Horn prototype telescope on Mount Etna, in Italy (Credit E. Giro).

while the special characteristics of ASTRI Cherenkov camera, developed by INAF, are reported in section 3.3. To begin, the next section contains an overview of the ASTRI–Horn prototype telescope, the MiniArray project, and the whole scientific program.

3.1 Overview

The ASTRI telescope is an innovative instrument, developed by INAF in all its components, following an end-to-end approach for the first time, from the design phase to the realization and the final data analysis. The major novelty is the optical system, presenting a modified Schwarzschild–Couder design: ASTRI is actually the first IACT in the world with a dual-mirror configuration, a very innovative solution. In fact, despite some technical difficulties related to the production of aspheric mirrors and the managing of the system (e.g. in the alignment procedure), there are several advantages in adopting this optical scheme. In particular, it provides a

short focal length, resulting in a large plate-scale allowing to cover a wide field of view, while the mechanical structure of the telescope remains very compact. A large FoV is mandatory for the study of VHE cosmic radiation: the most energetic gamma rays produce longer air showers, that can be detected at larger impact parameters, hence requiring a good imaging performance up to high off-axis angles. Moreover the dual-mirror design, thanks to the large plate-scale, allows to implement a camera with a typical lateral dimension that is about one half in comparison to single-mirror telescopes. This is a crucial feature of the design, because such a reduced detection area allows to cover the focal surface with miniaturized silicon photo-multipliers sensors (SiPM, [129]), presenting very fast response and an excellent single photo-electron resolution.
There are two versions of the mechanical structure of the ASTRI telescope, with slight changes: the first one was implemented in the prototype instrument called ASTRI–Horn (see figure 3.1), while a second consolidated version (see figure 2.28 on page 65) will be adopted for the MiniArray and the SSTs. The main structural differences are in the mirrors actuators and the secondary mirror support equipment [130]: the mast has been redesigned with three legs instead four, while the shape of the shield and the optical baffle has changed from a cylinder to a truncated cone (reducing the weight from $150\,\mathrm{kg}$ to $40\,\mathrm{kg}$). The improvement of the mechanical design permitted to lower the mass and have a better access to elements subjected to maintenance operations, in particular the actuators of the mirrors, but the resulting structure is still robust and compact, ensuring stiffness during tracking observations, while the remarkably low weight of the Cherenkov camera further reduces the risk of gravity flexures [131]. In table 3.1 are reported the general parameters of the mechanical structure with refer to the prototype version.

General mechanical characteristics	
Height (pointing horizontally/vertically)	$7.5\,\mathrm{m}/8.6\,\mathrm{m}$
Footprint on the ground (max)	$5.3\,\mathrm{m}$
Total mass	$19.72 \times 10^3\,\mathrm{kg}$
Mass of the camera	$73\,\mathrm{kg}$
Primary mirror diameter (segmented)	$4.3\,\mathrm{m}$
Secondary mirror diameter (monolithic)	$1.8\,\mathrm{m}$

Table 3.1: Technical specifications of the ASTRI–Horn telescope [124].

3.1.1 The prototype Astri-Horn

The first telescope realized in the context of the ASTRI project was dedicated to the memory of Guido Horn d'Arturo, an Italian-Jewish astronomer pioneer in the production of segmented mirrors [132]: for this reason, that instrument was given the name of ASTRI–Horn. The telescope was inaugurated in September 2014 and it is currently the biggest telescope on the Italian soil in the UV–IR range. It is located at the INAF "M.C. Fracastoro" observing station in Serra La Nave, on Mount Etna, Sicily. This observatory is one of the best sites in Italy in terms of sky darkness and weather conditions [133], but it is also very close to an active volcano whose dust and gases, released during eruptive activities, are extremely corrosive for the coatings of the mirrors. Fortunately, the proximity of the volcano had also positive consequences, opening the investigation about the possibility to exploit an IACT for studying the magma chambers and the internal structure of the volcano through the muography technique [134].

Position of the ASTRI–Horn telescope		
Lat 37.6932°N	Lon 14.9746°E	Alt $1739\,\mathrm{m}$ a.s.l.

Table 3.2: Observing station of Serra La Nave, on Mount Etna (Sicily).

The main goal of the ASTRI–Horn prototype telescope is manifold. First of all, it constitutes a technological demonstrator to validate the novelties implemented in this telescope, in particular the optical design and the Cherenkov camera. Moreover, ASTRI–Horn serves as a training facility for telescope and maintenance operations that will be performed also on the MiniArray. Finally, it can be used as a test bench for the implementation of new methods and tools, both hardware and software: this is exactly the case of the astrometry techniques that will be presented in this thesis.

The major achievement of ASTRI–Horn is undoubtedly the detection of the Crab Nebula at 5σ confidence level[86], demonstrating that the modified SC optical design can be successfully implemented for the realization of IACTs. However, during the observing campaign for this detection, between December 2018 and March 2019, a large amount of data was discarded due to problems with the pointing of the telescope and with the alignment of the primary mirror segments: three elements lost their position and it was necessary to cover them, reducing the effective area, rather then returning them to the correct position with the risk of hitting nearby segments. One of the goals of the work presented in this thesis is to find a strategy to monitor the pointing and the imaging quality in order to pre-

vent such experiences with the prototype telescope from happening again on the MiniArray.
In autumn 2021 a new set of mirrors were mounted on ASTRI–Horn (see figure 3.12) together with an upgraded version of the Cherenkov camera, the same one that will be implemented also in Tenerife.

3.1.2 Mini–array

The scientific objectives of the ASTRI project will be achieved thanks to the MiniArray: a group of nine ASTRI telescopes that will be installed at the *Observatorio del Teide* in the Canary Island of Tenerife (Spain) [135]. The deployment of the telescopes is already ongoing, in the positions of table 3.3, and it is expected to be over by the end of 2022, while scientific operations will start in 2024. Meanwhile, Monte Carlo simulations of the MiniArray performances are at an advanced stage [136] and hence its main scientific features can be summarized as follows: energy range from 1 TeV up to 200 TeV, angular resolution $\sim 3'$ at 10 TeV, energy resolution $\sim 10\,\%$ at 10 TeV. The preliminary plot of the differential flux sensitivity of the MiniArray is reported in figure 3.2.

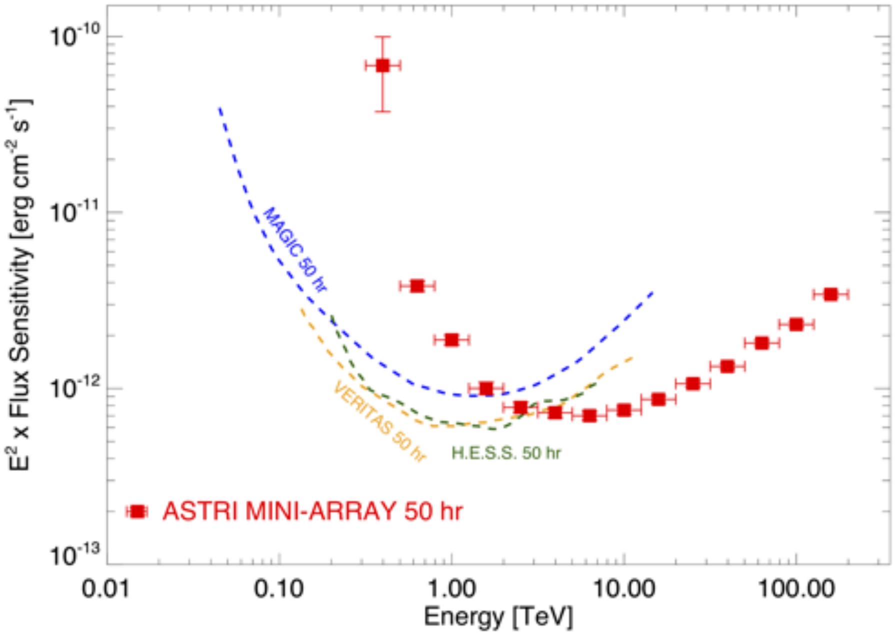

Fig. 3.2: ASTRI MiniArray on-axis differential sensitivity for 50 h integration time, compared with those of current IACTs (preliminary plot taken from [137]).

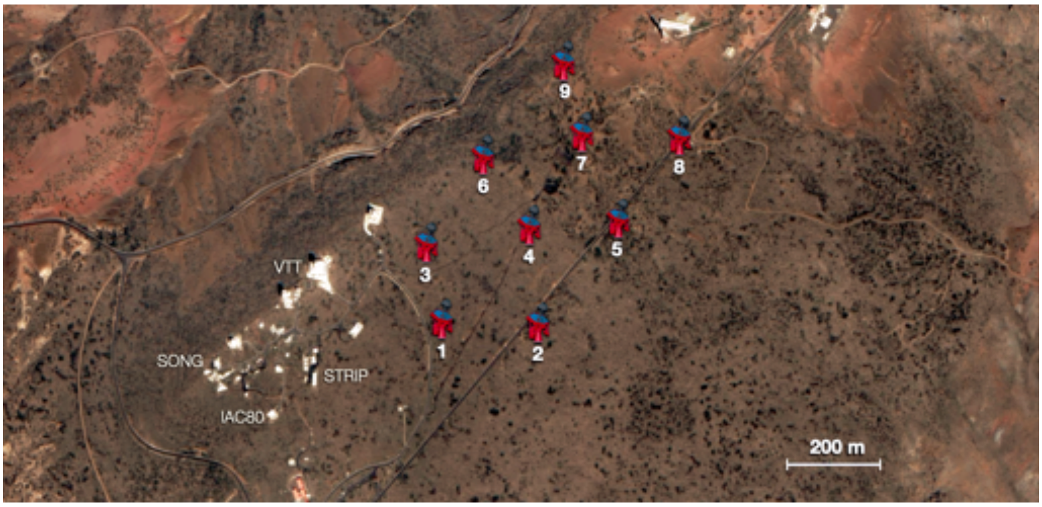

Fig. 3.3: Final layout of the MiniArray telescopes in Tenerife.

Differently from ASTRI–Horn the MiniArray will take advantage of the stereoscopic vision, exploiting the large FoV providing a better overlap between the telescopes, to increase the angular resolution despite the modest raw aperture of the optics in comparison to other IACTs. Several improvement in the mechanical design allowed to reduce the total mass with respect to ASTRI–Horn, without decreasing the stiffness of the structure which is a key feature to ensure the stability of the point spread function in time and the mirror alignment during operations [138]. In particular, an important modification involves the Active Motion Control (AMC) actuators: now they are three for each panel (instead of two), permitting piston

Position of the MiniArray telescopes			
Tel	Lat (N)	Lon (W)	Altitude
1	28.301 025°	16.507 969°	2359 m
2	28.300 675°	16.506 606°	2348 m
3	28.302 369°	16.508 283°	2364 m
4	28.302 308°	16.506 639°	2356 m
5	28.302 425°	16.504 897°	2358 m
6	28.304 142°	16.506 911°	2351 m
7	28.304 322°	16.505 156°	2342 m
8	28.299 292°	16.508 706°	2376 m
9	28.300 764°	16.509 439°	2359 m

Table 3.3: Observatorio del Teide in Tenerife, Canary Islands (Spain).

and tilts, and the whole set of actuators will not be permanently mounted on the telescope, but only during the Assembly Integration Verification (AIV) phase and corrective maintenance operations (e.g. re-alignment or replacement of the panels) [130]. Some improvements are present also in the hardware components of the camera [139] and in electronics, but they will be discussed in section 3.3.2 after an adequate presentation of the acquisition system.

The MiniArray will serve as a pathfinder for CTA, where 70 ASTRI SSTs will be implemented. However, it will pursue also an independent scientific program, whose pillars are reported in section 3.1.3, and hence it is important to optimize the whole system not only for the validation phase, but for the regular data taking as well. The astrometry techniques developed in this thesis constitute an effort in this direction, and some of them here have already been inserted into the Online Observation Quality System (OOQS) and the Calibration Plan of the MiniArray [140] [141].

Fig. 3.4: Bird view of the Teide Observatory in Tenerife, Canary Islands (Spain), where the MiniArray is currently under construction. In the bottom-right corner it is possible to see the VTT and SONG telescopes, already presented in the render of figure 3.3. On the background, the Teide volcano.

3.1.3 Science pillars

The ASTRI MiniArray will be the first instrument able to join together the very high energy threshold typical of Water Cherenkov Detectors Arrays with the accurate energy and angular resolutions typical of IACTs. This is unprecedented, and will allow ASTRI to shed light on several open questions of VHE astrophysics [137]. For this reason, the first four years of observations will be dedicated to specific science topics with the aim to provide robust answers to a few well-defined open questions, while the second four years of operation will be devoted to observatory science [see 142, 143]. In the following paragraphs we briefly present the "pillars" of the ASTRI science program, i.e. science fields in which the MiniArray will contribute breakthrough pieces of evidence to vastly improve our understanding of few key arguments. Of course, also other topics will be explored, as the field of time-domain astrophysics, direct measurements of CRs, stellar intensity interferometry studies and the search for axion-like particle and Lorentz-invariance violations (section 1.3.3).

The origin of cosmic rays Recently, the LHAASO Collaboration [24] reported on the discovery of 12 galactic sources as possible PeVatron candidates, i.e. sources able to accelerate protons up to $\sim 10^{15}$ eV. Most of these objects are also diffuse gamma-ray emitters, with articulated structures and angular extensions up to $1°$, but the actual sources responsible for the UHE gamma-ray emission have not been definitely identified yet, leaving the nature of these extreme accelerators uncertain [144]. This discovery is very important for the MiniArray science, especially because its angular resolution at energies of about $100\,\mathrm{TeV}$ is $0.08°$, a factor 3 to 4 times better than LHAASO. For this reason, the ASTRI MiniArray will investigate these and future PeVatron sources providing important information on their morphology in the $10\,\mathrm{TeV}$ to $100\,\mathrm{TeV}$ energy range. An example is the case of the galactic source `2HWC J1908+063` (also known as `VER J1907+062`, [145]), which is one of the possible PeVatron counterparts of the newly-detected source `LHAASO J1908+0621` [137]. Another important region to investigate is the Galactic Center, that the MiniArray will observe at high ($\sim 60°$) zenith angle for a couple of months in Summer: the large field of view will allow to map the whole Galactic Center region in a single observation, while the excellent angular resolution of the MiniArray will help to identify any high-energy source among several candidates.

Cosmology and fundamental physics As previously explained in section 1.3.2, extra-galactic sources, such as blazars, can successfully probe the level and the evolution of the extra-galactic background light (EBL), a very important instrument to constraint cosmological models. Unfortunately, direct measurements of the EBL are prevented by the overwhelming dominance of local emission from both the Galaxy and our Solar system [146], but its characteristics can be retrieved from the alteration of the spectra in very distant gamma-ray sources. More in detail, the MiniArray can play a fundamental role in investigating the IR component of the EBL, with dedicated observations of low-redshift radio galaxies (such as M 87, IC 310, Centaurus A) and local star-bursting and active galaxies (such as M 82, NGC 253, NGC 1068).

Relativistic Jets Blazars are an important class of gamma-ray sources, but the dominant mechanism responsible for their photon production has not been identified yet. In particular, beside the standard leptonic emission model there is another possible scenario based on collimated beams of high-energy protons/nuclei originated in the relativistic jets of extreme BL Lac objects. Such hadrons would trigger the production of gamma-ray photons and neutrinos through photo-meson and pair production mechanisms. The ASTRI MiniArray will be able to disentangle between the two emission models by means of deep observation of near Blazars (e.g. `1ES 0229+220`), as their gamma-ray photons experience a less severe EBL absorption due to their reduced distance, and hence the observed gamma-ray spectrum extends at much higher energies (E $>10\,\mathrm{TeV}$) allowing a deeper insight on the physics processes.

3.2 Optical system

The optics of the ASTRI telescope was designed to cope with the basic scientific requirements of large effective area and wide field of view. The first one implies a large primary mirror, while the second translates into a large plate–scale (in order to have a reasonable dimension of the camera) and hence a short focal length. These characteristics lead to the choice of the dual-mirror Schwarzschild-Couder (SC) optical configuration, already presented in section 2.2.3.2, and miniaturized[1] acquisition sensors (SiPM) to cover the focal surface. Table 3.4 reports the main parameters of the ASTRI optical design.

---

[1] Their side is $\sim 7\,\mathrm{mm}$ which is very small compared to PMTs, but extremely large with respect to the most common SiPM sensors [147].

General optics parameters	
Optical Configuration	Modified SC
Effective collecting area	$6.5\,\mathrm{m}^2$
Focal length	$2.15\,\mathrm{m}$
f/#	0.5
FoV (of prototype)	$10.5°$ ($7.5°$)
PSF (@ $100\,\%$ of FoV diameter)	$\leq 0.19°$
Average plate-scale	$92.6\,''/\mathrm{mm}$
Pixel size (side)	$6.975\,\mathrm{mm}$

Table 3.4: These values applies to both ASTRI–Horn and the MiniArray [124].

The SC configuration ensures an *aplanatic* FoV of more than $10°$, i.e. free of spherical aberration and coma, while the astigmatism is also limited thanks to the spherical focal surface. However, ASTRI actually implements a *modified* version of this optical scheme: the profiles of the reflective surfaces were optimized with a polynomial function in order to produce a flat response of the point spread function (PSF) up to large off-axis angles. In particular, the sagitta[2] function $z(r)$ of each of the two mirrors (M1 and M2) can be represented by the sum of a sphere with a series of polynomials introducing aspheric corrections [104],

$$z(r) = \frac{cr^2}{1+\sqrt{1-c^2r^2}} + \sum_{i=2}^{N} \alpha_i \left(\frac{r}{r_{max}}\right) , \tag{3.1}$$

where $r = \sqrt{x^2+y^2}$ is the radial coordinate and r_{max} is its maximum value, c is the curvature of the sphere (the inverse of the radius of curvature), and α_i are the coefficients of the aspheric correction terms[3]. This peculiar geometric profile for the reflectors produces an enlargement of the PSF on-axis, with respect to the pure SC configuration [148], but in turns it ensures a flat response up to large viewing angles, contrary to what happens for example in the spherical or parabolic single mirror solutions, with an overall dimension much smaller compared to the DC design [e.g. 149, pp.247]. Figure 3.5 presents a plot of the PSF size along the FoV, for different optical configurations. The size of the PSF is evaluated in terms of the D_{80} parameter, representing the diameter of the circle containing

---

[2] The sagitta function (*sag*) describes the conic section of which the telescope is the revolution around the polar axis.

[3] Numerical values reported in [104].

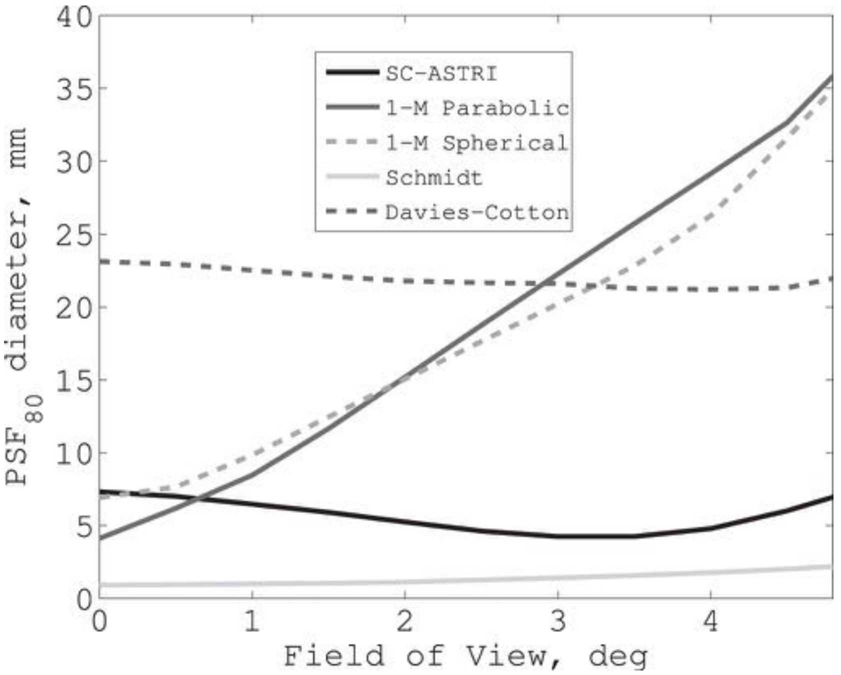

Fig. 3.5: Comparison of the off-axis PSF size for different optical configurations (taken from [150]). The modified-SC is the only solution with a quasi-flat response and an adequate size. A pure-SC (not reported in figure) would start from zero and grow less than the parabolic and spherical designs, as it is an aplanatic optical scheme.

the 80 % of the light focused by the optics[4]. As it is clear from the image, the behavior of the PSF in the modified-SC design is extremely positive for the aims of the ASTRI project, but there are two main drawbacks: the production of mirrors with such peculiar profiles and the calibration of the system to produce the correct shape of the PSF. The following two sections are dedicated on each of these topics.

3.2.1 Mirrors

It should be noted that the optimized radial profiles for both M1 and M2, reported in equation 3.1, are strongly aspheric. As a consequence, the realization of the mirrors represented a technological challenge, both for the manufacturing process and the subsequent characterization. Two different solutions have been investigated and implemented for the production of primary and secondary mirrors, as it is explained hereafter, while their

---

[4] The amount of energy within is a circle of given radius is called *encircled energy* (EE).

quality was verified with an *ad hoc* ray-tracing software taking into account the measured surface of both mirrors and their alignment [151]. The main general parameters of the mirrors are reported in table 3.5.

General mirrors parameters	
Primary mirror diameter (segmented)	4.3 m
Number of segments	18
Size of a segment (face-to-face)	849 mm
Nominal Radius of Curvature Ring 1	8.52 m
Nominal Radius of Curvature Ring 2	9.87 m
Nominal Radius of Curvature Ring 3	12.54 m
Profile Error (RMS)	< 30 µm
Micro-roughness (RMS)	< 2 nm
Secondary mirror diameter (monolithic)	1.8 m

Table 3.5: The micro-roughness is evalued in the spatial wavelength range 0.1 mm to 200 mm [124], while the nominal radii of curvature refer to the best fitting sphere.

Primary mirror The optical surface of the primary mirror was segmented in a mosaic of 18 hexagonal panels, distributed among three concentric rings or *coronas*. Each ring was characterized by its radial distance from the optical axis and defines a different type of mirror segment with a specific radius of curvature referring to the best fitting sphere. Figure 3.6 *right* reports the name scheme of the primary mirror segments arranged on the dish, in front view, while in the image on the *left* there is a simulation of the PSF composition with the contributions from all the rings. For the manufacturing of the M1 aspheric segments was adopted the cold glass slumping technology [152] while for their quality control and characterization it was developed a metrology testing method based on deflectometry [153].

Secondary mirror Unlike the segmented M1, the secondary mirror is an aspheric monolithic element. It is composed of a glass structure 19 mm thick, ~ 120 kg weight, manufactured via the hot slumping technology [154]. Figure 3.7 shows a picture of M2 (*left*) in contrast with an hexagonal panel of M1 (*right*). After the production of the glass substrate a reflecting *Al* coating and a protective layer are applied in order to guarantee the maximum reflectivity together with good resistance to atmospheric agents [155, 156]. The qualification was performed by means of optical tests [150].

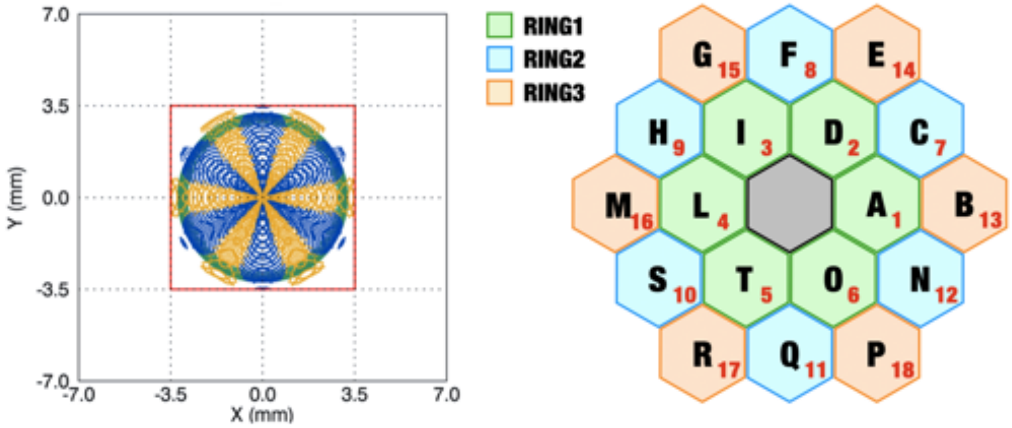

Fig. 3.6: *Right*: arrangement and nomenclature of the primary mirror segments (front view, the basement of the telescope is downwards). *Left*: on-axis simulation of the PSF with contributions from the different segment types (same color scheme). The red square represents the dimension of the ASTRI camera pixel [104].

Active Motion Control (ACM) system Every reflective element of the optical system is installed on a moving structure, so that its position can be finely tuned to obtain and maintain the correct alignment of the whole optical configuration. In particular, the M1 segments are mounted on three points, endowed with active supports (actuators) to perform tilts of the panels with a range of 1.5° and resolution of few arcsec. The piston of the segments is operated during the assembly phase on ASTRI–Horn, with the mechanical adjustable third point, while on the MiniArray a third active element allows to perform the operation remotely, in every moment. The set of actuators constitutes the Active Motion Control (ACM) system,

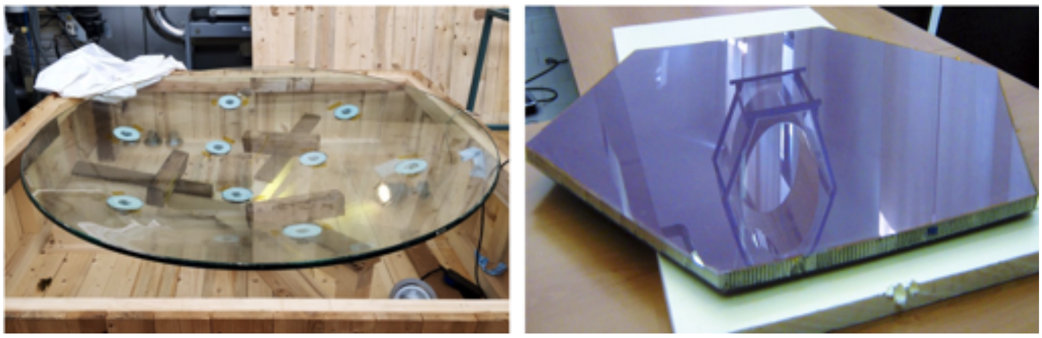

Fig. 3.7: Pictures of the M2 glass structure and a hexagonal segment of M1 [153].

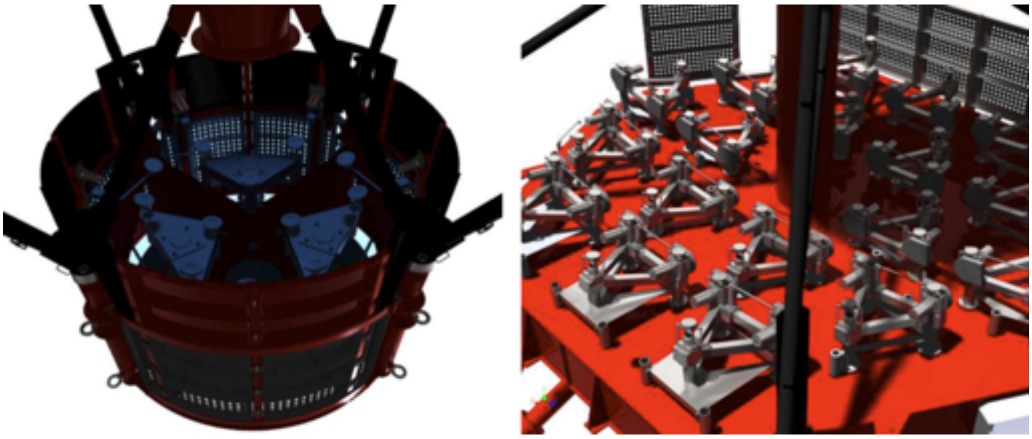

Fig. 3.8: CAD rendering of the AMC system for M2 (*left*), inside the support structure, and for M1 (*right*) on the telescope dish [130].

that will not be mounted permanently on each telescope of the MiniArray: thanks to the stiffness of the entire structure, after the alignment procedure the mirrors will keep their position being mechanically anchored to rigid supports, while the full set of actuators will be removed and re-used on another telescope. In figure 3.8, on the right, is shown the AMC system of the primary mirror, while the left-hand image presents the solution for the secondary mirror: 9 pads are glued on the back of the mirror and three actuators support a whiffle-tree structure to distribute the mirror loads on them. With a range of $15\,\mathrm{mm}$ the motors permit to control focus and tilt of the telescope with a resolution of $0.1\,\mathrm{mm}$ for each actuator.

3.2.2 Point spread function

The Point Spread Function (PSF), is the response of an imaging system to a point source, the light spot obtained on the focal surface. Cherenkov telescopes are usually designed so that the size of the PSF is about half of the linear dimension of the sensors. However, the dominance of aberrations for large viewing angles often worsens the response of the instrument off-axis. Thanks to the peculiar modified-SC design, the ASTRI telescope is the first IACT whose PSF lies within a single Cherenkov pixel up to $5°$ off-axis [104]. In terms of D_{80} the average size of the ASTRI PSF along the FoV is $\sim 11.4'$, with a minimum at $\sim 3°$ off-axis. In figure 3.9, the image on the left reports the nominal D_{80} and the measured points with the ASTRI–Horn telescope, in comparison with the size of the Cherenkov pixels, while the plot on the right shows the profile of the radial integral (encircled energy) for each of the measured points. Despite degradation with respect

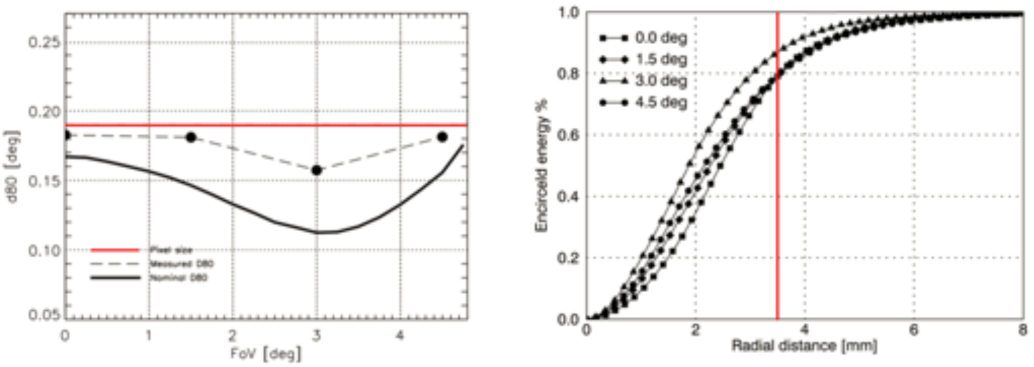

Fig. 3.9: *Left*: Comparison of D_{80} as a function of field angle (off-axis) between its ideal (solid curve) and measured at ASTRI–Horn (dashed curve) values. The SiPM pixel size (red line) is also shown for reference. The pixel size of the CCD camera used for these measurements is about 2″ on the focal plane. *Right*: EE parameter measured as a function of radial distance for different angular positions on the focal plane. The vertical lines represent the SiPM pixel size (red). Adapted from [104].

to the nominal configuration, the PSF is well inside the ASTRI Cherenkov pixel size and measurements follow the trend of what foreseen by the optical design, with a minimum at 3° from the optical axis.

As in every other telescope with segmented mirrors, the overall PSF is the sum of different contributions coming from the single panels. In fact, the ASTRI PSF is a composition of 18 figures, divided into three types of shapes, produced by the different profiles of the three coronas of the primary mirror. Figure 3.10 reports a simulation of the PSF on-axis, with an explicit visualization of the contributions from the coronas. Figure 3.10 also highlights another peculiarity of the ASTRI optical system: the PSFs from different aspheric segments do not superimpose at the center of the image, but they need to be arranged in a certain configuration, in order to

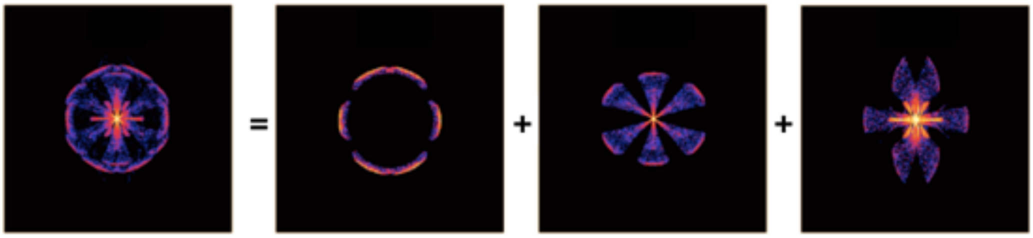

Fig. 3.10: Simulation of the PSF on-axis, as a sum of the contributions from ring 1, 2 and 3 (from left to right, see figure 3.6).

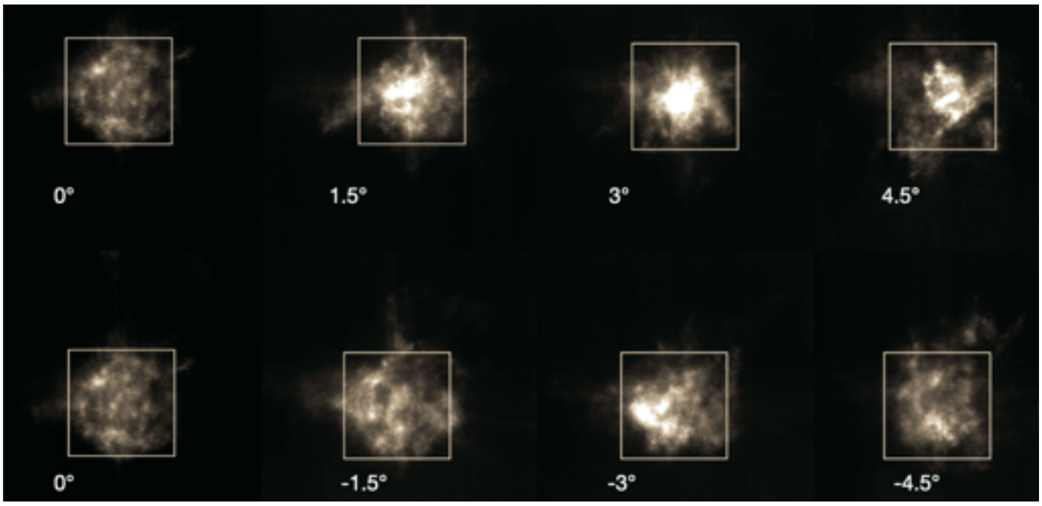

Fig. 3.11: PSF evaluation at different distances from the optical axis of the ASTRI–Horn telescope. The white squares represent the Cherenkov pixel (adapted from [130]).

obtain the correct behavior of the optics both on- and off-axis [157]. This peculiar composition is achieved moving the mirror segments with the AMC actuators, with a specific alignment procedure and a suitable CCD camera on the focal plane.

Composition of the PSF The alignment of the mirror segments is a procedure that aims at optimizing the resolution of the telescope producing the correct PSF composition by design. Differently by other IACTs, in the case of a modified-SC telescope such operation is quite complicated, as it cannot be performed illuminating all the panels with a calibrated light source (e.g. a divergent laser beam [76]) because of (i) the shadowing of the masts and the secondary mirror support structure [158] and (ii) the articulated composition of the individual PSFs from the aspheric segments which is required. As a consequence, the only chance is to analyze directly the shape of the PSF on the focal plane pointing at a source at infinite distance (tipically the Polaris star, so that the telescope do not have to track it). To this end, of course the Cherenkov camera cannot be used, or the articulated shape of the PSF would be lost into its coarse angular resolution, and hence a CCD camera was installed on the focal plane of ASTRI–Horn to perform the qualification of the optical system during the AIV phase. Figure 3.11 reports the simulated images of the PSF at different off-axis angles. The FoV of the CCD optical camera was $\sim$1° in order to follow most of the scan movements of panels PSF performed by the AMC, and the angular resolution $\sim 2''$. For different off-axis positions (obtained moving both the telescope in the sky and the CCD on the focal plane) all the segments were initially tilted away, and then re-positioned one at a time, in order to find the best settings for the actuators with multiple measurements all over the FoV. A similar iterative procedure will be adopted also for the MiniArray, but the manual alignment strategy used in the case of the prototype will be upgraded to an automatic version [130].

3.2.3 Frequency response

The total frequency response of the whole ASTRI optical system is given by the sum of different elements, designed on purpose to cope with specific needs. As explained in section 2.1.3 the Cherenkov emission from the extended air showers peaks in the range $300\,\mathrm{nm}$ to $350\,\mathrm{nm}$, but the SiPM sensors are sensitive from $200\,\mathrm{nm}$ up to $1000\,\mathrm{nm}$ and hence the transmission of the system must be reduced in the red side of this range, or the signal of interest will be covered by the night sky background (NSB) [139]. The first solution is an IR filter applied directly on the SiPM sensors, acting as both a filter and a protective cover. The filter is a thin layer designed to cut the signal above $550\,\mathrm{nm}$, producing a remarkable $70\,\%$ drop-off at $\sim 700\,\mathrm{nm}$ [139]. In front of the focal surface there is a protective window made of fused silica [159] (transparent to UV light) where it is applied another IR filtering film which is a crucial element of the whole optical chain. In fact, the behavior of filters is difficult to be characterized in a

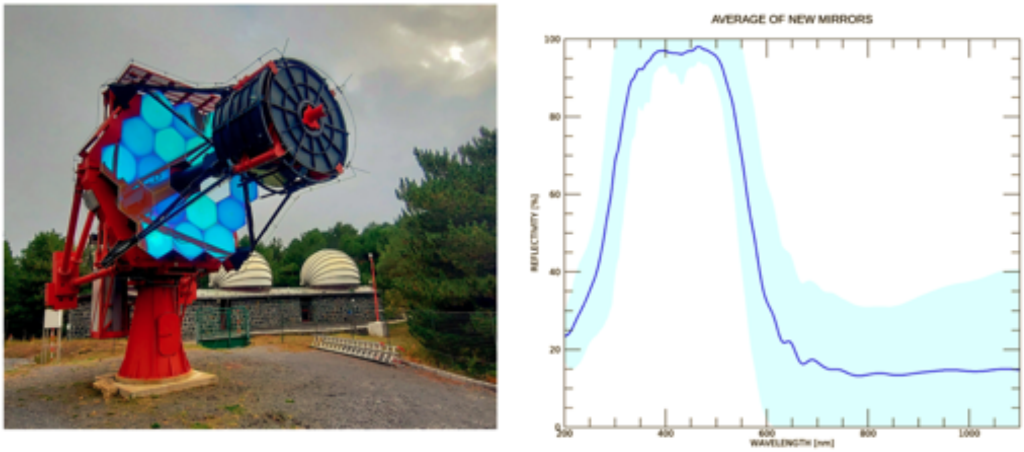

Fig. 3.12: New set of mirrors mounted on ASTRI–Horn (autumn 2021). The coating of the mirrors was tuned so that the reflectivity peaks in the blue range part of the spectrum.

SC telescope, because the focal surface is interested by rays spanning a huge range of incidence angles ($20°$ to $70°$), challenging the uniformity of the filter transmittance. For this reason, the most effective frequency cut in the case of the ASTRI telescope was obtained by tuning the reflectivity curve of the primary mirror, where the incidence angle spans the range $0°$ to $15°$, while already the secondary mirror works under incidences in the wide $20°$ to $60°$ interval [158, 155]. In figure 3.12 is reported a picture of ASTRI–Horn in autumn 2021, when a new set of mirrors was installed: the bluish tint of the reflected light is evident. Such a result is obtained with the so-called "dielectric" coating: an innovative solution based on multiple layers producing the effect of a band-pass filter. In future months the performance of such mirrors will be reported in dedicated papers, after the end of the next observing campaign.

3.3 Cherenkov Camera

The dual-mirror SC design that characterizes the optical system of the ASTRI telescopes results in a large instrument plate-scale, leading to a camera of compact dimensions, that implements modern SiPM sensors. The development of the camera hardware, together with dedicated software and firmware, was entirely led by INAF for the first time, with the partnership of several industries. The body of the camera has a truncated-cone shape, whose dimensions are $520\,\mathrm{mm}$ (bottom diameter), $660\,\mathrm{mm}$ (height) and $560\,\mathrm{mm}$ (top diameter), for a total mass of $\sim 73\,\mathrm{kg}$ [139]. The camera is located between the two reflecting surfaces, at the heart of the compact configuration of the telescope. In particular, the focal surface is $2589\,\mathrm{mm}$ ahead of the primary mirror, only $520\,\mathrm{mm}$ far from the secondary.
The structure of the camera assembly is presented in figure 3.13, where it is reported an exploded-view drawing of the ASTRI camera and the main hardware components can be easily recognized. A lid system is present on the top of the structure, to open or close the red *basket* which is actually the backbone structure of the whole assembly. Inside the basket there is a pile of different sub-systems, namely the filter window, the focal plane assembly, the back-end electronics and the power supply system, which is composed of several voltage distribution boards in charge of providing the required regulated power to all the electronics devices of the camera. Another component is the thermal system, distributed along the whole camera, to assure a proper working temperature of electronics at $(15 \pm 2)\,°\mathrm{C}$, and to maintain the SiPMs at a constant temperature moving the heat from the focal plane to fin stacks where it is dissipated by forced-

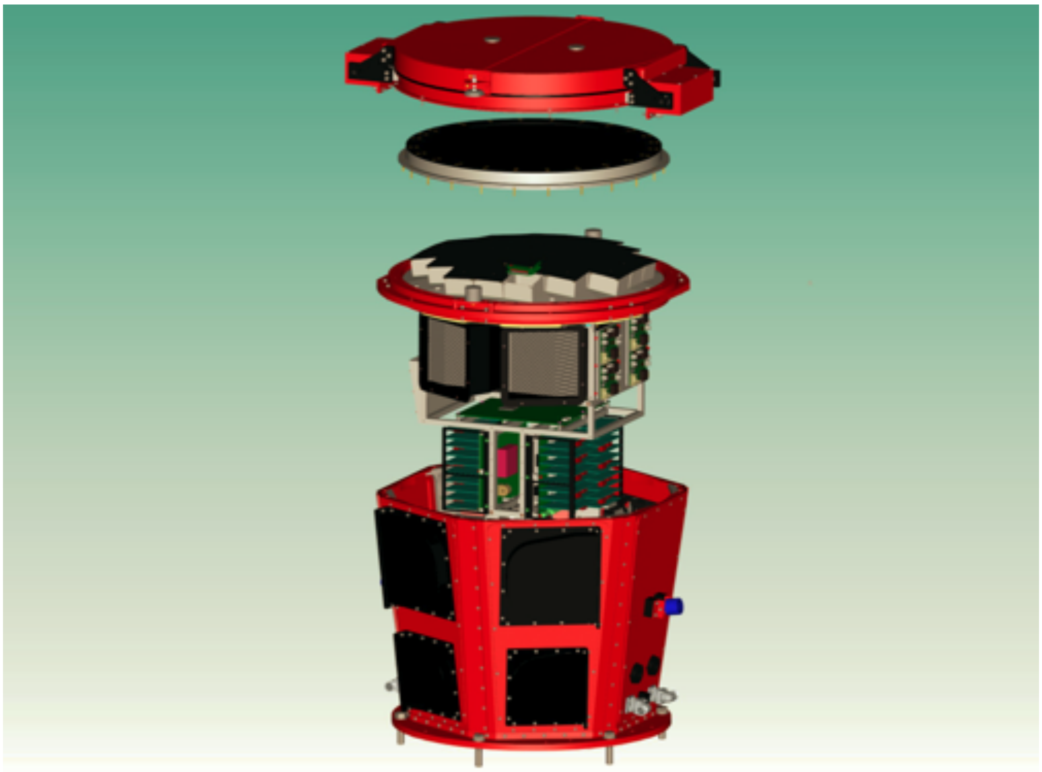

Fig. 3.13: Exploded-view drawing of the Camera assembly. Lids (A), window (B), focal plane assembly and FEE (C), BEE (D), power supply (E), and the "basket" (F).

convection using fans. Lastly, in the basket there are also ancillary devices for specific purposes, as a stable and precise GPS receiver (10 ns resolution) used for time synchronization and providing time tags to cherenkov events [159], or the novel inner fiber-optic equipment, located along the window circumference, used for the on-field relative gain calibration of the sensors [160].

For the purposes of this thesis, the most important feature of the camera system is the geometry of focal plane assembly, which is presented in details in section 3.3.1. However, an essential overview of the signal acquisition and elaboration process is necessary to understand the fundamentals of the Variance Method, that will be presented in chapter 4. For this reason, also a basic introduction to the camera electronic system is provided hereafter, in section 3.3.2, focusing on three main sub-systems: Front-End Electronics (FEE), Back-End Electronics (BEE) and Data Acquisition system (DAQ). The analogic FEE is specifically design to interface the SiPM sensors ensuring a very fast read-out, which is essential to detect the rapid pulses generated by the Cherenkov flashes. It is directly attached to the sensors and it is contained in suitable aluminum case located on the focal plane (figure 3.14).

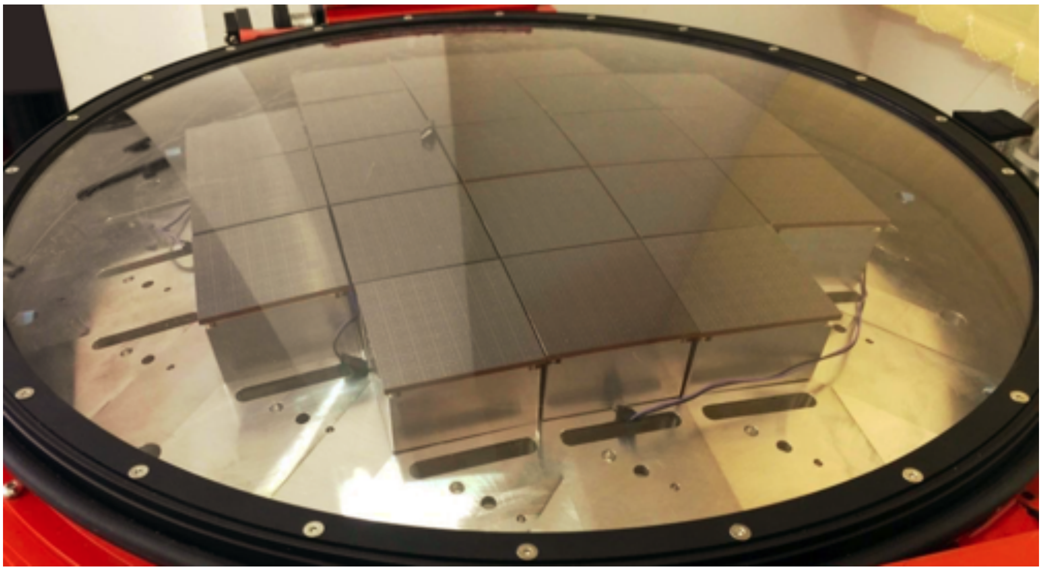

Fig. 3.14: Focal plane assembly of the ASTRI camera in the reduced configuration (only 21 PDMs).

3.3.1 Focal plane assembly

The focal surface of the ASTRI telescope has a spherical shape with radius of curvature $1060\,\mathrm{mm}$. It is covered by a matrix of 2368 SiPM sensors[5] organized in 37 flat tiles (Photo Detection Modules, PDMs), each composed of 8×8 elements. The center point of each PDM is tangent to the focal sphere of reference, in order to have the least deviation from that ideal surface. The whole composition of the tiles is $410.4\,\mathrm{mm}$ large and has a FoV of $10.9°$. However, on the ASTRI–Horn prototype it was implemented only a reduced configuration, composed of only 21 PDMs (1344 SiPMs) with a linear size of $293\,\mathrm{mm}$ and $7.8°$ FoV. This solution is presented in the picture of figure 3.14, where also the support structure is visible: it is made with traditional manufacturing out of standard flat plates of aluminum alloy (EN AW-6082) [139]. Each SiPM sensor constitutes a pixel of the resulting image and has a square shape of approximate $7\,\mathrm{mm}$ size, corresponding to a sky-projected angle of $\sim 0.19°$, matching the

---

[5] Hamamatsu Silicon Photomultiplier LCT5 Multi-Pixel Photon Counter (MPPC) S11828-3344M [161, 162] [*link* 244].

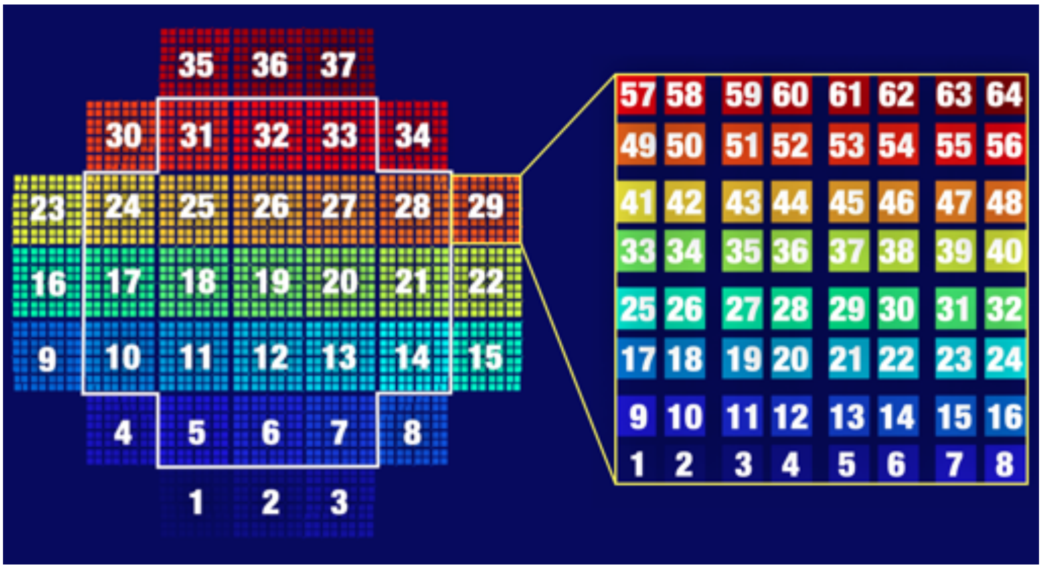

Fig. 3.15: Naming convention of the ASTRI focal plane elements. On the right there is the numbering scheme of the PDMs, while on the left the one for the pixels (dimension of sensors and gaps are not in scale). The white contour identifies the reduced camera configuration of only 21 PDM tiles adopted for ASTRI–Horn.

resolution of the optical system. More precisely, the actual dimension of each pixel is $7.175\,\mathrm{mm}$, but there is a dead area at the edge of the sensor, $0.1\,\mathrm{mm}$ wide, and hence the effective size of the sensitive part is $6.975\,\mathrm{mm}$. An extra $0.1\,\mathrm{mm}$ border is present at the edge of the PDM, whose overall size is hence $7.175 \times 8 + 0.1 \times 2 = 57.6\,\mathrm{mm}$. Behind each PDM tile, there is a PDM box, an aluminum case hosting the FEE, whose dimension are $56\,\mathrm{mm} \times 56\,\mathrm{mm} \times 30\,\mathrm{mm}$. The width of the gap between PDM tiles spans in the range $0.8\,\mathrm{mm}$ to $1.6\,\mathrm{mm}$. A detailed description can be found in [163], while for the aims of this thesis the position of each pixel center was taken from the CAD drawing of the focal plane. In the first prototype camera, mounted on ASTRI–Horn until 2020, some PDMs were equipped with SiPM sensors presenting a different size of internal micro-cells ($50\,\mu\mathrm{m}$ instead of $75\,\mu\mathrm{m}$), their location is reported in [163] and will be reported when necessary in this document.

Due to the particular disposition of the sensors in the focal plane assembly, the PSF of a star perfectly on-axis spreads among the four central pixels.

3.3.1.1 Naming convention

Within the ASTRI project there is a unique naming convention to identify the elements in the focal plane. Each PDM is addressed by a number, from 1 to 37, from bottom left to top right looking at the camera in front view. Inside every PDM, there is a similar numbering scheme for the pixels, from 1 to 64. In this way, each sensor is uniquely spotted by two numbers: its identifier and the code of its PDM. This naming convention is adopted both on ASTRI–Horn and the MiniArray, regardless of the complete or reduced camera configuration. In figure 3.15 is represented this numbering scheme.

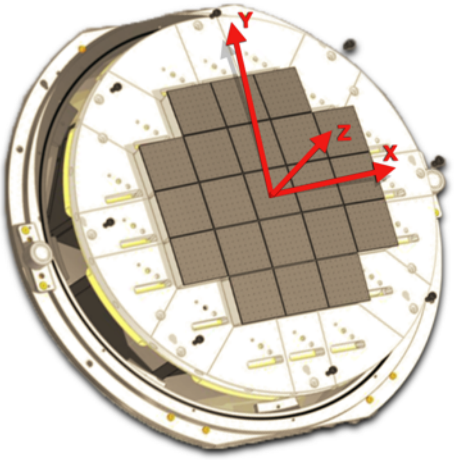

Fig. 3.16: Definition of the Cartesian coordinate reference system on the spherical surface of the ASTRI camera.

3.3.1.2 Camera coordinate reference system

Following the convention adopted in the ASTRI project [163], along this document we will make use of a unique reference system for the camera, a set of three-dimensional Cartesian coordinates which is defined as follows. The origin of the reference system is located at the center of the PDM labelled 19. The Z axis is oriented along the telescope optical axis, perpendicular to the camera, pointing from the focal surface towards the M2 mirror. The X axis is parallel to the elevation axis of the telescope and its positive direction points to the right, looking at the camera in front view[6]: in terms of labels it is oriented from the center towards PDM 22. The direction of the Y axis is consequently determined to form a right-handed

---

[6] Standing in front of the camera.

coordinate system. A graphic representation is reported in figure 3.16.
The reference system we have presented is defined with respect to the ASTRI telescope axes, assuming that the camera was installed so to match the design with infinite accuracy. If in real applications the camera has an offset or a tilt, then the reference system must be considered as rigidly joined to the camera and therefore co-moving with it.
Especially for the astrometric operations it is useful to define also a convenient 2D polar reference system on the xy plane, with the same origin, using $r = \sqrt{x^2 + y^2}$ as a radial distance and θ as an angular coordinate, in the range $(0, 2\pi)$ starting in the $+x$ direction and increasing towards $+y$.

3.3.2 Electronics

Extended air showers are extremely fast and their Cherenkov light flash has a remarkably short duration (few ns). To record their signal, the SiPM sensors of the ASTRI camera are excellent devices, as they exhibit very rapid response and fine single photo-electron resolution, but they need properly tailored electronics. For this reason, a specific acquisition chain was developed on purpose, patented by INAF, devoted to directly interface the SiPM sensors and to perform some fundamental operation completely automatically, in order to be as fast as possible. In particular, the most important task is to recognize a Cherenkov event and consequently to auto-generate the *trigger*, or the logic signal to start the data acquisition. The read-out of the SiPM pulses represents again an innovative solution, as the dedicated analog circuit is based on a custom peak-detector operation mode rather than the sampling technique commonly adopted by other IACT telescopes [164]. Data registered by the ASTRI camera are then converted to digital signals and finally sent to the camera server, external to the telescope. The whole customized acquisition chain is presented in section 3.3.2.1, while the basic features of the signal processing are reported in section 3.3.2.2.

3.3.2.1 The acquisition chain

The electronics is divided into three main subsystems, devoted to different purposes: Front-End Electronics (FEE), Back-End Electronics (BEE) and Data Acquisition system (DAQ).
The first element immediately after the sensors is the fully analog FEE, designed to interface and read-out the SiPMs as fast as possible. Every PDM unit has its own FEE, hosted in the aluminum case behind the sensors, and composed of two Printed Circuit Boards (PCBs) mechanically

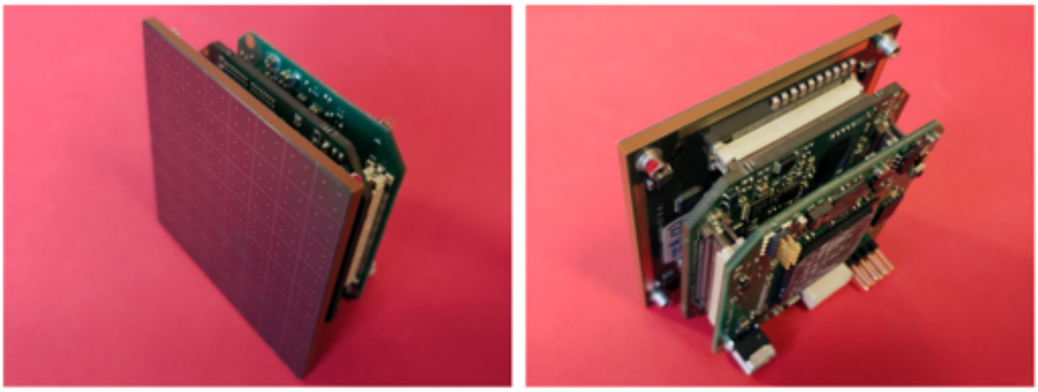

Fig. 3.17: Pictures of a PDM unit: a tile of 64 SiPMs with dedicated front-end electronics. Behind the sensors, the first PCB contains two CITIROC micro-chips, while the second one hosts the FPGA.

connected to the PDM module by means of four through screws [159]. The first PCB constitutes the true heart of the FEE, containing two Application-Specific Integrated Circuit (ASICs) designed on purpose to process the signal pulses recorded by 32 SiPMs each, working on two different channels at the same time: high-gain (HG) and low-gain (LG). This is the most demanding task of the entire electronics chain, carried out successfully by the ASIC developed for the ASTRI camera, the Cherenkov Imaging Telescope Integrated Read Out Chip[7] (CITIROC), whose design is intellectual property of INAF.
The second PCB hosts a Field Programmable Gate Array (FPGA), which is a general-purpose integrated electronic device used to control the two ASICs from the external computer. used to govern and control all the input/output operations from/to CITIROCs and SiPMs, with the external computer. In particular, the FPGA is a Xilinx ARTIX 7 chip [*link* 282] and its main functions are setup the CITIROC registers, read-out and deliver digitalized data, manage the trigger signals and perform topological discrimination (see section 3.3.2.2). In figure 3.17 are presented two pictures showing a PDM tile together with the two PCBs of the FEE, without the aluminum case. On the PCBs there are also other miniaturized circuits for specific operations: amplifiers, signal shapers, the peak-detector (PD) and the Analog-Digital Converter (ADC), commuting the analog signals from the CITIROC into digital data for the FPGA. Once the working parameters have been set, the entire FEE is completely independent and

---

[7] The CITIROC, realized by WEEROC [*link* 280] for ASTRI, is an improved version of the Extended Analogue Silicon photo-multiplier Integrated Read Out Chip (EASIROC, [165]): a commercial ASIC by Omega Micro [*link* 266] for SiPM read out [166].

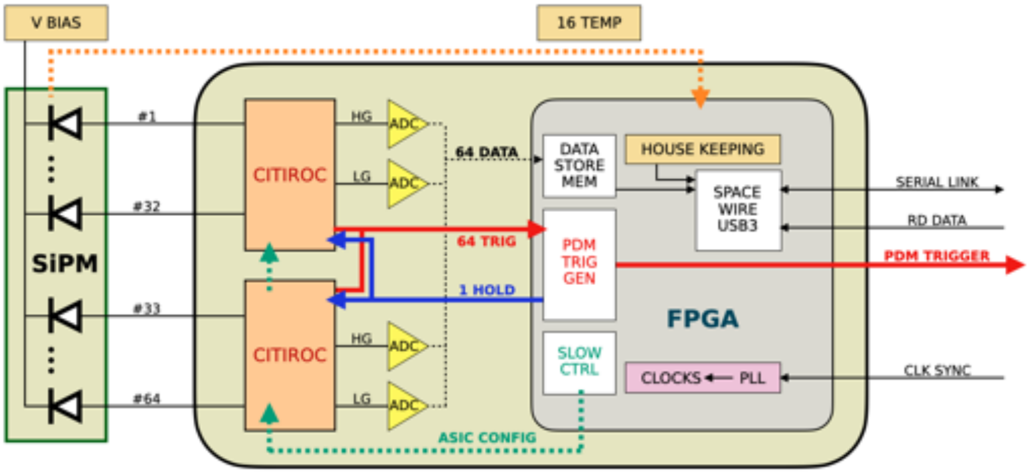

Fig. 3.18: Diagram of the ASTRI camera FEE (adapted from [164])

automatic, providing high efficiency auto-trigger capability and very fast camera pixel read out [160]. Figure 3.18 presents a diagram of the FEE, constituting a summary of the description proposed here.

The second module of the acquisition chain is the BEE, working at slower speed in comparison to the extremely fast FEE and located inside the basket, not on the focal plane, as it is shown in figure 3.13. The BEE represents the elaboration unit of the ASTRI camera, in charge of the complete data and command management of the instrument, interfacing the detector to the external world. In particular, the BEE receives data from the FEE in real time and delivers them in the required ASTRI packet format; it receives commands from the camera client software and performs related procedures, and lastly it monitors auxiliary devices [167]. From the BEE begins the stream of telemetry packages towards the last element of the acquisition chain, the DAQ server [168, 169]. It is the central component of the DAQ pipeline and consists of the workstation responsible for receiving and storing the different data packets produced by the camera (see section 3.3.3).

3.3.2.2 Signal processing

The operating principle of the ASTRI camera is the following: at the occurrence of a Cherenkov flash illuminating a set of neighboring SiPMs, the CITIROC auto-generates a trigger, which is sent back to the BEE and hence propagated to all PDMs, enabling the acquisition mode in the entire camera. After that, the measurement of the signal amplitude is activated for every pixel at the same time. Differently from other IACT, in our case this operation is not based on a sampling procedure, but rather on a peak detection strategy, thanks to an analog circuit (the *peak-detector*, PD) able to identify and record the maximum value of a signal within a characteristic time interval. With this basic scheme, the Cherenkov signal is acquired and converted to raw data for scientific analysis. More in details, the different steps of the signal processing can be described as follows. The first signal in response to the Cherenkov photons is generated by the SiPM sensors, emitting a short pulse with a very steep initial rise [164]. This signal is sent to a high gain pre-amplifier, and then to a bipolar Fast Shaper circuit (FS), that performs the prompt detection of any impulsive variation of the input signal. The FS has a *shaping time* of 15 ns, corresponding to the temporal RMS of the impulse, which is in relation to the very im-

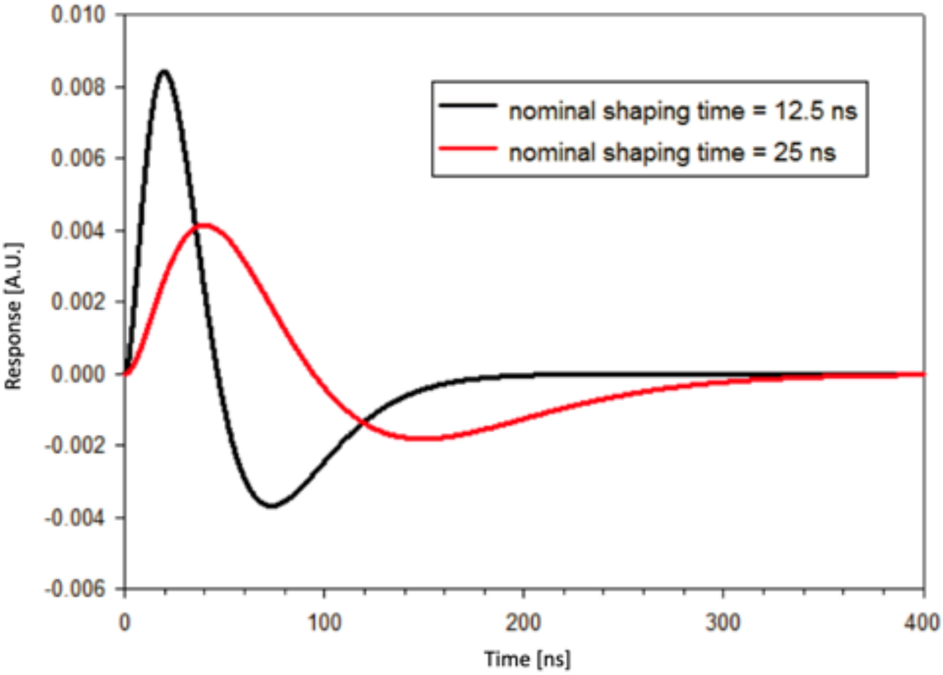

Fig. 3.19: The fast shaper is the element performing the promptly detection of every impulsive variation of the input level. This is the characteristic shape of the output signal, for two values of the shaping time, with the typical negative undershoot phase below the steady-state value.

portant *peaking time* representing the acceptance time window in which subsequent signals are added. Therefore, the peaking time corresponds to the maximum time-length of the signal integration for a single impulse: if no further signals are received within the peaking time, the FS output returns to the steady-state value, after a negative undershoot phase typical for this type of circuit [170], which is ultimately due to the conservation of energy (see figure 3.19). The output of the FS is strictly coupled to a fast discriminator, with a $10\,\mathrm{bit}$ programmable threshold E_t: if the signal exceeds the threshold level, then the discriminator produces a digital trigger which is sent to the FPGA board. Here a special topological algorithm sets a flag if n contiguous pixels within the PDM present a signal above the discriminator threshold. In this case, the trigger is sent to the BEE that, in turns, routes back to all the PDMs of the focal plane another logic signal, enabling the signal read out all over the focal plane. This operation is performed activating another circuit, the PD, which is connected to the output of the FS: at the end of the shaping time, the maximum value of the shaped pulse height is hold by the PD and then sent to a $12\,\mathrm{bit}$ ADC, for the final digital conversion. After this acquisition process, the digital signals are sent to the FPGA boards, where they are forwarded to the BEE for subsequent data processing.

The number n of contiguous pixels for the topological discriminator (aka *topo-trigger*) is programmable in the range 2 to 7: if a very low value is set also bright stars can trigger the data acquisition. The energy threshold is also programmable ($\geq 4\,\mathrm{pe}$) and its best value depends on the Night Sky Background (NSB) level, but $8\,\mathrm{pe}$ is in general a good assignation. During the observation campaign with ASTRI–Horn in 2018/2019, we verified that with an adequate set of parameters the trigger freqeuncy is in the range $50\,\mathrm{Hz}$ to $60\,\mathrm{Hz}$ for a clear night, while it is in the range $\sim 400\,\mathrm{Hz}$ to $500\,\mathrm{Hz}$ in case of clouds. In general, about $2\,\%$ to $3\,\%$ of these triggered events are produced by gamma rays.

3.3.3 Output data

The ASTRI camera produces different types of output data, classified in four categories: housekeeping (HK) calibration (CAL), scientific (S) and Variance (VAR). A separated classification (TECH) is reserved for engineering and auxiliary data, needed for scientific analyses. For every data type, the ASTRI project adopted a specific data format for raw binary files (RAW) produced by the BEE. The scheme of raw files is defined at a very low level, with hierarchical block structures for hosting the variables, specifying the Most/Least Significative Word[8] (MSW/LSW) indicating the correct direction to read every bit sequence[9], the so-called *endianness* or *endianity* of the file [171]. After the transmission to the ASTRI archive [*link* 224], the original raw files are converted in the FITS[10] format [173]: this is the first input of every data process pipeline, the level-zero data FITS packages (DL0). Among these files, in this thesis work we will focus on the VAR-DL0 subset: the Variance is an ancillary output of the ASTRI Cherenkov camera, providing a measure of the NSB and allowing to produce sky images using the ASTRI telescope as a common astronomical UV-optical instrument. Chapter 4 is entirely dedicated to the presentation of the Variance method and its potentialities.

3.3.3.1 Conversion from ADU to physical units

The data written in the output files are measured in Analog-to-Digital Units (ADU, or *ADC counts*), as they are taken after the digital conversion operated by the ADC circuit. As a consequence, in order to express the output values in physical units, it is necessary to operate a conversion from ADU to photo-electrons (pe), the electric charge produced by the sensors after stimulation by the incoming Cherenkov photons. For this purpose, a specific procedure was developed in the INAF laboratory of Palermo, in Italy, where the characterization of every single pixel was carried out with the following scheme.

Each PDM unit was inserted into a small climatic chamber (figure 3.21), maintaining the temperature at $(15.0 \pm 0.3)\,^{\circ}\mathrm{C}$. Inside the chamber the pixels were illuminated with a pulsating blue LED, at the constant rate of $10\,\mathrm{kHz}$, with a pulse duration of $5\,\mathrm{ns}$. For every pixel, $10\,000$ events triggered by LED pulses were acquired: an example of the histogram of the pulse height distribution in ADU is reported in figure 3.20. The first peak in the plot represents the so-called *pedestal value* (PED): the constant ADC output when the pixel do not see any photon. The subsequent peak of the distribution represents the first pe (ADC^1_{pe}), the third peak is the second pe, and so on. The distance between the peaks, expressed in ADU, has a

---

[8] Historically, a sequence of $8\,\mathrm{bit}$ is equivalent to $1\,\mathrm{B}$ (byte), while $16\,\mathrm{bit}$ were called $1\,\mathrm{word}$. In the ASTRI raw data format the MSW/LSW is indicated instead of the more common Most/Least Significative Byte (MSB/LSB).

[9] For example, `01011` is equal to 11 from right to left, 26 otherwise.

[10] A very common digital file format in astronomy, acronym of *Flexible Image Transport System* [172] [*link* 264].

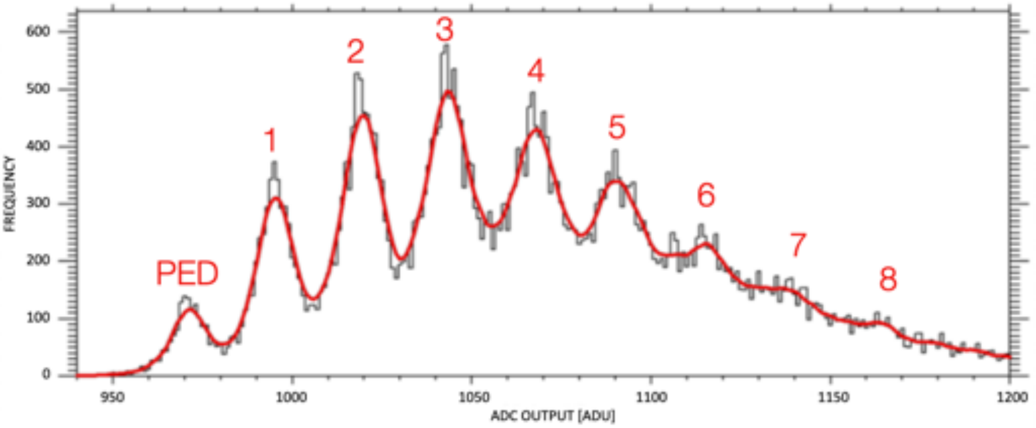

Fig. 3.20: Histogram of the ADC output for the characterization of a single pixel (black) smoothed with a boxcar averaging of fixed width (red). The pulse height distribution demonstrates the SiPM capability to resolve single photo-electrons: the distance between consecutive peaks measures the pixel gain in ADC counts (ADU).

constant width, reflecting the constant ADC/pe ratio, the so-called *photo-electron equivalent* (PE_{eq}). With refer to the HG channel, this quantity can be calculated as

$$\mathrm{PE}_{eq}\left(ADC\right) = \frac{1}{N}\sum_{i=1}^{N}\left(\mathrm{ADC}_{pe}^{i+1} - \mathrm{ADC}_{pe}^{i}\right) \,, \tag{3.2}$$

where ADC_{pe}^{i} is the ADC value of the local maximum related to the i-th peak, while N is the number of intervals considered. Pixel gains and pedestals as obtained from this analysis are then tabulated and used in the calibration of the ASTRI data. In particular, making use of the following three quantities for every pixel:

- the ADC value of the pedestal in LG (PED_{LG});
- the ADC value of the first pe in HG ($\mathrm{ADC}_{1^{st}pe}$);
- the constant ratio ADU/pe in HG (PE_{eq});

and the following formulas for the conversion between every ADC value and pe [139]

$$\mathrm{PE}_{HG} = 1 + \frac{\mathrm{ADC}_{HG} - \mathrm{ADC}_{1^{st}pe}}{PE_{eq}} \,, \tag{3.3}$$

$$\mathrm{PE}_{LG} = \frac{(\mathrm{ADC}_{LG} - \mathrm{PED}_{LG})}{\mathrm{PE}_{eq}} \times \eta \,, \tag{3.4}$$

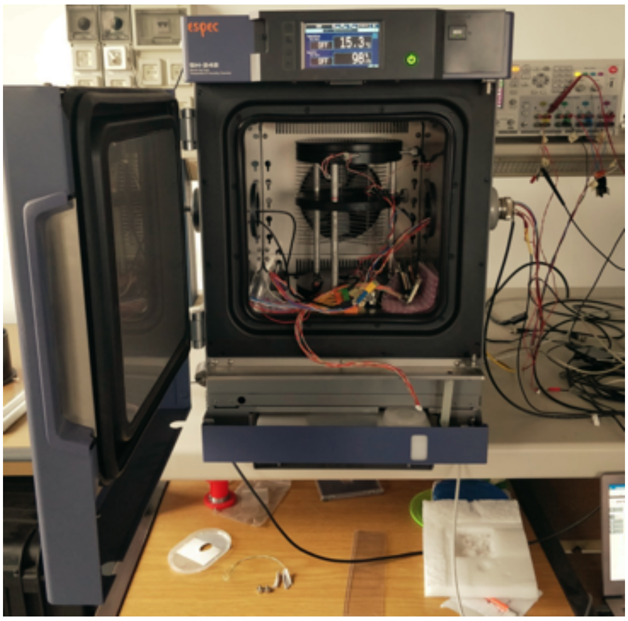

Fig. 3.21: Climatic chamber at the INAF laboratory in Palermo (Italy) for the calibration of single PDM tiles.

where $\eta = G_{HG}/G_{LG}$ is the amplification ratio between HG and LG, whose value is ~ 20 for the ASTRI–Horn prototype camera. It is interesting to notice that the envelope of the peaks in the calibration plot of figure 3.20 has a Poissonian profile, as it is typical in photon statistics, and that the mean value of the distribution corresponds to the light intensity emitted by the LED source.

After the conversion from ADC to pe, it is possible to retrieve the original number of photons hitting the sensor by dividing the result for the Photon-Detection Efficiency (PDE, [174]), which is a percentage number measured and tabulated for every SiPM. Lastly, to obtain the original number of photons produced by the extended air shower it is necessary also to divide for the efficiency of the filter and the transmittance of the optics.

3.4 Pointing

The ASTRI telescope design presents an alt-azimuth mount and therefore two motors are constantly in operation to ensure the correct pointing of every celestial source, and its tracking in time. These motors are equipped with encoders able to provide the absolute position of main axes with an angular accuracy of $\sim 2''$ [124]. However, the actual pointing accuracy of the telescope is affected by several factors, as for example gravity flexures or mis-alignments due to mechanical tolerances of the assembly. For this reason, a specific *pointing model* of the telescope was studied and implemented in the Telescope Control System (TCS), using first the `T-POINT` software [175] and then a custom IDL routine developed on purpose. The resulting pointing performance is monitored using several sub-systems: the housekeeping values from motor encoders, the Pointing Monitoring Camera (PMC, see section 3.4.2.1 below), and the data from the Variance ancillary output of the Cherenkov camera (which is presented in details in chapter 4 and constitutes the heart of the present thesis). The synergy of these sub-systems is discussed in the following chapters, while the present section is focused on fundamental concepts related to the pointing monitoring and auxiliary devices. In particular, section 3.4.1 reports the scientific requirements for the pointing performances, together with a detailed focus on the definition of the *optical axis*. Section 3.4.2 presents the PMC sub-system and another auxiliary device for monitoring the NSB in the pointing direction, i.e. the "UVSCOPE" instrument [176].

3.4.1 Requirements

In general, the situation of IACTs is very peculiar with regard to the pointing requirements. Despite Cherenkov cameras typically present only a modest angular resolution (a few arc minutes), for Cherenkov telescopes a pointing accuracy at the level of few tens of arc seconds is mandatory for scientific purposes. This is exactly the situation of the ASTRI project, where the requirement on the pointing *accuracy* is $35''$ for a single target (i.e. the difference between the position set to the telescope and the one read out from encoders after the slewing), and 0.1° for a tracking observation [177]. The requirement for the *precision* on the pointing reconstruction after data calibration is far more challenging: when every sub-system is in optimal conditions (and the weather is fine), the astrometric error should be less than $7''$ [177]. The present thesis work is based on archive data taken with the prototype telescope ASTRI–Horn when several sub-systems were still in the validation phase or under development (e.g. an automated feedback routine between the PMC and TCS was still missing), and hence we consider in the following chapter only an average reference value of $20''$, for both accuracy and precision, just as a rule of thumb for the design and assessment of our calibration procedures[11]. Of course, more

---

[11] This value was originally proposed in the context of CTA, and it was adopted in the following also for the ASTRI project. In the current version of the requirements document

detailed and technical evaluations will be presented in future internal reports when our novel techniques will have been consolidated.

3.4.1.1 The optical axis

To monitor the pointing *accuracy* means to consider the difference between the coordinates set to the telescope and its actual pointing direction, which is defined by the coordinates individuated by the *optical axis* of the system. In general, into an imaging device, the optical axis can be defined as the line along which there is the maximum rotational symmetry, and hence it can be adopted to indicate the direction of light propagation, in a first approximation. In the case of the ASTRI telescope, there are at least three different axes that must be considered to obtain a complete characterization of the pointing performances. They can be presented as follows.

υ_M The motors act on the perpendicular azimuth and elevation axes, individuating two planes that intersect on a straight line υ_M; during long observing runs, υ_M is the direction actually tracked by the motors (this is the so-called *mechanical* axis).

υ_C The curvature vertices of mirrors M1 and M2 define the axis of the optical system, υ_C. The geometric center of the Cherenkov camera is assumed to lay on this axis, if the assembly of the telescope is ideal.

υ_P The PMC shares with ASTRI the mount (and consequently the movements), but presents an independent optical system, with its own optical axis υ_P.

In an ideal configuration υ_M, υ_C and υ_P are not only parallel, but also coincident, allowing us to consider a unique optical axis υ, whose definition corresponds to any of the three provided above. However, in chapter 6 and 7 we show that in the case of ASTRI–Horn there are strong evidences that these three axes are not perfectly aligned. Therefore, we investigate the position of the Cherenkov camera (υ_C) and the PMC (υ_P) with respect to a generic "optical axis" equivalent to υ_M. Further details and definitions about the opto-mechanical structure of the system require additional tools and concepts that are beyond the scope of this work.

---

for the mechanical structure assembly of the MiniArray ([177]) this value does not appear anymore, but it is still a consolidated practice in internal operations to consider it for a first evaluation of new methods and techniques.

3.4.2 Dedicated hardware

As previously explained in section 3.4.1, due to the high pointing requirement in comparison to the low angular resolution of ASTRI, the Cherenkov camera is not suitable to monitor the pointing direction of the telescope and hence an auxiliary optical instruments is adopted for this purpose, i.e. the Pointing Monitoring Camera (PMC, see section 3.4.2.1). Such a device is equipped with a suitable optical system and presents a dedicated acquisition chain which is introduced in the following paragraph.

3.4.2.1 The Pointing Monitoring Camera (PMC)

The Pointing Monitoring Camera (PMC) is an auxiliary optical device (a CCD) aiming at the monitoring of the pointing direction of the ASTRI telescope. Due to the dual-mirror configuration and the consequent compactness of the mechanical structure, the PMC does not share the same optical system of the ASTRI telescope, but it is installed on the back of the support structure of the M2 mirror, with its own dedicated optics. The PMC presents a true FoV of $2.8° \times 2.1°$ and a pixel resolution of $1280\,\mathrm{px} \times 960\,\mathrm{px}$, resulting in a pixel size of $7.3\,''$, with a physical dimension of $12\,\mu\mathrm{m}$ for every pixel. The files from the PMC are saved in the FITS format and they are processed with a suitable software[12] in order to determine the astrometry solution of every image. This allows us to assign physical coordinates to the camera pixels using the standard Word Coordinate System (WCS, [178, 179]), obtaining a new "calibrated" FITS file.
The alignment of the PMC geometric center with the Cherenkov camera axis (υ_C) is a characteristic of the optical system that must be measured and monitored in time, in order to avoid systematic errors in the calibration of the telescope. In fact, the de-centering offset is one of the terms of the *pointing model* which is obtained with the PMC, but its rigid shift can be different from the one of the Cherenkov device, as it is shown in chapter 6.

3.4.2.2 UVSCOPE

In order to monitor the Night Sky Background (NSB) in the direction of the pointing, there is another ancillary devices mounted on board ASTRI–Horn: the small UVSCOPE instrument (see figure 3.22, *right*). UVSCOPE is devoted to the measure of the NSB in the same sky region that ASTRI is observing. It has a very simple optical system, composed of a pupil and a

---

[12] I.e. Astrometry.net [*link* 229].

Fig. 3.22: Two pictures of the ancillary devices mounted on board the telescope ASTRI–Horn. The Pointing Monitoring Camera (PMC) is mounted inside the red cylinder on the back of the M2 support structure (*left*) and the auxiliary instrument UVSCOPE is installed below the primary mirror (*right*).

protective quartz window, while the acquisition of the signal is based on Multi-Anode Photo Multiplier Tubes (MAPMTs) manufactured by Hamamatsu (series R7600-03-M64) allowing moderate imaging properties with a sensitive unit composed of 64 elements arranged in a matrix of 8×8 pixels [176]. The full field of view is $\sim 4.35°$, similar the sum of 9 ASTRI PDMs, and the response of the sensors allow an easy comparison with the NSB flux recorded by the SiPMs of the Cherenkov camera, very useful for calibration purposes [180].

4

The Variance Method

The ASTRI camera was specifically designed to detect short Cherenkov flashes indirectly produced by the cosmic radiation entering the Earth atmosphere. As it is explained in chapter 3, the camera electronics is based on a sequence of integrated circuits performing the prompt detection of any impulsive variation of the incoming signal from neighboring SiPM sensors. As a result, the coupling of the instrument to the sky is such that any steady or slow-varying optical signal from a celestial source cannot be detected with the ASTRI telescope. However, the camera presents also an ancillary output that actually provides a measure of the Night Sky Background (NSB) light, allowing to produce stellar images as if ASTRI were a common UV-optical telescope, without requiring any additional hardware. This is possible thanks to the so-called *Variance method*: a statistical procedure implemented in the FEE, which is based on the random sampling of the ADC pedestal output signal for every pixel. This strategy is inherited from the PMT technology, and it has never been implemented before on a telescope endowed with SiPM sensors to produce sky maps. This chapter is entirely dedicated to the Variance method, whose general features are discussed in section 4.1. Afterwards, section 4.2 presents the procedures to create sky images and perform their calibration, starting from the Variance data packages. Lastly, an overview of the intriguing possibilities provided by the Variance is reported in section 4.3.

4.1 General Features

The Variance is a peculiar feature of the ASTRI Cherenkov camera, a secondary output allowing to image the star field despite the AC coupling of the instrument with the sky. In fact, together with the Cherenkov flashes, also the photons of the NSB are conveyed by the optics on the sensors, but they will not trigger the scientific acquisition mode (SCI) and hence the camera will not record their signal. However, this radiation generate photo-electrons too, and hence a pulse signal is produced anyway at the output of the ADC in coincidence of their arrival. Consequently, considering the light emission of a steady celestial source, the FEE will produce a sequence of repeated bumps in the ADC, oscillating around the pedestal (see figure 3.19), increasing the variance (σ^2) of the output signal. As a result, a visualization of the σ^2 of each pixel actually constitutes a map of the NSB light: this is the so-called Variance method of the ASTRI camera [164, 181]. Figure 4.1 (*left*) presents an image produced with the Variance method, in comparison with the visualization of SCI data, where a Cherenkov flash is clearly visible. In order to obtain an estimate of σ^2, the variance acquisition mode (VAR) is based on the continuous sampling of the ADC output, in absence of trigger signals. This task is implemented in the FPGA as it is reported in details in section 4.1.2, while in the next one a focus on the relation between σ^2 and the NSB flux is presented.

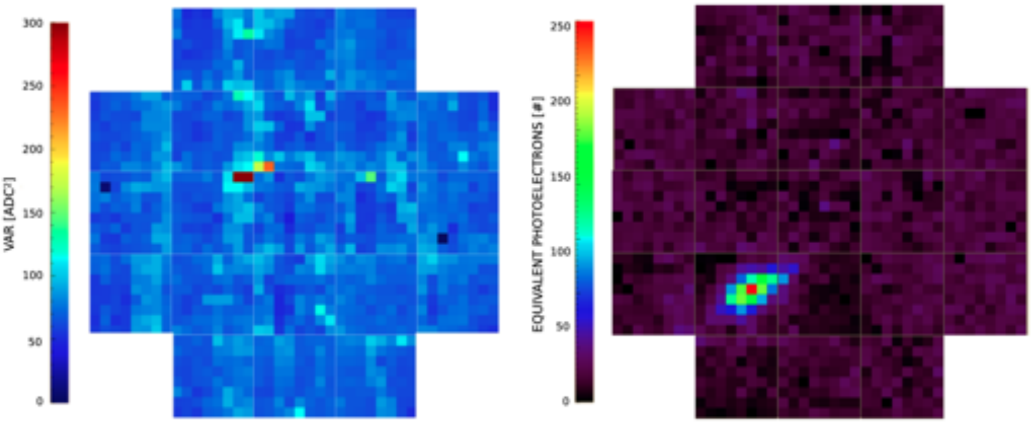

Fig. 4.1: Difference between a raw Variance frame (*left*) and a Cherenkov image (*right*), taken with ASTRI–Horn in the same period, towards the region of the Crab nebula (center of the FoV). In the Cherenkov image a light flash is clearly visible, while in the Variance only the noisy contribution of the NSB is present.

4.1.1 The NSB flux

The NSB photons are always present in the acquisitions of the ASTRI camera. In scientific images the intense radiation of extended air showers predominates, but in order to extract the true Cherenkov signal the average NSB level must be subtracted in every pixel, with a *cleaning* procedure. The Variance is the most effective method to estimate the level of the NSB contamination, obtaining its value from the σ^2 of the ADC pedestal. However, the fluctuations of the ADC output are not only generated by the NSB flux, as in general there is also the contribution of the electronics dark current,

$$\sigma^2 = \sigma^2_{\text{Dark}} + \sigma^2_{\text{Sky}} \ . \tag{4.1}$$

In the specific case of the ASTRI camera, the intrinsic dark noise is negligible with respect to the sky contribution, being 40 times smaller at maximum [166]. On the other hand, regarding the component due to the sky signal σ^2_{Sky}, by statistical considerations it is possible to show that it is proportional to the incoming NSB photon flux ϕ_{Sky}. In fact, the sky flux is proportional to the number of photons n hitting the surface of the sensors in the unit time t. The distribution of photons is described by a Poissonian statistics and hence the probability $P(n)$ is given by

$$P(n) = \frac{\lambda^n}{n!} e^{-\lambda} \ , \tag{4.2}$$

where λ is the expected value, or the mean number of incoming photons in the time interval t, that we do not know[1]. However, in a Poissonian process the variance of the distribution is equal to λ too, and hence the σ^2 of the photon sequence provides a measure of the amount of photons. As the radiation impinging on the pixels produces a certain number of pe which is detectable in the multiple pulses of the ADC output, we can conclude that the variance of the pedestal is proportional to the sky flux[2]. This linear relation is well verified with laboratory measurements over a wide range of values, considering for example σ^2 versus the current of photo-electrons generated by the sensors (see figure 4.8). As a result, the equation (4.1) translates into the simpler relation

$$\sigma^2 = \kappa \phi_{\text{Sky}} \ , \tag{4.3}$$

---

[1] It is possible to estimate *a posteriori* this value multiplying the photon-detection efficiency (PDE) for the total number of photo-electrons recorded by the electronics: the camera *rates* (see section 4.1.3.2).

[2] Exception made for the case of saturation effects such as the *pulse rate non-linearity* or the *pulse amplitude non-linearity*, but they require very advanced topics in electronics.

where κ is a constant of proportionality. Equation 4.3 allows us to adopt the Variance of every pixel as a measure of the NSB light in the FoV. This estimation presents a statistical uncertainty related to the number of samples N_s considered for the calculation of the variance. Assuming they follow a normal distribution, the relative error is

$$\frac{\delta\left(\sigma^2\right)}{\sigma^2} = \sqrt{\frac{1}{N_\mathrm{s}-1}}\,, \tag{4.4}$$

equal to κ times the relative error on the sky flux. For the typical value of $65\,535$ samples ($16\,\mathrm{bit}$ Variance), the relative error is $\sim 0.5\,\%$.

4.1.2 Signal sampling

At the electronics level, the Variance originates from the continuous sampling of the ADC output. In particular, after the acquisition of N_s subsequent samples x_i of the ADC digital output x, in absence of trigger signals, the variance can be calculated with the usual formula

$$\sigma^2 = \frac{\sum x_i^2}{N_\mathrm{s}} - \left(\frac{\sum x_i}{N_\mathrm{s}}\right)^2 \,. \tag{4.5}$$

The task of sampling the ADC signal and elaborate the raw variables for the VAR packages is implemented in the FPGA logic board of the FEE. The number of samples is calculated with the user-defined variable `VARSAMP`, trough the relation $N_\mathrm{s} = 2^{\mathrm{VARSAMP}} - 1$, while the constant sampling frequency f_s is set to $2\,\mathrm{MHz}$, in order to have a reasonable high statistics without overloading the electronics. However, the readout of the 32 pixels from every CITIROC is operated in series, and hence the effective frequency for the Variance acquisition is reduced to $f_\mathrm{VAR} = f_\mathrm{s}/32 = 62.5\,\mathrm{kHz}$. Consequently, the total amount of time to collect N_s samples from every sensor is $T_\mathrm{VAR} = N_\mathrm{s}/f_\mathrm{VAR}$.

In the typical configuration `VARSAMP`$=16\,\mathrm{bit}$ and consequently the duration of every single Variance acquisition, or *frame*, is $T_\mathrm{VAR}{\sim}1.05\,\mathrm{s}$. Every frame will give origin to a different Variance image. This implies that in this configuration every image has an intrinsic error due to the Earth rotation $\omega_\oplus = 15''/\mathrm{s}$, but on the other hand the large number of samples ensures a very low relative uncertainty on the measure of the flux (see equation 4.4). In order to obtain sky maps with improved time resolution, it is possible in principle to reduce the `VARSAMP` value (e.g. to $10\,\mathrm{bit}$) and exploit the wide FoV of the ASTRI telescope for monitoring the light curve of several objects at the same time. However, in this case the statistical relative uncertainty would be much larger and hence the resulting magnitude error would allow to perform interesting measurements only on the position of bright transient objects like satellites or asteroids and so on, but not on their flux.

The estimation of T_{VAR} as the time required for the acquisition of a single frame actually represents only an inferior limit, because the readout of the pixels by the CITIROC is interrupted when a trigger signal is generated. In this case, the samples not already sent to the FPGA are lost, and the CITIROC resumes the reading operation starting again from the first pixel. Considering that the average trigger frequency is $\sim$60 Hz and that every CITIROC manages the readout of 32 pixels, it is easy to verify that the delay in the VAR acquisition due to the triggers is negligible, being $\lesssim 1\,\mathrm{ms}$.

In practice, a much larger delay in the production of VAR files is due to the BEE. In fact, the time distance T_{FRAME} between the delivery of a Variance package and the next one is much greater than T_{VAR} which is required for their acquisition. The reason is that a new VAR readout cycle is started by the FPGA only when the BEE has collected the data from *all* the PDMs, and it takes $\sim$2 s for this operation because a broadcast communication is implemented only from the BEE to the FEE, and not vice versa. On the ASTRI cameras for the MiniArray this aspect will be improved and $T_{\mathrm{FRAME}} \sim T_{\mathrm{VAR}}$, but in the data taken with ASTRI–Horn the average value for T_{FRAME} is $\sim$3.15 s, as it is shown in the plot of figure 4.2.

4.1.3 Non-correlated events

As a consequence of the NSB flux, a huge number of pulses in the ADC signal continuously propagate in the camera without being registered by the electronics: they are usually referred to as *non-correlated events* The incoming photons induce the production of photo-electrons, or *events*, but they do not start the generation of the trigger because they do not pass both the threshold and the topological discriminators. The Variance is undoubtedly the most effective method to detect the contribution of non-correlated events, but there is also another possible way.

In coincidence of a Cherenkov flash, passing both the threshold level and the topological discriminator, the acquisition of the data is performed on every pixel and hence a large number of non-correlated events is recorded as well, outside the region illuminated by Cherenkov photons. Considering the cumulative histogram of all the pulse heights recorded in subsequent triggered acquisitions, the contribution of non-correlated events

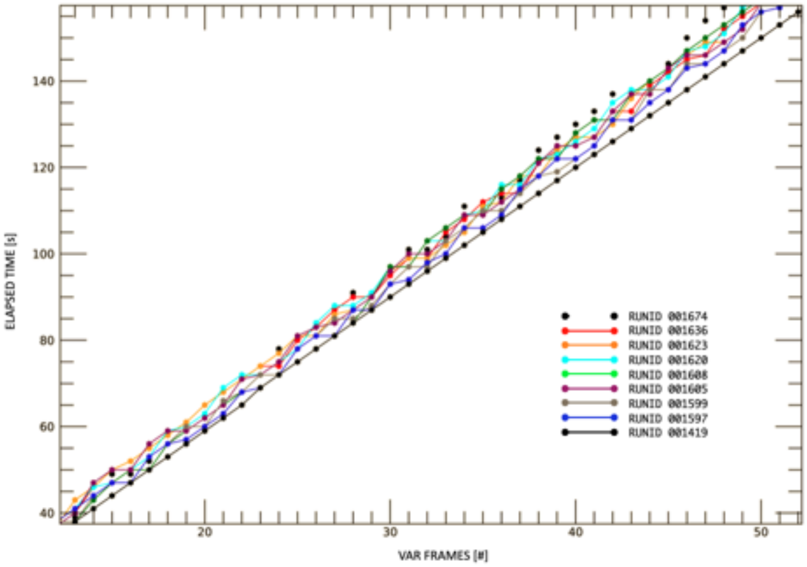

Fig. 4.2: Each dot in this plot represents a VAR frame of a specific observing run with ASTRI–Horn (see the color scheme). The y is the time elapsed since the beginning of the observing run, while the x axis reports the frame number. The mean slope of the linear regressions shows that a VAR frame is delivered every $\sim 3.15\,\mathrm{s}$ on average.

appears as a Gaussian broadening of the pedestal value, whose squared σ is exactly the same value that we measure with the Variance method. In fact, the result of repeated random acquisitions generated by the triggers, is equivalent to the sampling carried out in the Variance method, with a lower frequency. A detailed analysis of this alternative method provides some useful insights into the functioning of the ASTRI camera and also of the Variance method. For this reason further considerations about it are reported in the next section.

4.1.3.1 Further considerations

Figure 4.3 reports the cumulative histogram of the ADC output (in pe) for all the pixels of PDM 19 during a scientific run with ASTRI–Horn. This plot is the same of figure 3.20, but with the true sky signal instead of the pulsating LED light as a source of photons: in this case the signal acquisition is triggered by real Cherenkov flashes illuminating some pixels. The resulting continuous distribution presents two different components. On the right there is the slope of the pixels that saw a large amount of radiation: they are probably responsible for the generation of the triggers

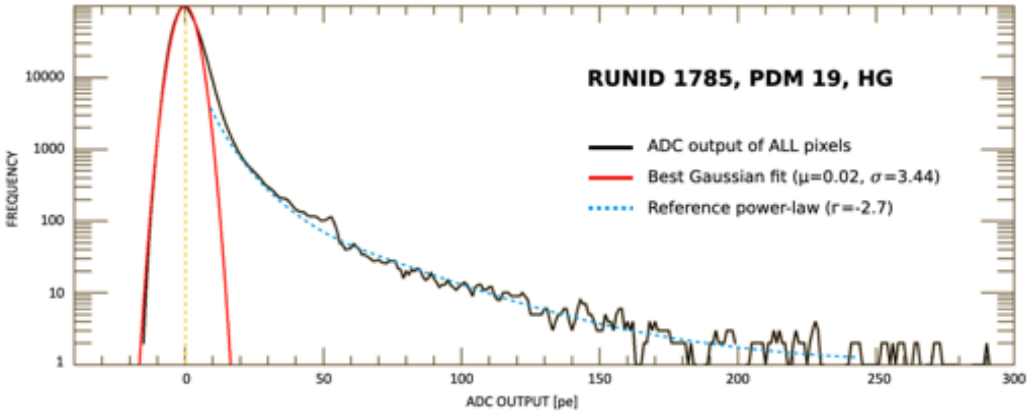

Fig. 4.3: Cumulative histogram of the pulse height distribution of PDM 19 (HG) during a scientific observing run with ASTRI–Horn (*black*). The component due to non-correlated events is fitted with a Gaussian bell (*red*) which in centered in zero, indicating a good calibration of the system. A power-law is overplotted in *blue* for comparison.

and they constitute the so-called *correlated events*. On the left, there is a broad dispersion around the zero, perfectly fitted by the red overplotted Gaussian curve. The right tail of the bell is overwhelmed by correlated events, but the left hand side is evident. In this region the negative pe values are produced by the fluctuations of the ADC signal below the pedestal (see figure 3.19), yielding non physical negative results because the steady-state level has already been subtracted during the conversion in pe. This Gaussian bell is produced by non-correlated events due to the NSB: the mean value is centered in zero, indicating the absence of systematic errors, while the square of the σ is exactly equivalent to the variance that we compute with the Variance method. As a proof, when a bright star enters the PDM under consideration the slope on the right does not change, while the Gaussian bell gets visibly larger. This is exactly the process on which the Variance method is based: the RMS of the pedestal signal increases when a bright source illuminates the sensors.

In principle, it is possible to produce several plots similar to figure 4.3 but relative to single pixels: with this procedure we will obtain sky maps directly from scientific data, without using the Variance[3]. However, because of the low trigger frequency ($\sim$60 Hz) with respect to the $\sim$65 kHz of the Variance, this new method presents a quite large statistical uncertainty, about 12 % instead of 0.5 %. Moreover, with the Variance it is possible to

---

[3] This possibility was investigated in [182], with the variable called `PHDVAR`.

have a good time resolution and observe transient phenomena or study the movements of the telescope, while the imaging procedure based on SCI data requires a longer integration time and hence only steady sources with respect to the ASTRI FoV can be identified. However, this technique provides also some interesting connections with the ASTRI science, that are briefly discussed in the next paragraph.

4.1.3.2 Additional scientific topics

The analysis of the plot in figure 4.3 constitutes undoubtedly a useful and interesting tool to understand the functioning of the ASTRI camera and the Variance method, but it offers also some surprising insights on the ASTRI science. First of all, the accumulation of correlated events on the right constitutes actually a differential spectrum $dN/d(\mathrm{pe})$. The slope of their distribution is well described by a power-law (the blue dashed line) whose spectral index is $\Gamma \sim -2.7$, corresponding exactly to the measured value for cosmic rays (section 1.1.1). As a consequence, this plot becomes immediately of interest for scientific purposes in two different ways. First, by comparing this curve with a calibrated differential plot from other IACTs, it is possible to provide an estimation of the ASTRI energy threshold. The point where the slope of correlated events detaches from the fluctuations of the pedestal (at $\sim$8 pe, which is also the best value to set the energy threshold into the discriminator) corresponds to $\sim$1.12 TeV in the comparison with the flux-calibrated spectrum[4]. This result is remarkable close to the reference value for the energy threshold of $\sim$1 TeV obtained with simulations or from the approximated formula

$$E_{thr} \propto \sqrt{\frac{\Omega\tau\phi}{A\eta}}\,, \tag{4.6}$$

where Ω is the solid angle subtended by the detector, τ is the electronic integration time of the system, ϕ is the photon flux from the NSB, A is the area of the mirror and η is the photon-detection efficiency (PDE) of the sensors [183, 184].

Another interesting application of the plot in figure 4.3 is that the slope of correlated events does not depend on the optics efficiency, being generated by the shape of the cosmic ray spectrum, but the total number of recorded events actually does. As a consequence, while the analysis of the profile shape guarantees that the camera is working properly, the number of total pe, or the *rate* of the ASTRI camera (measured in MHz), can

---

[4] Thanks to Osvaldo Catalano for this difficult estimation.

be exploited to detect any eventual loss of effective area, due for example to degradation of mirror reflectivity, as it was demonstrated in the experience with ASTRI–Horn. To have a good estimation of the camera rate, it is sufficient to take the σ of the Gaussian bell in figure 4.3 and divide for the time length of the signal acquisition window, the *peaking time*, whose typical value is $\sim 75\,\mathrm{ns}$ for a pulse shaping time of $15\,\mathrm{ns}$. From a physical point of view, the camera rate R represents the average number of photoelectrons generated per second, and hence it provides also a measure of the total current I with the formula

$$I = eGR\,, \tag{4.7}$$

where e is the electronic charge and G is the gain of the SiPM sensors, representing the increase of the electron number after their typical cascade mechanism.

4.2 Image production

The most of the analysis presented in the following chapters are based on sky maps of the NSB light obtained with the Variance method. However, the output of the VAR acquisition chain are not image files, but a long sequence of data files relative to the sampling of the ADC output pedestal for every pixel of the Cherenkov camera. Therefore, this section is dedicated to describe the structure of such files (section 4.2.1) and to present the procedures that we developed to transform them into VAR images (section 4.2.2). Lastly, the delicate process of calibration is presented in section 4.2.3, together with the outline of further calibration procedures to be implemented in the VAR analysis pipeline for the MiniArray.

4.2.1 Raw data

The data acquisition of the ASTRI telescope is organized into consecutive observing runs, each denoted with a univocal value of the tag `RUNID`. Each run contains a different number of VAR packages (or *frames*, as they will give origin to different Variance images), depending on the time length of the run. Each frame is produced with N_s samples of the ADC signal, taken from the FPGA and sent to the BEE after a specific elaboration. In fact, in order to reduce the bit usage and to speed up the calculation, a fixed offset[5] is subtracted to every single ADC sample and then only the

---

[5] In the case of ASTRI–Horn it was set to $1950\,\mathrm{ADU}$.

result of their sum and the sum of their squared values are stored into the memory. With this strategy, the values of the N_s samples are not saved individually and a lot of computational resources is saved. The resulting binary files constitute the level-zero data production (DL0). As explained in section 3.3.3, these files are converted into the FITS format (VAR-DL0, with extension .lv0) and uploaded in the ASTRI web archive [*link* 224] with a suitable nomenclature: a letter indicates the status of the camera[6] while the code 1002 at the end of the file name indicates that it actually contains VAR-DL0 data. In every VAR file, and more specifically in every VAR frame, the values of the following keywords are important for our purposes:

`TIME_UTC`	providing the time tag in UTC of the frame acquisition (end);
`VARSAMP`	defining the the number of samples $N_\mathrm{s} = 2^{\mathrm{VARSAMP}} - 1\,;$
`SUMSQ`	equal to $\sum x_i^2$, for every pixel;
`SUM`	equal to $\sum x_i$, for every pixel.

Starting from these data, the value of the variance for every pixel v_i can be computed with the usual formula (4.5), and this is the true starting point for the image visualization.

4.2.2 Visualization

In order to obtain a visualization of the ASTRI FoV there are different strategies to produce an image staring from the values of the Variance v_i recorded in every pixel. The simplest way is to display the data using a matrix 40×40 (for the reduced camera configuration adopted with ASTRI–Horn), where every element corresponds to a pixel of the Cherenkov camera, reproducing their true arrangement. This procedure allows to obtain a *quick-view* (QV) of a Variance frame and it is very useful for inspecting the contents of the files by eye, but it is inadequate for carrying out scientific elaborations because the true distance relations of the pixels are not considered, having removed for example the gap between the PDM tiles and between the sensors. As a consequence, in order to determine the exact position of a light spot on the focal surface or to study the contribution of dead areas between the pixels, it is necessary to introduce a

---

[6] Idle status (I), observing status (R) or “first idle” status (F) after turning on the BEE. The VAR acquisition is available in all these modes.

larger matrix, constituting a grid with much higher spatial resolution, allowing the possibility to visualize also the details of the ASTRI camera structure. Both these methods for the data visualization are presented in the following sections.

4.2.2.1 Quick-viewers

The QV procedures are based on 2D arrays of only 40×40 elements, ensuring a very fast elaboration of images. To assign the Variance values v_i to the correct matrix elements, we adopt the usage of specific *masks*: equivalent matrices containing in their elements the label of the corresponding PDM tile or the pixel number (PIX). For example, to set the value v_{pq} in the position of the q-th pixel of the p-th PDM into a QV image, it is sufficient to identify the unique matrix element where the PDM mask is equal to p and the PIX mask is equal to q. Figure 4.4 presents an image of the PDM and PIX masks. The elements outside the camera are initialized with a conventional `NULL_VALUE` (that we set to zero) in order to be easily recognized and removed during further elaborations.

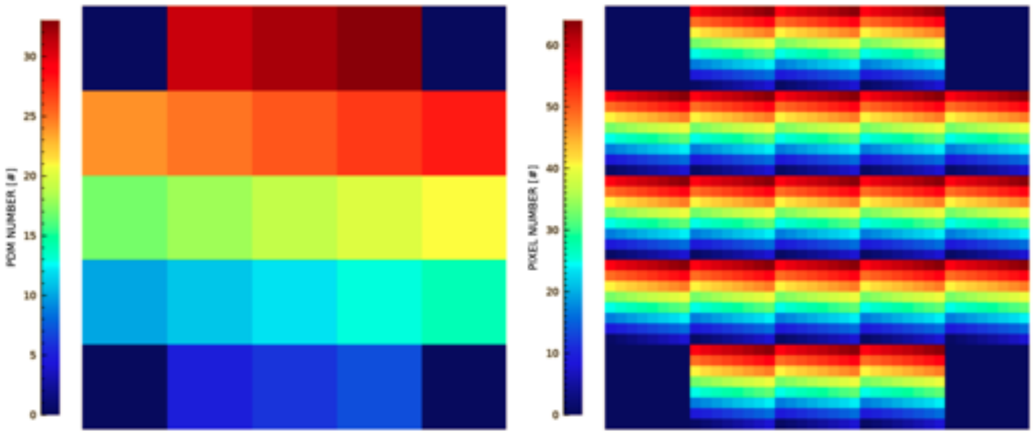

Fig. 4.4: PDM and PIX mask matrices for Quick-viewers. Elements outside the ASTRI camera are initialized with a `NULL_VALUE` that we conventionally set to zero.

We developed three QV routines for three different purposes. They are all coded in the IDL language [*link* 253] and a brief description of this software is provided in the following list.

`DISPLAY` is a custom function wrapping the standard *image* utility of the IDL library, equipped with some special extra-features extremely useful for the visualization of VAR data. This function allows to visualize a single frame at a time.

`VAR_QV40` is a procedure implementing an interactive widget with a very essential Graphical User Interface (GUI), allowing to visualize a VAR frame but also to change image by moving a scroll bar (see figure 4.5). This procedure is useful for inspecting by eye all the frames of a RUNID, or a specific subset.

`VAR_QVMOVIE` is a procedure to produce a movie (in the .mp4 format) of an entire observing run mounting a certain number of VAR frames per second. Thanks to this very fast visualization it is possible to detect transient phenomena as comets, meteors, or satellite flares.

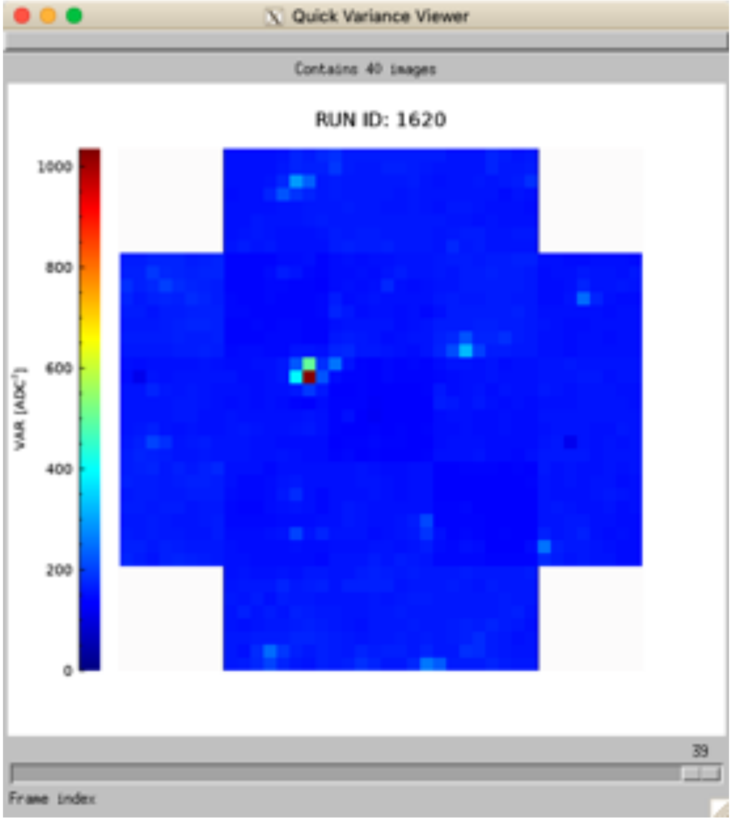

Fig. 4.5: The GUI of the `VAR_QV40` widget for the visualization of VAR data. In the case reported, a set of 40 frames is loaded from the run 1620 and it is possible to change image moving the horizontal scrollbar on the bottom of the window.

The codes 4.1 and 4.2 present the typical IDL procedure to visualize a VAR frame in a QV image. The images produced by the quick-viewers are very useful to see the content of VAR frames and they will be shown several times along this document. However, even if the pixel arrangement is preserved in such images, there is no way to retrieve the exact position of the pixels with respect to the camera coordinate reference system presented in section 3.3.1.2. For this reason, when it is necessary to perform manipulations or measurements on the VAR frames, another strategy is adopted for data visualization, making use of images with higher resolution.

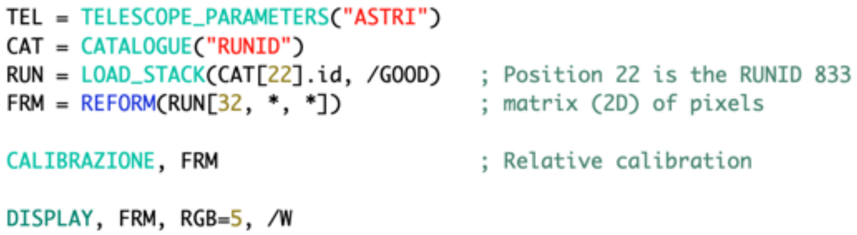

```
TEL = TELESCOPE_PARAMETERS("ASTRI")
CAT = CATALOGUE("RUNID")
RUN = LOAD_STACK(CAT[22].id, /GOOD)    ; Position 22 is the RUNID 833
FRM = REFORM(RUN[32, *, *])            ; matrix (2D) of pixels

CALIBRAZIONE, FRM                      ; Relative calibration

DISPLAY, FRM, RGB=5, /W
```

Code 4.1: Typical IDL source code to obtain a QV image of a Variance frame through the `DISPLAY` custom procedure. The functions colored in cyan have been developed on purpose to ease the data handling and visualization.

```
DISPLAY, FILE=“PATH/TO/FITS.lv0“, FRAME=42
VAR_QV40, FILE=“PATH/TO/FITS.lv0“, FRAME=[0:42], /ALL
VAR_QVMOVIE, FILE=“PATH/TO/FITS.lv0“, FRAME=[0:42], /ALL
```

Code 4.2: Calling sequence in IDL language of the three QV procedures described in section 4.2.2.1. If the `/ALL` keyword is provided the frame interval is ignored and all the run is visualized.

4.2.2.2 High resolution images

To provide a better visual description of VAR frames, including the articulated mechanical structure of the ASTRI camera, it is possible to increase the size of the square matrix adopted for the visualization, reducing the corresponding physical dimension of every element, allowing to represent smaller details as the gaps between the pixels or between the PDM tiles. However, this strategy has two serious problems. First, in order to consider the geometry of the camera with high accuracy it is necessary to define a very huge matrix for every frame. Second, such large variables require a lot of computational resources and every operation becomes in turns very time-consuming. For this reason, when the small details of the camera matter, it is better not to work with images, but rather to introduce another procedure based on the geometrical parameterization of the profile of every Cherenkov pixel (see section 5.3). On the other hand, if the visualization of the gap between the pixels is not necessary, the usage of high resolution images is still probably the best solution to have a good visual description of the VAR data, because it allows to introduce interpolation and smoothing algorithms providing a better representation of the full FoV of the ASTRI telescope. The details of the procedure can be reported as follows.

In the camera reference system, the center of every pixel has a precise position, that we measured on the CAD drawing of the focal plane assembly. Consequently, we can assign the values of the Variance v_i to the positions x_i and y_i of the centers and then we can use a 2D interpolation algorithm to obtain the values of the Variance in correspondence of a grid of new (x, y) points. The output of this procedure is a matrix with the interpolated Variance data and two matrices with the x and y values associated to the new elements, the so-called *meshgrids*[7]. The resolution of the resulting images is determined by the separation of the new points adopted for the interpolation. In addition, a smoothing process with a proper radius can help to further remove the residual effects of the original large pixel size, obtaining a better visualization of the full FoV. Figure 4.6 shows the quick-view of a VAR frame on the left, and its elaboration with this procedure on the right.

The production of high resolution images through interpolation and smoothing of Variance data represents not only a technique to obtain sky maps with better visual quality, but also a method for providing likely reproductions of the true NSB features. In fact, considering a star in the FoV, if its light spot falls between two pixels, they record half of the total intensity each, and the interpolation algorithm assigns that value to all the new sub-pixels located between the centers of the old pixels. Afterwards, the smoothing algorithm softens the edges of such high intensity region, producing a new local maximum close to the original position of the light spot centroid. As a consequence, images with sub-pixel resolution provide the

---

[7] In general, a meshgrid is a 2D array of coordinates for the evaluations of 2D scalar/vector fields over a 2D grid of points.

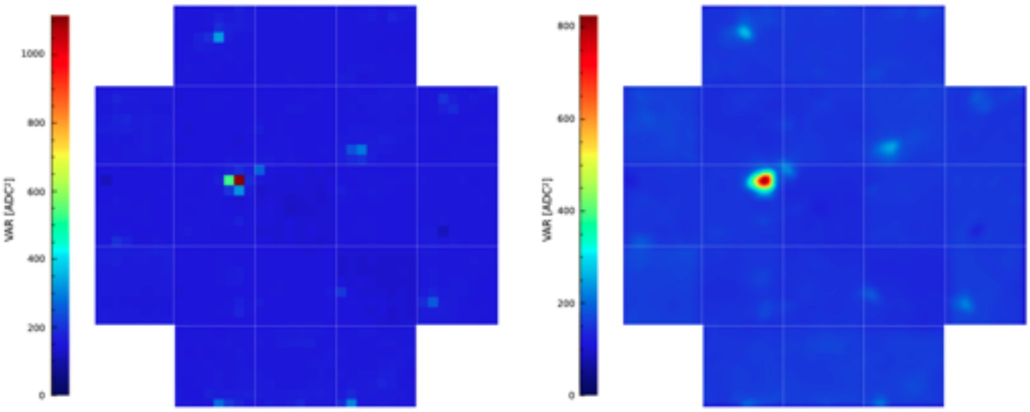

Fig. 4.6: This is the frame 280 of the RUNID 1597. *Left*: QV image of the VAR data. *Right*: elaboration of the image with an interpolation resolution of 1 mm and a Gaussian smoothing with σ =2 mm.

possibility of locating the exact position of a star in the FoV, by fitting the resulting data with suitable 2D functions. More details about this process are reported in section 5.2, where a deep analysis of the convolution between the ASTRI PSF and the pixel distribution is presented. For now, the simplified heuristic explanation reported here already gives a taste of the important applications of high-resolution images obtained with sub-pixel interpolation.

4.2.2.3 Standard projection and views

The masks adopted for the production of VAR images, both QV and interpolated ones, contain the displacement of the PDM tiles in the order that an observer would see standing in front of the Cherenkov camera when it is mounted on the telescope in parking position (elevation equal to zero). This is the standard view that we adopt for the VAR data throughout this document and it is referred to with the name *CamView*. When it is necessary to match the VAR images with the sky representations available in stellar catalogs, another standard view is adopted, obtained with a N-S flip of the CamView. This is the so-called *SkyView* visualization, presenting a perfect match with the sky maps, having considered the focal plane assembly and the response of the optical system. With refer to the camera coordinate reference system reported in section 3.3.1, these standard views can be defined as follows:

- *CamView*, the x axis points right and y axis the top of the image;
- *SkyView*, the x axis points right and y axis the bottom of the image.

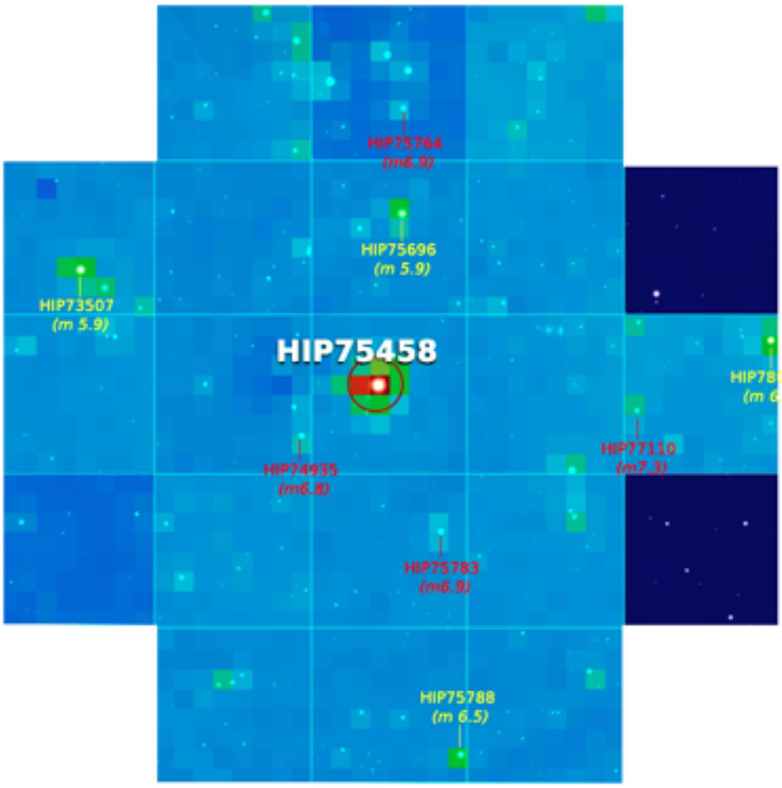

Fig. 4.7: A Variance image in SkyView (frame 24, RUNID 1233) is superimposed on an optical representation of the sky in the same region. The star in the center is Iota Draconis (HIP75458), while the labels of fainter objects are colored depending on their magnitude: *yellow* for $\mathrm{mag} > 5$ and *red* for $\mathrm{mag} > 6.7$. On the right, two PDM tiles (14 and 28) were off. VAR and optical images were matched manually.

Figure 4.7 presents an image where a QV Variance frame is superimposed on a sky map taken from a star catalog for demonstrating the adequacy of the SkyView transformation.
The perfect matching of the images in figure 4.7 can be surprising, because the `DISPLAY` procedure does not provide actually a much accurate visualization of the ASTRI camera. In fact, besides the removal of the gaps between the pixels that was already reported before, also another important feature is neglected in the QV images: the projection of the spherical focal surface. In general, throughout this document, we will always consider the (x, y) coordinates of the pixels without considering their z, which is equivalent to working in the normal projection of the camera onto the plane tangent to the central PDM tile. This operation is not an

approximation to simplify the analysis, but actually it constitutes the correct procedure to perform any astrometric evaluation of the FoV, because the plate-scale of the ASTRI telescope is measured exactly on that tangent plane rather than on the curved paths of the true spherical focal surface (namely, it constitutes a *linear* plate scale). Therefore, this *standard projection* is adopted for example in the extremely accurate analysis of the convolution between the PSF and the pixel distribution presented in section 5.2, or in the astrometry technique developed in chapter 5. In principle, it should be considered also for the production of high precision sky maps: the size of external pixels would be reduced as a consequence of the tilt angle of the outermost PDM tiles (which is $\sim 11°$, corresponding to a compression of $\sim 0.13\,\mathrm{mm}$ per pixel in the case of the tiles at the edge of the camera[8]). However, this correction is small compared to the true size of the pixels and hence the QV strategy, in which the pixels are displayed as if they were arranged on a plane, is still a good solution for visualization purposes only. Moreover, in such images the absence of the gaps introduces a much bigger error of $\sim 13\,\mathrm{mm}$ across the whole camera ($\sim 4.4\,\%$), but again it is possible to adopt anyway the QV strategy for quick cross-checks with star catalogs, simply considering a $\sim 4.4\,\%$ larger plate-scale and obtaining the good match reported in figure 4.7 as a result.

4.2.3 Calibration

The calibration of SCI data is different from that of Variance frames: a procedure for elaborating the raw SCI signal has been already developed and tested [86], while a definitive approach for the calibration of VAR images is still missing at present. In this section, we present the solution that we adopted for the work of this thesis.

Of course, the raw values in the pixels of Variance images must undergo a delicate process of calibration before any further scientific elaboration. In fact, there are several factors producing a non-uniform response of the camera to the sky signal, as it is shown if the upper-left image of figure 4.9: gain differences, dead pixels, different micro-cell sizes[9], PDM saturation effects, and lots of other phenomena affect the VAR level in every pixel contaminating the sky contribution. In general, the electronics is responsible for the *intrinsic* or *gain* calibration (each pixel has a different board, sensor, PDE, bias voltage, etc.), while the so-called *flat-field* calibration is de-

---

[8] These values refer to the camera in the full configuration, while in this document we are considering the reduced assembly of only 21 tiles (instead of 37) adopted for ASTRI–Horn.

[9] See section3.3.1.

termined by the optical system (mirror reflectivity, vignetting, filter transmittance, etc.). Both these contributions must be considered for a complete calibration process that allows to convert the Variance values in a measure of the NSB flux in physical units. This is the ultimate goal of the *absolute* calibration of Variance frames: converting the ADU^2 values into magnitudes. However, for the purposes of this thesis it is sufficient a *relative* calibration: to equalize the response of the pixels in order to obtain a clear image of the star field on a uniform background (not necessary flat). The procedures for both these calibrations, absolute and relative, are discussed in the next sections.

4.2.3.1 Absolute calibration

The procedure presented hereafter is divided into two parts: the first one aims at uniforming the intrinsic response of the pixels in the camera, while the second provides the conversion of the calibrated signal in physical units (i.e. magnitudes).

Within each PDM unit, every pixel has a different intrinsic gain (due to the electronic components) and hence it presents a different linear coefficient between its Variance and the intensity of the current of its photo-electrons (figure 4.8, *left*). In order to obtain a uniform behavior, it is possible to chose a reference pixel (REF) and re-scale all the others using the ratio of the respective *photo-electron equivalent*[10] PE_{eq},

$$v_i = v_{\mathrm{raw},i} \times \left(\frac{\mathrm{PE}_{eq,\mathrm{REF}}}{\mathrm{PE}_{eq,i}} \right) . \tag{4.8}$$

As a result, the gain of the pixels in the same PDM unit are now identical (see figure 4.8, *right*), but the response of the entire PDM tiles must be calibrated as well. In fact, every PDM is characterized by a peculiar overall PDE, still related to the electronics (or to the micro-call size, in the case of ASTRI–Horn), and hence the average of the *rates* will be different for every tile even if the illumination is equal. Through specific laboratory measurements, it is possible to obtain the multiplicative factors to equalize the PDM units, completing the intrinsic calibration of the camera[11].

The next step is the conversion in physical units. To begin, the transformation of the ADC output signal x from ADU to pe is operated with equation

---

[10] See section 3.3.3.1.

[11] Actually, also the bias voltage can introduce additional effects, such as a different average level of the PDM tiles, requiring a further last compensation.

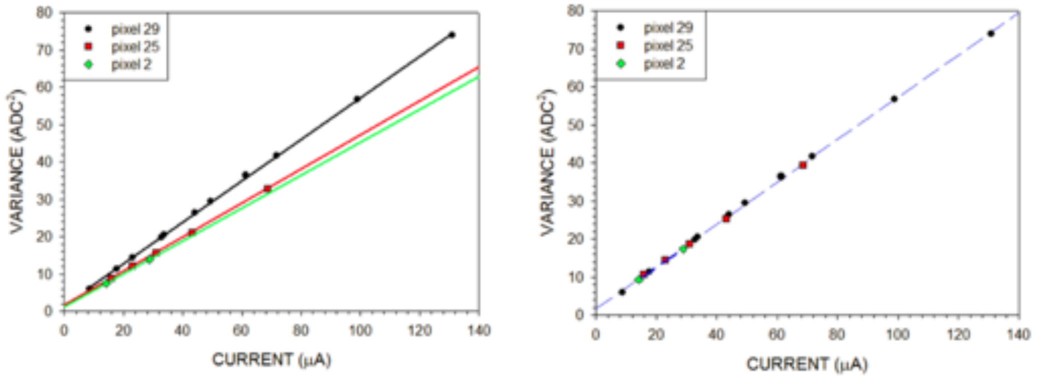

Fig. 4.8: Every pixel has a peculiar coefficient for the conversion between the Variance and the current (*left*), but an appropriate calibration process can equalize their response (*right*). In the example reported here, the pixel number 29 was adopted as a reference for this PDM tile (courtesy of O. Catalano).

3.4, and consequently for the Variance we have

$$V[x_{\text{pe}}] = V\left[\frac{(x_{\text{ADU}} - \text{PED}_{LG})}{\text{PE}_{eq}} \times \eta\right], \tag{4.9}$$

where $\eta = G_{HG}/G_{LG}$ as usual and PE_{eq} is the REF pixel value re-scaled for the equalization factors of the PDM tiles. Using the definition of the variance $V[x] = E[x]^2 - (E[x])^2$, it is straightforward to show that

$$V[x_{\text{pe}}] = \frac{V[x_{\text{ADU}}]}{\text{PE}_{eq}} \times \eta\,, \tag{4.10}$$

where $V[x_{\text{ADU}}]$ is exactly the Variance value v_i recorded in every pixel. After this conversion, the number of incident photons can be obtained using the standard process described at the end of section 3.3.3.1, including also the geometrical and physical properties of the optical system.
The receipt that we have outlined here constitutes an effective strategy for the absolute calibration of VAR data, but it is not feasible at present, as some necessary measurements were not carried out in laboratory for the prototype camera of ASTRI–Horn (but a complete procedure has already been planned for the cameras of the MiniArray [141]). As a consequence, in the work of this thesis, instead of an absolute calibration for the VAR frames we adopted a *relative* strategy.

4.2.3.2 Relative calibration

The procedure presented here constitutes a statistical equalization of the pixels, based on their average signal level over a very large number of VAR frames. The output of this procedure is a calibration matrix, which is a mask to be adopted to uniform the response of hot and cold pixels.
The first step is the selection of a set of *long* observing runs[12] pointing at different sky regions. We chose 9 `RUNID`, namely 1674, 1636, 1623, 1620, 1608, 1605, 1599, 1597 and 1419, and we removed the bad frames after a visual inspection with the `VAR_QV40` procedure (ASTRI–Horn is a prototype instrument and therefore several tests were performed to verify the response of the subsystems even during the acquisition runs, resulting in inadequate frames for our calibration purposes). For every run, we calculated the *median* value in every pixel: this is the best strategy to obtain a reference level which is not affected by the contribution of the stars occasionally transiting over certain sensors in certain frames increasing the level of the Variance signal. Lastly, for every pixel we considered the average of the 9 median values, obtaining a matrix of coefficients C_i to calibrate the camera. This procedure is conveniently expressed by the following formula

$$C_i = \frac{1}{N} \sum_{\text{RUNS}} \text{median}(v_i, f) \ , \tag{4.11}$$

where f is the set of frames composing every observing run and N is their number. Finally, to obtain the calibrated values $v_{\text{cal},i}$ it is sufficient to multiply the Variance for the inverse of the coefficients $\widetilde{C}_i$, obtained with an appropriate normalization of the C_i to their maximum,

$$v_{\text{cal},i} = v_i \times \frac{1}{\widetilde{C}_i} \ . \tag{4.12}$$

Figure 4.9 shows the remarkable outcomes of this effective relative calibration, which is adopted as a standard procedure in the following of this document.
In conclusion, a similar statistical method for the relative calibration of the pixels can be adopted also for the cameras of theMiniArray, but a more interesting solution has been recently proposed as an alternative. A sheet of photo-luminescent material, can be applied on the PMMA window of the telescope, during a specific calibration phase, in order to produce a uniform illumination of the camera and record a set of Variance frames to be

---

[12] See section 6.2.1 for a more detailed description of the criteria for the sample selection.

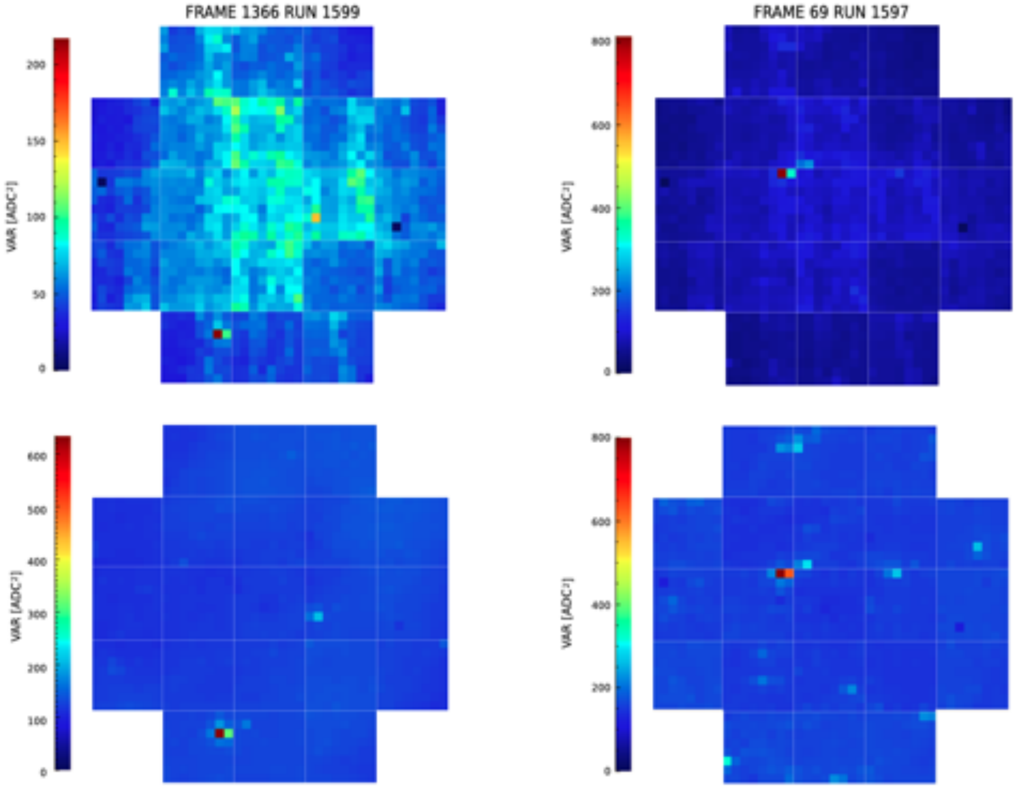

Fig. 4.9: Example of two Variance frames before (*top*) and after (*bottom*) the relative calibration. On the left there is the frame 1366 of the run 1599, while on the right we have the frame 69 of the run 1597: the quality of the image is remarkably increased and, in particular, the signal of the star field is now visible, while it was overwhelmed by noise in the raw images.

adopted for the equalization of the pixels. This solution is probably more reliable than our statistical method, but the contribution of the optical system must be studied separately in this scenario. With the new operating period of the ASTRI–Horn telescope, beginning in fall 2021, the feasibility of this proposal will be investigated in detail.

4.3 Applications

The Variance method presented in this chapter allows to use ASTRI as a common UV/optical telescope for imaging the NSB. As a consequence, the Variance constitutes a technique to exploit ASTRI not only for the research on cosmic VHE gamma rays, but also for more traditional sky observations, as for example the monitoring of bright objects into the FoV. However, the most important application of the Variance is not the study of celestial sources, but the analysis of the telescope itself. In fact, VAR frames are sky images taken directly with the Cherenkov camera, hence providing a unique opportunity to verify the performances of the same imaging system adopted for Cherenkov detection, in terms of both optics and electronics. Moreover, also the sky region actually framed by the camera can be individuated thanks to the VAR images, allowing to investigate any eventual little mis-pointing of the telescope or mis-alignment of the support structure, thus assessing the overall opto-mechanical behavior of the instrument without introducing potential systematic errors due to secondary systems. A general overview of these techniques and their potential is reported in the next section.

4.3.1 Techniques overview

The Variance is the only method to verify the true imaging quality of the ASTRI telescope and to assess the opto-mechanical performance of the structure on the basis of the sky region actually framed by the camera. There are a lot of possible applications of this powerful method: the most important techniques are briefly presented in the following paragraphs.

Alignment of the Cherenkov camera
In principle, it is possible that the Cherenkov camera is not perfectly aligned with the optical axis of the telescope, due for example to gravity flexures or mechanical tolerances in the assembly. The Variance is the only method to detect and measure any eventual discrepancy, and chapter 5 presents a pipeline that we developed for this purpose. Afterwards, the offset value is inserted in the pointing model of the telescope, ensuring an improved accuracy for the tracking of any celestial object. The PMC camera is the instrument adopted for monitoring the pointing performances during observations, but again a specific calibration procedure is necessary to align the optical axis of the PMC with that of the Cherenkov camera, exploiting the VAR frames (see chapters 6 and 7 for details).

Monitoring of the tracking accuracy
The PMC camera is the ancillary instrument devoted to the monitoring of the pointing performances of the telescope, but also the Variance can be exploited for the same purpose. In fact, despite the much coarse angular

resolution of the VAR images in comparison to the PMC ones, it is possible to obtain anyway a quite precise astrometric calibration of the FoV and consequently to estimate the true pointing direction of the telescope using the Cherenkov camera only. Chapter 6 is entirely dedicated to the astrometry of the Variance frames: such procedure can be used to cross-check the result of the PMC images analysis, but it has been also implemented in the system for the quick data-analysis in real time (the Online Observation Quality System, OOQS [140]), ensuring a prompt intervention in case of anomalies during observations .

Ghost images and PSF size

The true reason why the astrometry of the VAR frames has been implemented in the OOQS is that it allows to accomplish not only the monitoring of the pointing accuracy, but also another fundamental task: the analysis of ghost images. When one or more segments of the primary mirror lose their original position due to wind gusts, night frost, or other causes, the PSF is altered and isolated light spots may appear in the FoV, out of the nominal position of celestial sources. These artifacts are the so-called *ghost images* and they are impossible to be detected without using the Variance method. In fact, the alignment of the panels is performed in the assembly integration testing (AIT) phase, with the AMC actuators and a suitable optical camera on the focal plane (see section 3.2.2), but afterwards the stiffness of the structure is the only element to keep the segments in position, without the possibility to verify their stability. The presence of ghost images in the VAR frames can be easily detected if the nominal position of the stars in the FoV is well known: it constitutes a strong evidence that at least one mirror segment is mis-aligned and that the telescope needs a specific maintenance operation[13]. Figure 4.10 report a VAR sky map of the Orion belt region, where 4 ghost images for each of the brightest stars are clearly visible.

If the mis-alignment of the mirror segments is small, the alteration of the PSF is slight and consequently there are no ghost images in the FoV. In this case, the easiest solution to measure any eventual little modification of the PSF is to schedule a dedicated observation: pointing the meridian at the celestial equator with the telescope in staring mode, the stars cross the FoV in parallel and also tiny changes of the D_{80} can be revealed. This

---

[13] In principle, it is possible to re-align the panels using the VAR images, also taking advantage of the secondary mirror shadowing to identify the "guilty" segment. However, such operation is very complex due to the articulated shape of the PSF, and hence it is more convenient to replace temporarily the Cherenkov camera with a suitable optical device (the same operation of AIT).

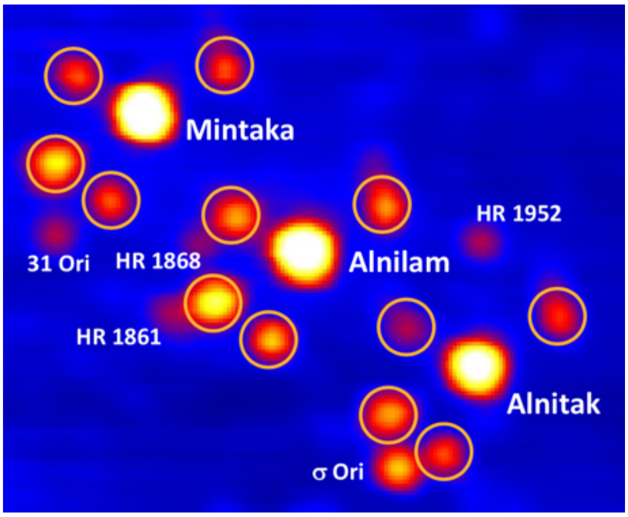

Fig. 4.10: Example of ghost images in a Variance frame (`RUNID` 833, Orion belt region): the three brightest stars have four evident ghost images each, about 10 % intensity (masterful image elaboration by A. Segreto [181]).

strategy has never been tested on ASTRI–Horn but in principle it can provide also an improvement of the optical qualification of the system, since such a measure with the Cherenkov camera has never been performed.

Optical throughput

The *optical throughput* (OT) of the ASTRI telescope is in practice the percentage of photon flux from the sky that actually reaches the focal surface after the path across the optical system. The monitoring of the OT is fundamental for the characterization of the telescope efficiency,but also for the fine tuning of Monte Carlo simulations that are necessary for the data analysis. There are several independents methods for measuring the OT, as the camera *rates* or the muon-ring analysis [141], but again the Variance can provide a decisive contribution. In fact, the VAR signal due to the flux of a steady celestial source must be constant over long time intervals (several months) if the telescope OT is unperturbed. As a consequence, periodic VAR observations of a few reference stars, in similar atmospheric conditions and moon phases, can indicate the level of the optical system transmittance. This strategy is based on a *relative* approach, comparing different measurements of the same object, and hence it constitutes a reliable solution despite the difficulties of an absolute calibration (reported in section 4.2.3). The usage of an ancillary telescope, as the UVSCOPE instrument presented in section 3.4.2.2, can help to monitor the atmospheric condition during the acquisition of the VAR signal from reference stars.

Bright transients

With a quite coarse angular resolution (∼11′), but an extremely wide FoV (∼10°), ASTRI–Horn can be exploited also for the monitoring of several bright transients in the sky, as comets, meteors, satellites, and others. Figure 4.11 reports an example of a bright satellite that crossed the FoV of ASTRI–Horn leaving an evident imprint on six subsequent VAR frames. With a suitable algorithm it is possible to detect such phenomena automatically in the images of the ASTRI data archive, and produce an adequate light curve (ADU^2 versus time) for every object. Such information is useful for example to improve the atmospheric transmittance model up to high zenith angles, but also for providing a better cleaning of Cherenkov images and to carry out statistical studies on the impact of transients on astronomical observations.

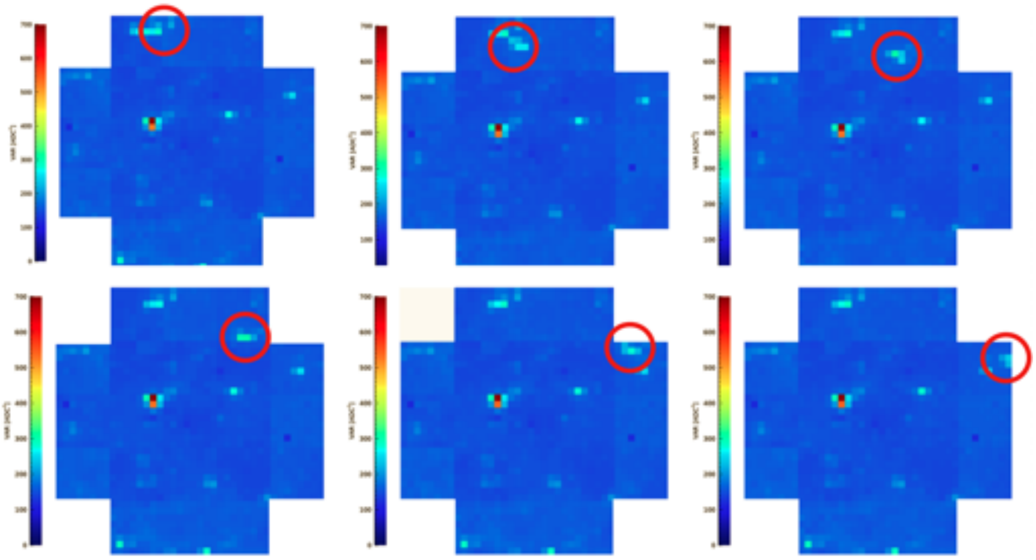

Fig. 4.11: Examples of a moving bright transient visible in subsequent VAR frames: `RUNID` 1597, frames 195 to 200, acquired in 2019 on February 26th, from 18:46:48 to 18:47:07 UTC. The track is fragmented because the acquisition of every VAR frame has a dead time of ∼2 s.

4.3.2 MiniArray

The lesson learned with the prototype ASTRI–Horn leads to convey a very important role to the Variance method in the procedures for the calibration and assessment of MiniArray telescopes. In this context, several applications of the Variance have already been reported and discussed along this chapter, but the new cameras for the MiniArray present also remarkable improvements under the technological point of view regarding the acquisition of the VAR frames. In particular, some of the most important enhanced features are reported in the following list:

- the Variance will be acquired in both LG and HG, at the same time, contrary to the situation of ASTRI–Horn where only the LG channel is available;
- the Variance will be acquired simultaneously to Cherenkov flashes (actually this is already possible now, but only since February 2019);
- the communication protocol between BEE and FEE will be improved and consequently the $\sim$2 s dead-time between the acquisition of subsequent VAR frames will be removed.

Most of the procedures presented in the following chapters have been developed for the implementation on the MiniArray with these enhanced features in mind.

5

Variance images analysis

Images generated with the Variance method provide a picture of the NSB in the FOV of the telescope, reporting the position of bright objects similarly to what happens in traditional UV/optical instruments for astronomy. However, the ASTRI telescope is not optimized for imaging the night sky, but rather for the detection of Cherenkov flashes, and consequently the Variance images require a very special analysis before being exploited for scientific purposes. In fact, the most of conventional tools for the elaboration of astronomical images are not adequate for processing Variance data. This chapter is just dedicated to discuss the custom procedures and methods that we developed for the treatment of Variance images, considering the peculiar optical response of the instrument. In particular, our aim here is to understand what is the most accurate way to identify the center of every bright spot with sub-pixel precision. Moreover, we studied the way to assign a celestial coordinate to these points, in order to extract the true astronomical position of point-like sources contained in the FoV of the telescope. To this end, section 5.1 reports the so-called astrometric calibration of the FoV, allowing us to map the camera coordinates into the celestial reference system and vice versa. Afterwards, section 5.2 presents a deep analysis of the convolution between the PSF and the camera pixel distribution. This represents a very crucial aspect for retrieving the position of the centroid of every source with high precision. Finally, section 5.3

is focused on a detailed study of the effects of the gaps between the pixels, resulting in a transformation matrix that we adopted to correct the position of bright objects in the FoV, obtaining a better reconstruction of the star field and enhancing the accuracy of the whole VAR imaging system.

5.1 Astrometric calibration

From light spots onto the focal surface, it is possible to retrieve the true astronomical coordinates of the correspondent celestial sources, if we know exactly the optical properties of the imaging apparatus. This is the concept at the heart of the branch of astronomy focused on the precise measurement of the positions and movements of stars and other celestial bodies, which is known as *astrometry*. Of course, the ASTRI telescope is not adequate to perform accurate astrometric measurements because of its coarse angular resolution. However the evaluation of bright spots in the Variance images can be anyway very helpful, as they can be successfully exploited for the monitoring of the telescope itself, rather than for measuring the star field. This is somehow a reverse usage of astrometry, as we do not use ASTRI to measure the position of the stars, but instead we use the well-known coordinates of bright objects to measure the position of the Cherenkov camera with respect to the celestial sphere[1]. To this end, it is necessary to perform an *astrometric calibration* of the FoV. This means to define a set of parametric equations allowing to map the camera coordinates into the celestial reference system and vice versa. Beautiful examples of such procedures can be found in the papers of satellite missions dedicated to astrometry (such as Gaia [185, 186]) or in the peculiar works relative to the calibration of instruments with ultra-wide FoV angles (the so-called *fish-eye* cameras, [see 187, and references therein]). For the case of the ASTRI telescope we developed a specific custom procedure which is described in the following sections, starting from the most fundamental aspect: the definition of a strategy for the transformation and conversion of data inferred from Variance into astrometric information.

5.1.1 Transformation strategy

For the conversion between the celestial coordinates into the camera reference system we adopted a transformation strategy which is based on a

---

[1] Chapters 6 and 7 are entirely devoted to this aim, focusing on two different aspects: the alignment of the camera with the optical axis and the pointing accuracy of the telescope, respectively.

relative approach. In this respect, we consider the coordinates associated to the camera geometric center and then we process any other point using its position relative to the center (in terms of distance and angle). This is also a *selective* strategy, in the sense that not all the pixels are associated to a celestial coordinate at the end of procedure, but only those for which the conversion was required. This approach is very different for example from the typical elaboration scheme of astronomical FITS images, where the astrometric calibration ends up with a solution for all the pixels, using the Word Coordinate System (WCS) standard [179, 178]. Our custom procedure represents an effective strategy for the case of the ASTRI camera, presenting a small number of pixels (namely $21 \times 64 = 1344$), each with a large angular dimension ($\sim 11'$). In these conditions it is impossible to apply the most common programs for the astrometric calibration[2]. The steps of our algorithm can be summarized as reported in section 5.1.2, after having introduced (hereafter) the adopted notation and the relevant astronomical quantities involved.

5.1.1.1 Notation

Being S an astronomical point source, in the wavelength range of our interest, its celestial position in the Equatorial Coordinate System (ECS) is expressed by the Right Ascension and Declination, (α_S, δ_S). In the local Horizontal Coordinate System (HCS), centered at the latitude φ and longitude λ of the ASTRI–Horn telescope[3], the celestial position of S is defined by the Azimuth and Elevation (Az_s, El_s). When S falls inside the FoV of the ASTRI–Horn telescope, it produces a bright spot into the VAR images which is located in the position (x_s, y_s), or equivalently (r_s, θ_s), using the reference system previously defined in section 3.3.1.2 and the standard projection of the camera geometry onto the tangent plane discussed in section 4.2.2.3. Similarly, we indicate with P the *pointing direction*, or the intersection between the optical axis of the telescope and the celestial sphere, which is identified by suitable couples of astronomical coordinates in both ECS and HCS, and by the position (x_p, y_p) onto the camera.
In our procedure, P is the reference point for the calculation of celestial distances and, in this chapter only, we assume a *perfect pointing* performance of the telescope: the position of P is coincident with the origin of the camera reference system, $(x_p, y_p) \equiv (0, 0)$.

---

[2] Such as SourceXtractor [188, 189] or Astrometry.net [190] [*link* 229], they do not find an astrometric solution due to very peculiar optical features of ASTRI intended as an optical instrument.

[3] Reported in table 3.2 on page 70.

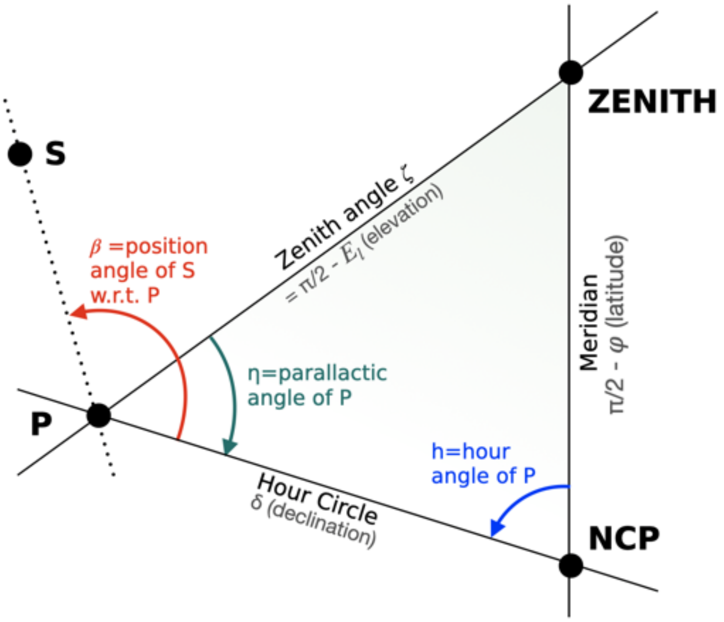

Fig. 5.1: Conceptual drawing representing the relevant sky angles for our analysis. The scheme is in SkyView and the East direction is clockwise about the NCP.

5.1.1.2 Relevant astronomical angles

The astronomical position of S with respect to P is uniquely defined by the angular distance d_s and the *Position Angle*, β_s. The Haversine formula for spherical triangles [191] allows us to calculate d_S using the Right Ascension and the Declination of P and S,

$$\cos(d_s) = \sin(\delta_p)\sin(\delta_s) + \cos(\delta_p)\cos(\delta_s)\cos(\alpha_p - \alpha_s)\,, \tag{5.1}$$

while β_s is the aperture of the angle between the celestial meridian containing P and the great circle containing P and S, positive in the sense North through East[4] rotating about P. The geometrical drawing in figure 5.1 reports a schematic representation with the relative position of P, S and the North Celestial Pole (NCP). In the same figure, it is also reported the position of the Zenith (the sky point with the maximum elevation). Its angular distance from P is the so called *Zenith Angle* (ζ), which is the complementary angle to the elevation El_p. The angle between the Zenith and the NCP, with vertex in the pointing direction P, is the *Parallactic Angle*

---

[4] At every celestial position we define *North* moving along a celestial meridian towards the North Celestial Pole, while *West* is the direction in which the stars appear to move (in SkyView).

of P denoted with the symbol η_p. It should be noted that the name of the parallactic angle has nothing to do with the phenomenon of the parallax, but instead it refers to the fact that every celestial point moves along a celestial *parallel* around the NCP. As a consequence, the amplitude of the parallactic angle is a function of time $\eta = \eta(t)$, as it is shown in details in section 6.1.1, where the time evolution of the parallactic angle is exploited for a specific purpose. At any time the value of η_p is given by the spherical sine theorem [192]

$$\frac{\sin \eta_p}{\sin\left(\frac{\pi}{2} - \varphi\right)} = \frac{\sin h_p}{\sin \zeta_p} \,, \tag{5.2}$$

where ζ_p is the zenith angle of P and h_p its hour angle, that can be obtained from the Local Sideral Time[5] (LST) with the formula

$$h_p = LST - \alpha_p \,. \tag{5.3}$$

The time dependence of η_p in equation 5.2 is embedded into h_p and ζ_p. However, in this chapter we can avoid to consider the passage of time and consider η_p as a fixed quantity. The sign convention that we adopted is that η increases clockwise (CW) in SkyView, starting from the Zenith direction, in the range $(0, 2\pi)$.

5.1.1.3 Orientation of the FoV

The ASTRI telescope has an alt-azimuth mount. As a consequence, its Cherenkov camera has a fixed orientation with respect to the ground and not to the celestial sphere. This aspect is completely different to what happens in telescopes with equatorial mounts, where the *top* of the camera is always directed towards the NCP, and hence the orientation of the star field does not change with time [193]. On the contrary, in the case of an alt-azimuth mount, the top of the camera is always oriented towards the Zenith, while the *bottom* side is always parallel to the ground, and hence the image of the star field presents different rotations at different times (see section 6.1.1 for details). In order to characterize this effect it is sufficient to notice that in the camera FoV the angle between the vertical axis and the NCP direction with vertex in the pointing direction P is exactly the parallactic angle η that we have introduced in section 5.1.1.2. As a consequence, the apparent orientation of the star field in the ASTRI FoV is definitely determined at any time: every star S has a fixed position angle β

---

[5] To calculate the LST it is important to consider the precession from J2000.0 to the actual epoch, defined as ((JD - 2451545.0)/365.25)+2000, where JD is the Julian Date associated to the actual time value in UTC.

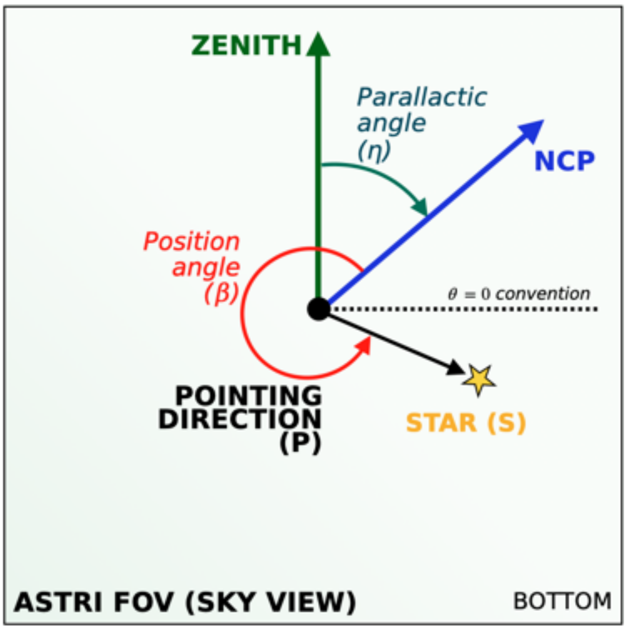

Fig. 5.2: Schematic drawing of the relevant angles for the orientation of the FoV. See section 5.1.1.3 for a detailed explanation of every element.

with respect to the NCP direction, which presents an evolving parallactic angle η with respect to the ASTRI camera vertical axis. Figure 5.2 reports a conceptual drawing of the situation, presenting a scheme involving the same elements of figure 5.1 and highlighting their role in determining the apparent orientation of the FoV with respect to celestial sphere.

5.1.2 Coordinate conversion

The *relative* and *selective* transformation strategy presented in section 5.1.1 translates into the algorithms for the coordinate conversion which are presented hereafter. In particular, there are two different goals to be achieved, that must be treated separately. The first one is to display the sky map into the camera reference system considering the true orientation of the FoV at a given time t. This procedure, exploited for the star identification, is presented in chapter 7. The second task is the opposite transformation and it is much more complicated. It is the calculation of the celestial coordinate of a given point in the camera reference system. This operation is used for the evaluation of the telescope mis-pointing in chapters 6 and 6. Here we discuss the first problem.

From the sky to the camera The angular separation d_s between P and S, calculated with equation (5.1), can be converted into the the radial distance r_s using the linear plate-scale P_S defined in section 2.2.3, through the relation

$$r_s = \frac{d_s}{P_S} \,. \tag{5.4}$$

On the other hand, the polar coordinate θ_s is determined by the expression

$$\theta_s = \pi/2 + \beta_s - \eta \,, \tag{5.5}$$

where the sign are coherent with the convention described in section 5.1.1.2 and reported in figure 5.2, while $\pi/2$ has been added to obtain the NCP axis towards the top of the FoV in SkyView when the telescope is pointing at high zenith angles in direction of the geographic North ($\beta = \eta = 0$), remembering that the zero point of the θ coordinate is conventionally set along the $+x$ axis. Lastly, the results of equations (5.4) and (5.5) can be converted in Cartesian coordinates, obtaining the final output of the conversion procedure. In conclusion, the whole transformation from the sky to the camera can be summarized with the following scheme,

$$\underbrace{\begin{pmatrix}\alpha\\ \delta\end{pmatrix} \longrightarrow \begin{pmatrix}d\\ \beta\end{pmatrix}}_{\text{SKY}} \xrightarrow{\eta} \underbrace{\begin{pmatrix}r\\ \theta\end{pmatrix} \longrightarrow \begin{pmatrix}x\\ y\end{pmatrix}}_{\text{CAM}} \,. \tag{5.6}$$

The work flow reported in (5.6) has been implemented in a routine written in the IDL programming language, exploiting several functions of the astronomical library[6], as for example `POSANG`, `PARANG`, and others. This routine can be applied to all the sources in a certain region around the pointing direction of the telescope, obtaining a map of the positions that the stars would have in the FoV of the ASTRI telescope. For example, figure 5.3 presents the star field in the region of Navi (HIP4427) in the constellation of Cassiopeia, in the camera reference system, as it would be observed by ASTRI–Horn at midnight UTC between November 24 and 25, 2021.

From the camera to the sky The procedure presented in (5.6) represents an effective strategy to map the celestial sphere into the camera reference system of the ASTRI telescope. However, it is not straightforward to reverse such procedure to perform the opposite operation, i.e. to assign a

---

[6] See appendix B for further details.

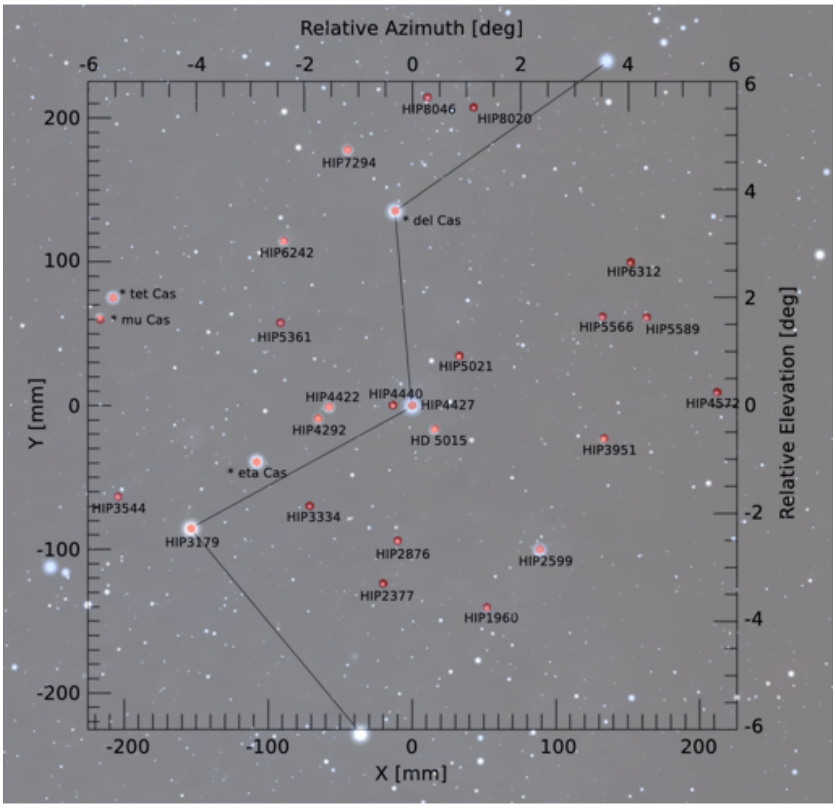

Fig. 5.3: Example of the projection in the camera reference system of the star field in the region of Navi (*Gam Cas - HIP4427) in the constellation of Cassiopeia (grey segments). The red dots represents the position of the stars in camera coordinates (taken from the SIMBAD catalogue, within $6°$ from Navi and below $6.5\,\mathrm{mag}$), while the superimposed image is an optical representation of the same sky region. Azimuth and Elevation values are relative to the central axes of the figure.

celestial coordinate to a specific (x, y) position in the camera. To solve this problem the standard approach is to calibrate the camera reference system using a set of six parameters, the so-called *Plate Constants* [194][7]. However, in the case of the ASTRI telescope, even a simplified strategy is suitable for our purposes, as we will use the transformation from the camera to the sky only for the evaluation of the mis-pointing (section 7.4), where only small displacements are involved (a few arc-minutes maximum). This allows us to adopt an approximated solution, without implementing a general algorithm that works on the entire camera. Nevertheless, it is useful to present the standard technique anyway for comparison, and for introducing the

---

[7] See also this useful summary presentation by T.M.Girard [*link* 275].

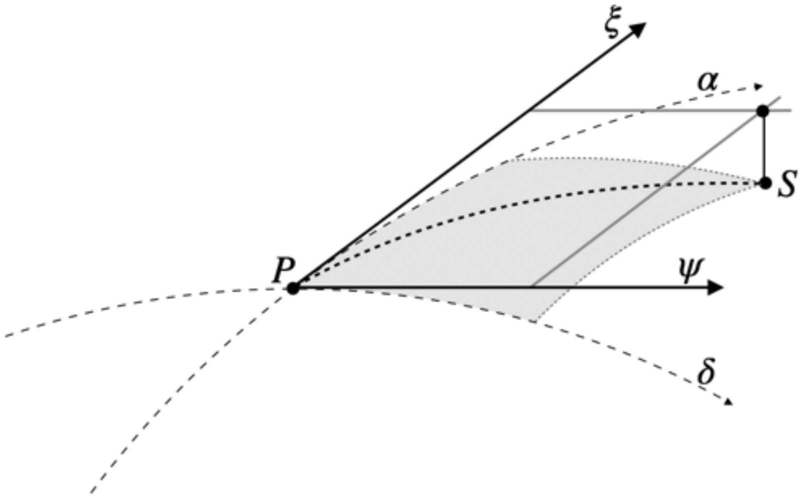

Fig. 5.4: Conceptual scheme representing the *standard coordinates* (ξ, ψ) for the astrometric calibration. The position of S on the celestial sphere, spanned by (α, δ) is projected on the camera plane which is tangent in the pointing direction P.

traditional nomenclature.

5.1.2.1 The plate constants

Let be (ξ, ψ) the projection of the directions (α, δ) onto the tangent plane in P to the celestial sphere (see figure 5.4). In literature they are often referred as the *standard coordinates* on the focal plane, and they can be calculated for a generic source in (α, δ) considering the pointing direction P (at the center of the camera) with the following relations [194],

$$\xi = \frac{\cos\delta\ \sin(\alpha - \alpha_p)}{\sin\delta \sin\delta_p + \cos\delta\cos\delta_p\cos(\alpha - \alpha_p)}\,, \tag{5.7}$$

$$\psi = \frac{\sin\delta \sin\delta_p - \cos\delta\cos\delta_p\cos(\alpha - \alpha_p)}{\sin\delta \sin\delta_p + \cos\delta\cos\delta_p\cos(\alpha - \alpha_p)}\,. \tag{5.8}$$

For every celestial source in the FoV, of well-known astronomical position, it is possible to compute the standard coordinates with equations (5.7) and (5.8), but also the *measured coordinates* (x, y), in mm, using its pixel position in the camera. Consequently, considering a large number of sources, it is possible to use a fitting procedure for estimating the best values of six constants allowing to convert the measured coordinates into the standard ones, assuming a linear relation between them [195],

$$\xi - x = ax + by + c\,, \tag{5.9}$$

$$\psi - y = dx + ey + f\,. \tag{5.10}$$

The constants a, b, c, d, e, and f, are known as the *plate constants* of an imaging system [*link* 233]. After the calculation of the plate constants, it is possible to convert every (x, y) position into (ξ, ψ) and, finally, into astronomical coordinates inverting the equations (5.7) and (5.8):

$$\alpha = \alpha_p + \tan^{-1}\left(\frac{\xi}{\cos\delta_p - \psi\sin\delta_p}\right)\,, \tag{5.11}$$

$$\delta = \tan^{-1}\left(\frac{(\psi\cos\delta_p + \sin\delta_p)\sin(\alpha - \alpha_p)}{\xi}\right)\,. \tag{5.12}$$

This approach leads in principle to the full astrometric calibration of the FoV of the telescope, allowing to perform astrometry measurements on the positions of bright spots in the images. However, it is impossible to apply this method in the case of the ASTRI telescope due to its intrinsic coarse angular resolution, producing large errors in associating a precise (x, y) position to the bright spots. Moreover, our aim is not to perform astrometry measurements, but rather to consider the apparent position of the star field in the FoV as a diagnostic tool for monitoring the pointing performances of the telescope (see Chapter 7). For this reason, it is sufficient to adopt the approximate method presented below, that constitutes a simpler but satisfactory solution.

5.1.2.2 Approximated solution

Instead of calculating the plate constants, it is possible to assign the celestial coordinates to a given (x, y) point of the camera using the following simplified procedure. After the conversion in polar coordinates (r, θ), the true angular distance d from the reference direction P can be calculated using the linear plate-scale (equation 5.4), while the position angle β can be obtained inverting the equation 5.5, as the parallactic angle η is known at any given time t. Actually, the polar angle represents the direction of the NCP, and hence it is possible to obtain the standard coordinates with the formulas[8]

$$\xi = d\sin\beta\,, \tag{5.13}$$

$$\psi = d\cos\beta\,, \tag{5.14}$$

---

[8] Of course, this is not really a right triangle, but the projection on the plane of a spherical triangle (see figure 5.4). As a consequence, this approximation works well only if the distances involved are small and the "curvature" of the α and δ axes is low, i.e. far from the NCP. A quantitative evaluation is reported below in the text.

and lastly (α, δ) using equations 5.11 and 5.12. Of course, this is an approximated solution, but we verified with numerical simulations that this approach provides quite accurate results: if the distance d between P and the source of interest is $\sim 1°$, the accuracy in the calculation of its coordinates is lower than $1''$ at $80°$ declination (and it is much smaller towards the celestial equator).

There is another possible approach, implementing a further approximation, that consists in adopting ξ and ψ directly as an estimation of the difference in Right Ascension and Declination. In this case, the resulting coordinates are

$$\alpha = \alpha_P + \xi / \cos(\delta)\,, \tag{5.15}$$

$$\delta = \delta_P + \psi\,, \tag{5.16}$$

where the correction with the cosine in (5.15) accounts for the shrinking of Right Ascension with Declination [196]. However, this approach presents a worse accuracy, as the square sum of the errors in α and δ in the same conditions presented above is $\sim 20''$. Nevertheless, it is interesting to notice that the last strategy can be automatically adopted also in the HCS reference frame in the case of the ASTRI telescope, as the alt-azimuth mount of its structure ensures that the vertical axis of the camera indicates the Elevation direction, while the horizontal axis is always parallel to the Azimuth (obviously considering a small sky region around the camera geometric center).

As previously mentioned, in this work we adopt the transformation from the camera to the sky only for the correction of the mis-pointing (see chapter 7), where the size of the translation is only a few arc-minutes, allowing us to adopt the approximated solutions presented above. Furthermore, during every run of the procedures presented in the following chapters, the precision of the approximation adopted is always verified through dedicated simulations in the specific sky region of interest.

5.1.3 Dedicated measurements

The transformation strategy presented above, as well as its relative coordinate conversion, are based on some fundamental assumptions related to the opto-mechanical properties of the telescope, as for example the constant plate scale, the assembly of the camera with infinite accuracy, and others. For the new period of data acquisition for the prototype telescope ASTRI–Horn, in winter/spring 2022, we have scheduled a set of dedicated observations aiming at the verification of these assumptions, assessing the astrometric calibration presented here. In particular, using a long-time

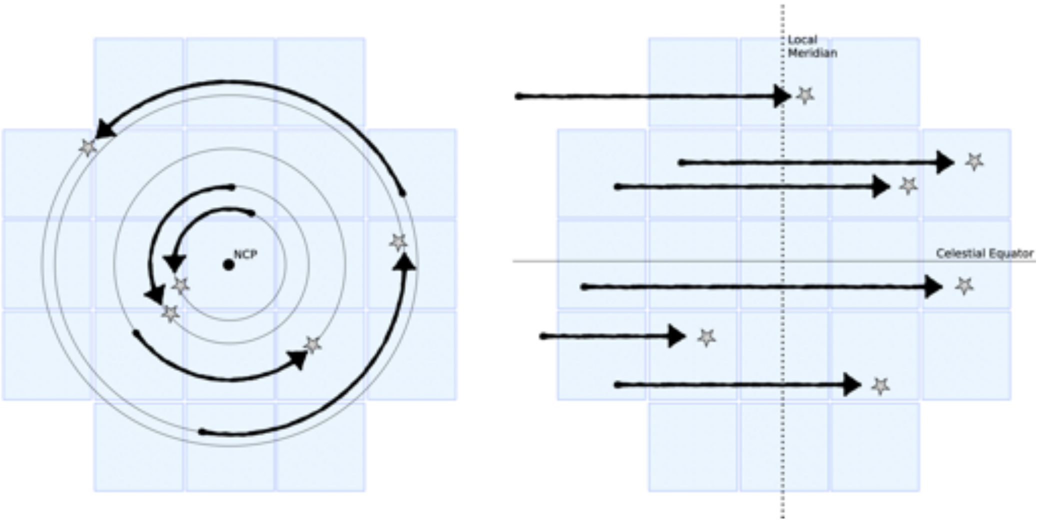

Fig. 5.5: Scheme of the two observations proposed for the assessment of the astrometric calibration with the telescope in staring mode (i.e. without tracking any source). *Left*: pointing at the NCP the stars move along perfect circles. *Right*: pointing at the intersection between the celestial equator and the local meridian, the stars transit perfectly parallel to the ground.

Variance data-taking with the telescope in staring mode pointing at the NCP, it is possible to obtain light arches due to the diurnal motion. Using the average arch radius r of every star with declination δ, it is easy to verify experimentally the linearity of the plate-scale P_S down to very large off-axis angles using the simple relation

$$r = P_S \cdot \delta \,. \tag{5.17}$$

Another useful observation is to leave the telescope in staring mode pointing at the intersection between the celestial equator ($\delta = 0°$) and the local meridian ($Az = 180°$), so that the stars move parallel to the elevation axis of the telescope. In this position it is possible to measure (i) the actual orientation of the camera x axis and (ii) the true size of the PSF in correspondence of the outermost pixels, where the effects of eventual tilts in the mirrors are more evident. Both these procedures have been implemented in the calibration plan of the ASTRI MiniArray and they are just waiting to be tested on the prototype ASTRI–Horn. Figure 5.5 reports a conceptual drawing of the two scenarios presented above.

5.2 The position of centroids

When a point-like source produces a bright spot into Variance images, we retrieve the astronomical position of the object from the position of the *centroid* of the light distribution. We use on purpose the generic word "centroid" because it is calculated with different techniques depending on the context: the center-of-gravity (COG) of several points, the peak of a Gaussian, the output of an average process. In any case, the position of this point must be determined with a precision as high as possible, in order to have the most accurate reconstruction of the position of the sources. In this respect, unfortunately it is impossible to exploit the peculiar profile of the PSF, as it is approximately of the same size of the pixel side and, as a consequence, the light signal usually falls inside a single pixel only. However, when the PSF crosses several sensors it is possible in principle to define a strategy for evaluating the centroid position with sub-pixel accuracy, considering the different illumination of each sensor, given by the PSF convolution over the pixel distribution. In order to choose which is the best procedure to adopt, we developed a software tool for the creation of simulated Variance images starting from the astronomical position of some bright objects (section 5.2.1). Afterwards, we tested two different algorithms to de-convolve the light signal and retrieve the position of the original object, using the residual error as a figure of merit (section 5.2.2). This process begins with the simulation of the PSF of the ASTRI telescope.

5.2.1 Simulation of the PSF

To obtain a Variance-like set of images, first we simulated the illumination by a point-like source off-axis, and then we integrated its light spot over the pixels. We performed a full ray-tracing of $83\,518$ photons from the source, using the same custom software that was adopted during the commissioning phase of the ASTRI–Horn telescope [130], where its output was validated through direct measurements on the focal plane with an optical camera[9]. The result is a realization of the theoretical PSF on the focal plane. The plot of traced photons is reported in figure 5.6, where the profile of four ASTRI pixels is also clearly visible, with their large size in comparison to the articulated structures of the PSF shape. In fact, what happens in practice is that the details of the PSF are lost in the Variance images, when it is integrated over the ASTRI pixels. This process is well

---

[9] Refer to section 3.2.2 for both the validation procedure and the general properties of the PSF.

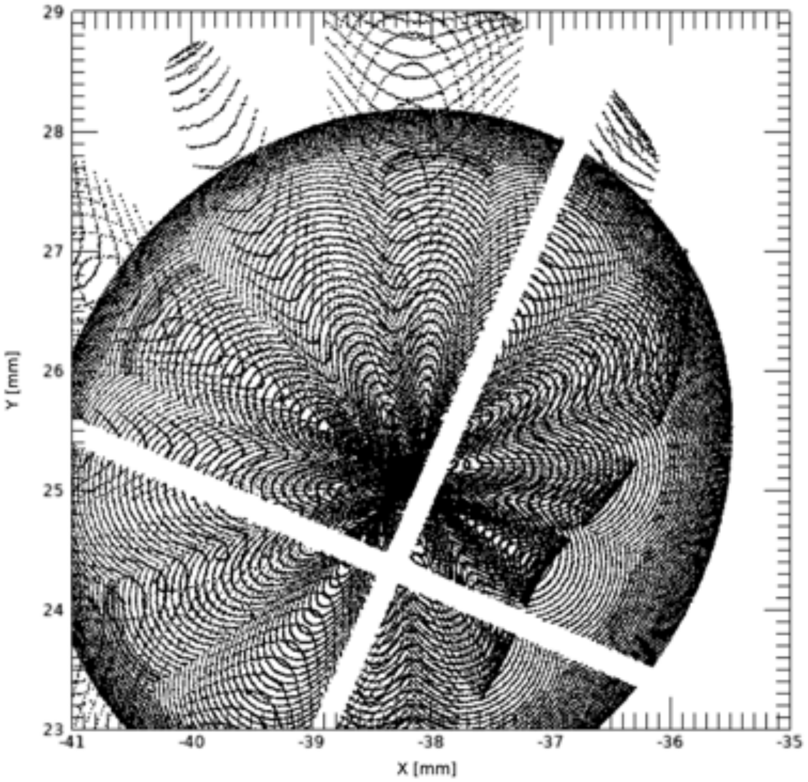

Fig. 5.6: The PSF obtained with a full ray-tracing simulation of 83 518 photons from a point-like source 1.25° off the optical axis of the ASTRI telescope. The blank regions inside the PSF are produced by the gaps between the pixels.

described in figure 5.7, where the convolution of the PSF over the pixel distribution is reported: the resolution of the original PSF simulation is drastically reduced to the coarse scale of the pixel size. In section 5.2.2 it is presented our algorithm to retrieve the original PSF centroid from the Variance-like images, but first it is necessary to spend a few words about the strategy to simulate the integration process over the pixels, as it is a key operation to ensure the accuracy of the whole analysis.

5.2.1.1 Strategy for the integration over the pixels

The ray-tracing software provides the final position of every single photon on the true focal surface, with a spherical shape, determining the correct distribution of the light with respect to the arrangement of the pixels, presenting the geometric scheme reported in section 3.3. For the integration algorithm, we consider the standard projection on the tangent plane as

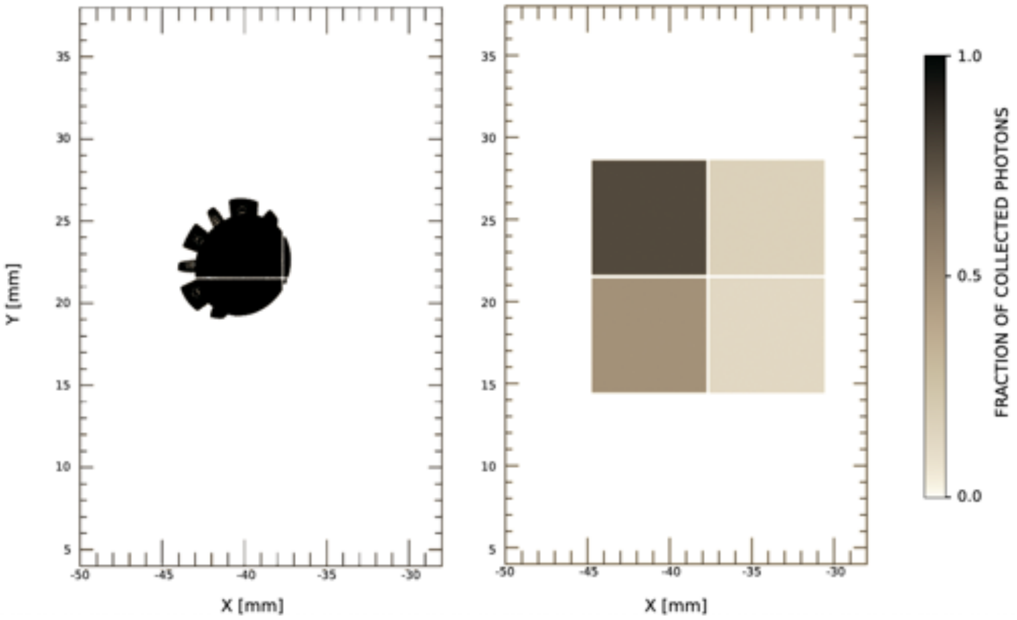

Fig. 5.7: The optical PSF of the ASTRI telescope (*left*, the same of figure 5.6) is integrated over the pixels of the Cherenkov camera resulting in the distribution presented on the right. The gray scale is proportional to the number pf photons collected by every pixel, while the white separation lines represent the gaps between them.

usual(discussed in section 4.2.2.3). Moreover, we use the total number of photons in every pixel for the value of the integrated light intensity, in arbitrary units. With this approach, the integral function consists of only a simple sum. However, an interesting problem rises now, i.e. how to define the perimeter of the pixels. The immediate answer is to adopt suitable *masks* (see section 4.2.2): matrices containing the values of every pixel and their (x, y) position. In this scenario, the attribution of a photon to a certain pixel is achieved comparing its coordinates with the extremal (x, y) values of mask elements equal to that specific pixel index. On the other hand, in order to obtain a precision of $1''$ in the assignation, corresponding to a linear distance of $\sim 10.4\,\mu\mathrm{m}$, the required mask to cover the whole camera results in a double-precision square matrix of $\sim 40\,000$ elements per side. This is a very huge variable to be handled by a common computer of the year 2021, requiring an unnecessary consumption of time and computational resources[10]. As a consequence, we adopted a different numerical

---

[10] For comparison, just an increment of a factor 10 in the number of the matrix elements produces an overflow in my computer, exceeding the size of the 16 GB RAM, causing the

strategy to perform the pixel assignation of every photon. We take the CAD position of all pixel centers and we fitted with a 1^{st} order polynomial each of the 8×8 rows and columns within every PDM (they are not all parallel to the x and y axes because of the PDM tilting, projected on the tangent plane). In this way, the area of every pixel is individuated by the 8 parameters of the straight lines describing its edges, calculated considering the projection of the pixel size on the appropriate direction. To integrate the photon distribution over the pixels it is sufficient to consider the 9 pixels closest to the PSF centroid (COG) and for each of them calculate the minimum and maximum y (x) values in correspondence of every x (y) coordinate of the photons, and count the points that satisfy both the vertical and horizontal boundary conditions. This procedure represents an effective strategy for the convolution of the PSF over the pixels, ensuring a high precision (namely the precision of the pixel center measurements, $\sim 1\,\mu\mathrm{m}$) without requiring to handle heavy masks, but only matrices of angular coefficients and intercepts.

5.2.2 Deconvolution algorithm

Once that the convolution of the PSF over the pixel has been simulated, it is necessary to define a strategy to retrieve the original light spot centroid from the resulting Variance-like image. This is similar to a de-convolution procedure, even if we do not want to obtain the full PSF function, but only the position of its centroid. We developed two different algorithms for this purpose, and we chose the best one on the basis of their performance. In order to have a good statistics for evaluating them, we didn't consider just a single realization of the PSF, but a set of 2275 frames, where the original star position is moved along a circumference about the camera geometric center, for $\sim 30°$, as if the telescope were pointing at the NCP in the scheme of figure 5.5 for $\sim 2\,\mathrm{h}$ (it is shown in chapter 6 that this peculiar movement of a star in the FoV is very similar to what really happens in tracking observing runs).
The first algorithm (*Gauss*) is based on a Gaussian 2D fitting of the high resolution image resulting from the data processing described in section 4.2.2.2. The fit is performed with the `MPFIT` routine of the IDL library[11], implementing a standard user-defined Gaussian function. The coordinates of the fitted maximum are assumed to be associated with the position of the light source in the camera reference system. The second algorithm (*WA*)

---

operating system to reboot.

[11] See appendix B for further details.

adopts a weighted-average strategy: the pixel with the highest value is considered together with its eight nearest neighbor[12], and the coordinates of the centroid are computed as the averages of pixel center positions, weighted by the respective recorded intensities. Figure 5.8 reports two images for visualizing the methods presented here.

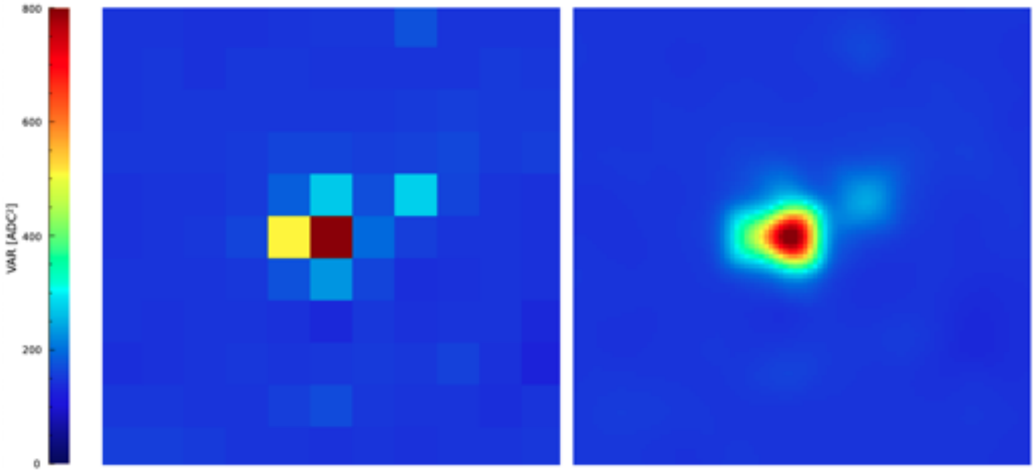

Fig. 5.8: These two images are made with real Variance data (frame 440 of `RUNID` 1597) to show the possible strategies for retrieving the original light spot centroid. On the left, a QV image: the center can be calculated with a weighted-average (*WA*) algorithm. On the right, a high resolution image: the center can be defined with an adequate 2D Gaussian fitting (*Gauss* method).

The accuracy of each algorithm is evaluated using the standard deviation (SD) of the reconstructed points with respect to the original position of the simulated light source. The *Gauss* method presents a SD of $2.39'$, while for *WA* it is only $0.81'$. Consequently, the second method is adopted as a standard solution for the analysis discussed in the following chapters.
Figure 5.9 reports the outcome of the simulation presented in this section. In general, the *WA* method presents a better match with the original curve, while the *Gauss* approach denotes a larger discrepancy. Interestingly, both methods present little jumps in correspondence of the gaps between the pixels: this suggests that their role must be studied in details to get a further improvement of the reconstruction.

---

[12] In order to include also the tails of the PSF.

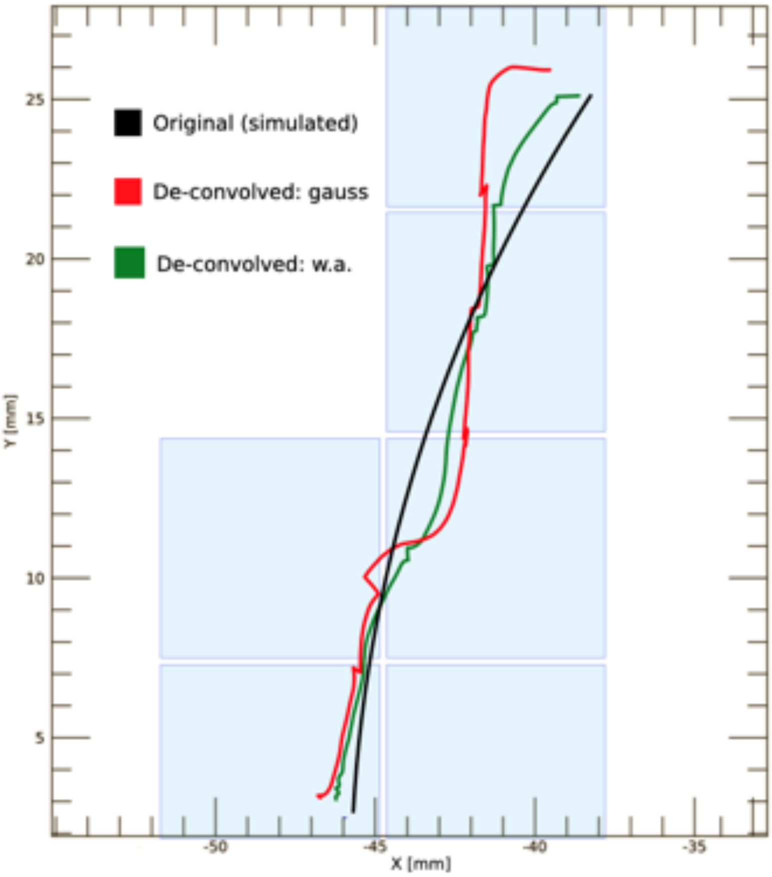

Fig. 5.9: Track of the PSF centroid of the original off-axis star (black) and its reconstructions with different algorithms after the integration of its light over the pixels, for all the subsequent 2275 frames considered in this simulation. Light blue squares represent six pixels of the camera.

5.3 Effects of the gaps

Gaps between pixels constitute small dead areas that subtract photons to the light spots, as it is shown in figure 5.6. This effect is completely negligible for the analysis of Cherenkov flashes, as they typically cover a total surface made of several pixels, while dead areas are very small in comparison. However, for our analysis of Variance images, the presence of gaps must be taken into consideration, as it modifies the actual shape of the PSF, distorting the outcome of the de-convolution algorithm presented in section 5.2.

The effect of gaps in the reconstruction of the simulated star trail is en-

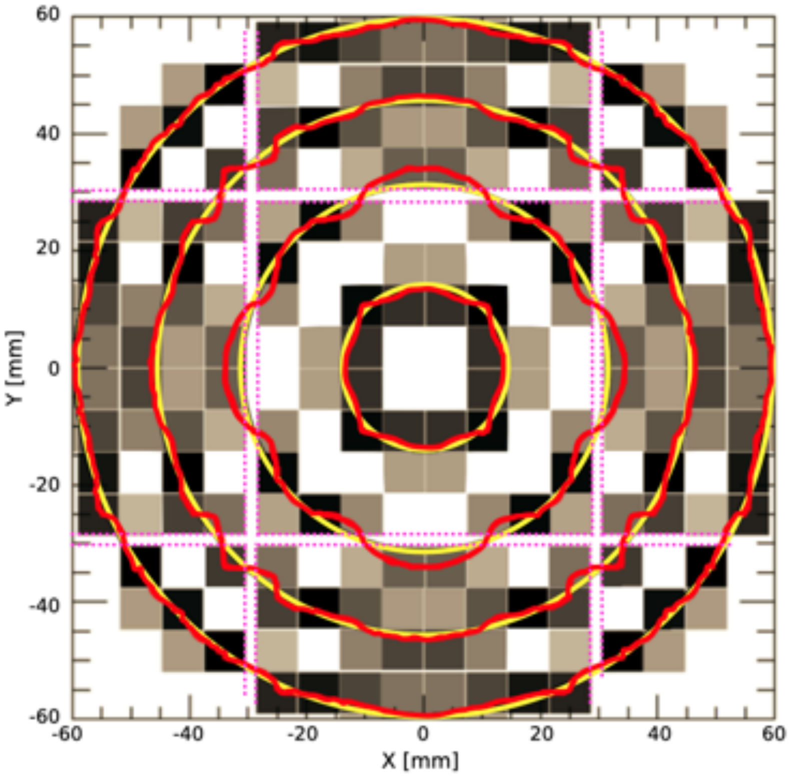

Fig. 5.10: Central portion of the ASTRI camera with the simulation of the tracks of 4 imaginary stars rotating along perfect circles (360°). The reconstruction of the tracks (red line) presents considerable deviations from the theoretical curve (yellow) when the spot crosses the gaps between PDMs (dashed magenta lines). The grey scale of the pixels is proportional to their illumination.

hanced in correspondence of the edge of PDMs, where the gaps are larger ($0.8\,\mathrm{mm}$ to $1.6\,\mathrm{mm}$) in comparison to those between "internal" pixels (equal to $0.2\,\mathrm{mm}$). Figure 5.10 highlights this phenomenon, reporting a virtual star rotation of $360°$ together with the track retrieved with the de-convolution (*WA*) algorithm.

5.3.1 Transformation matrix

In order to characterize and reduce the effect of pixel gaps, we adopted a numerical approach. We simulated the presence of a PSF in every point of a fine grid of possible positions in the camera, and we measured the distance between such original spot centers and the ones calculated with the de-convolution algorithm (*WA*). With this strategy, we obtained a map of

the distortion introduced by the geometry of the camera, which is reported in figure 5.11). This map can be used as a transformation matrix to correct the position of the centroids calculated with the *WA* algorithm, using the following procedure: every point is associated to its nearest element in the transformation matrix, and it is translated (both in r and θ) of the quantity associated to that element. The output is reported in figure 5.12.
The parameters of the grid of positions, i.e. the distance in radius and polar angle between each point, are optimized so to minimize the standard deviation of the corrected centroids with respect to the original simulated track. In particular, we chose a point every $0.5\,\mathrm{mm}$ in radius and $0.5\,\mathrm{mm}$ along the circumference, and we verified that further increasing the resolution of the grid do not generate a correspondent enhancement of the procedure accuracy. With the parameters adopted, the correction provides a reduction of $\sim 40\,\%$ in the standard deviation of the centroids, equivalent to a residual dispersion of $\sim 0.3'$. Consequently, this gap transformation matrix is accepted for the standard correction procedure of the data. However, it is important to remember that it provides an improvement of the reconstruction accuracy *on average*, and therefore it may happen that some points get worse with such treatment, as it is clear from figure 5.12. For this reason, in the following chapters this correction procedure is applied to a large number of frames, when possible, so to take advantage of a good statistics.

Summary of the procedure

In conclusion of this section, we can outline a complete procedure to evaluate the astronomical position of a bright celestial source in Variance images with the highest possible precision. The pixel containing a local maximum of intensity together with its eight nearest neighbor[13] are processed with the *WA* algorithm to retrieve an estimation of the original PSF centroid position. The result is corrected with the gap transformation matrix that we have produced, improving (on average) the accuracy of the previous calculation. The resulting output is converted in astronomical coordinates thanks to the astrometric calibration of the FoV.
The whole procedure presented here has been developed and tested on simulated Variance-like images, but in the next chapter it is implemented for the analysis of real data taken with ASTRI–Horn.

---

[13] Obtaining a square sub-image of nine pixel in total.

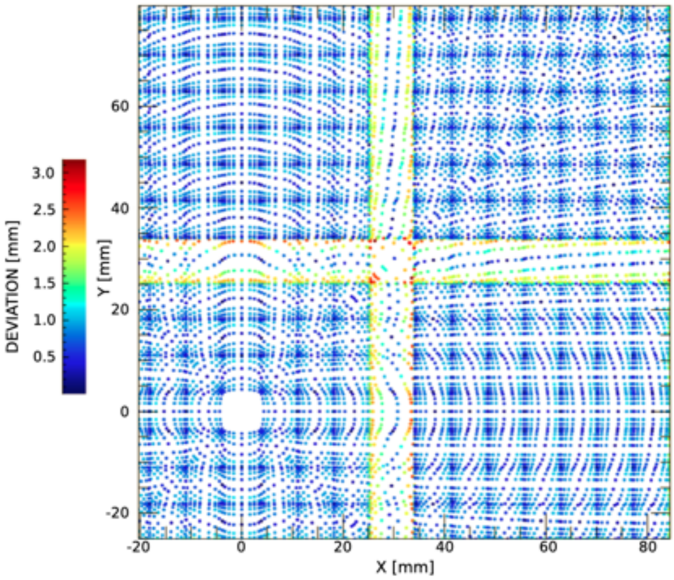

Fig. 5.11: The gap transformation matrix in the central region of the ASTRI camera. The points were originally produced in a regular grid, but their position has changed after the process of integration and de-convolution that we have simulated: the color scale expresses the displacement of each point from its original position.

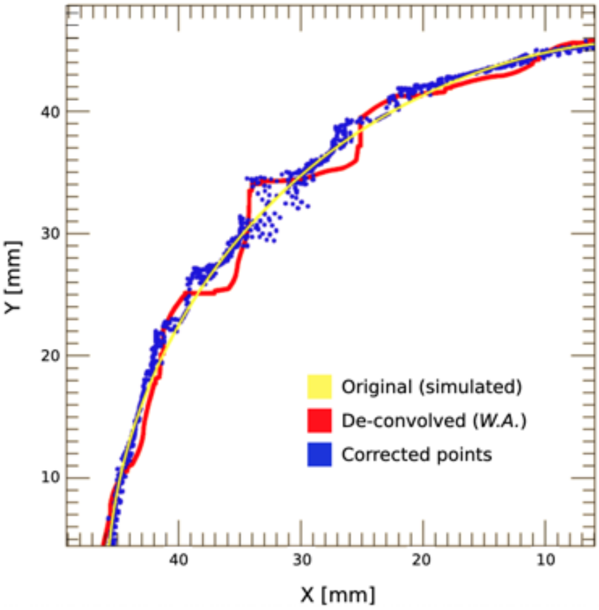

Fig. 5.12: Original PSF centroids (yellow dots) and their reconstructed positions (red dots), corrected with the transformation matrix (blue dots). On average, the matching with the initial star trail is improved (the standard deviation is decreased) even if the maximum displacement is not changed.

6

Camera Axis Alignment

As previously discussed in section 3.4, the pointing accuracy of the ASTRI telescope is monitored using a dedicated optical camera (PMC) which is mounted on the back of the M2 support structure. In fact, due to the compactness of the telescope design, it is impossible to install a pointing monitoring system directly on the focal surface or in its proximity. As a consequence of this situation, it is crucial to develop a strategy to verify that the Cherenkov camera is perfectly aligned with the PMC, so that the center of the focal plane corresponds exactly to the astronomical coordinates individuated by the optical axis of the telescope, excluding the possibility of mis-alignments in the camera mount system due to gravity flexures, mechanical tolerances, or any other undesirable effect. The Variance method, allowing us to image the star field with the Cherenkov camera, actually offers the chance to achieve this goal, and this chapter is dedicated to the procedure that we developed for the detection and measurement of any possible offset in the camera axis alignment, exploiting Variance data. In particular, section 6.1 reports the strategy adopted for the analysis, focusing on the peculiar effect of the FoV rotation during long observing runs in tracking mode. Section 6.2 presents the data sample from the ASTRI–Horn archive that we selected for the validation of our procedure, together with some preliminary operations. Lastly, section 6.3 focuses on data reduction and discussion of results.

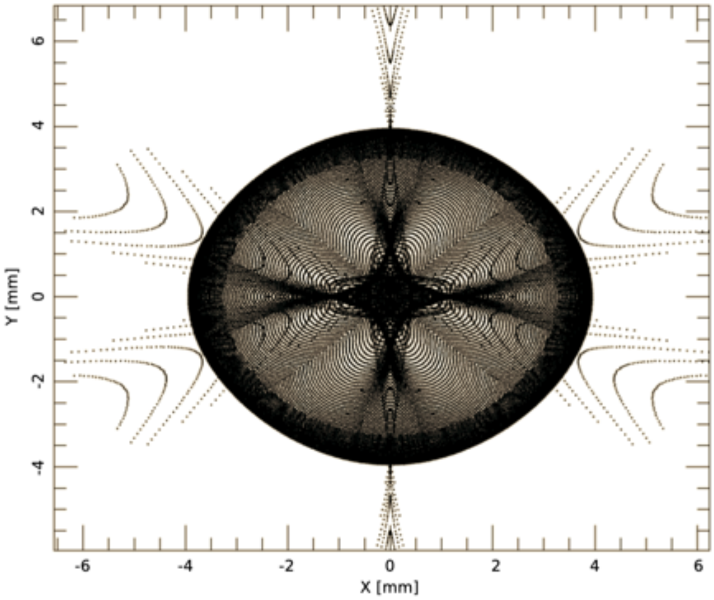

Fig. 6.1: Profile of the simulated ASTRI PSF on-axis, where different contributions from M1 segments can be identified. To obtained this peculiar profile the positioning of segments must be finely tuned: if one of them is tilted, the PSF can still be within the D_{80} requirement, but the symmetry of the composition is lost.

6.1 Measurement strategy

The first approach to verify the alignment of the Cherenkov camera with the optical axis is to point at a bright star and check if the PSF is equally divided among the four central pixels, so that they present the same level in Variance images. This method constitutes a very immediate solution, but provides only an approximate result for several reasons: the lack of an absolute calibration of the pixels in Variance data can introduce systematic errors, and also the articulated profile of the PSF on-axis can be responsible for mis-alignments if one of the M1 segments is not perfectly in position (see figure 6.1). Fortunately there is a much more robust method that can be adopted to verify the camera alignment: to exploit the apparent rotation of the FoV during long observing runs. This technique is inherited from optical astronomy [197], but it has been implemented for the first time on a Cherenkov telescope in the context of the ASTRI project [181, 198, 199]. It is based on a very simple consideration: if the camera is perfectly on-axis, then the trajectories of the stars must be circles around its geometric center. Consequently, fitting the star motion into Variance images with a suitable function, the center of the best-approximating figure must coincide with the camera center, if the system is perfectly aligned. Using long acquisition runs, it is possible to detect any deviation from this ideal configuration with sub-pixel precision, exploiting the considerable length of light arcs to mitigate the artifacts introduced by the large pixelization. This is the strategy that we have implemented in the procedure presented in this chapter. There are two situations where the apparent rotation of the stars in the FoV can be observed, and consequently exploited: with the telescope in staring mode pointing at the NCP, or during a tracking observation. In the first scenario, the rotation of the star field is due to the diurnal motion of the Earth while the telescope is stationary: this is undoubtedly the best condition for the analysis, as the dynamics of the telescope is completely ruled out. A dedicated observation of this kind has already been inserted in the calibration plan of the ASTRI MiniArray [141]. Unfortunately, the ASTRI–Horn telescope was never used for a long observation of the NCP, and hence we have no data taken in this configuration available in the ASTRI archive yet. For this reason, hereafter we consider only the other situation, i.e. when the rotation of the star field can be observed by means of long observations in tracking mode. In this case, the circular trajectories of stars are determined by the effect of the FoV rotation, which is presented in details in section 6.1.1.

6.1.1 FoV rotation effect

As previously discussed in section 5.1.1.3, when the telescope is pointing a certain astronomical direction P, at a given time t, the orientation of the FoV is completely determined by the parallactic angle η, provided by equation (5.2). If the telescope performs a tracking observation, the center of the FoV remains associated to the astronomical direction P while every object off-axis undergoes a rotation around the center, due to the usage of an alt-azimuth mount to follow the sideral motion: the net result is the effect of the apparent rotation of the FoV. The characteristics of this phenomenon depend on the pointing direction of the telescope: if the declination of the source is greater than the latitude of the observer ($\delta > \varphi$) then the rotation of the FoV is complete ($360°$ for a virtual observation of $24\,\mathrm{h}$) and CCW in SkyView, otherwise the rotation is more similar to an oscillation, as it is shown in figure 6.2. This behavior is due to the coordinates of P with respect to the declination of the zenith. In particular, considering that the distance of the zenith from the NCP is $\pi - \delta$, while the distance of the source from the NCP is $\pi - \delta$, if P culminates *between* the NCP and the

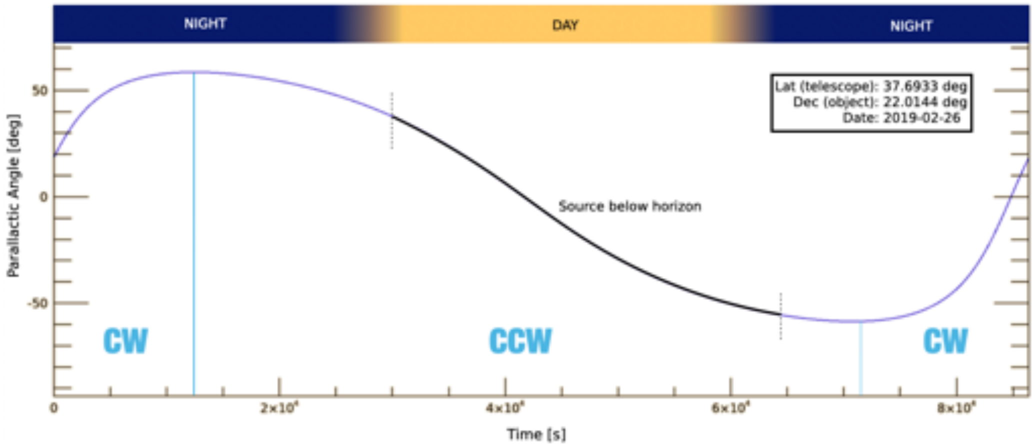

Fig. 6.2: Example of the evolution of the parallactic angle as a function of time for a non-circumpolar source in a virtual acquisition of $24\,\mathrm{h}$. The direction of rotation changes from clockwise (CW) to counterclockwise (CCW) while the source is above the horizon (blue line) during the night.

zenith, $\pi - \delta < \pi - \varphi$, hence $\delta > \varphi$ and the FoV rotation is complete. On the other hand, if P transits across the meridian *below* the zenith ($\delta < \varphi$) then the telescope performs a full rotation about the azimuth axis to track the source, partially compensating the sidereal motion, resulting in an apparent oscillation of the FoV rather than a full rotation.

In the case of the ASTRI–Horn telescope, as for any other observatory where $\varphi \sim 45°$, we have that $\pi - \varphi \sim \varphi$ and we can say approximately that the rotation is complete if the source is *circumpolar* (i.e. never goes below the horizon, $\pi - \delta < \varphi$).

In general, regardless to the complete or partial rotation of the FoV, the speed of this apparent effect is not uniform, as it is reported in figure 6.2. For this reason, we developed a simple and handy software to be adopted in the simulations where the FoV rotation matters: the “Star Coverage” tool.

6.1.2 The “Star Coverage” software

The evolution of the parallactic angle η is given by equation (5.2) on page 131, depending on both the coordinate of the observer and the pointing direction. Unfortunately, the time dependence is embedded into h and z, and there is not an analytic relation between the amplitude of the FoV rotation $\Delta\eta$ and the time length of the observation Δt. As a consequence,

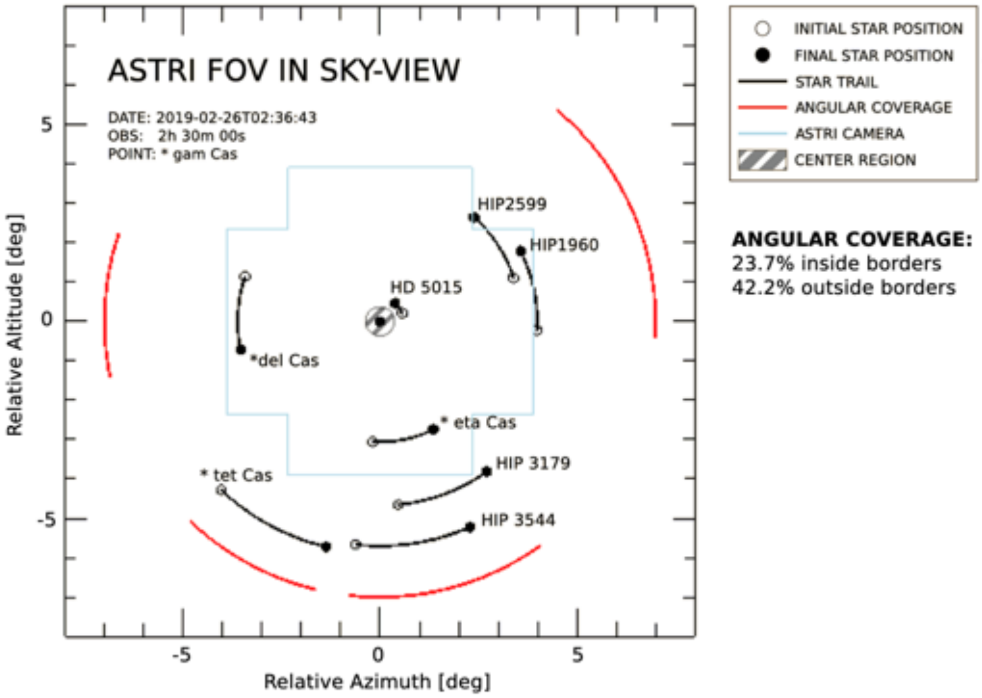

Fig. 6.3: Example of the output from the software "Star coverage", set for the ASTRI–Horn telescope. The rotation is counterclockwise and the blue polygon is the shape of the camera. Red arcs represent the total angular coverage (42.2 %), considering stars outside the borders as well, while the coverage inside the camera is 23.7 %.

for simulating in detail the rotation of the FoV in the context of the present thesis work we developed a dedicated software, "Star Coverage", that can be used not only for ASTRI–Horn, but also for any other telescope, at any time [200]. Given the position of the instrument (φ, λ), the coordinate of the pointing (α, δ), and the date of the observation, the software calculates the position of all the stars within a distance d below the magnitude m, taken their position from the SIMBAD catalog [201] [*link* 270]. For a certain time length Δt, the software simulates the evolution of η and provides the extension of the FoV rotation giving the angular percentage covered by the star trails (considering possible overlaps). If the geometry of the camera is provided, the angular coverage is computed for both inside and outside the borders of the detector system. An example of the typical output is reported in figure 6.3, where the same stellar region of figure 5.3 is shown, in the constellation of Cassiopeia. Both SkyView and CamView options are implemented. The software is written in the IDL language, and the source code has now made available online[1]. In the context of the analysis presented in this chapter, *Star coverage* was adopted for studying the FoV rotation in the specific cases of the observing runs selected for the data processing.

6.2 Data selection and pre-processing

ASTRI–Horn is a prototype telescope and hence several technical tests were performed during data acquisition, especially in the observing runs dedicated to the Variance method. For this reason, to find out suitable files for our analysis of the FoV rotation it was necessary to examine the whole ASTRI web archive [*link* 224], checking the content quality of hundreds of runs. Logbooks of the observing nights are available on handwritten spreadsheets, shared via DropBox [*link* 238] among the collaboration. They contain useful notes about the history of operations: updates of the firmware, hardware failures, upgrades of any kind and more. Unfortunately, not every run is documented and hence very often it was necessary a visual inspection of the files, to check the status of the lids, the number of PDMs on, the tracking mode, and so on. We created a Google Spreadsheets [*link* 277] with a summary table of the observing runs that we checked, so that it is simple to access the information using for example dedicated Application Programming Interfaces (APIs) for Python or other languages [*link* 243]. Moreover, we created an IDL function called `CATALOGUE` to access a local copy of the VAR data selection downloaded from the archive. In figure 6.4 is reported the distribution in azimuth and elevation of observing runs in such selection. Starting from this "clean" catalog we defined the sample to perform our analysis.

6.2.1 Definition of the sample

To test our procedure, we selected those cases where the telescope was in tracking mode and $\Delta\eta \geq 25°$: the so-called *long* observing runs. In fact, it is reasonable to suppose that longer light arcs provides a better constraint on the study of the FoV rotation. We individuated 8 long observing runs among the data sets available in the selection that we made[2].

---

[1] See appendix B for details.

[2] In principle, *short* consecutive runs on the same target can be concatenated producing a *long* data set, suitable for our analysis. However, for testing the procedure we decided to work on *single* runs only.

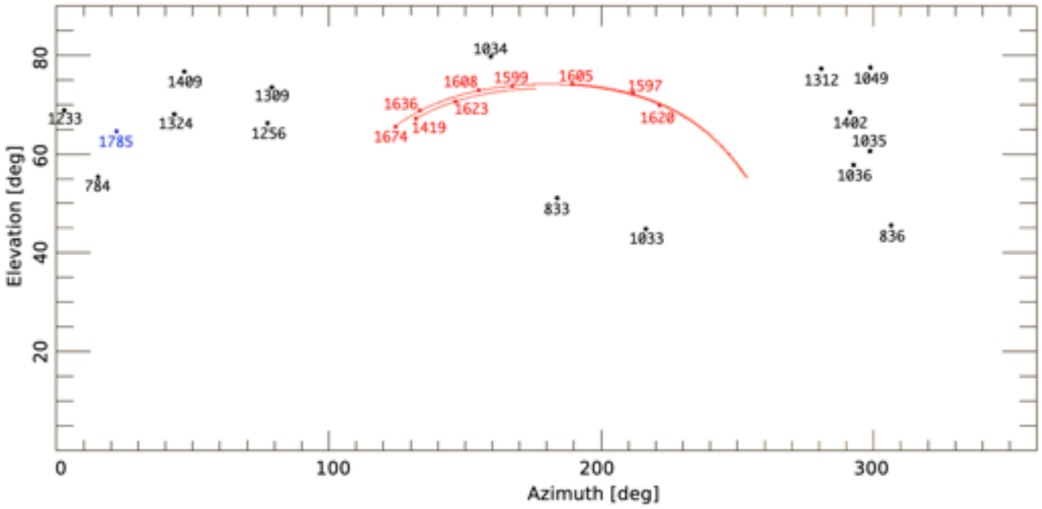

Fig. 6.4: Distribution in azimuth and elevation of the observing runs in our selection. Both short (black) and long (red) runs are reported. A long run in staring mode is also reported (blue).

In principle, also the number of bright stars available in the FoV can influence the result of the analysis. Fortunately, in winter 2018/2019 the target of the first observing campaign with ASTRI–Horn was the Crab Nebula, which is in a pretty crowded region (Taurus constellation), and hence in our data selection of long runs there are 3 cases where 4 stars are available. In the other cases, the telescope was pointing in the constellation of Leo, and 2 bright stars only are present in the FoV. Table 6.1 reports the final selection that we made, together with the main parameters of each run. All the cases in the Leo constellation presents a larger evolution of the parallactic angle, $\Delta\eta \geq 55°$.

6.2.2 Star isolation by pixel clustering

Before starting the true processing of Variance data it is necessary a preliminary operation: to isolate the pixels containing the signal of the stars available for the analysis. This process must consider the FoV rotation effect, which is clearly visible by eye in all the runs reported in table 6.1, using for example the procedure `VAR_QVMOVIE`, with all the Variance frames. However, to select automatically in every frame the pixels containing the star light is not trivial, as the signal to noise ratio (SNR) can be small (few units), especially when the spot falls across two or more pixels, or even lower when faint stars are occasionally veiled by a thin cloud. At first, in order to reduce the area where to look for the intensity maximum, we

Run ID	Date	Pointing	Frames	Time length	Coverage
1597	2019-02-26	Crab Nebula	2275	1h 59m 44s	33.4°
1605	2019-02-27	Crab Nebula	2569	2h 14m 04s	40.1°
1620	2019-02-28	Crab Nebula	1986	1h 43m 39s	25.5°
1599	2019-02-26	Leo	1820	1h 27m 57s	55.1°
1608	2019-02-27	Leo	1640	1h 29m 0s	56.9°
1623	2019-02-28	Leo	1392	1h 16m 33s	50.2°
1636	2019-03-01	Leo	4368	3h 48m 47s	99.1°
1674	2019-03-06	Leo	4216	3h 50m 16s	99.5°

Table 6.1: Parameters of observing runs that we selected to study the alignment of the Cherenkov camera through the rotation of the FoV. Only two bright stars are visible in runs on the Leo constellation, four in the others.

tried to follow each spot with a movable $3\,\mathrm{px} \times 3\,\mathrm{px}$ box, assuming that any possible deviation from the ideal trajectory is smaller than the box side. However, we soon implemented a more effective strategy which is based on the following consideration. Moving objects in Variance frames can be detected because of the change in pixel levels, while sensors not illuminated present constant values. As a consequence, the full set of pixels interested by the star light during the rotation of the FoV can be detected with a map of the "variance of the Variance": considering for each pixel the standard deviation of the whole observing run, we can actually visualize the star trails. Figure 6.5 reports the resulting image for the run `1674`, where the movement of two stars is visible as in a long exposure picture. The next step is isolating the groups of pixels belonging to the same moving spot, hence identifying the tracks of the brightest stars. To this end, we adopted a clustering algorithm (centroid-based, of the k-means family [202]) implemented in the standard library of IDL[3]. Figure 6.6 shows the output of such procedure in the case of the run `1597`, presenting a quite complex situation due to the presence of a crowded star field. Tuning the parameters of the algorithm it is possible to obtain an adequate division of the pixels in subsets, and also to assign a priority scale to the clusters, based on star intensities and distances from the center, using the alphabetical order starting from the letter A. In the following part of the analysis, only pixels within clusters will be considered in every frame to retrieve the position of stars.

---

[3] See appendix B for more details.

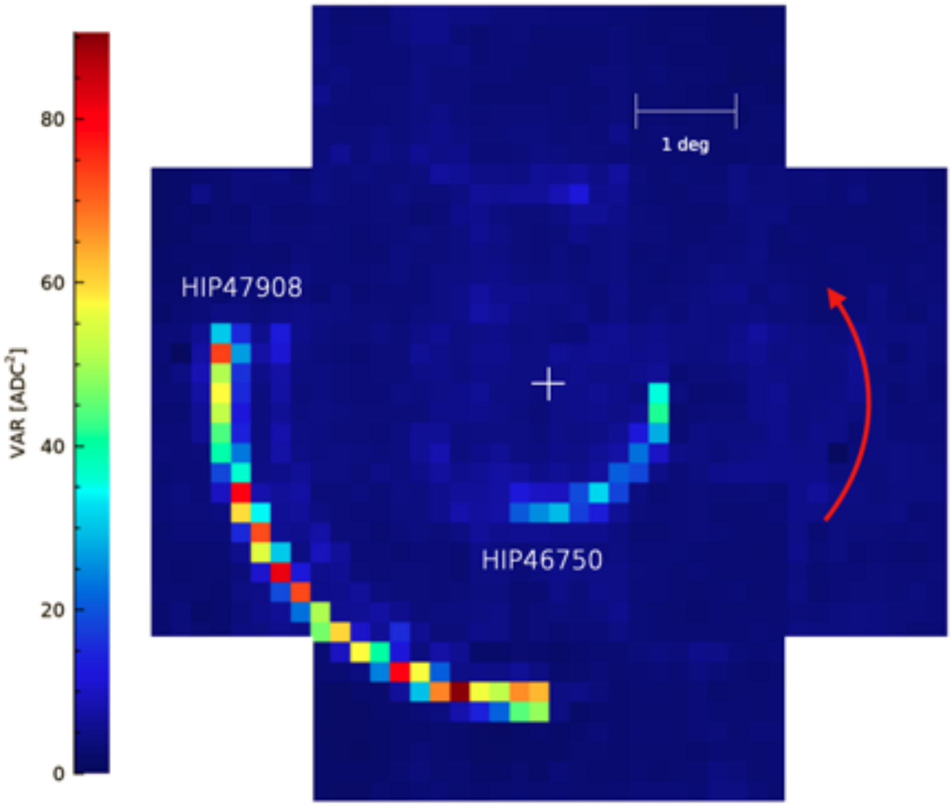

Fig. 6.5: The FoV rotation in CamView detected using the "variance of the Variance" method, in the observing run `1674`. The pointing direction is α =9h 35m 49.06s, δ =21°54′36.42″. The brightest star in the FoV (HIP 47908) is *Algenubi* (*Eps Leo), the other one is *Alterf*.

6.3 Star trail analysis

To evaluate the alignment of the Cherenkov camera it is necessary to fit with a suitable function the star trails individuated in the *long* observing runs selected, in order to obtain the position of the intersection between the telescope optical axis and the camera. To this end, in each frame the position of each star is evaluated using the de-convolution algorithm presented in section 5.2.2, improved by the transformation matrix of section 5.3, within the pixel sub-set individuated by the clustering procedure presented in section 6.2.2. Once that the trails of the stars are individuated with sub-pixel accuracy, the fit of their trajectories can be performed, using a custom function that we defined in order to consider all the stars *together* and not individually: the *multiellipse* fit function. Lastly, the posi-

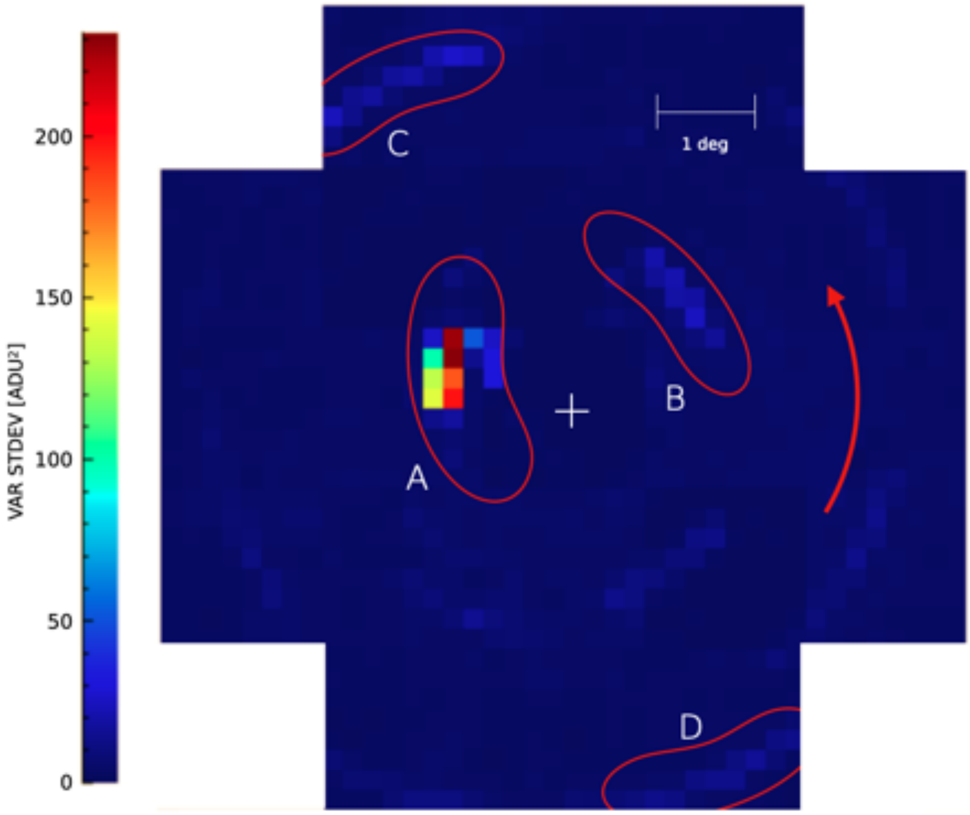

Fig. 6.6: Star trails isolated by the clustering algorithm, in CamView. The camera center is pointing at the Crab Nebula. Star A is 123 Tau (Tianguan, $3.0\,\mathrm{mag}$), B is 114 Tau ($4.8\,\mathrm{mag}$), C is 119 Tau ($4.3\,\mathrm{mag}$) and D is 125 Tau ($5.2\,\mathrm{mag}$) [values taken from SIMBAD, V band].

tion of the centroid of the fit is exploited to evaluate the alignment of the Cherenkov camera. Figure 6.7 reports a schematic representation of the complete procedure for the star trails analysis: we implemented such a work flow into a unique IDL routine, which is called `V_AXIS`. The following sections provide a detailed description of the most important parts of the routine: the Variance image elaboration (section 6.3.1), the multiellipse fit procedure (section 6.3.2) and the output values obtained (section 6.4), together with a long discussion about possible improvements and limitations of this method.

6.3.1 Elaboration procedure

After the calibration with the relative strategy discussed in section 4.2.3, in each Variance frame it is possible to retrieve the position of the stars

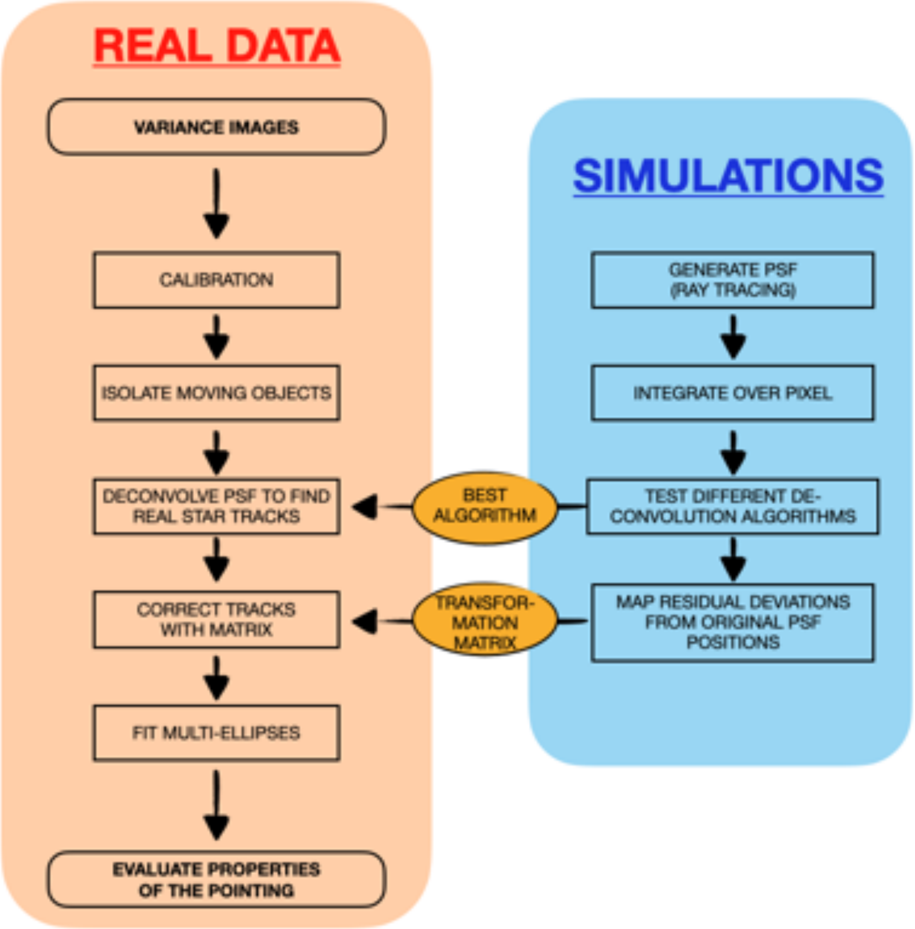

Fig. 6.7: Schematic representation of the procedure for the star trail analysis. The simulation part (*right*) is presented in sections 5.2 and 5.3, while the real data analysis (*left*) is discussed in this chapter.

with sub-pixel precision using the following procedure. Within every cluster, the position of the star is retrieved with the de-convolution algorithm (section 5.2.2) applied on the pixel with the maximum intensity and its eight nearest neighbor, so to consider also the tails of the PSF. The resulting (x, y) position is corrected with the transformation matrix to reduce the effects of gaps between pixels (section 5.3). Iterating this operation on every frame of the run considered, we obtain a sequence of coordinates constituting the trails of the stars: an example is shown in the left-hand image of figure 6.8. However, very often happens that a further elaboration is necessary, as in the case reported in figure 6.8, *right*. In fact, the de-convolution algorithm only considers the pixels above a certain inten-

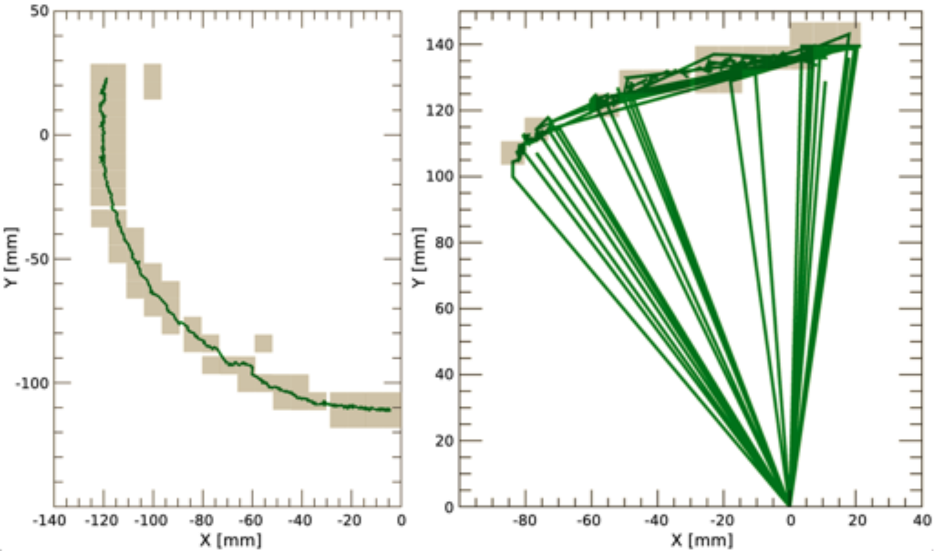

Fig. 6.8: *Left*. The trail of star B in run `1674` (the same of figure 6.5), an example of clean trajectory without any manipulation. *Right*. The case of star C in run `1597` (the same of figure 6.6): due to the faint intensity of this star it is necessary a cleaning procedure to obtain the final trail reported in figure 6.9.

sity threshold, given by the median level of the calibrated image plus n_σ times its standard deviation, where n_σ ranges from 0.5 to 2.5. As a consequence, it is possible that no pixels are above the threshold in the cluster (and in this case the position returned is zero), but also that the intensity maximum does *not* correspond to the true position of the star, e.g. when the spot of a very faint source falls across two pixels or more and its intensity drops below the threshold, while the level in other pixels can be higher due to statistics fluctuations of the background. In this case, the resulting star trail jumps back and forth along the pixel cluster and hence a cleaning procedure is necessary. We operated a selection by removing those points that are further than $d_{\mathrm{MAX}} = 1.5\,\mathrm{px}$ from the x and y median value of the last ten consecutive (accepted) positions[4]. An example of the output of such procedure is shown in figure 6.9, where the cleaned star trails of the run `1597` are reported.

---

[4] In the automated IDL routine, the user must visualize and confirm this result before proceeding, or eventually repeat this part changing the values of d_{MAX} and/or n_σ.

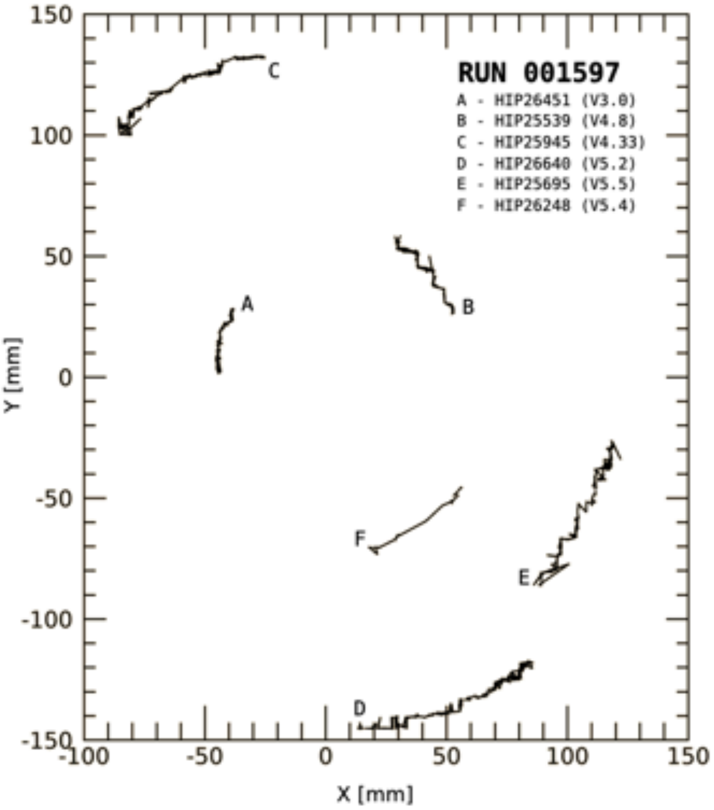

Fig. 6.9: Clean trails of stars in the run `1597` (see figure 6.6 for comparison). Values of V magnitude reported in the legend are taken from SIMBAD.

6.3.2 Multiellipse fit

In the ideal situation, the star trails present a circular shape, centered on the origin. However, in our analysis we must consider any possible deviation from the expected pattern: a rigid shift could be introduced by an accidental camera mis-alignment, while a deformation of the circular shape can be associated with residual errors in the telescope pointing model. In fact, the observing runs available to develop and test our procedure are all in tracking mode, and hence the contribution of the telescope dynamics must be considered simultaneously with that of the camera static alignment. As a consequence, star trails generally lie along arcs of different *ellipses*, sharing the same center, eccentricity and tilt angle. To perform the fit of an ellipse, none of the fit libraries available in IDL or Python provides a built-in procedure, so in the context of the present thesis work we defined a custom function for this purpose, which is presented hereafter.

6.3.2.1 Fit strategy using free points

As the ellipse is not the graph of a function, it is impossible to fit such figure in one dimension, unless using a complicated series of conditions to divide the problem into separate regions where different portions of data can be described with suitable explicit functions. An alternative and simpler approach is to embed the problem in two dimensions, considering the ellipse as a set of ordered *free points* that must be simply replicated optimizing the parameters $\boldsymbol{p}$ of a function $f : \mathbb{R}^2 \to \mathbb{R}^2$, defined by

$$(\boldsymbol{x}, \boldsymbol{y}) \longmapsto (\boldsymbol{x}', \boldsymbol{y}') = f(\boldsymbol{x}, \boldsymbol{y}|\boldsymbol{p}) , \tag{6.1}$$

where bold symbols denote arrays and the output of the function is indicated with the prime symbol. In this context, Variance data $(\boldsymbol{x}, \boldsymbol{y})$ constitutes the independent variable, but also the desired output: with the right choice of parameters $(\boldsymbol{x}', \boldsymbol{y}') = (\boldsymbol{x}, \boldsymbol{y})$, and f is simply the identity function.

Of course, the function f has not an analytic expression, but we can describe its implementation in the IDL program as follows. To begin, a fake ellipse is produced starting from the parameters $\boldsymbol{p}$ and a generator of random angles in the range 0 to 2π. After that, only the portion of ellipse in the polar-angle range of real data is considered: at this level, the points of the fake ellipse have coordinates $(\tilde{\boldsymbol{x}}', \tilde{\boldsymbol{y}}')$, while $\boldsymbol{\theta}'$ is their polar angle. Finally, an interpolation of the couples $(\tilde{\boldsymbol{x}}', \boldsymbol{\theta}')$ and $(\tilde{\boldsymbol{y}}', \boldsymbol{\theta}')$ yields respectively the output values of $\boldsymbol{x}'$ and $\boldsymbol{y}'$ in correspondence of the true $\boldsymbol{\theta}$ of Variance data.

The implementation of the custom function f constitutes an effective solution for the fit of both full and partial ellipses, with the only requirement that the origin of the reference system be *inside* the area of such figures. Moreover, a huge advantage of this procedure is that it is straightforward to implement the possibility to fit multiple ellipses (or arcs) at the same time, sharing the same center, eccentricity and tilt angle, without imposing any limit on their number. This is exactly our necessity, as it is reported in the next section, dedicated to the fit procedure.

6.3.2.2 The fit procedure

The fit of the star trails is performed using the `MPFIT` procedure of the IDL library[5], implementing the custom function described in section 6.3.2.1. The number of free parameters is $p = 4 + n$, where n is the number of stars considered in the observing run under study. In particular, the parameters

---

[5] See appendix B for more details.

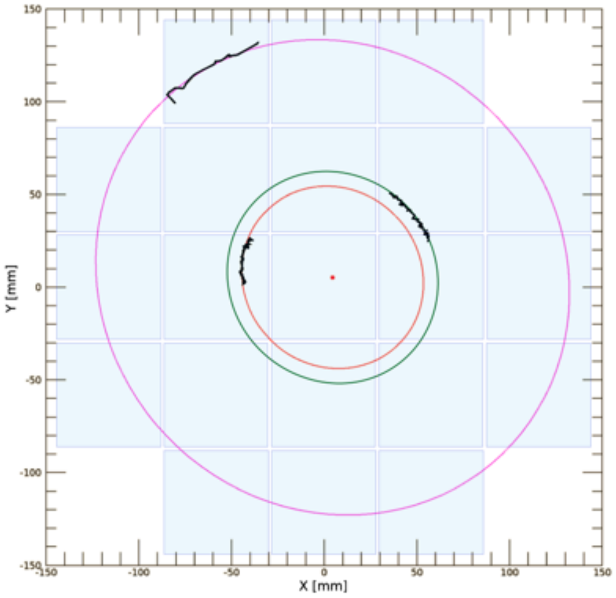

Fig. 6.10: Output of the multiellipse fit procedure on the run `1597`, with 3 stars considered *together*. Star trails from real Variance data are colored in black, while light-blue squares represent the PDMs of the ASTRI–Horn camera.

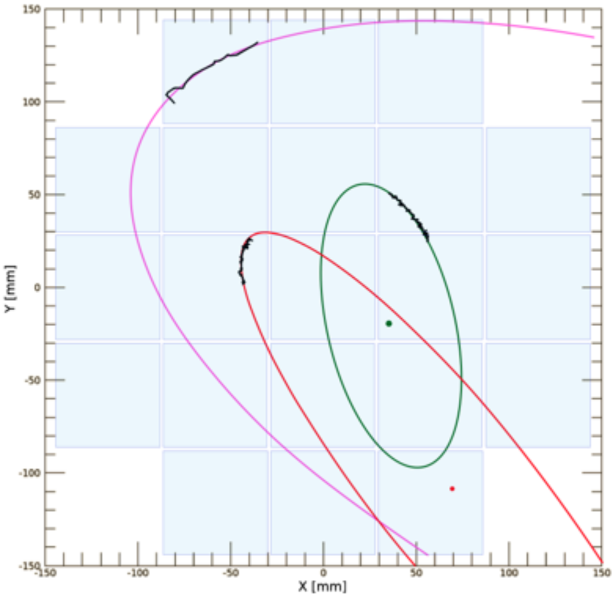

Fig. 6.11: The same situation of figure 6.10, but stars are now considered *individually*. For each of them, the multiellipse fit suffers from residual artifacts introduced by the large pixel size, and hence the resulting output is non-realistic.

of the fitting functions are

- X_0 and Y_0 of the center;
- θ tilt angle;
- major and minor semi-axes of the innermost star trail;
- major semi-axis of other star trails.

The fit function is called several times, with random changes to the initial parameters and without constraints: the dispersion of the results is adopted as an estimation of their uncertainty, being of the same order as the error extracted from the covariance matrix. We see that the accuracy of the final result strongly depends on both the number of stars considered and their angular coverage: if multiple stars are considered *together* the fit is more reliable, while if they are processed individually then the result is influenced by the edgy shape of the star-trail reconstruction, due to the large pixel size, and hence the outcome is non-realistic, too far from the expected circular shape. Figures 6.10 and 6.11 present this phenomenon, using the case of three stars from the observing run `1597`. In this example, if the stars are fitted together then the center of the ellipse falls $\sim 10.5'$ far from the camera geometric center, while if the stars are considered individually then the centroids are not even inside the central PDM (with huge error bars). A more quantitative and detailed analysis of this situation is reported in the next section, which is dedicated to results and their discussion.

6.4 Results and discussion

As previously demonstrated in figures 6.10 and 6.11, for those cases where $\Delta\eta \geq 25°$ the fit result is much more reliable if the star tracks are considered together for the analysis and not individually. We investigated this effect using the 3 observing runs on the Crab Nebula reported in table 6.1, presenting 4 bright stars each, allowing us to consider different combinations of 2 stars (6), 3 stars (4) and 4 stars (1), in every run. The dispersion of outputs from different calls to the fit procedure is adopted to evaluate the position of the telescope optical axis in the camera with its uncertainty. The result of this analysis is reported in figure 6.12. Considering the only 3 cases including 4 stars each, the position of the optical axis is $X_0 = (-4.3 \pm 2.2)\,\mathrm{mm}$, $Y_0 = (6.9 \pm 2.1)\,\mathrm{mm}$, where the uncertainties are equivalent respectively to $3'44''$ and $3'27''$ in the sky. The precision is lowered by a factor of ~ 2 considering only 3 stars, and by a factor of ~ 10 if the stars considered are 2 at a time instead. This result demonstrates that the error due to the small FoV rotation angle ($25°$ to $40°$) can be mitigated if 4 stars at least are considered together for the analysis, but the final result still presents a quite large statistical uncertainty. However, in this condition we already obtain a relevant information for optimizing the accuracy of the system in the case of ASTRI–Horn, as our analysis reveals that the Cherenkov camera is de-centered of $\sim 12.6'$ (radial distance), but we are still far from the $20''$ accuracy of the ASTRI pointing requirement (3.4).

The same analysis carried out on observing runs with 4 bright stars can be replicated on the others of table 6.1, where only 2 stars are available, but the rotation of the FoV is much larger ($55°$ to $100°$). In this case the constraint of the fit is ensured by the conspicuous extension of the star trails: in fact, the dispersion of results is much smaller than in the case of 2 stars with a minor FoV rotation. For every observing run considered, the fitted position of the optical axis is reported in figure 6.13: the mean and the standard deviation of such points are adopted as the best estimators for the true position of the optical axis with its uncertainty. In particular, we obtain $X_0 = (-4.1 \pm 1.7)\,\mathrm{mm}$, $Y_0 = (6.2 \pm 1.5)\,\mathrm{mm}$, where the uncertainties are equivalent respectively to $2'47''$ and $2'29''$. This result contains all the observing runs presented in table 6.1, it is consistent with the previous one, and the error bar is about $30\,\%$ smaller. Again, this information is useful for the optimization of the ASTRI–Horn telescope, but it is not enough to match the pointing accuracy required. However, it is important to remember that we are now considering data taken in different nights, with a prototype telescope on which several technical tests were performed during operations, and that we know it was heavily affected by pointing and tracking problems[6]. As a consequence, it is not surprising that we cannot further increase the precision of this method using archive data in tracking mode. We had planned to test this procedure with new data taken on purpose in summer 2021, maybe with the telescope in staring mode pointing at the NCP so to rule out all the possible tracking errors (see section 5.1.3). However, the maintenance operations on the telescope were heavily delayed by the COVID-19 pandemic in the last two years and hence, up to January 2021, it is still impossible to acquire new Variance data with ASTRI–Horn. Therefore, the only chance to fully explore

---

[6] During the data analysis for the Crab detection [86] it emerged that serious pointing issues affected the telescope during operations: this is one of the reasons behind the birth of the present thesis.

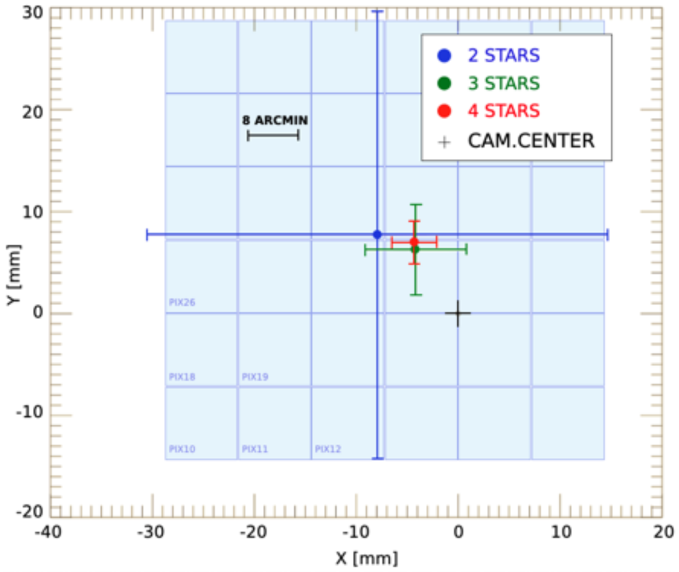

Fig. 6.12: Precision improvement of our method with the increasing number of stars, for the 3 observing runs pointing at the Crab Nebula (see table 6.1). The final result is calculated with the mean and standard deviation of all the possible combinations of 2 (*blue*), 3 (*green*) and 4 (*red*) stars.

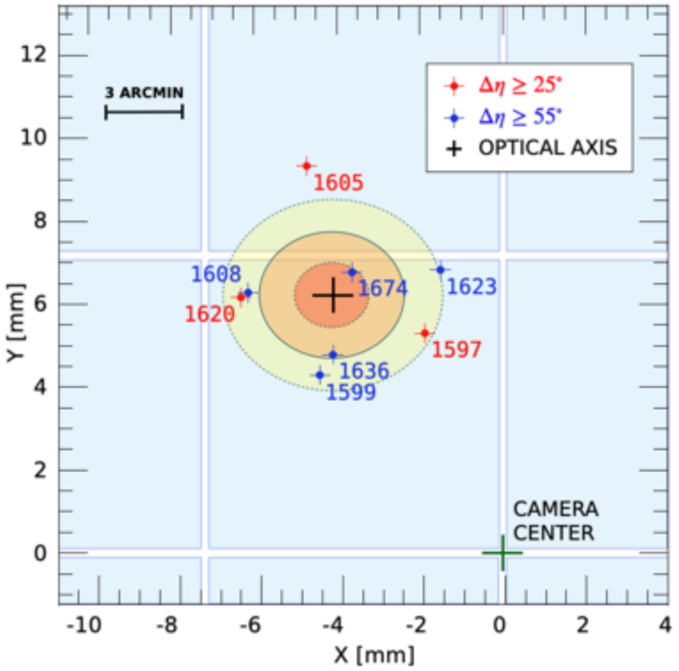

Fig. 6.13: De-centering offset of the Cherenkov camera revealed with our analysis. The ellipses represent the confidence level of 0.5, 1.0 and 1.5 σ. Light blue squares represent the pixels of the ASTRI Cherenkov camera.

the potentialities of this method is to set up a numerical toy simulation.

Using the IDL language[7] we developed a software tool to simulate the whole process of image creation and subsequent analysis, supporting any number of stars and observation time-length. We introduced an artificial offset in the Cherenkov camera with respect to the telescope optical axis, and we study how accurately our pipeline measures such mis-alignment. Of course, several simplifications are introduced in our toy simulation: we assume a perfect tracking, a perfect mirror alignment, and no gravity flexures. We find that with a FoV rotation of $100°$, the offset is reproduced with an accuracy of $\sim 19''$ using 4 stars, and $\sim 21''$ using only 2 stars, if an adequate gain calibration of the camera is provided so to produce a perfect flatfield in Variance images (figure 6.14, *right*). Without such a good gain calibration, the accuracy is lowered to $\sim 28''$ with 4 stars and $\sim 37''$ using 2 stars only (figure 6.14, *left*): the flatfield-like gain calibration procedure proposed in section 4.2.3 becomes a crucial operation in light of this result.

The toy simulation confirms that when the FoV rotation angle is very large ($\sim 100°$) the fit is well constrained even if only 2 stars are present in the FoV. This is a very important information, because it is possible to use only 2 stars[8] in our analysis to perform the calibration of the camera axis alignment with the telescope in staring mode pointing at the NCP, as that region is not a crowded stellar field. A FoV rotation of about $100°$ corresponds to $\sim 6\,\mathrm{h}\ 40\,\mathrm{min}$ observation pointing at the NCP, hence it is possible to carry out an accurate calibration with this strategy. Incrementing the time-length of the observation the accuracy slightly increases, but it never reaches the level of $\sim 1''$ as it was initially indicated in the first works about the application of this technique to the ASTRI camera [181, 198]. In fact, as it is shown by the simulations above, the large pixelisation of the camera introduces an intrinsic limit on the accuracy of our method for the calibration of the axis alignment that cannot be exceeded despite we are currently using an improved version of the fit function with respect to the past, and we have implemented several additional parameters to constraint the behavior of the software in both simulations and data analysis. Nevertheless, as already pointed out, this result is remarkably useful for the optimization of the whole system, and further considerations about the analysis presented in this chapter are reported in the following final section.

---

[7] See appendix B for details.

[8] Namely `HIP5372` and `HIP85822`, as Polaris is too close to the pointing direction.

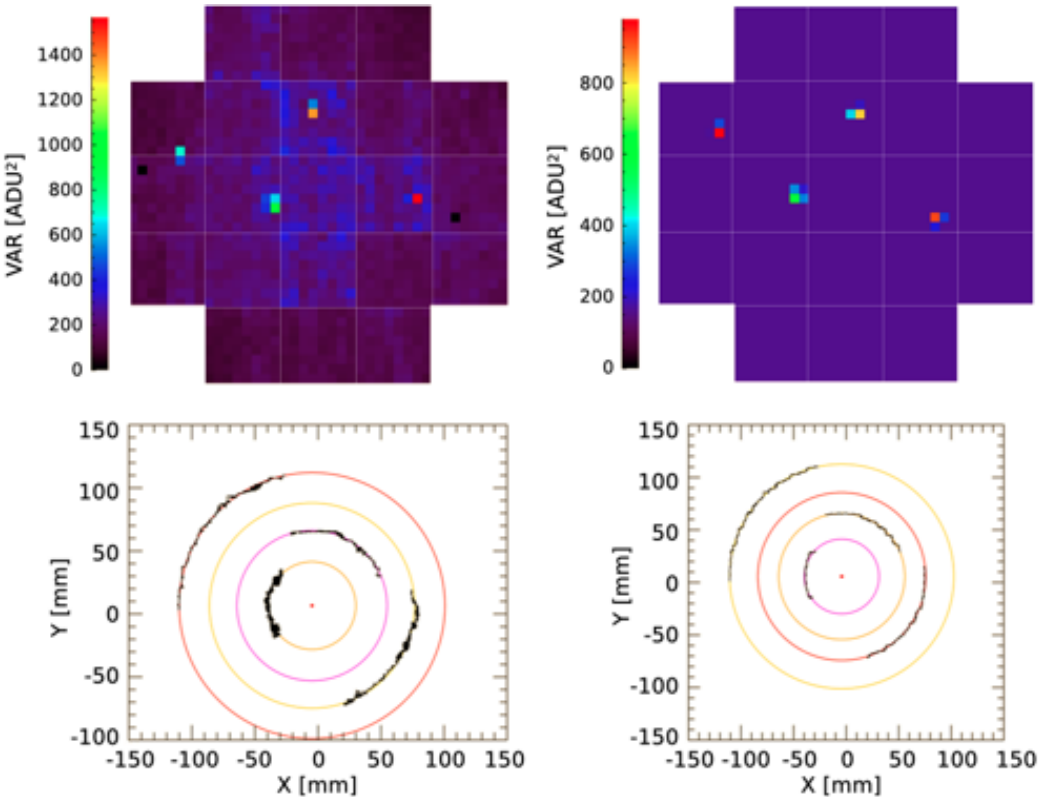

Fig. 6.14: Toy simulation of an observing run with a rotation of 100° and 4 bright stars in the FoV. A poor gain calibration is simulated on the *left*, while a perfect flatfield is presented on the *right*, enhancing the accuracy of the output. The artificial camera misalignment here is $X_0 = -4.00\,\mathrm{mm}$, $Y_0 = 6.00\,\mathrm{mm}$, similar to the one obtained in real data analysis: our procedure measures the simulated offset with an accuracy of $19''$ (situation on the right).

6.4.0.1 Final considerations

In this chapter we have outlined an original procedure for verifying the alignment of the Cherenkov camera to the optical axis of the telescope owning the potentiality to achieve the accuracy of $\sim 20''$ with a long observing run pointing at the NCP with the telescope in staring mode, if a good gain calibration of the pixels is provided for Variance images. For testing purposes, we applied this method to real data taken in the past with ASTRI–Horn and we obtained an interesting result despite they were taken in non-optimal conditions: the camera has a radial de-centering of about $(0.19 \pm 0.06)^\circ$. The precision of this estimation do not satisfy the ASTRI requirement of $20''$ for the pointing accuracy post-calibration, but

it constitutes anyway a very important result for the optimization of the whole system, as it highlights the presence of an important systematic error and provides a value to correct *post-facto* the data of the last observing campaign. In the future, this technique will be part of the calibration procedures for the ASTRI MiniArray, being implemented both during the assembly verification phase and dedicated calibration sessions.
A possible limitation of our method is that it provides only an *average* estimation of the camera de-centering: for example, if the mount system undergoes gravity flexures during tracking observations it is very difficult to detect such an effect with our analysis of the FoV rotation. Similarly, if in some frames there are external agents introducing distortions in star trails, like clouds, bright satellites, or strong wind gusts, again it is difficult to detect their presence and hence the final output of the analysis will be inevitably affected by them. To overcome this problem a possible solution is to constantly monitor the FoV of the telescope with the PMC and to exclude the frames presenting an excessive mis-pointing or other problems for identifying the stars, ensuring a clean data set for investigating the camera alignment with the procedure presented here. Also a custom Variance astrometric software could be adopted for the same purpose, and in the next chapter we present the one that we developed for the ASTRI project.

7

Star field astrometry

The peculiar features of the ASTRI imaging system, designed for Cherenkov events rather than astronomical sources, make it impossible to adopt common astrometry software for the analysis of Variance images. Nevertheless, in chapter 5 we showed how to evaluate the position of bright spots in Variance frames with sub-pixel precision, and how to provide an effective *astrometric calibration* of the FoV, mapping the celestial coordinates into the camera reference system. With this basis, it is possible to develop a routine for identifying the stars in the FoV automatically, matching bright spots with the expected position of stars in the telescope pointing direction. Such operation is equivalent to providing an *astrometric solution* for Variance frames, implementing a custom procedure developed on purpose, and paving the way for several further analysis: to detect ghost images (i.e. bright spots not associated to any real star) due to misaligned mirror segments, to monitor constantly the pointing direction of the telescope, to reveal transient objects such as satellites or meteors, and so on. The present chapter is dedicated to the astrometry of the star field in Variance images and its applications. In section 7.1 the pointing direction of the telescope is calculated using data from motor encoders, and the expected sky map is produced after a query to stellar catalogs. The specific strategy for the identification of stars is reported in section 7.2, while sections 7.3 and 7.4 presents the application of this technique to the data of the ASTRI–Horn archive, together with a discussion of the main results.

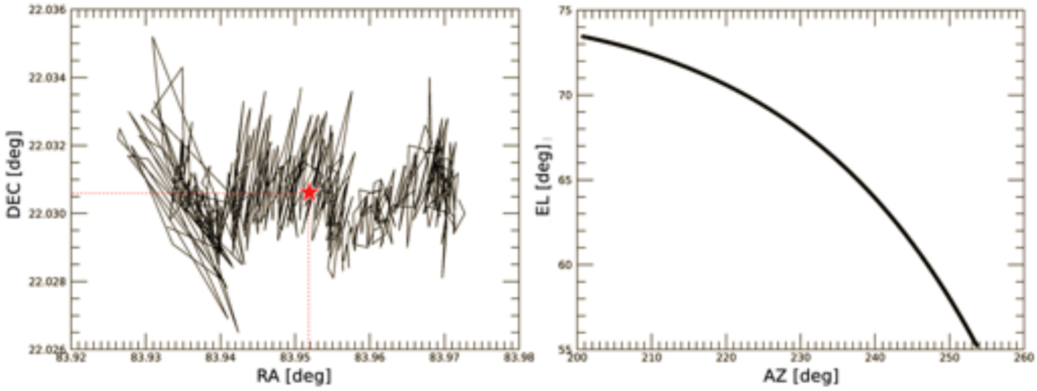

Fig. 7.1: Data from motor encoders in ECS (*left*) and HCS (*right*), at the epoch J2000.0, for the run `1597`. We assumed the average value (red star) as the nominal pointing of the telescope: $\alpha = (83.951 \pm 0.012)°$, $\delta = (22.031 \pm 0.001)°$. The standard deviation is larger in Right Ascension, where it is equal to $\pm 43.4''$.

7.1 Sky map in the pointing direction

The starting point of our custom pipeline for the identification of stars in Variance frames, is the map in camera coordinates of the sources that we expect to be visible in a certain observing run. To obtain such information we need first to know the true pointing direction of the telescope, that can be obtained using the data of the motor encoders. Second, the list of bright sources available in the corresponding sky area can be retrieved by querying a suitable star catalog. The following paragraphs present in more detail the respective procedures.

Motor encoders

The position of the azimuth and elevation axes are measured by dedicated encoders, monitoring the action of the motors. Their output is saved every $15\,\mathrm{s}$ in a local computer at the astronomical site of Serra La Nave and then copied every $24\,\mathrm{h}$ in the database of the INAF–OAS Bologna observatory (Italy, [*link* 256]). Here, the values of encoders can be accessed with a dedicated tool written in Java [203] or using a MySQL remote query from the command line [*link* 263]: we implemented the second solution into an IDL program, allowing to visualize a plot of the pointing direction in astronomical coordinates, as it is shown in figure 7.1.
In every observing run we considered as the pointing direction P the mean

value of the (calibrated) α and δ astronomical coordinates[1] retrieved by motor encoders. For example, in the case of run `1597`, reported in figure 7.1, we obtained $\alpha = 5\mathrm{h}\ 35\mathrm{m}\ 48.47\mathrm{s}$ and $\delta = 22\mathrm{d}\ 01\mathrm{m}\ 50\mathrm{s}$, which is very close[2] to the preferred position of M1 (the Crab Nebula) indicated by both TeV catalogs [e.g. *link* 273, 274, 265] and optical ones [e.g. *link* 270], which is $\alpha = 5\mathrm{h}\ 34\mathrm{m}\ 31.97\mathrm{s}$ and $\delta = 22\mathrm{d}\ 0\mathrm{m}\ 52.06\mathrm{s}$. In the same figure, we can see that the pointing direction seems to fluctuate in Declination and to drift in Right Ascension: this behavior can probably be cured by improving the pointing model of the telescope, but for our analysis we decided to consider anyway this run, as the standard deviation (in R.A.) is $\pm 43.4''$, which is still small for our purposes. In general, in the data selection presented in section 6.2, we excluded those cases where the standard deviation of the pointing in α or δ is larger than $0.1°$. Once that the pointing direction P is available, we can calculate the expected sky map in the FoV using a suitable query to an adequate stellar catalog.

Stellar catalogs

In order to calculate the expected position on the camera of bright sources in the FoV, it is necessary to start with the list of all the objects below the maximum magnitude m^*, whose distance from P is lower than a certain angle D^*. We obtained such a list with a query to the catalogue `USNO-B` [204], whose filter `B1` is exactly in the wavelength range in which the ASTRI sensitivity peaks, i.e. between $350\,\mathrm{nm}$ and $500\,\mathrm{nm}$. The query is made through the Vizier service [205] [*link* 279] using a calling sequence implemented in our IDL routine. The standard parameters that we adopted for the query are $D^* = 5°$ and $m^* = 6.5\,\mathrm{mag}$.

The USNO catalogue uses a peculiar nomenclature for its sources, but we want to have a naming convention that allows an easy cross-check with other catalogues and to make quick visual comparisons with commercial sky simulators such as *Stellarium* [*link* 271] or *Cartes du Ciel* [*link* 231]. For this reason, we search the USNO sources in the SIMBAD database [201] [*link* 270], and we adopt the name scheme of another survey: the *Hipparcos* catalogue [206, 207]. Lastly, to obtain a simulation of the actual sky map with high accuracy, we also considered the correction for the proper motion of the stars, introducing a displacement up to $7''$, while we neglected the parallax due to the Earth motion (always lower than $0.4''$).

---

[1] We always assume the epoch `J2000.0`, unless otherwise stated.

[2] It is very close, but not exactly coincident. Remember that for a Cherenkov observation in "ON-mode" it is not necessary to point exactly at the source: very often it is better to point at its proximity, so to improve the training of the pipeline for data reduction.

Using the strategy described in section 5.1.2, we display the position of bright objects in the camera reference system, with the proper orientation, obtaining sky maps similar to the one reported in figure 5.3, on page 134. From now on we consider only the (x, y) position of these objects, and we always refer to them with the term *stars*.

7.2 The astrometric solution

In the case of the most advanced astronomical survey, a full astrometric solution of a sky image usually includes six parameters [208]: barycentre in α and δ, parallax, proper motion in α and δ, and radial proper motion [209]. Of course, in the case of the ASTRI telescope the astrometric solution cannot be so elaborated, as a Cherenkov telescope is equipped for different scientific objectives. Our goal here is to provide an effective procedure to identify the sources in Variance frames, allowing to exploit those images for further analysis (sections 7.3 and 7.4). To this end, we developed the custom strategy which is presented in the following sections (7.2.1, 7.2.2), but also other collaborations have adopted similar solutions for their telescopes, that will be presented in future articles that are currently in preparation by the relative groups at work. For example, the CHEC camera[3] for the SSTs (CTA) implements an approach which is based on a blind FoV calibration using the *plate-constants* method (see section 5.1.2.1), while the identification of the sources is carried out with a free-point fit procedure (see section 6.3.2.1) for matching the arrangement of spots in images with the position of known stars in stellar catalogues [210]. The LST-1 telescope of CTA (section 2.3.4.1) implements a different solution: they retrieve the pointing direction from motor encoders, they calculate the expected position of nearby stars on the camera, and then they adopt a free-point fit procedure for assigning a name to every bright spot. Our procedure is very similar to this approach, except for the last part, as we do not use a fit algorithm for the star identification, but rather a more articulated procedure that allows us to better control the process parameters, and makes it easier to handle errors. This algorithm is presented in section 7.2.2, after having discussed the strategy for the bright spot isolation in Variance images.

---

[3] Presented in section 2.3.4.3.

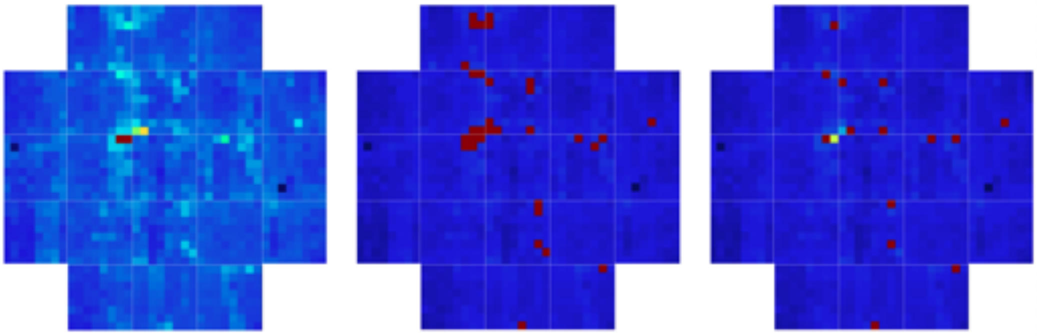

Fig. 7.2: Isolation of bright spots in the Variance frame 134 of run `1597`. From the calibrated image (*left* image) we select the n_B brightest pixels (*center*) and then we considered only the "true spots" within every sub-group (*right*). See figure 7.3 for a plot of these points together with the expected position of bright stars in the FoV.

7.2.1 Spot isolation

As a first thing, the calibration of every Variance frame is carried out with the relative-gain procedure presented in section 4.2.3. After that, bright spots are isolated by sorting the pixels according to the intensity values recorded, and considering the n_B most bright ones, where n_B is equal to the number of stars expected in the field multiplied for a generic "safety" factor, that we set to 4 after some tests. This factor accounts for possible stars visible in VAR images despite being faint (above the magnitude limit that we set for the catalog query), but also for the spreading of the PSF over different pixels as well as the eventual presence of ghost images.

It happens very often that bright pixels in a certain image are arranged in small groups. In this case a further selection is necessary, in order to indicate how many real light spots are responsible for the illumination of a pixel cluster. To this end, we considered the brightest pixel of the list, we removed its eight nearest neighbors from the selection (being fainter than it), and we iterated this process to the whole image. The result is a "cleaned" map of the hot pixels, which is reported in figure 7.2.

Lastly, the definitive sub-pixel position of every spot centroid is calculated starting from the clean list of brightest pixels using the *WA* procedure introduced in section 5.2.2 and the transformation matrix of section 5.3. An example of such definitive positions are shown in the plot of figure 7.3 together with those of the expected stars in the FoV: a detailed discussion of this situation is reported in the following section.

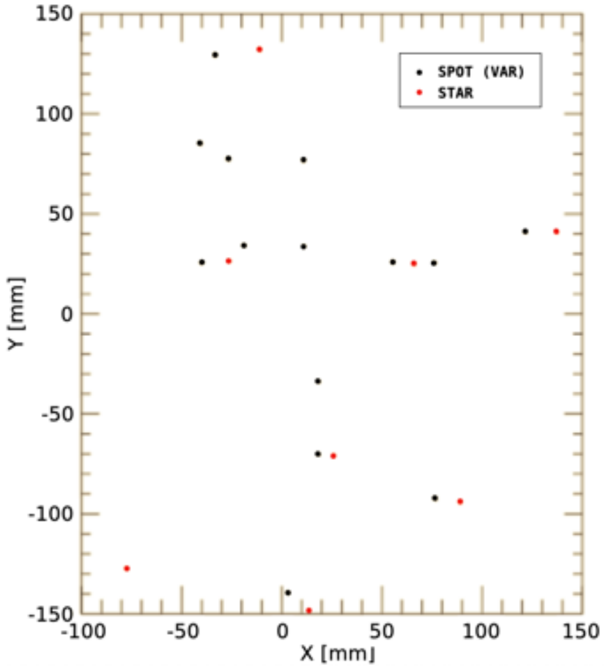

Fig. 7.3: Plot of the position of stars (*red*) and sposts (*black*) in frame 134 of run `1597`. The association is not trivial as there are both stars without spots and spots without stars, because of the situations discussed in the text.

7.2.2 Star identification

The plot of figure 7.3 demonstrates that it is not trivial to associate a VAR spot with a certain star, as there can be a long list of undesirable problems. For example, a spot may be without a nearby star if it is a ghost image, or if the related star is not in our list (e.g. too faint). Inversely, a star can be without a nearby spot for multiple reasons: a dead pixel, the effect of gaps, or again a thin cloud in that region. As a consequence, we develop a custom procedure for the association of spots and stars, so to have a better control of the process and possible errors, which is safer than relying only on a fit algorithm.

7.2.2.1 Description of the procedure

As in general the number of *spots* is larger, our procedure aims at the assignation of *stars*, using an iterative algorithm and adopting the following criterion: given a certain star, if the first spot is closer than $1/2$ the distance of the second one, then the star considered is associated to that spot. In

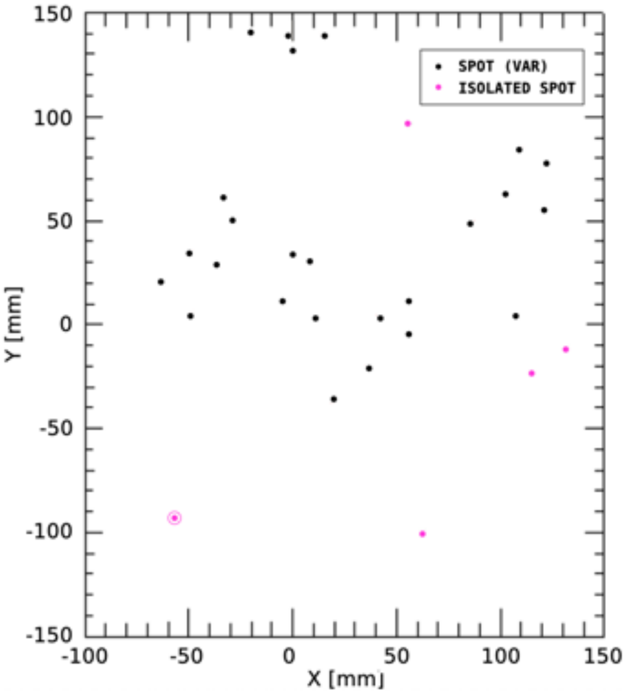

Fig. 7.4: Example of VAR spots (black), and the most isolated ones (magenta), in the case of frame 22 in run `833`, pointing at the very crowd region of the Orion's Belt (CamView). The spot with the double circle is the most isolated one, but in this case it is not adequate for the preliminary balancing of the field, as there are no isolated stars in its proximity.

case of success, both the star and the associated spot are removed from the list of objects available for subsequent iterations, and all the *other stars* are shifted of the quantity $(\Delta x, \Delta y)$ necessary to get a perfect superimposition of the examined couple, in order to facilitate the matching of the remaining ones. Of course, as in every iterative process, it is necessary to choose carefully the starting point: in the first cycle of the loop, only the 3 most *isolated* spots are considered, where the "isolation" is evaluated through the mean distance of each spot from the 5 closest to it. In this case, $(\Delta x, \Delta y)$ is given by the average shift. In figure 7.4 it is reported an example of the spot detected in a Variance frame and the "isolated" sub-set, in the case of the very crowded region of the Orion's Belt. Actually, there is a further preliminary operation that we make before the iterative routine. If the most isolated spot has a star in its proximity (i.e. the nearest star is less than half the distance of the second one), then only such spot is adopted for the first rigid shift of stars in that frame and the relative assignation. This initial *single-spot procedure* provides better "balance" of the star field

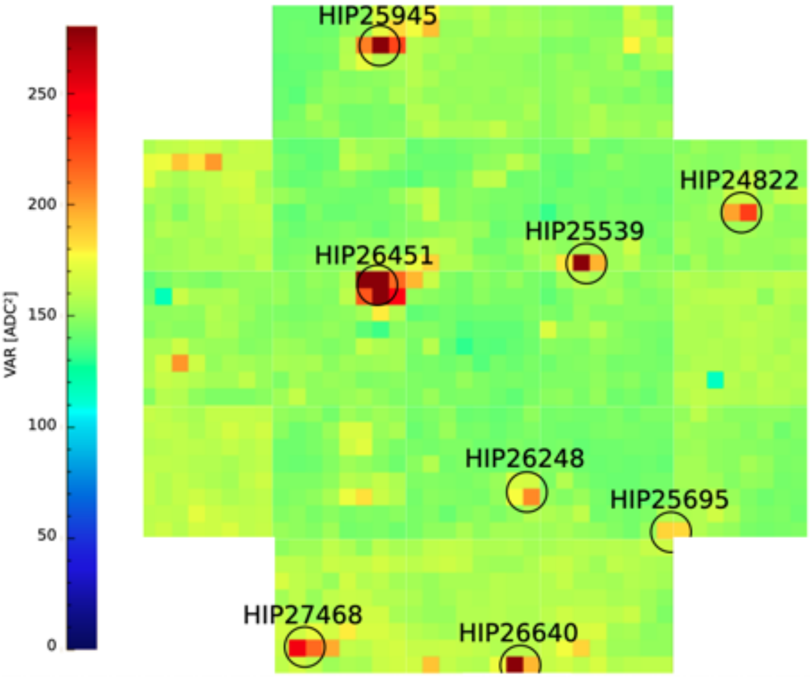

Fig. 7.5: Astrometric solution for the frame 218 in the observing run `1597`, pointing at the Crab Nebula region.

and increases the success rate of subsequent iterative assignments.

We decided to set an absolute limit in the matching procedure, which is equal to $28\,\mathrm{mm}$ ($\sim 45'$): if the distance between the expected star positions and VAR spots is larger than this amount, then the star identification routine cannot converge. When the single-spot procedure is applicable, such a limit is reduced to just $14\,\mathrm{mm}$, since moving all stars using a single isolated spot is still a risky operation. In all the other cases, the execution of the iterative routine terminates when no spots are associated to any star, and hence it is impossible to calculate the new shift.

When at least one spot is identified, the procedure returns a positive exit status and produces a plot of the Variance frame with the name of the assigned stars, similar to the one reported in figure 7.5.

We tested this procedure in both empty regions (see figure 4.7 on page 116) and very crowded stellar fields, as for example the Orion's Belt region, whose astrometric solution is reported in figure 7.7. In all the cases the software behaved as expected.

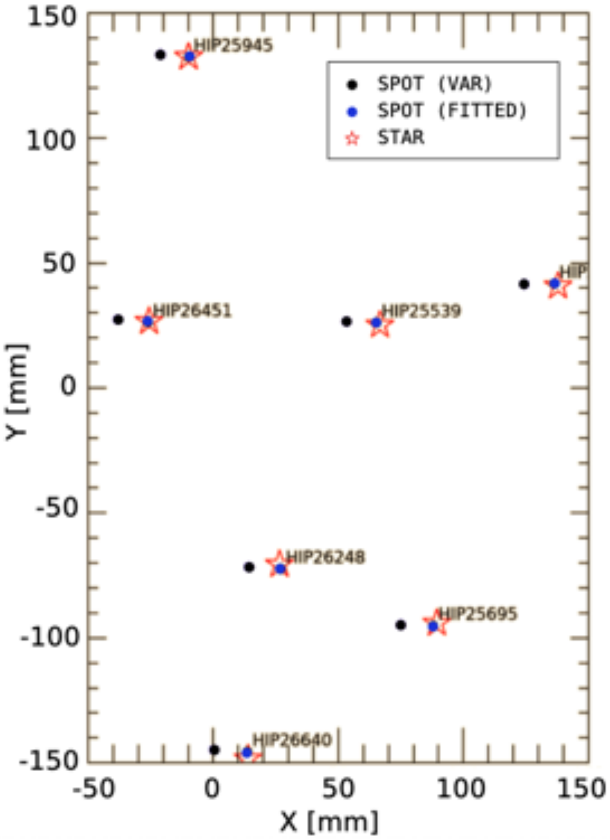

Fig. 7.6: Star identification using a free-point fit algorithm. In order to match the expected position of stars (*red*), the original arrangement of VAR spots (*black*) is transformed into the new one (*blue*) obtained with a rigid roto-translation whose parameters are extracted from the fit.

7.2.2.2 Cross-check with a fit algorithm

In the context of this thesis work, we also developed a second star-identification procedure based on a fit algorithm, both as a cross-check and for extracting further information. In particular, using the `MPFIT` procedure of the IDL library[4] we implemented a free-points function with the same approach presented in section 6.3.2.1: VAR spots can be rigidly translated and rotated so to match the arrangement of expected stars (3 free parameters). The resulting $(\Delta x, \Delta y)$ has the same meaning of the overall shift given by the custom identification procedure, but a new quantity is now accessible: the rotation angle to be considered for the perfect match. In principle, if we find a rotation angle not compatible with zero in every

---

[4] See appendix B for more details.

frame of every run, this is a strong evidence that the camera's horizontal axis is not perfectly parallel to the ground (see section 5.1.3 for a detailed discussion). We applied this routine to the archive data of the ASTRI–Horn telescope, and results are reported in the following section.

7.3 Ghost images detection

The first application of our custom astrometry procedure is to detect the possible presence of ghost images in Variance frames, due to the accidental mis-alignment of one or more mirror segments in the primary reflector. During the execution of the IDL program for the astrometric solution, a sub-routine called `V-GHOST` isolates the VAR spots not associated with bright stars and saves their position in the database of the Online Observation Quality System (OOQS [140]), for long term monitoring and analysis. In fact, if the presence of a ghost image persists, confirming that it is due to a tilted segment, then it is necessary to identify the defective mirror and consequently cover it or try to move it back to the position by design (depending on the "weight" of the mirror in the analysis of degraded modes). The automatic detection of ghost images is one of the most important tasks of the Variance images analysis, as the mirror alignment can be monitored only with the Cherenkov camera in the ASTRI design. As we can see in figure 7.7, the possibility of having multiple ghost images actually exist, and a prompt intervention is crucial for ensuring a better quality of scientific data and the full exploitation of the observing time.

7.4 Monitor the pointing direction

A very important application of our custom astrometry procedure is to monitor the pointing direction of the ASTRI telescope. In fact, using the position of the stars identified, the astronomical coordinates associated with the geometric center of the camera can be retrieved with the precision of a few arc-minutes using a *single* Variance frame. Of course, thanks to its higher angular resolution, the PMC can provide an estimation much more precise than the Cherenkov camera, but (i) it can be less accurate if the alignment of the two devices has not been properly characterized, and (ii) Variance images are immediately available during the data acquisition. In this respect, it should be noted that our astrometry procedure has been inserted into the Online Observation Quality System (OOQS) pipeline for the ASTRI MiniArray [140], while PMC data are downloaded and ana-

Fig. 7.7: An optical representation of the sky in the region of the Orion's Belt is superimposed on our astrometric solution of frame 22 in run `833` (in SkyView). Stars identified by our routine are labeled using the *white* color. Fainter objects that were excluded from the automatic procedure are colored depending on their magnitude: *yellow* for $\mathrm{mag} > 5$ and *red* for $\mathrm{mag} > 6.7$. Two objects in *green* seem to have no counterpart in the VAR image, despite they are both $\sim 5.3\,\mathrm{mag}$: this probably happens because of the central PDMs saturation, due to the presence of very bright stars. In the VAR frame it is easy to recognize the regular pattern of ghost images around the brightest stars: two spots below, one on the right, and one in the upper-left direction (consider for example the case of `HIP25281` and `HIP25930`). VAR and optical images have been matched manually to obtain this figure.

lyzed off-line. As a consequence, to monitor the pointing direction with the VAR frames is fundamental to detect in real time any possible (coarse) problem in the tracking performance of the telescope, due for example to residual errors in the pointing model or in the analysis of motor encoders[5], ensuring a prompt intervention in order not to waste precious observing time.

In the following section we present the strategy to calculate the pointing direction and the validation process of such a technique. Then we applied our procedure to the selection of ASTRI–Horn archive data presented in section 6.2, and we report the results of the subsequent analysis.

7.4.1 Strategy

Both the custom procedure for the star identification and the free-point fit algorithm provide an estimation of the rigid shift $(\Delta x, \Delta y)$ to be applied for matching spots in Variance images with the expected star field. However, this quantity does not necessarily represent the true pointing offset of the telescope, as in general it can be affected by possible errors in the reconstruction of the star field or in the analysis of the motor encoders. Consequently, to evaluate the mis-pointing error we adopted a custom strategy that relies on VAR spots only, without considering the expected (x, y) position of bright stars in the FoV. For this reason, our approach is "safer" than any fit-based procedure, and it is presented in detail in the following paragraph.

7.4.1.1 Obtaining the nominal pointing direction

Assuming a perfect alignment of the instrument, we indicate with Q the *true* pointing direction of the telescope, individuated by the astronomical coordinates associated to the camera geometric center $(0, 0)$. Considering that every VAR spot now corresponds to a bright star whose astronomical position is known, then the question is to find what is the position in the camera of the *nominal* pointing direction P. If it falls exactly in the geometric center of the camera, then $P \equiv Q$ and there is no evidence of a pointing offset. Inversely, if the position of P is not $(0, 0)$ then we can calculate the coordinates of Q using its distance from P (see section 5.1.2). The resulting $(\Delta Az, \Delta El)$ is a measure of the telescope mis-pointing. Figure 7.8 provides a graphical explanation of this procedure.

---

[5] As it happened during the observing campaign for the detection of the Crab Nebula [86], in winter 2018/2019, when a lot of data were discarded due to pointing errors.

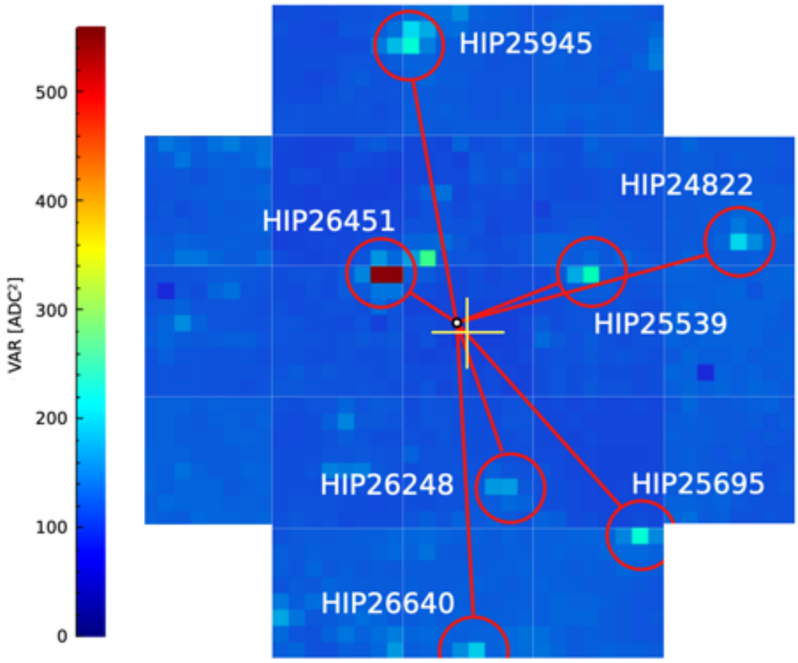

Fig. 7.8: Strategy to find the *true* pointing direction of the telescope using VAR spots (*red* circles). We know the distance (*red* segments) of each spot from the nominal pointing direction P and hence we can triangulate its position in the camera (*white* circle). If it is coincident with the geometric center of the camera (*yellow* cross) then there is no evidence of pointing error, otherwise we must measure the mis-pointing as in the case reported in this figure (frame 21 of run `1597`).

To obtain the position of P using VAR spots only, we implemented a triangulation algorithm. We consider two spots at a time, with their associated stars, and we calculate their angular distance (great circle) to the nominal pointing direction. The results are converted in mm using the plate scale and they are adopted as the radii of two circumferences, centered in the spots, whose intersection provides the position of P (see figure 7.9). This procedure is replicated with all the possible couples among the spots available in each Variance frame, obtaining a set of points, whose mean value and dispersion constitutes an estimation for the position of P and its uncertainty. An example of the output of this 'triangulation procedure through circumferences" is reported in figure 7.11.

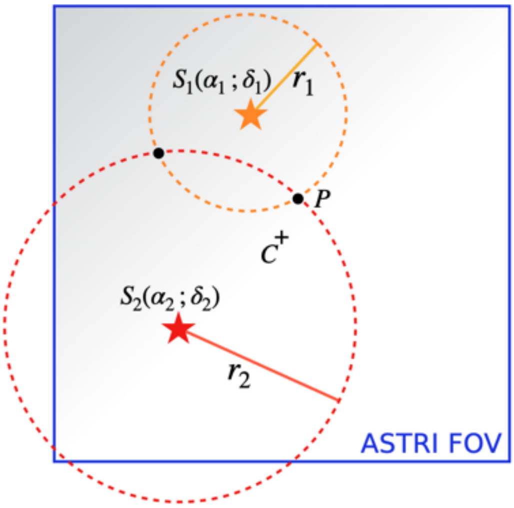

Fig. 7.9: Conceptual drawing to present the triangulation strategy using a couple of stars at a time. Among the two intersection points, to estimate the pointing P we choose the one which is closer to the camera geometric center C.

7.4.1.2 Removing outlier spots

As it is discussed in section 7.4.3, dedicated to results of the analysis, the large dispersion of triangulated points depends on the accuracy of VAR spots, and therefore on the de-convolution algorithm ultimately. We know from simulations that it retrieves the true star position with a standard deviation of $\sim 0.5\,\mathrm{mm}$: this error propagates on the triangulation method, producing an intrinsic uncertainty of a few mm in the position of P. However, having several stars in the frame (i.e. ≥ 6), it is possible to check if a certain spot is particularly far from its expected position and hence to remove such an "outlier" point from the analysis. This operation is carried out considering for each spot the measured distance from all the others in comparison to the theoretical one (using catalogs): every time that the discrepancy is greater than a chosen threshold[6] then the spot is flagged with a *"hit"* mark. Considering the resulting distribution of the *hits*, if there is a spot further than $3\,\sigma$ from the mean value then it is considered an outlier case, since its distance from the others is suspiciously high on average, probably due to the poor accuracy of its sub-pixel position reconstruction.

---

[6] Which is equal to $1\,\mathrm{mm}$ in the beginning, and increases by one unit each cycle up to $8\,\mathrm{mm}$.

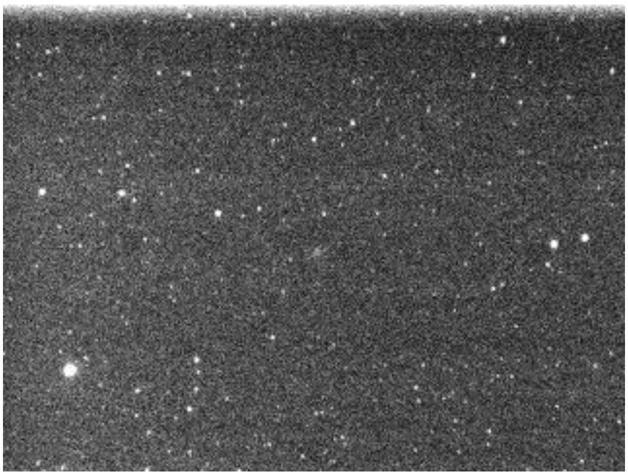

Fig. 7.10: PMC image taken at the same time of VAR frame 218 in run `1597`. The bright star in the lower-left corner is Tianguan, while in the center there is the Crab Nebula (M1) region.

7.4.2 Technique validation

Before applying our custom procedure for the monitoring of the pointing direction to the analysis of real ASTRI–Horn data, it is necessary to validate our method with dedicated tests. Instead of using a full simulation of the whole process, we adopted two independent validation cross-checks based on archive data: the application of our procedure on an ideal star field and the comparison of preliminary results with PMC images.

Using theoretical coordinates of stars taken from stellar catalogs, it is possible to test the functioning of the triangulation algorithm without being affected by the difficult evaluation of spot positions with sub-pixel precision. With this approach, we choose a pointing direction P, we calculate the position in the camera of stars in the FoV and then we use the triangulation procedure to get back the position of P in a blind way. The result of this test shows that our algorithm is able to retrieve the pointing direction with a precision of 10^{-12} arc-seconds, having in input the correct position of eight stars at least. This is undoubtedly a strong evidence that our algorithm for triangulation is reliable.

The second validation test aims at cross-checking preliminary results from Variance data with images from the PMC. In particular, we present now the interesting case of the comparison between the frame 218 in run `1597` (figure 7.5), taken on Feb 26th 2019, at `18:48:29 UTC`, with the correspondent PMC image with the same time stamp (reported in figure 7.10). The actual position of the telescope (from the header of the PMC `FITS` image

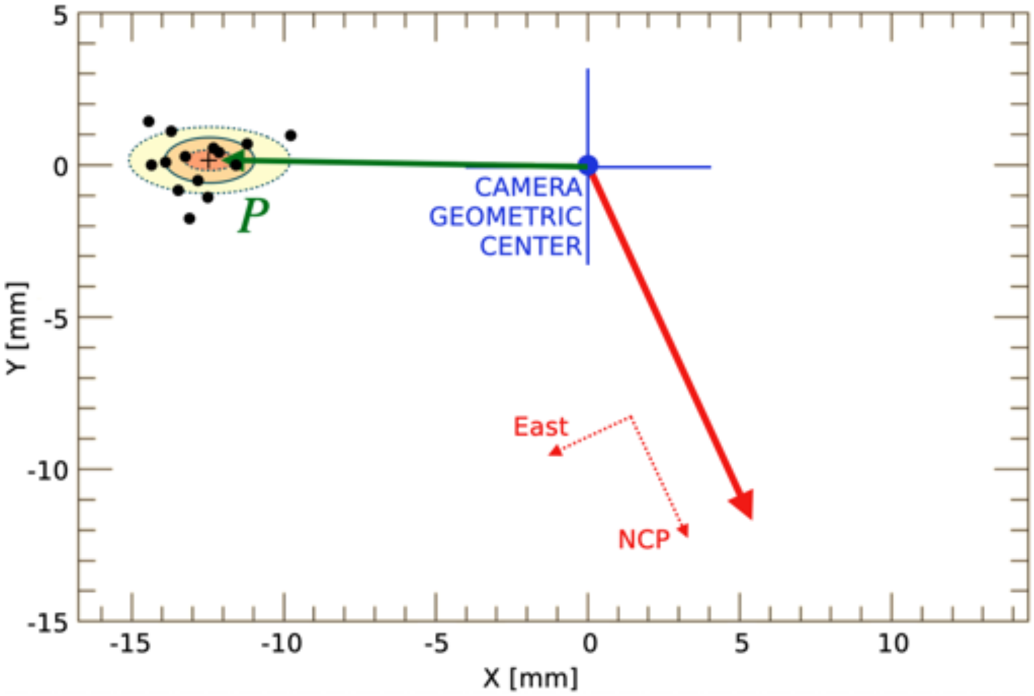

Fig. 7.11: Result of the pointing monitoring procedure in frame 218 of run `1597` (CamView), where 8 stars are available for the analysis (figure 7.5). The nominal pointing direction P (*black* cross) is obtained as the average of the triangulated positions (*black* dots) considering all the possible couples of spots, excluding eventual outliers. The mis-pointing of the telescope is obtained converting in Az, El the calculated position of P, which is $x = (-12.5 \pm 1.4)\,\mathrm{mm}$ and $y = (0.2 \pm 0.8)\,\mathrm{mm}$ (confidence levels of 0.5, 1.0 and $1.5\ \sigma$ are reported with ellipses in the plot). The *red* arrow indicates the NCP.

file) is $\alpha = 83°56'26''$, $\delta = 22°1'46''$, while the average pointing P of that observing run (taken from motor encoders) is $\alpha = 83°57'7''$, $\delta = 22°1'50''$. The distance (great circle) between these points is $\sim$39″, the typical error that we make adopting P as the reference value for the analysis of the whole run (see figure 7.1). The processing of the VAR frame with our procedure provides that the true pointing direction is $\alpha = 83°40'25''$, $\delta = 22°10'27''$ (see figure 7.11), highlighting a mis-pointing of $(17.7 \pm 2.3)\,'$. On the other hand, the astrometric solution of the PMC image (made with the software[7] *astrometry.net*) reveals that the true pointing coordinates are $\alpha = 83°40'19''$, $\delta = 22°4'6''$, i.e. about $15.8'$ far from the nominal pointing direction P. Again, this result represents an evidence that our algorithm is reliable.

---

[7] Full astrometric solution available on this web page [*link* 228].

The warning about mis-pointing raised by the VAR analysis is confirmed by the PMC image (both systems reveal that there was an error of about $0.25°$). On the other hand, they do not agree on the celestial position of their image centers: we see that there is a distance of $\sim 6.4'$ between the coordinates provided by the VAR and the PMC. This is likely due to the fact that also the PMC is not perfectly aligned with the optical axis of the telescope, similarly to what happens for the Cherenkov camera (see our demonstration summarized in section 6.4.0.1). Moreover, the offset of the PMC is different to the VAR de-centering and consequently the two systems reveal different sky coordinates at their centers. A deeper (and quantitative) discussion about this situation is presented in the following section, dedicated to results of the VAR analysis with our custom astrometry software.

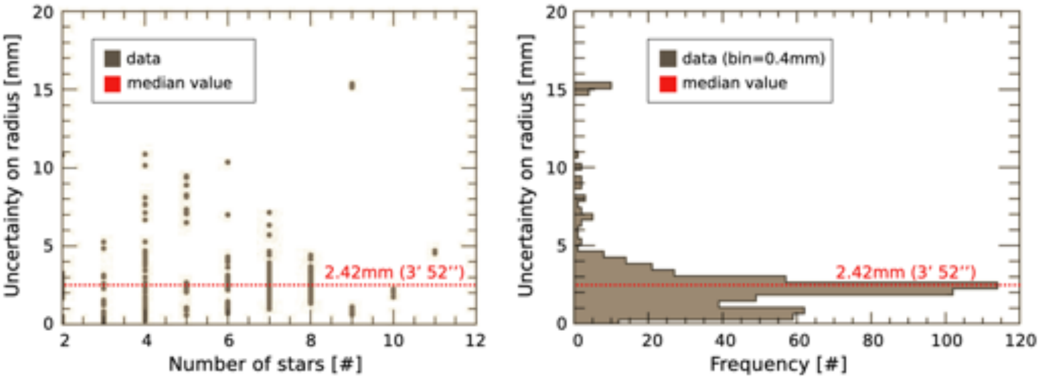

Fig. 7.12: Statistical analysis of the typical uncertainty associated to our technique, using a random sample of 603 stars from 24 different observing runs. *Left*: uncertainty versus the number of stars considered for the analysis. *Right*: histogram of the same values.

7.4.3 Results

The custom astrometry software that we developed for the ASTRI project calculates the position of the nominal pointing direction P with reference to the camera geometric center, starting from the position of the stars identified in Variance images. As it is shown in figure 7.11, the final position is calculated as the average of several points obtained with a triangulation-like algorithm that works on a couple of stars at a time, while the dispersion of such points is adopted to evaluate the uncertainty in the x and y direction (standard deviation). This technique is effective and reliable, but it presents only a coarse precision: in the case reported in figure 7.11 the square sum of the errors provides an overall uncertainty of $2'34''$, and unfortunately there are some cases where the error is even larger.

Using a high number of VAR frames from different observing runs, we investigated the properties of our technique using a statistical approach. First, considering the distribution of errors (squaring sum of δx and δy) reported in figure 7.12 *right*, we see that the median value is $3'52''$: we can hence say that the typical precision of this technique is $\sim 4'$. Second, with the plot reported in figure 7.12 *left*, we verify that there is not a strong dependency of the precision with the number of stars. Actually, this is a typical feature of the algorithm we have implemented: a single spot retrieved with poor accuracy is enough to produce a large error in a certain frame, even if several stars are available for the analysis.

Despite the large uncertainty value, the most important output of our analysis is that the position of the nominal pointing direction P is never compatible with the camera geometric center (the distance is 3 to $4\ \sigma$, or larger) and this is a strong evidence that a serious pointing problem actually affected the ASTRI–Horn prototype telescope. To investigate this possibility, we carry out a deep analysis of the observing run `1636`, which is the only *long* one ($\sim$100° FoV rotation) with a full monitoring set of PMC images. Using the software *astrometry.net*, we obtain the celestial coordinates associated to the center of every PMC image: they are reported in figure 7.13 (*black* line). The first interesting aspect is that they are *not* coincident with the pointing direction that was ordered to the telescope (*blue* dot) nor with the tracking coordinates that are reported by motor encoders (*green* line). Furthermore, the trajectory of the PMC individuates an arc in the sky, suggesting that the mis-pointing can be measured as the mean radius of curvature of that figure. However, the circle that better approximates the PMC data is not centered in the pointing direction desired for that run: there must be a de-centering offset also for the PMC, similar to the one that we detected in chapter 6 for the Cherenkov camera. In summary, if our hypothesis is correct, we are facing a pretty complex situation where the overall mis-pointing is given by the sum of two terms: a de-centering offset and a pointing error.

In the astrometry analysis of Variance frames we do not get the astronomical coordinates of the camera center[8], but rather the position of the nominal pointing direction P with respect to the origin. In the case of run `1636`, P is equal to $\alpha = 143°56'40''$ and $\delta = 21°54'42''$, and we verified that its position is never coincident with the Cherenkov camera geometric center. In particular, as it is shown in figure 7.14 (*red* dots), again the

---

[8] Even if in principle it is straightforward to obtain this value with our method.

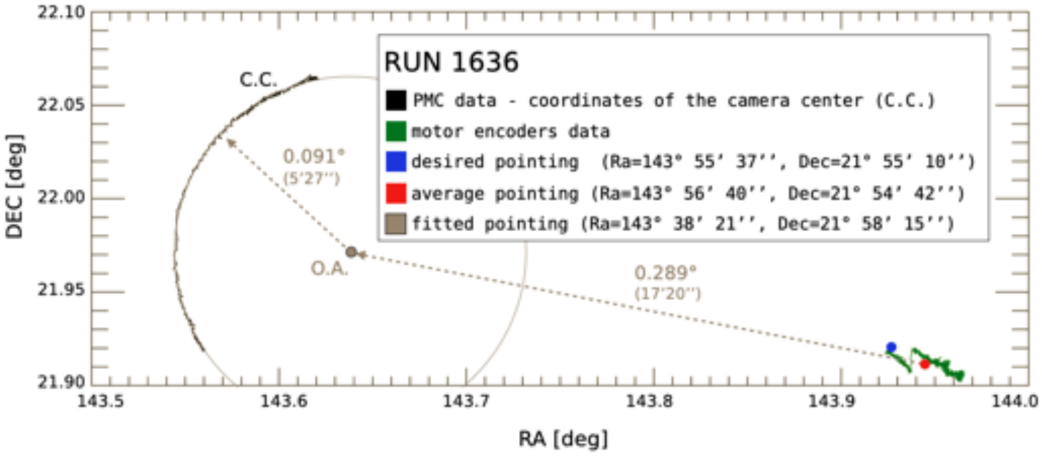

Fig. 7.13: Drift in celestial coordinates of the PMC geometric center (*black* line) during the observing run `1636`. The pointing direction set on the telescope is represented by the *blue* dot. The *green* line represents the pointing coordinates provided by the motor encoders, and the *red* dot their average value: the jump in the green line may correspond to a macroscopic correction carried out by the control software or by the telescope operator. Elements in *grey* represents raw estimations: the dot is the position of the optical axis (O.A.) obtained with a fit (solid circle) of the PMC data (black line), while dashed arrows represent the possible de-centering ($5'27''$) and pointing error ($17'20''$). An improved calculation of these quantities can be obtained applying the analysis of chapter 6 to the *stars* of the PMC (and not to the coordinates of its center).

position of P describes an arc which is not centered in the origin of the camera, but rather it seems to rotate about the position of the optical axis calculated in section 6.4. This situation confirms that the ASTRI–Horn telescope was affected in parallel by two systematic errors: a de-centering of the Cherenkov camera and an offset in the pointing. The average distance of data points from the position of the optical axis is $0.26°$ with a standard deviation of $0.02°$, which is equivalent to $15'19''$ with an uncertainty of $1'12''$, very close to the extremely raw estimation reported in figure 7.13 (*grey* arrow).

The conclusive step of this analysis is to understand what is the relative position of the Cherenkov camera and the PMC, in order to have a complete picture of their arrangement with respect to the optical axis of the telescope. To this end, we process the PMC data with the same procedure adopted for VAR frames: we calculate the position of the nominal pointing

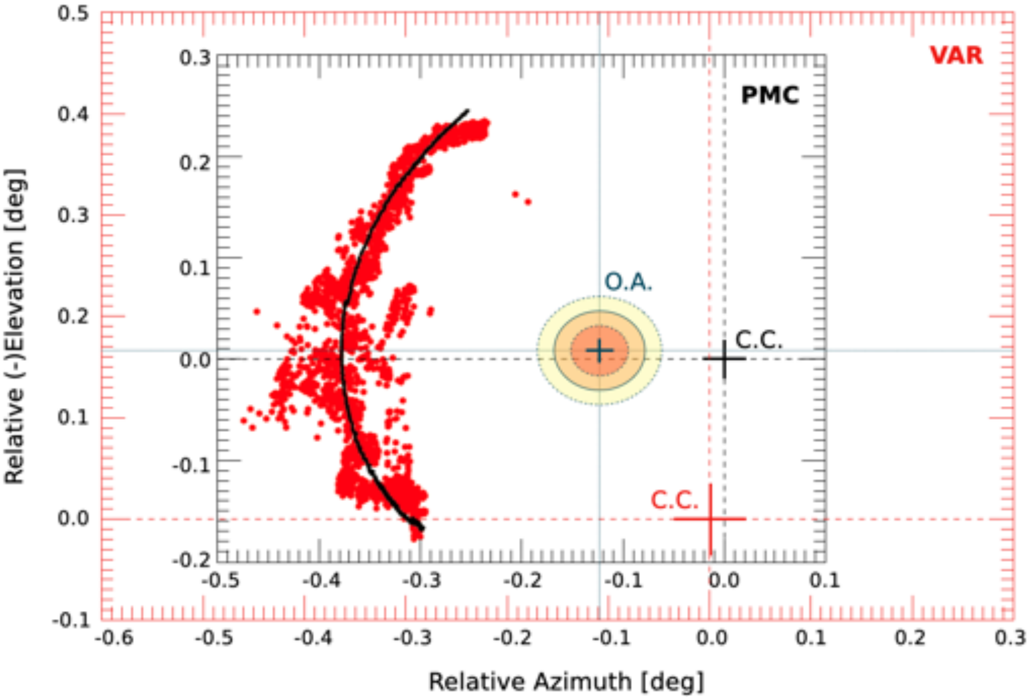

Fig. 7.14: Drift of the nominal pointing direction P with respect to the geometric center (C.C.) of the PMC (*black*) and the Cherenkov camera (*red*). The position of the optical axis (O.A.) of the ASTRI–Horn telescope is reported on the plot, using the position calculated in section 6.4 with respect to the Cherenkov camera, together with three contour lines representing the 0.5, 1.0 and 1.5 σ confidence areas. The error bars on red dots are omitted to facilitate the visualization, their value is on average $\sim 0.06°$ $(4')$.

(P) with respect to the sky coordinates associated to the camera geometric center (taken from *Astrometry.net*), using the algorithm presented in section 5.1.2 involving position angles and great circles. The result is reported in figure 7.14: there is a perfect matching between data from the VAR (*red* dots) and the PMC (*black* line), after the application of a rigid shift accounting for the offset between the two devices. The arc-like shape of the data points distribution is due to the error in the pointing, which is the same for both the VAR and the PMC, as they share the same mounting structure (the ASTRI–Horn telescope). Inversely, the mean distance from data points to the camera center is different for the VAR and the PMC, as each device has its own de-centering offset with respect to the telescope optical axis. In particular, from figure 7.14 we can estimate that the position of the Cherenkov camera relative to the PMC is $X_C = -0.02°$ and $Y_C = -0.16°$,

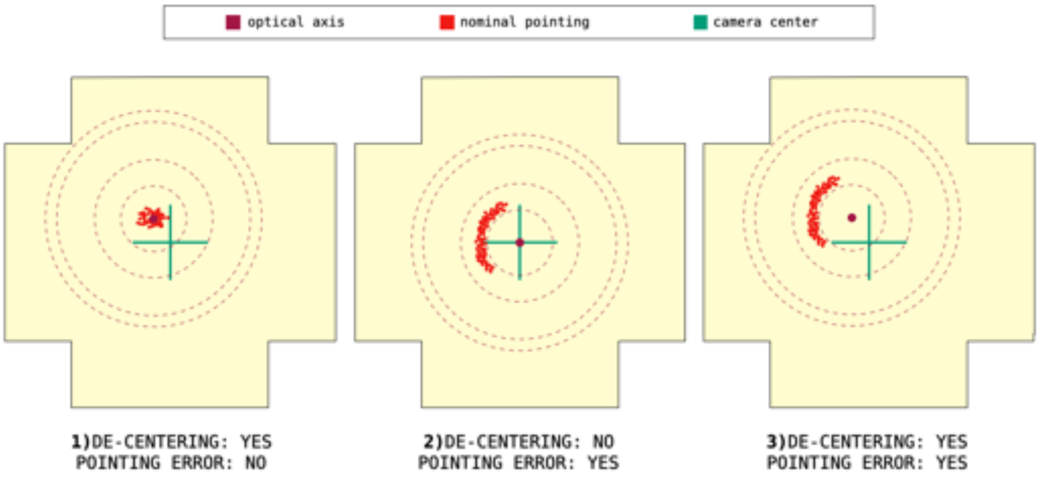

Fig. 7.15: Conceptual scheme of the effects due to the pointing and centering errors. Red dots indicate the position of the nominal pointing direction P: in an ideal configuration they are distributed around the geometric center of the camera. In the drawings reported here we can see a conceptual representation of their distribution in case of a de-centering offset (1), a pointing offset (2), or both (3). The position of the optical axis (concentric circles) is obtained using the method of the FoV rotation presented in chapter 6.

with an uncertainty smaller than that on the position of the optical axis[9] obtained in section 6.4, which is $0.06°$ (equivalent to$\sim 3.5'$). This quantity can be inserted in the pointing model of the telescope, which is made using the PMC, optimizing both the accuracy of the pointing and the precision of the tracking (in figure 7.13 the trajectory of the PMC does not individuate a perfect circle, probably because of a small drift in the tracking). A more in-depth discussion of all the results presented above is given in the next concluding section.

7.4.3.1 Discussion

Adopting our custom astrometry software using Variance images for monitoring the pointing direction of the ASTRI–Horn telescope, we discovered that such instrument was affected by an important pointing error that we revealed and measured, cross-checking our results with images taken from the PMC. In particular, we outlined that there are two sources of system-

---

[9] This value for the uncertainty constitutes only an upper limit. See the discussion at the end of section 7.4.3.1 for further details.

atic errors: a de-centering offset (previously detected with the analysis of the FoV rotation presented in chapter 6) and a pointing-offset, that we revealed also in the images of the PMC. In our analysis, which is based on the triangulation of the telescope nominal pointing direction with respect to the camera geometric center, the sum of the two mis-pointing contributions produces a peculiar arc-like shape (see figure 7.15, *right*), that we exploited for measuring the relative position of the Cherenkov camera, the PMC, and the optical axis of the telescope (i.e. the axis individuated by the action of motors), obtaining a complete characterization of their arrangement. For the first time a detailed analysis of the pointing performances is carried out on the ASTRI–Horn telescope, demonstrating that the analysis of Variance images constitutes a unique opportunity to ensure a complete calibration of the telescope. In the case of the ASTRI–Horn prototype, our results can be adopted in principle for the correction of data taken in the past, while in the context of the incoming ASTRI MiniArray observatory our procedures will be implemented for the calibration of the telescopes.

The custom technique for measuring the direction of the pointing using a single Variance frame presents only a coarse precision, about $4'$, and hence it cannot be adopted alone for the monitoring of the telescope performance, as it does not match the ASTRI requirement for the pointing *after calibration* which is equal to $20''$ (section 3.4). However, our procedure is implemented in the online observation quality system (OOQS) of the ASTRI MiniArray, as it is adopted for the detection of possible ghost images due to mirror mis-alignments (section 7.3), and consequently it can be also used to detect any macroscopic deviation of the telescope pointing in real time, that can be caused by external/occasional agents, as wind gusts, mechanical failures, software problems, and so on. This ensures a prompt intervention without losing precious observing time. Furthermore, we demonstrated that with a long acquisition our astrometry procedure can be adopted not only for monitoring the pointing direction, but also for the characterization of eventual offsets between the Cherenkov camera, the PMC, and the optical axis of the telescope, allowing a complete description of their arrangement.

The most important limitation of the technique presented in this chapter is the modest precision, ultimately due to the large pixel size of the ASTRI camera, as it is the true source of uncertainty in the determination of spot positions, and consequently in the triangulation of the pointing direction. The poor precision implies a low accuracy in the determination of the offset (X_C, Y_C) between the two cameras, which is a fundamental feature of the optical system to obtain an effective pointing model of the telescope. A possible improvement would be to apply the analysis of the FoV rotation to the images of the PMC, as previously suggested in the caption of figure 7.13, in order to obtain an independent estimation of the position of the optical axis. In fact, such a measurement would have a better precision in comparison to the Variance, as the pixel size of the PMC is only 7″ and, consequently, this information can be exploited to match the two plots reported in figure 7.14 without using the shape of the arc, affected by a larger uncertainty. With this strategy, the final error is equal to the mean of the errors reported in the two independent estimations of the optical axis position, and it would provide a more precise determination of the offset (X_C, Y_C). This approach will be adopted for the calibration of the future ASTRI MiniArray.

8

Conclusion

In this work we started from the presentation of open challenges in modern VHE astrophysics to focus in the following on possible solutions provided by the innovative ASTRI project, presenting the potentiality to play a key role in this research field thanks to the MiniArray of 9 telescopes which is currently under construction. We presented in this thesis the first complete and detailed study of a very peculiar feature of the ASTRI instrument: the Variance method. It constitutes an ancillary output of the Cherenkov camera, allowing us to monitor the night sky background and reveal the position of stars in the FoV with outstanding sensitivity for an IACT. We carried out a deep analysis of real Variance data taken with the prototype telescope ASTRI–Horn, developing on purpose powerful diagnostic tools to assess the pointing performances of such instrument, optimizing the accuracy of scientific observations. Using our techniques, we verified that ASTRI–Horn was affected by heavy systematic errors in the pointing (already known in the past) and we defined an effective strategy not only to detect and measure other similar eventual offsets in the future, but also to finely calibrate incoming instruments right from their assembly verification phases. This operation is fundamental to match the demanding ASTRI requirement for the pointing accuracy after calibration of $20''$, which is a key point to achieve the scientific objectives of the ASTRI project. In fact, while a low pointing accuracy is sufficient for technology demonstration purposes[1], in order to study the morphology of extended sources[2] or to determine the position of point-like emitters with remarkable precision, an enhanced pointing performance is a very crucial feature for next-generation telescopes. This constitutes a technological challenge for the ASTRI project, as the Cherenkov camera is not optimized for precise astrometry measurements and the compactness of the structure prevent from installing an auxiliary pointing monitoring device sharing the same optical system of the telescope. For this reason, the Pointing Monitoring Camera (PMC) with its dedicated optics is located behind the secondary mirror (on its mechanical support structure), and in this configuration important systematic errors arise if its geometric center is not well aligned with the Cherenkov camera and the optical axis of the telescope. The analysis of Variance data therefore represents a unique opportunity to avoid similar problems and finely calibrate the whole system, offering the possibility to reach the precision level required, as we demonstrated in this work.

Our astrometry techniques for Variance images were validated and tested on real archive data. They do not only constitute a numerical tool for data analysis, but also they indicate an effective calibration procedure to be implemented in the Assembly Integration Verification phases of future ASTRI telescopes. This is a fundamental aspect of this thesis work: taking advantage of the experience that we gained with archive data, we outlined a precise operational strategy that has already been inserted in the plan for the calibration of the incoming ASTRI MiniArray observatory.

A brief summary of major results regarding the analysis of ASTRI–Horn data is reported in section 8.1, while section 8.2 is dedicated to possible improvements that can be implemented in our routines. Finally, section 8.3 presents an overview of the future perspectives of this work, with particular attention to the validation tests to be carried out with the prototype telescope ASTRI–Horn and the subsequent implementation on the incoming ASTRI MiniArray.

8.1 Review of main results

Using specific techniques that we developed for the gain calibration of Variance images and their astrometric evaluation, in this work we carried

---

[1] See the *alpha-plot* reported in figure 2.15 on page 48, relative to the first detection of the Crab Nebula with the ASTRI–Horn telescope.

[2] See for example figure 2.16 on page 49.

out a characterization of pointing performances of the ASTRI–Horn prototype telescope, using archive data only[3]. As a result of this study, we detected and measured a de-centering offset of the Cherenkov camera with respect to the optical axis of the telescope. The measured shift is equal to

$$X_0 = (-4.1 \pm 1.7)\,\mathrm{mm}, \;\; Y_0 = (6.2 \pm 1.5)\,\mathrm{mm}\,, \tag{8.1}$$

in camera coordinates units (pixel size $7\,\mathrm{mm} \times 7\,\mathrm{mm}$), equivalent to a sky-projected angular distance of $(0.19 \pm 0.06)°$.
In addition to such a mechanical offset, we also revealed that ASTRI–Horn was affected by an error in the pointing, that we detected and measured using the observing run `1636` as a study-case, as it is the only *long* one in the archive with a full set of PMC images available for cross-checking our results[4]. Using Variance data we calculated that the average pointing offset in this run is

$$\Delta_P = (0.26 \pm 0.02)°\,, \tag{8.2}$$

and PMC images provide a similar results (within 2 σ).
The value reported in (8.1) could be adopted in principle for the correction of data taken in the past with ASTRI–Horn, improving the accuracy of the system, while the analysis that led us to the value in (8.2) can be replicated on other long observing runs, characterizing the average pointing offset in each of them. However, their uncertainties still do *not* allow us to match the ASTRI pointing requirement of $20''$, being equal respectively to $3'36''$ and $1'12''$. For this reason, despite these results are undoubtedly useful and interesting, we developed an improved strategy to enhance their precision when the telescope will be available again to take new data.
With a full numerical simulation of an observing run with our telescope, we demonstrated that the position of the optical axis with respect to the Cherenkov camera geometric center can be measured with the precision of $\sim$$20''$ using a dedicated observation with the telescope in staring mode pointing at the NCP for $\sim$$6\,\mathrm{h}$ and $40\,\mathrm{min}$. In this time interval the same analysis can be carried out in parallel also with the PMC, obtaining a measurement in its reference system with a better precision, as the pixel size is almost 100 times smaller. Matching these results it is possible to measure the offset between the two cameras, and hence the pointing performances can be safely monitored using the PMC, taking advantage of its better resolution. In this scenario the Variance ensures the alignment of the

---

[3] As it was impossible to take new data, because the telescope was under maintenance in the last two years.

[4] This is one of the last observing run taken with ASTRI–Horn in the observing campaign for the Crab detection.

Cherenkov camera to the PMC, which is adopted in turns to monitor the pointing of the telescope without systematic errors down to the accuracy level required. During long observations in tracking mode the alignment of the devices can be constantly monitored using the same procedure presented above. Meanwhile, our custom astrometry routine can be adopted for monitoring the presence of eventual ghost images in Variance frames, due to tilted segments in the primary mirror. Moreover, as this analysis is performed *online* during regular data taking, the same routine is in charge of producing quick alerts in real-time if a macroscopic pointing error is generated by occasional/external agents, e.g. strong wind gusts, mechanical failures, software anomalies, and so on, allowing a prompt intervention by the telescope operator without wasting precious observing time.

8.2 Further improvements

In order to further characterize the properties of our astrometry technique, an interesting additional tool would be a full toy simulation of the whole VAR data acquisition and reduction process. This would allow us us to evaluate the best precision that our method can provide in terms of triangulation of the nominal pointing direction in ideal observing conditions. The toy simulation developed for the analysis of the FoV rotation showed that the large pixel size limits the precision of such a technique even in the case of optimal observing conditions. We expect that a similar effect arises also in the case of the astrometry analysis, but it is reasonable to suppose that an improvement with respect to the uncertainty reported in (8.2) can be achieved (for example assuming a perfect flat-field calibration in the images). Actually, we know well that the pixel equalization of Variance is a crucial aspect for our analyses and, in fact, we took part in the realization of a hardware tool dedicated to this purpose: a rigid shell with a photo-luminescent film to be occasionally inserted inside the camera lids for the gain calibration of pixels. Such a device has already been realized and currently it is just waiting to be tested on the ASTRI–Horn telescope. It will surely introduce remarkable improvements in the image calibration and cleaning, enhancing the accuracy of all the subsequent analyses. Several other validation tests are waiting to be carried out at the astrophysical station of Serra La Nave, especially regarding the Variance. Unfortunately, due to the COVID-19 pandemic and other accidental events, the maintenance operations on the ASTRI–Horn telescope lasted for more than 2 years, and they are still in progress now (December 2021). As a consequence of this, all the procedures reported in this thesis still need to be validated (and their accuracy stated) with new experimental data taken on purpose. It is reasonable to assume that only such dedicated tests in the near future will provide or suggest the most important further improvements, as often happens in experimental activities.

8.3 Future perspectives

At the time we are finalizing this thesis (December 2021) the ASTRI–Horn telescope is expected to be ready again for observations before spring 2022, after a long period of important maintenance operations. After the validation of the structure and the camera, an important amount of time will be reserved to test our procedures with the Variance, following a specific test plan that we elaborated. Observations will be mainly dedicated to the North Celestial Pole region and the celestial equator at the local meridian, but we proposed and obtained time to perform also additional tests relative to other tasks not presented in this document, as the measure of stellar magnitudes, the monitoring of satellites and meteors, and the relative measurement of the telescope optical throughput.

After the validation test period with ASTRI–Horn, and the subsequent data analysis, the optimized version of our calibration procedures will be implemented in the pipeline of the ASTRI MiniArray, which is already in an advanced stage of development. Our calibration procedures have already been inserted in both the plan for the Assembly Integration Verification and the Online Observation Quality System, that will be constantly running during regular data taking. Other additional procedures that we are developing still need to be optimized and implemented, as for example the automated routine for the alignment of mirror segments, or the deployment of the *AstriTool* Python package, a unified framework for different calibration activities.

The work presented in this document will be of paramount importance for the ASTRI telescopes of the MiniArray, allowing them to point and track any celestial source with sufficient accuracy for new scientific discoveries. In conclusion of this thesis, we can undoubtedly affirm that achieving such an objective currently constitutes the most important future perspective of our work.

Appendix

A

Measurements on the mirrors

During the doctoral period, my work for the ASTRI project was mainly focused on the pointing calibration using the Variance method, as it is reported in the chapters of this document. However, I took part in several side activities regarding especially the properties of the mirror and their measurement. In particular, I helped in the characterization of the reflectivity and the actual focal length, as it is reported very briefly in the following sections. Moreover, I was involved in the development of an automated routine in Python for the alignment of primary mirror segments, moving the actuators in order to obtain a composition of the PSF as close as possible to the design. This activity is still in progress and the resulting procedure will be tested first on a prototype telescope[1], and then on the MiniArray in Tenerife.

A.1 Reflectivity

The ASTRI telescope operates outdoors without a dome, and its mirrors are constantly exposed to bad weather condition as well as to the atmosphere in proximity of the sea and a volcanic environment, which is very

---

[1] Probably at EIE Group s.r.l. [*link* 239], which is in charge of the construction of the mechanical structure.

hostile to mirrors. For this reason, the coatings must be optimized not only to satisfy requirements for reflectivity, but also to last in time. To this end, several solutions were considered in the past, including both traditional Al coatings and more advanced multi-layer of Al, SiO_2 and ZrO_2. At the facility of Zaot s.r.l. in Italy, we participated in a measurement campaign with a portable spectro-photometer to acquire new data about the reflectivity of the ASTRI secondary mirrors, and to characterize the presence of halos and micro-holes in the surface coatings[2]. We are still elaborating the results of such measurements: they will determine the final solution to be adopted for the the mirrors of the incoming ASTRI MiniArray.

A.2 Focal length

During the doctoral period I partecipated in the measurement campaign of the actual focal length of primary mirror segments of MST telescopes for CTA (see section 2.3.4.2). Such mirrors present a hexagonal shape and their curvature profile is spherical, hence their focal length f is half their curvature radius R, $f = R/2$. Consequently, using a point-like light source in the position $p = R$, the image is focused at a distance q which is also equal to R, as a result of the well-known equation

$$\frac{1}{f} = \frac{1}{p} + \frac{1}{q}\,. \tag{A.1}$$

This situation offers the chance to measure the actual curvature radius of each mirror segment using the so-called "$2f$" configuration[3]. A point-like source oriented towards the mirror translates along the optical axis of the system together with a CCD camera recording the image of focused light. Scanning different distances from the mirror, the size of the light spot varies in diameter (D_{80}). Fitting data points with a second-order polynomial it is possible to identify the true distance associated to the minimum spot size (the *waist* of the beam): this distance is equal to the actual radius of curvature ($R = 2f$) of the mirror under study, that can be compared with the nominal value by design ($\sim 33\,\mathrm{m}$). In figure A.1 it is reported a picture of two facilities adopted for the measuring campaign, while results are presented in a dedicated paper in preparation [211].

---

[2] For an image of the M2 mirror see figure 3.7 on page 79, where it is shown the substrate of Pilkington glass ($18\,\mathrm{mm}$ thick, manufactured by Flabeg s.r.l.) with nine pads glued on the back to host the actuators.

[3] This strategy cannot be applied on ASTRI mirrors as they are *aspheric*.

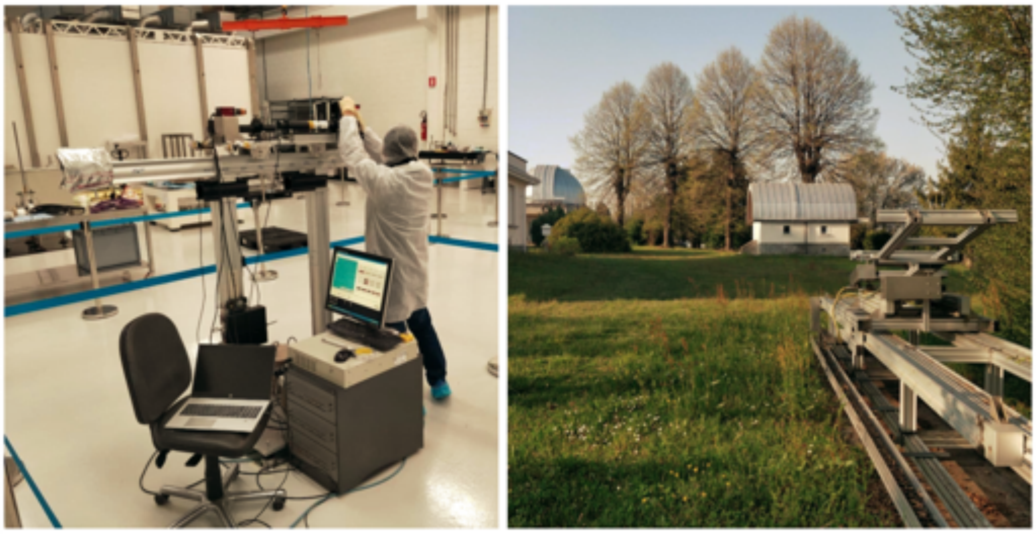

Fig. A.1: Facilities for measuring the focal length of spherical mirrors in the "$2f$" configuration. *Right*: outdoor facility at the INAF-Osservatorio Astronomico di Brera (Merate), Italy. The mirror is placed in vertical position on the moving support (foreground in picture), while the light source and the CCD are located in the white dome in front of the trees. *Left*: indoor facility at Media Lario s.r.l. (Bosisio Parini), Italy. The operator is adjusting the mount of the camera and the light source, while the mirror is on the right, at the end of a corridor.

B

Software details

All the programs that we produced for this thesis are coded in IDL[1] v8.7.1, using the workbench of the IDL's Interactive Development Environment (IDE). In particular, for astronomical calculations we made an extensive use of the IDL Astronomy User's Library ([212], [*link* 251]), while for image analysis we often adopted the interactive display tool for astronomical images ATV [*link* 252].

The fit procedures presented in this thesis are carried out using the the non-linear fitting routines included in the MPFIT Markwardt-IDL Library ([213], [*link* 254]), which implements the Levenberg–Marquardt optimisation algorithm [214, 215, 216] applied to chi-square minimisation.

We adopted the Python language [*link* 268] using the PyCharm IDE [*link* 269] for special routines dedicated to specific tasks, for example to handle the Application Programming Interface (API) from Astrometry.net or to store information in Google Spreadsheets (also managed using the Google Script programming language [*link* 242]).

To access the ASTRI database we used a MySQL query [*link* 263] from the command line. The complete list of the Code Listings reported in this thesis is available on page 251.

---

[1] IDL – Interactive Data Language, Harris Geospatial Solutions [*link* 253].

B.1 Public repository and data access

The software that I developed for my doctoral project is freely available in a public git repository. The repository may be accessed at the following web address:

https://ict.inaf.it/gitlab/simone.iovenitti

The original raw data used for my doctoral work, as well as the intermediate and final elaborated stages, are proprietary, and belong to the ASTRI Project (of which I am part). External scientists interested in analyzing such data may request to access them sending an email to the ASTRI Principal Investigator contact address [*link* 227].

C

Outreach activities

During the doctoral period, I devoted a huge amount of my spare time to outreach activities. Only a small part of this “side job” is on behalf of the ASTRI project but, as it is deeply related to physics and astronomy, I think it is important anyway to mention this work here. Furthermore, outreach activities belong to the so-called “third mission” of universities, and researchers with a natural inclination should be encouraged to give their help, following precise guidelines. For this reason, it seems natural to me to dedicate an appendix of my doctoral thesis to the work carried out in both outreach and education, also because I strongly believe that it is important for my professional career in both science and communication. The following sections report only those activities related to the ASTRI project or VHE astrophysics in general, however several other scientific initiatives for both schools and the general public were realized in the last three years with the help of the cultural association *PhysicalPub* [*link* 267], of which I am honored to be the president now.

C.1 ASTRI graphic materials and social media

All the slide presentations on behalf of the ASTRI project must adopt a unique template, for both internal meetings and conferences or symposiums, in order to guarantee the uniformity of the layout and the correct

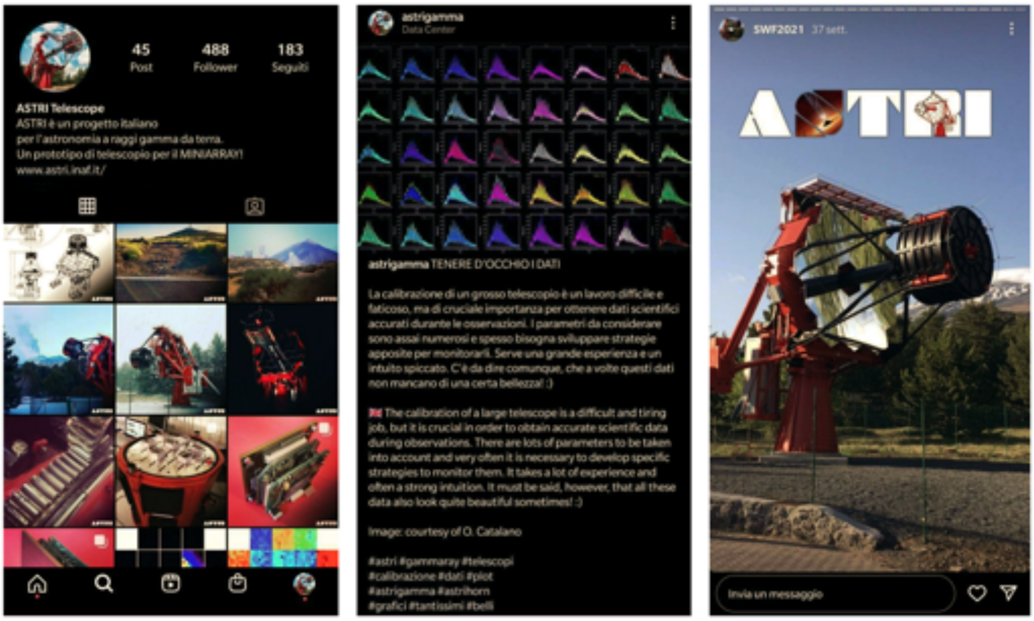

ASTRI Telescope
ASTRI è un progetto italiano
per l'astronomia a raggi gamma da terra.
Un prototipo di telescopio per il MINIARRAY!
www.astri.inaf.it/

astrigamma TENERE D'OCCHIO I DATI

La calibrazione di un grosso telescopio è un lavoro difficile e faticoso, ma di cruciale importanza per ottenere dati scientifici accurati durante le osservazioni. I parametri da considerare sono assai numerosi e spesso bisogna sviluppare strategie apposite per monitorarli. Serve una grande esperienza e un intuito spiccato. C'è da dire comunque, che a volte questi dati non mancano di una certa bellezza! :)

The calibration of a large telescope is a difficult and tiring job, but it is crucial in order to obtain accurate scientific data during observations. There are lots of parameters to be taken into account and very often it is necessary to develop specific strategies to monitor them. It takes a lot of experience and often a strong intuition. It must be said, however, that all these data also look quite beautiful sometimes! :)

Image: courtesy of O. Catalano

#astri #gammaray #telescopi
#calibrazione #dati #plot
#astrigamma #astrihorn
#grafici #tantissimi #belli

Fig. C.1: The account of the ASTRI project on the Instagram platform. The homepage with the *feed* (left), an example of *post* format (center), and a static *story* (right).

figuration of all the institutions involved in the collaboration. To this end, a few members of the project end I elaborated a dedicated layout for Microsoft PowerPoint and Apple Keynote [*link* 223], in both 4:3 and 16:9 formats, that were circulated among the projects mailing lists and uploaded in the official repository.

For the participation to scientific festivals and fairs we usually produce little gadgets of the ASTRI project, with its name and logo, to be distributed free to the public. I designed a re-styled version of the ASTRI logo for the realization of custom stickers that were printed in occasion of festivals in Genova (Italy, 2021) and Castellaro Lagusella (Italy, 2021), obtaining a large appreciation from the public.

Lastly, in the last year and a half I was in charge of the management of the social media account of the ASTRI project on the Instagram platform [*link* 226]. The page already existed but was completely blank. Due to the characteristics of that social network I proposed a unified format for the posts: squared images, with the logo and a black shadowing in the lower right corner, and a short description in both Italian and English, with capital title (see figure C.1). The content was diverse: from technical features to very general astrophysics topics of interest. All the posts are prepared and then archived in a dedicated repository online: the P.I. and the INAF su-

Fig. C.2: Cover image of the national exhibition "A che Punto è la NOTTE", where the ASTRI project participated with a picture of the prototype telescope and a 3D model of the MiniArray. More details can be found in the *Overview* presentation of the initiative [*link* 262].

pervisor of outreach activities for ASTRI and CTA always review the post before the publication. The synergy with other social networks (in particular Facebook, Twitter and YouTube) was proposed but only partially implemented so far due to a long and slow process for approval.

C.2 Scientific exhibition of astro-photography

Despite difficulties due to the COVID-19 pandemic, in September 2020 the cultural association PhysicalPub realized the largest scientific exhibition of astro-photography ever made in Italy [*link* 262, 261, 260], the name of the project is 'À che Punto è la NOTTE" (*What is left of the NIGHT?*). The selection of pictures was divided in three areas: night landscape, deep sky and instrumentation. The ASTRI project participated in the exposition with a picture of ASTRI–Horn and a 3D model of the incoming MiniArray. Other IACT facilities participated in this initiative, like MAGIC or CTA (see section 2.3), and several research institutes gave their support: the University of Milan [*link* 276], INAF [*link* 255], ESO [*link* 240] and oth-

Fig. C.3: Cover image of the conference "Una costellazione di ASTRI per lo studio del Cosmo - I nuovi occhi Cherenkov dell'astronomia gamma" (A constellation of ASTRI to study the Cosmos - New Cherenkov eyes for gamma-ray astronomy), which is my public talk in permanent evolution about technology and science of the ASTRI project.

ers[1]. The main goal of the project was not just the exhibition of beautiful pictures, but rather the dissemination of their scientific content using the free audio guide developed on purpose [*link* 260], thematic conferences, webinars and guided tours [*link* 261]. After the first exhibition in Milan, this project was replicated in the festival of science in Genova (2020, Italy) and Bergamo (2021, Italy). Moreover, this project was discussed in the Outreach Session of the CTA Meeting in 2020, and it was presented with an oral contribution to the International Cosmic Ray Conference[2] (ICRC) in 2021.

C.3 Public talks and conferences

I prepared a scientific conference for the general public on topics of both astrophysics and technology related to the ASTRI project (see figure C.3).

---

[1] See figure C.2 for a complete list of sponsors and partners, while the full list of participants can be found here [*link* 262].

[2] See the web-poster on page 257, while the reference to the proceeding article is reported in the publication list on page 253.

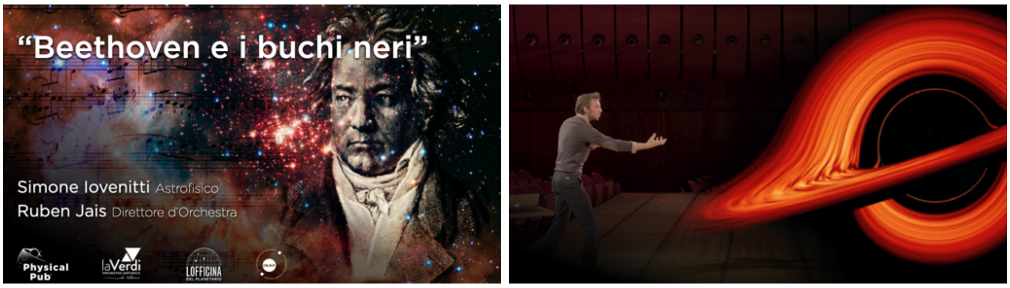

Fig. C.4: Music and astrophysics: the symphonic concert “Beethoven and black holes”. *Left*: cover page of the presentation. *Right*: a stop-frame of the movie released online [*link* 272].

The English translation of the title is “A constellation of ASTRI to study the Cosmos - New Cherenkov eyes for gamma-ray astronomy” and in the last year this conference was replicated at the Planetarium of Milan, at the Merateneo Festival (LC, Italy) and at the Science Web Festival (online), achieving good success overall.

Every year, I deliver in general a high number of public talks ($\sim$40) to both school groups and the general public, focusing on astronomy or astrophysics related topics. In particular, an interesting and innovative event regarding the VHE astrophysics was the symphonic concert “Beethoven and Black Holes” (see figure C.4), that I realized together with the Symphonic Orchestra of Milan G.Verdi, conducted by maestro Ruben Jais. In this initiative some peculiar aspects of compact objects were presented in analogy to specific features of the Fifth Symphony by Beethoven: I introduced the scientific content with talks and images, then the conductor explained the music part, afterwards the orchestra played the relative movement of the component. A similar concert was never realized in Italy before, and the full performance is still available online on demand, free of charge [*link* 272].

Bibliography

[1] V. F. Hess, “über Beobachtungen der durchdringenden Strahlung bei sieben Freiballonfahrten,” *Phys. Z.*, vol. 13, pp. 1084–1091, 1912. [Cit. on page 1]

[2] R. A. Millikan and G. H. Cameron, “High Frequency Rays of Cosmic Origin III. Measurements in Snow-Fed Lakes at High Altitudes,” *Physical Review*, vol. 28, pp. 851–868, Nov. 1926. [Cit. on page 1]

[3] D. J. B. et al., “Detection of a Cosmic Ray with Measured Energy Well Beyond the Expected Spectral Cutoff due to Cosmic Microwave Radiation,” *The Astrophysical Journal*, vol. 441, p. 144, Mar. 1995. [Cit. on pages 1 and 5]

[4] I. B. Zeldovich, A. A. Ruzmaikin, and D. D. Sokolov, “Magnetic fields in astrophysics,” *New York*, vol. 3, p. 381, Jan. 1983. [Cit. on page 2]

[5] A. M. Hillas, “Evolution of ground-based gamma-ray astronomy from the early days to the Cherenkov Telescope Arrays,” *Astroparticle Physics*, vol. 43, pp. 19–43, Mar. 2013. [Cit. on pages 2, 19, 32, 47, 48, 50, and 55]

[6] J. W. Cronin, T. K. Gaisser, and S. P. Swordy, “Cosmic Rays at the Energy Frontier,” *Scientific American*, vol. 276, pp. 44–49, Jan. 1997. [Cit. on page 3]

[7] M. Vietri, *Foundations of High-Energy Astrophysics*. Theoretical Astrophysics, Chicago: University of Chicago Press, 2008. [Cit. on pages 3, 6, and 7]

[8] R. Aloisio, E. Coccia, and F. Vissani, eds., *Multiple Messengers and Challenges in Astroparticle Physics*. Cham: Springer International Publishing, 2018. [Cit. on page 3]

[9] W. D. Apel, J. C. Arteaga, A. F. Badea, *et al.*, "Energy spectra of elemental groups of cosmic rays: Update on the KASCADE unfolding analysis," *Astroparticle Physics*, vol. 31, pp. 86–91, Mar. 2009. [Cit. on page 3]

[10] ARGO-YBJ Collaboration, LHAASO Collaboration, B. Bartoli, *et al.*, "Knee of the cosmic hydrogen and helium spectrum below 1 PeV measured by ARGO-YBJ and a Cherenkov telescope of LHAASO," *Physical Review D*, vol. 92, p. 092005, Nov. 2015. [Cit. on page 4]

[11] A. R. Bell, "Cosmic ray acceleration in pulsar-driven supernova remnants," *Monthly Notices of the Royal Astronomical Society*, vol. 257, pp. 493–500, Aug. 1992. [Cit. on page 4]

[12] K.-H. Kampert and P. Tinyakov, "Cosmic rays from the ankle to the cutoff," *Comptes Rendus Physique*, vol. 15, pp. 318–328, Apr. 2014. [Cit. on page 5]

[13] G. T. Zatsepin and V. A. Kuz'min, "Upper Limit of the Spectrum of Cosmic Rays," *ZhETF Pisma Redaktsiiu*, vol. 4, p. 114, Aug. 1966. [Cit. on page 5]

[14] K. Greisen, "End to the Cosmic-Ray Spectrum?," *Physical Review Letters*, vol. 16, pp. 748–750, Apr. 1966. [Cit. on page 5]

[15] E. Fermi, "On the Origin of the Cosmic Radiation," *Physical Review*, vol. 75, pp. 1169–1174, Apr. 1949. [Cit. on page 6]

[16] A. R. Bell, "The acceleration of cosmic rays in shock fronts – I," *Monthly Notices of the Royal Astronomical Society*, vol. 182, pp. 147–156, Feb. 1978. [Cit. on page 7]

[17] A. Balogh and R. A. Treumann, *Physics of Collisionless Shocks: Space Plasma Shock Waves*. Springer Science & Business Media, Jan. 2013. [Cit. on page 7]

[18] R. V. Lobato, J. G. Coelho, and M. Malheiro, "Ultra-high energy cosmic rays from white dwarf pulsars and the Hillas criterion," *Journal of Physics: Conference Series*, vol. 861, p. 012005, June 2017. [Cit. on page 8]

[19] M. Bustamante, G. D. C. Montoya, W. de Paula, *et al.*, "High-energy cosmic-ray acceleration," Mar. 2009. [Cit. on page 8]

[20] R. Aloisio, "Acceleration and propagation of ultra high energy cosmic rays," *Progress of Theoretical and Experimental Physics*, vol. 2017, July 2017. [Cit. on page 8]

[21] A. Hillas, "The Origin of Ultra-High-Energy Cosmic Rays," *Annual Review of Astronomy and Astrophysics*, vol. 22, pp. 425–444, Nov. 2003. [Cit. on page 8]

[22] K.-H. Kampert, "Puzzling hot spots in the cosmic-ray sky," *Physics*, vol. 1, p. 37, Nov. 2008. [Cit. on page 9]

[23] E. Fiandrini, "Fisica dei Raggi Cosmici," 2017. [Cit. on page 9]

[24] Z. Cao, F. A. Aharonian, Q. An, *et al.*, "Ultrahigh-energy photons up to 1.4 petaelectronvolts from 12 γ-ray Galactic sources," *Nature*, vol. 594, pp. 33–36, June 2021. [Cit. on pages 9, 22, and 74]

[25] G. B. Rybicki and A. P. Lightman, *Radiative Processes in Astrophysics*. June 1986. [Cit. on page 10]

[26] F. A. Aharonian, *Very High Energy Cosmic Gamma Radiation : A Crucial Window on the Extreme Universe*. World Scientific Publishing Co. Pte. Ltd, Jan. 2004. [Cit. on page 10]

[27] K. S. Krane, *Introductory Nuclear Physics*. Wiley, Nov. 1987. [Cit. on page 12]

[28] Particle Data Group, P. A. Zyla, R. M. Barnett, *et al.*, "Review of Particle Physics," *Progress of Theoretical and Experimental Physics*, vol. 2020, p. 083C01, Aug. 2020. [Cit. on page 12]

[29] A. J. Dean, D. J. Clark, J. B. Stephen, *et al.*, "Polarized Gamma-Ray Emission from the Crab," *Science*, vol. 321, pp. 1183–1185, Aug. 2008. [Cit. on page 12]

[30] M. S. Longair, *High Energy Astrophysics*. Cambridge: Cambridge University Press, third ed., 2011. [Cit. on pages 12, 34, and 39]

[31] E. Aliu, H. Anderhub, L. A. Antonelli, *et al.*, "Observation of Pulsed γ-Rays Above 25 GeV from the Crab Pulsar with MAGIC," *Science*, vol. 322, pp. 1221–1224, Nov. 2008. [Cit. on pages 13 and 17]

[32] V. L. Ginzburg and S. I. Syrovatskii, *The Origin of Cosmic Rays*. Jan. 1964. [Cit. on page 13]

[33] R. L. Coto, *Very-High-Energy Gamma-ray Observations of Pulsar Wind Nebulae and Cataclysmic Variable Stars with MAGIC and Development of Trigger Systems for IACTs*. Springer Theses, Springer International Publishing, 2017. [Cit. on page 14]

[34] A. Cooray, "Extragalactic Background Light: Measurements and Applications," *arXiv:1602.03512 [astro-ph]*, Feb. 2016. [Cit. on page 15]

[35] G. T. Jones, "Positron annihilation in flight," *Physics Education*, vol. 34, pp. 276–286, Sept. 1999. [Cit. on page 16]

[36] S. P. Reynolds, "Supernova remnants at high energy.," *Annual Review of Astronomy and Astrophysics*, vol. 46, pp. 89–126, Sept. 2008. [Cit. on page 17]

[37] K. Koyama, R. Petre, E. V. Gotthelf, *et al.*, "Evidence for shock acceleration of high-energy electrons in the supernova remnant SN1006," *Nature*, vol. 378, pp. 255–258, Nov. 1995. [Cit. on page 17]

[38] The LHAASO Collaboration*†, Z. Cao, F. Aharonian, *et al.*, "Peta–electron volt gamma-ray emission from the Crab Nebula," *Science*, vol. 373, pp. 425–430, July 2021. [Cit. on pages 17 and 22]

[39] S. Ansoldi, L. A. Antonelli, P. Antoranz, *et al.*, "Teraelectronvolt pulsed emission from the Crab Pulsar detected by MAGIC," *Astronomy & Astrophysics*, vol. 585, p. A133, Jan. 2016. [Cit. on page 17]

[40] B. M. Gaensler and P. O. Slane, "The Evolution and Structure of Pulsar Wind Nebulae," *Annual Review of Astronomy and Astrophysics*, vol. 44, pp. 17–47, Sept. 2006. [Cit. on page 17]

[41] J. J. Hester, "The Crab Nebula: An Astrophysical Chimera," *Annual Review of Astronomy and Astrophysics*, vol. 46, no. 1, pp. 127–155, 2008. [Cit. on page 17]

[42] M. Chernyakova and D. Malyshev, "Gamma-ray binaries," *arXiv:2006.03615 [astro-ph]*, June 2020. [Cit. on page 18]

[43] P. Schneider, *Extragalactic Astronomy and Cosmology*. Berlin, Heidelberg: Springer Berlin Heidelberg, 2015. [Cit. on page 19]

[44] T. H. Collaboration and F. Acero, "Detection of Gamma Rays From a Starburst Galaxy," *Science*, vol. 326, pp. 1080–1082, Nov. 2009. [Cit. on page 20]

[45] V. A. Acciari, E. Aliu, T. Arlen, *et al.*, "A connection between star formation activity and cosmic rays in the starburst galaxy M82," *Nature*, vol. 462, pp. 770–772, Dec. 2009. [Cit. on page 20]

[46] N. Gehrels, E. Ramirez-Ruiz, and D. B. Fox, "Gamma-Ray Bursts in the Swift Era," *Annual Review of Astronomy and Astrophysics*, vol. 47, pp. 567–617, Sept. 2009. [Cit. on page 20]

[47] S. J. Smartt, T.-W. Chen, A. Jerkstrand, *et al.*, "A kilonova as the electromagnetic counterpart to a gravitational-wave source," *Nature*, vol. 551, pp. 75–79, Nov. 2017. [Cit. on page 20]

[48] V. A. Acciari, S. Ansoldi, L. A. Antonelli, *et al.*, "Teraelectronvolt emission from the γ-ray burst GRB 190114C," *Nature*, vol. 575, pp. 455–458, Nov. 2019. [Cit. on page 20]

[49] H. Abdalla, R. Adam, F. Aharonian, *et al.*, "A very-high-energy component deep in the γ-ray burst afterglow," *Nature*, vol. 575, pp. 464–467, Nov. 2019. [Cit. on page 20]

[50] P. Gorenstein, "Focusing X-Ray Optics for Astronomy," *X-Ray Optics and Instrumentation*, vol. 2010, p. e109740, Dec. 2010. [Cit. on page 20]

[51] W. B. Atwood, A. A. Abdo, M. Ackermann, *et al.*, "THE LARGE AREA TELESCOPE ON THE FERMI GAMMA-RAY SPACE TELESCOPE MISSION," *The Astrophysical Journal*, vol. 697, pp. 1071–1102, May 2009. [Cit. on page 21]

[52] X. Bai, B. Y. Bi, X. J. Bi, *et al.*, "The Large High Altitude Air Shower Observatory (LHAASO) Science White Paper," *arXiv:1905.02773 [astro-ph]*, May 2019. [Cit. on page 22]

[53] T. C. T. A. Consortium, B. S. Acharya, I. Agudo, *et al.*, "Science with the Cherenkov Telescope Array," *arXiv:1709.07997 [astro-ph, physics:hep-ex]*, Mar. 2019. [Cit. on page 23]

[54] K. Garrett and G. Duda, "Dark Matter: A Primer," *Advances in Astronomy*, vol. 2011, p. e968283, Dec. 2010. [Cit. on page 27]

[55] S. Liberati, "Tests of Lorentz invariance: A 2013 update," *Classical and Quantum Gravity*, vol. 30, p. 133001, June 2013. [Cit. on page 27]

[56] R. D. Peccei, "The Strong CP Problem and Axions," in *Axions: Theory, Cosmology, and Experimental Searches* (M. Kuster, G. Raffelt, and B. Beltrán, eds.), Lecture Notes in Physics, pp. 3–17, Berlin, Heidelberg: Springer, 2008. [Cit. on page 27]

[57] A. De Angelis, O. Mansutti, and M. Roncadelli, "Axion-Like Particles, Cosmic Magnetic Fields and Gamma-Ray Astrophysics," *Physics Letters B*, vol. 659, pp. 847–855, Feb. 2008. [Cit. on page 27]

[58] D. Montanino, F. Vazza, A. Mirizzi, and M. Viel, "Enhancing the Spectral Hardening of Cosmic TeV Photons by Mixing with Axion-like Particles in the Magnetized Cosmic Web," *Physical Review Letters*, vol. 119, p. 101101, Sept. 2017. [Cit. on page 28]

[59] A. De Angelis, O. Mansutti, M. Persic, and M. Roncadelli, "Photon propagation and the very high energy γ-ray spectra of blazars: How transparent is the Universe?," *Monthly Notices of the Royal Astronomical Society: Letters*, vol. 394, pp. L21–L25, Mar. 2009. [Cit. on page 28]

[60] J. V. Jelley and N. A. Porter, "Čerenkov Radiation from the Night Sky, and its Application to γ-Ray Astronomy," *Quarterly Journal of the Royal Astronomical Society*, vol. 4, p. 275, Sept. 1963. [Cit. on page 31]

[61] P. Auger, P. Ehrenfest, R. Maze, J. Daudin, and R. A. Fréon, "Extensive Cosmic-Ray Showers," *Reviews of Modern Physics*, vol. 11, pp. 288–291, July 1939. [Cit. on page 31]

[62] P. M. S. Blackett, "A possible contribution to the night sky from the Cerenkov radiation emitted by cosmic rays," in *Proceedings of the International Conference on the Emission Spectra of the Night Sky and Aurorae*, pp. 34–35, Physical Society, July 1947. [Cit. on page 31]

[63] W. Galbraith and J. V. Jelley, "Light Pulses from the Night Sky associated with Cosmic Rays," *Nature*, vol. 171, pp. 349–350, Feb. 1953. [Cit. on page 31]

[64] M. Mori, "Recent results from CANGAROO-II&III," vol. 745, pp. 639–644, Feb. 2005. [Cit. on pages 32 and 55]

[65] G. G. Fazio, H. F. Helmken, G. H. Rieke, and T. C. Weekes, "An experiment to search for discrete sources of cosmic gamma rays in the 1011 to 1012 eV region," *Canadian Journal of Physics*, vol. 46, pp. S451–S455, May 1968. [Cit. on pages 32 and 52]

[66] T. C. Weekes, M. F. Cawley, D. J. Fegan, *et al.*, "Observation of TeV Gamma Rays from the Crab Nebula Using the Atmospheric Cerenkov Imaging Technique," *The Astrophysical Journal*, vol. 342, p. 379, July 1989. [Cit. on page 32]

[67] H. J. Völk and K. Bernlöhr, "Imaging very high energy gamma-ray telescopes," *Experimental Astronomy*, vol. 25, pp. 173–191, Aug. 2009. [Cit. on page 33]

[68] R. M. Wagner, "Measurement of Very High Energy Gamma-Ray Emission from Four Blazars Using the MAGIC Telescope and a Comparative Blazar Study," *Publications of the Astronomical Society of the Pacific*, vol. 119, pp. 1201–1203, Oct. 2007. [Cit. on pages 33, 40, and 42]

[69] R. B. Leighton, *Principles of Modern Physics*. New York: McGraw-Hill, 1959. [Cit. on page 34]

[70] A. Fernández Barral, *Extreme Particle Acceleration in Microquasar Jets and Pulsar Wind Nebulae with the MAGIC Telescopes*. Springer Theses, Cham: Springer International Publishing, 2018. [Cit. on pages 34 and 45]

[71] B. Rossi and D. B. Hall, "Variation of the Rate of Decay of Mesotrons with Momentum," *Physical Review*, vol. 59, pp. 223–228, Feb. 1941. [Cit. on page 35]

[72] M. de Naurois and D. Mazin, "Ground-based detectors in very-high-energy gamma-ray astronomy," *Comptes Rendus Physique*, vol. 16, pp. 610–627, Aug. 2015. [Cit. on pages 37, 38, 39, 41, 42, and 51]

[73] A. A. Watson, "The discovery of Cherenkov radiation and its use in the detection of extensive air showers," *Nuclear Physics B - Proceedings Supplements*, vol. 212–213, pp. 13–19, Mar. 2011. [Cit. on page 38]

[74] P. A. Cherenkov, “Visible luminescence of pure liquids under the influence of γ-radiation,” *Dokl.Akad.Nauk SSSR*, vol. 2, no. 8, pp. 451–454, 1934. [Cit. on page 38]

[75] I. M. Frank and I. E. Tamm, “Coherent visible radiation of fast electrons passing through matter,” *Compt. Rend. Acad. Sci. URSS*, vol. 14, no. 3, pp. 109–114, 1937. [Cit. on page 38]

[76] J. A. Barrio, Juan Abel, G. Blanchot, H. Borst, *et al.*, “The MAGIC Telescope - Design study for the construction of a 17 m Cerenkov telescope for Gamma-Astronomy above 10GeV,” tech. rep., MPI-PhE, May 1998. [Cit. on pages 40, 52, 57, and 82]

[77] A. Mishev, S. Mavrodiev, and J. Stamenov, “Approximation of lateral distribution of atmospheric Cherenkov light at different observation levels for different primary particles. Applications for cosmic ray studies,” *arXiv:astro-ph/0511790*, Nov. 2005. [Cit. on page 40]

[78] P. Vallania and F. D. Pierro, “Stima delle prestazioni del prototipo di telescopio Schwarzschild-Couder alle energie dei TeV.,” Technical Report ASTRI-MC-IFSITO-5000-1, July 2011. [Cit. on page 40]

[79] S. Collaboration, S. Oser, D. Bhattacharya, *et al.*, “High Energy Gamma-Ray Observations of the Crab Nebula and Pulsar with the Solar Tower Atmospheric Cherenkov Effect Experiment,” *The Astrophysical Journal*, vol. 547, pp. 949–958, Feb. 2001. [Cit. on page 41]

[80] G. Mie, “Beiträge zur Optik trüber Medien, speziell kolloidaler Metallösungen,” *Annalen der Physik*, vol. 330, pp. 377–445, Jan. 1908. [Cit. on page 43]

[81] A. Ostankov and MAGIC Collaboration, “The image camera of the 17m diameter air Cherenkov telescope MAGIC,” *Nuclear Instruments and Methods in Physics Research A*, vol. 471, pp. 188–191, Sept. 2001. [Cit. on pages 44 and 58]

[82] P. Buzhan, B. Dolgoshein, L. Filatov, *et al.*, “Silicon photomultiplier and its possible applications,” *Nuclear Instruments and Methods in Physics Research Section A: Accelerators, Spectrometers, Detectors and Associated Equipment*, vol. 504, pp. 48–52, May 2003. [Cit. on pages 44 and 53]

[83] H. E. S. S. Collaboration, A. Abramowski, F. Aharonian, *et al.*, “Diffuse Galactic gamma-ray emission with H.E.S.S,” *Physical Review D*, vol. 90, p. 122007, Dec. 2014. [Cit. on page 45]

[84] A. M. Hillas, “Cerenkov light images of EAS produced by primary gamma,” in *Proceeding of Science*, vol. 3, p. 445, SISSA Medialab, Aug. 1985. [Cit. on pages 46 and 47]

[85] A. V. Plyasheshnikov and G. F. Bignami, “Investigation on the effectiveness of VHE gamma-ray astronomy techniques based on imaging of Čerenkov light flashes,” *Il Nuovo Cimento C*, vol. 8, pp. 39–54, Jan. 1985. [Cit. on page 47]

[86] S. Lombardi, O. Catalano, S. Scuderi, *et al.*, “First detection of the Crab Nebula at TeV energies with a Cherenkov telescope in a dual-mirror Schwarzschild-Couder configuration: The ASTRI-Horn telescope,” *Astronomy & Astrophysics*, vol. 634, p. A22, Feb. 2020. [Cit. on pages 48, 70, 117, 165, and 182]

[87] C. B. Adams, R. Alfaro, G. Ambrosi, *et al.*, “Detection of the Crab Nebula with the 9.7 m Prototype Schwarzschild-Couder Telescope,” *Astroparticle Physics*, vol. 128, p. 102562, Mar. 2021. [Cit. on pages 48 and 63]

[88] J. Cortina, “Status and First Results of the MAGIC Telescope,” *Astrophysics and Space Science*, vol. 297, July 2004. [Cit. on pages 48 and 57]

[89] F. Aharonian, A. G. Akhperjanian, A. R. Bazer-Bachi, *et al.*, “Primary particle acceleration above 100 TeV in the shell-type supernova remnant RX J1713.7-3946 with deep HESS observations,” *Astronomy & Astrophysics*, vol. 464, pp. 235–243, Mar. 2007. [Cit. on page 49]

[90] H. Abdalla, A. Abramowski, F. Aharonian, *et al.*, “H.E.S.S. observations of RX J1713.7-3946 with improved angular and spectral resolution: Evidence for gamma-ray emission extending beyond the X-ray emitting shell,” *Astronomy & Astrophysics*, vol. 612, p. A6, Apr. 2018. [Cit. on page 49]

[91] D. J. Schroeder, *Astronomical Optics*. San Diego: Academic Press, 2nd ed ed., 2000. [Cit. on page 51]

[92] K. Bernloehr, O. Carrol, R. Cornils, *et al.*, "The optical system of the H.E.S.S. imaging atmospheric Cherenkov telescopes, Part I: Layout and components of the system," *Astroparticle Physics*, vol. 20, pp. 111–128, Nov. 2003. [Cit. on pages 52, 53, and 56]

[93] J. M. Davies and E. S. Cotton, "Design of the quartermaster solar furnace," *Solar Energy*, vol. 1, pp. 16–22, Apr. 1957. [Cit. on page 52]

[94] F. Krennrich, I. H. Bond, P. J. Boyle, *et al.*, "VERITAS: The Very Energetic Radiation Imaging Telescope Array System," *New Astronomy Reviews*, vol. 48, pp. 345–349, Apr. 2004. [Cit. on pages 52 and 56]

[95] A. Kawachi, Y. Hayami, J. Jimbo, *et al.*, "The optical reflector system for the CANGAROO-II imaging atmospheric Cherenkov telescope," *Astroparticle Physics*, vol. 14, pp. 261–269, Jan. 2001. [Cit. on page 52]

[96] K. Tayabaly, D. Spiga, R. Canestrari, *et al.*, "Roughness tolerances for Cherenkov telescope mirrors," in *Optics for EUV, X-Ray, and Gamma-Ray Astronomy VII*, vol. 9603, pp. 43–56, SPIE, Sept. 2015. [Cit. on page 52]

[97] R. N. Wilson, *Reflecting Telescope Optics I. Basic Design Theory and Its Historical Development.* Jan. 1996. [Cit. on page 52]

[98] G. Bonanno, D. Marano, G. Romeo, *et al.*, "Advances in Multi-Pixel Photon Counter technology: First characterization results," *Nuclear Instruments and Methods in Physics Research Section A: Accelerators, Spectrometers, Detectors and Associated Equipment*, vol. 806, pp. 383–394, Jan. 2016. [Cit. on page 53]

[99] V. V. Vassiliev, S. J. Fegan, and P. F. Brousseau, "Wide field aplanatic two-mirror telescopes for ground-based gamma-ray astronomy," *Astroparticle Physics*, vol. 28, pp. 10–27, Sept. 2007. [Cit. on pages 53 and 54]

[100] K. Schwarzschild, "Untersuchungen zur geometrischen Optik II,," *Astronomische Mitteilungen der Universitaets-Sternwarte zu Goettingen*, vol. 10, p. 1, Jan. 1905. [Cit. on page 53]

[101] A. Couder, "Sur un type nouveau de télescope photographique," *Comptes Rendus*, vol. 183, no. 45, pp. 1276–1279, 1926. [Cit. on page 53]

[102] D. Lynden-Bell, “Exact optics: A unification of optical telescope design,” *Monthly Notices of the Royal Astronomical Society*, vol. 334, pp. 787–796, Aug. 2002. [Cit. on page 53]

[103] K. Byrum, B. Humensky, W. Benbow, *et al.*, “A Medium Sized Schwarzschild-Couder Cherenkov Telescope Mechanical Design Proposed for the Cherenkov Telescope Array,” Sept. 2015. [Cit. on page 54]

[104] E. Giro, R. Canestrari, G. Sironi, *et al.*, “First optical validation of a Schwarzschild Couder telescope: The ASTRI SST-2M Cherenkov telescope,” *Astronomy & Astrophysics*, vol. 608, p. A86, Dec. 2017. [Cit. on pages 54, 76, 79, 80, and 81]

[105] M. Tluczykont and HEGRA Collaboration, *Highlight Results of the HEGRA Collaboration*. Dec. 2004. [Cit. on page 55]

[106] N. Götting, “Recent results from HEGRA,” *European Physical Journal C, Volume 33, Issue S1, pp. 932-934 (2004).*, vol. 33, no. S1, p. 932, 2004. [Cit. on page 55]

[107] W. Hofmann, “Status of the High Energy Stereoscopic System (H.E.S.S.) Project,” p. 4. [Cit. on page 55]

[108] C. Deil, C. van Eldik, A. Förster, *et al.*, “H.E.S.S. II—Telescope Structure, Reflector and Drive System,” *AIP Conference Proceedings*, vol. 1085, pp. 693–695, Dec. 2008. [Cit. on page 55]

[109] R. Winston, “Light Collection within the Framework of Geometrical Optics*,” *JOSA*, vol. 60, pp. 245–247, Feb. 1970. [Cit. on page 55]

[110] T. Nagai, R. Mckay, G. Sleege, and D. Petry, “Focal Plane Instrumentation of VERITAS,” p. 4. [Cit. on page 57]

[111] A. Biland, M. Garczarczyk, H. Anderhub, *et al.*, “The Active Mirror Control of the MAGIC Telescopes,” vol. 3, pp. 1353–1356, Jan. 2008. [Cit. on page 58]

[112] G. Ceribella, *Insights into the 10-100 GeV Gamma-Ray Emission of Pulsars from Extensive Observations of MAGIC*. PhD thesis, Technische Universität München, München, 2021. [Cit. on page 58]

[113] J. Cortina, F. Goebel, and T. Schweizer, “Technical Performance of the MAGIC Telescopes,” July 2009. [Cit. on page 58]

[114] D. Mazin, J. Cortina, M. Teshima, and t. C. Consortium, "Large Size Telescope Report," *arXiv:1610.04403 [astro-ph]*, p. 080001, 2017. [Cit. on page 60]

[115] T. Inada, S. Fukami, K. Noda, *et al.*, "Design and production of segment mirrors for the Large-Sized Telescopes of the Cherenkov Telescope Array," in *Advances in Optical and Mechanical Technologies for Telescopes and Instrumentation IV*, vol. 11451, pp. 95–104, SPIE, Dec. 2020. [Cit. on page 60]

[116] J. Cortina and CTA LST project, "Status of the Large Size Telescopes of the Cherenkov Telescope Array," in *Proceedings of 36th International Cosmic Ray Conference — PoS(ICRC2019)*, (Madison, WI, U.S.A.), p. 653, Sissa Medialab, July 2019. [Cit. on page 61]

[117] C. Perennes, M. Doro, D. Corti, *et al.*, "Optical feasibility of an upgrade of the CTA LST camera to SiPM," *Nuclear Instruments and Methods in Physics Research Section A: Accelerators, Spectrometers, Detectors and Associated Equipment*, vol. 984, p. 164485, Aug. 2020. [Cit. on page 61]

[118] M. Garczarczyk, "Medium size telescopes for the Cherenkov Telescope Array," *Proc. SPIE Int. Soc. Opt. Eng.*, vol. 10700, p. 1070023, 2018. [Cit. on page 62]

[119] M. Garczarczyk, S. Schlenstedt, L. Oakes, U. Schwanke, and t. M. Team, "Status of the Medium-Sized Telescope for the Cherenkov Telescope Array," *arXiv:1509.01361 [astro-ph]*, Sept. 2015. [Cit. on page 62]

[120] D. Tiziani, M. Garczarczyk, L. Oakes, *et al.*, "A pointing solution for the medium size telescopes for the Cherenkov Telescope Array," vol. 301, p. 803, Jan. 2017. [Cit. on page 62]

[121] V. Barbosa Martins and M. Garczarczyk, "The structure monitoring of the MST prototype of CTA," vol. 11445, p. 114456E, Dec. 2020. [Cit. on page 62]

[122] C. Adams, R. Alfaro, G. Ambrosi, *et al.*, "Alignment of the optical system of the 9.7-m prototype Schwarzchild-Coulder Telescope," vol. 11445, p. 114456A, Dec. 2020. [Cit. on page 62]

[123] C. B. Adams, G. Ambrosi, M. Ambrosio, *et al.*, "Design and performance of the prototype Schwarzschild-Couder Telescope camera," Sept. 2021. [Cit. on page 63]

[124] S. Scuderi, "From the Etna volcano to the Chilean Andes: ASTRI end-to-end telescopes for the Cherenkov Telescope Array," in *Ground-Based and Airborne Telescopes VII*, vol. 10700, p. 107005Z, International Society for Optics and Photonics, July 2018. [Cit. on pages 63, 69, 76, 78, and 96]

[125] O. L. Blanc, G. Fasola, J.-L. Dournaux, *et al.*, "Towards final characterisation and performance of the GCT prototype telescope structure for the Cherenkov Telescope Array," *arXiv:1709.03954 [astro-ph]*, Sept. 2017. [Cit. on page 63]

[126] M. Heller, I. A. Samarai, C. M. Alispach, *et al.*, "The SST-1M project for the Cherenkov Telescope Array," vol. 36, p. 694, July 2019. [Cit. on page 63]

[127] R. White, "CHEC: A Compact High Energy Camera for the Cherenkov Telescope Array," *Journal of Instrumentation*, vol. 12, pp. C12059–C12059, Dec. 2017. [Cit. on page 64]

[128] G. Pareschi, E. Giro, R. Banham, *et al.*, "Glass Mirrors by cold slumping to cover 100 m(2) of the MAGIC II Cherenkov telescope reflecting surface - art. no. 70180W," in *Proceedings of SPIE - The International Society for Optical Engineering*, vol. 7018, July 2008. [Cit. on page 67]

[129] F. Acerbi and S. Gundacker, "Understanding and simulating SiPMs," *Nuclear Instruments and Methods in Physics Research Section A: Accelerators, Spectrometers, Detectors and Associated Equipment*, vol. 926, pp. 16–35, May 2019. [Cit. on page 69]

[130] E. Giro, R. Canestrari, P. Bruno, *et al.*, "The ASTRI-Horn telescope validation toward the production of the ASTRI Mini-Array: A proposed pathfinder for the Cherenkov Telescope Array," in *Optics for EUV, X-Ray, and Gamma-Ray Astronomy IX*, vol. 11119, p. 111191E, International Society for Optics and Photonics, Sept. 2019. [Cit. on pages 69, 73, 80, 82, 83, and 139]

[131] R. Canestrari, O. Catalano, M. Fiorini, *et al.*, "The ASTRI SST-2M Prototype: Structure and Mirror," in *Proceeding of Science*, vol. 33, p. 2913, SISSA Medialab, 2013. [Cit. on page 69]

[132] F. Bònoli, “Guido Horn d’Arturo e i primi telescopi multi-mirror : 1932-1952,” *Guido Horn d’Arturo e i primi telescopi multi-mirror : 1932-1952*, pp. 5–18, 2019. [Cit. on page 70]

[133] G. Catanzaro and F. A. Catalano, “Measurements of the night sky brightness at the Catania Astrophysical Observatory,” *Memorie della Societa Astronomica Italiana*, vol. 71, p. 211, Jan. 2000. [Cit. on page 70]

[134] D. Mollica, M. Del Santo, O. Catalano, *et al.*, “An Imaging Atmospheric Cherenkov Telescope Prototype for Volcanoes Muography,” vol. 2019, pp. NS43B–0840, Dec. 2019. [Cit. on page 70]

[135] L. A. Antonelli, “The ASTRI Mini-Array at Teide Observatory,” in *Proceedings of 37th International Cosmic Ray Conference — PoS(ICRC2021)*, (Berlin, Germany - Online), p. 897, Sissa Medialab, July 2021. [Cit. on page 71]

[136] S. Lombardi, L. A. Antonelli, C. Bigongiari, *et al.*, “Performance of the ASTRI Mini-Array at the Observatorio del Teide,” *PoS*, vol. ICRC2021, p. 884, 2021. [Cit. on page 71]

[137] S. Vercellone, “The ASTRI Mini-Array Core Science Program,” *PoS*, vol. ICRC2021, p. 896, 2021. [Cit. on pages 71 and 74]

[138] G. Marchiori, A. Busatta, E. Marcuzzi, *et al.*, “ASTRI SST-2M: The design evolution from the prototype to the array telescope,” in *Ground-Based and Airborne Telescopes VII*, vol. 10700, pp. 1734–1743, SPIE, July 2018. [Cit. on page 72]

[139] O. Catalano, M. Capalbi, C. Gargano, *et al.*, “The ASTRI camera for the Cherenkov Telescope Array,” in *Ground-Based and Airborne Instrumentation for Astronomy VII*, vol. 10702, p. 1070237, International Society for Optics and Photonics, July 2018. [Cit. on pages 73, 83, 84, 86, and 95]

[140] N. Parmiggiani, A. Bulgarelli, L. Baroncelli, *et al.*, “The Online Observation Quality System for the ASTRI Mini Array.,” in *Proceedings of 37th International Cosmic Ray Conference — PoS(ICRC2021)*, vol. 395, p. 692, SISSA Medialab, July 2021. [Cit. on pages 73, 123, 180, and 253]

[141] T. Mineo, M. C. Maccarone, L. A. Antonelli, *et al.*, “Tools and Procedures for the ASTRI Mini-Array Calibration,” in *Proceedings of 37th International Cosmic Ray Conference — PoS(ICRC2021)*, vol. 395,

p. 197, SISSA Medialab, July 2021. [Cit. on pages 73, 119, 124, 151, and 253]

[142] A. Dai, E. Amato, A. Burtovoi, *et al.*, “Observatory Galactic Science with the ASTRI-Mini Array during the observatory phase of the project,” in *Proceedings of 37th International Cosmic Ray Conference — PoS(ICRC2021)*, (Berlin, Germany - Online), p. 900, Sissa Medialab, July 2021. [Cit. on page 74]

[143] F. G. Saturni, L. A. Antonelli, C. Arcaro, *et al.*, “Extragalactic Observatory Science with the ASTRI Mini-Array at the Observatorio del Teide,” in *Proceedings of 37th International Cosmic Ray Conference — PoS(ICRC2021)*, (Berlin, Germany - Online), p. 888, Sissa Medialab, July 2021. [Cit. on page 74]

[144] M. Cardillo, “"The ASTRI Mini-Array: A breakthrough in the Cosmic Ray study",” in *Proceedings of 37th International Cosmic Ray Conference — PoS(ICRC2021)*, (Berlin, Germany - Online), p. 807, Sissa Medialab, July 2021. [Cit. on page 74]

[145] E. Aliu, S. Archambault, T. Aune, *et al.*, “Investigating the TeV Morphology of MGRO J1908+06 with VERITAS,” *The Astrophysical Journal*, vol. 787, p. 166, June 2014. [Cit. on page 74]

[146] A. Franceschini, G. Rodighiero, and M. Vaccari, “Extragalactic optical-infrared background radiation, its time evolution and the cosmic photon-photon opacity,” *Astronomy & Astrophysics*, vol. 487, pp. 837–852, Sept. 2008. [Cit. on page 75]

[147] P. Eckert, H.-C. Schultz-Coulon, W. Shen, R. Stamen, and A. Tadday, “Characterisation studies of silicon photomultipliers,” *Nuclear Instruments and Methods in Physics Research Section A: Accelerators, Spectrometers, Detectors and Associated Equipment*, vol. 620, pp. 217–226, Aug. 2010. [Cit. on page 75]

[148] V. Vassiliev and J. Rousselle, “Optical System of 9.5m Schwarzschild-Couder Telescope for CTA,” Technical Report SCT-OPTMO/121108, CTA-US Collaboration, MRI Consortium, Nov. 2012. [Cit. on page 76]

[149] The CTA Consortium, M. Actis, G. Agnetta, *et al.*, “Design concepts for the Cherenkov Telescope Array CTA: An advanced facility for ground-based high-energy gamma-ray astronomy,” *Experimental Astronomy*, vol. 32, pp. 193–316, Dec. 2011. [Cit. on page 76]

[150] G. Rodeghiero, E. Giro, R. Canestrari, *et al.*, "Qualification and Testing of a Large Hot Slumped Secondary Mirror for Schwarzschild–Couder Imaging Air Cherenkov Telescopes," *Publications of the Astronomical Society of the Pacific*, vol. 128, p. 055001, Mar. 2016. [Cit. on pages 77 and 78]

[151] G. Sironi and R. Canestrari, "The ASTRI SST-2M prototype for the Cherenkov Telescope Array: Primary mirror characterization by deflectometry," in *SPIE Conference Proceedings* (S. L. O'Dell and G. Pareschi, eds.), (San Diego, California, United States), p. 960304, Sept. 2015. [Cit. on page 78]

[152] R. Canestrari, G. Pareschi, G. Parodi, *et al.*, "Cold-shaping of thin glass foils as a method for mirror processing: From basic concepts to mass production of mirrors," *Optical Engineering*, vol. 52, p. 051204, Mar. 2013. [Cit. on page 78]

[153] G. Sironi, R. Canestrari, G. Pareschi, and C. Pelliciari, "Deflectometry for optics evaluation: Free form segments of polynomial mirror," in *SPIE Astronomical Telescopes + Instrumentation* (R. Navarro, C. R. Cunningham, and A. A. Barto, eds.), (Montréal, Quebec, Canada), p. 91510T, July 2014. [Cit. on pages 78 and 79]

[154] M. Ghigo, S. Basso, R. Canestrari, and L. Proserpio, "Development of hot slumping technique and last optical performances obtained on a 500mm diameter slumped segment prototype for adaptive optics," in *SPIE Optical Engineering + Applications* (P. G. Warren, C. J. Marshall, R. K. Tyson, *et al.*, eds.), (San Diego, CA), p. 74390M, Aug. 2009. [Cit. on page 78]

[155] G. Bonnoli, R. Canestrari, O. Catalano, *et al.*, "Boosting the performance of the ASTRI SST-2M prototype: Reflective and anti-reflective coatings," *arXiv:1307.5405 [astro-ph]*, July 2013. [Cit. on pages 78 and 84]

[156] K. Tayabaly, D. Spiga, R. Canestrari, *et al.*, "Roughness tolerances for Cherenkov telescope mirrors," *arXiv:1610.00723 [astro-ph]*, p. 960307, Sept. 2015. [Cit. on page 78]

[157] E. Giro, G. Rodeghiero, G. Bonnoli, *et al.*, "Tests characterization and alignment for the optics of the ASTRI SST-2M telescope prototype for the Cherenkov Telescope Array," in *Advances in Optical and*

Mechanical Technologies for Telescopes and Instrumentation, vol. 9151, pp. 1176–1188, SPIE, July 2014. [Cit. on page 82]

[158] G. Sironi, "Optical parameter for ASTRI Chile demonstrator MC," Internal Technical Report ASTRI-MC-INAF-5000-018, INAF-OAB, Oct. 2017. [Cit. on pages 82 and 84]

[159] O. Catalano, M. C. Maccarone, C. Gargano, *et al.*, "The camera of the ASTRI SST-2M prototype for the Cherenkov Telescope Array," in *SPIE Astronomical Telescopes + Instrumentation* (S. K. Ramsay, I. S. McLean, and H. Takami, eds.), (Montréal, Quebec, Canada), p. 91470D, July 2014. [Cit. on pages 83, 85, and 90]

[160] D. Impiombato, O. Catalano, S. Giarrusso, *et al.*, "Procedures for the relative calibration of the SiPM gain on ASTRI SST-2M camera," *Experimental Astronomy*, vol. 43, pp. 1–17, Feb. 2017. [Cit. on pages 85 and 91]

[161] G. Romeo, G. Bonanno, S. Garozzo, *et al.*, "MPPC Hamamatsu Photonics characterization report for the ASTRI project," Technical Report ASTRI-TR-OACT-3200-007, Osservatorio Astrofisico di Catania, July 2013. [Cit. on page 86]

[162] D. Impiombato, S. Giarrusso, T. Mineo, *et al.*, "Evaluation of the optical cross talk level in the SiPMs adopted in ASTRI SST-2M Cherenkov Camera using EASIROC front-end electronics," *Journal of Instrumentation*, vol. 9, Dec. 2013. [Cit. on page 86]

[163] M. Capalbi and M. C. Maccarone, "Geometry of the Focal Surface Camera," Internal Technical Report ASTRI-DES-IASFPA-3200-008, INAF-IASFPA, Mar. 2017. [Cit. on pages 87 and 88]

[164] G. Sottile *et al.*, "ASTRI SST-2M camera electronics," *Proc. SPIE Int. Soc. Opt. Eng.*, vol. 9906, p. 99063D, 2016. [Cit. on pages 89, 91, 92, and 102]

[165] D. Impiombato, S. Giarrusso, T. Mineo, *et al.*, "Characterization of EASIROC as Front-End for the readout of the SiPM at the focal plane of the Cherenkov telescope ASTRI," *Nuclear Instruments and Methods in Physics Research Section A: Accelerators, Spectrometers, Detectors and Associated Equipment*, vol. 729, pp. 484–490, Nov. 2013. [Cit. on page 90]

[166] D. Impiombato, S. Giarrusso, T. Mineo, *et al.*, “Characterization and performance of the ASIC (CITIROC) front-end of the ASTRI camera,” *Nuclear Instruments and Methods in Physics Research Section A: Accelerators, Spectrometers, Detectors and Associated Equipment*, vol. 794, pp. 185–192, Sept. 2015. [Cit. on pages 90 and 103]

[167] P. Sangiorgi, M. Capalbi, O. Catalano, *et al.*, “The ASTRI Camera control software of the ASTRI SST-2M prototype for the Cherenkov Telescope Array,” *Nuclear and Particle Physics Proceedings*, vol. 306–308, pp. 28–36, Sept. 2019. [Cit. on page 91]

[168] V. Conforti, M. Trifoglio, F. Gianotti, *et al.*, “Software design of the ASTRI camera server proposed for the Cherenkov Telescope Array,” in *Software and Cyberinfrastructure for Astronomy IV*, vol. 9913, pp. 1252–1260, SPIE, July 2016. [Cit. on page 91]

[169] V. Conforti, F. Gianotti, M. Trifoglio, *et al.*, “The DAQ system support to the AIV activities of the ASTRI camera proposed for the Cherenkov Telescope Array,” in *Software and Cyberinfrastructure for Astronomy V*, vol. 10707, pp. 615–626, SPIE, July 2018. [Cit. on page 91]

[170] O. Catalano, “ASTRI Camera detection technique,” Internal Technical Report ASTRI-TN-IASFPA-3200-024, INAF-IASFPA, Aug. 2014. [Cit. on page 93]

[171] M. Trifoglio, “Camera Server/Interface Control Document,” Internal Technical Report ASTRI-IR-IASFBO-3700-026, INAF-IASFBO, Apr. 2017. [Cit. on page 94]

[172] R. J. Hanisch, A. Farris, E. W. Greisen, *et al.*, “Definition of the Flexible Image Transport System (FITS),” *Astronomy and Astrophysics*, vol. 376, pp. 359–380, Sept. 2001. [Cit. on page 94]

[173] S. Lombardi, “Fits data format for ASTRI DL0 data,” Internal Technical Report ASTRI-IR-OARM-3700-037, INAF-OARM, July 2017. [Cit. on page 94]

[174] A. N. Otte, D. Garcia, T. Nguyen, and D. Purushotham, “Characterization of Three High Efficiency and Blue Sensitive Silicon Photomultipliers,” *Nuclear Instruments and Methods in Physics Research Section A: Accelerators, Spectrometers, Detectors and Associated Equipment*, vol. 846, pp. 106–125, Feb. 2017. [Cit. on page 96]

[175] P. T. Wallace, “A Telescope Pointing Analysis System.” Feb. 1996. [Cit. on page 97]

[176] O. Catalano, G. L. Rosa, M. C. Maccarone, *et al.*, “UVscope: An instrument for multi-wavelength study of the diffuse Night Sky Background light,” p. 4, 2009. [Cit. on pages 97 and 100]

[177] C. Gargano, S. Scuderi, F. Russo, and V. Giordano, “ASTRI Mini-Array: Telescope mechanical structure assembly requirements specifications,” Technical Report ASTRI-INAF-SPE-7100-001, INAF-SPE, Dec. 2020. [Cit. on pages 97 and 98]

[178] M. R. Calabretta and E. W. Greisen, “Representations of celestial coordinates in FITS,” *Astronomy & Astrophysics*, vol. 395, pp. 1077–1122, Dec. 2002. [Cit. on pages 99 and 129]

[179] E. W. Greisen and M. R. Calabretta, “Representations of world coordinates in FITS,” *Astronomy & Astrophysics*, vol. 395, pp. 1061–1075, Dec. 2002. [Cit. on pages 99 and 129]

[180] M. C. Maccarone, “UVscope sul telescopio ASTRI-Horn. Pt.1,” Technical Report ASTRI-TN-INAF-3700-029, INAF, Oct. 2019. [Cit. on page 100]

[181] A. Segreto, O. Catalano, M. C. Maccarone, *et al.*, “Calibration and monitoring of the ASTRI-Horn telescope by using the night-sky background measured by the photon-statistics ("variance") method,” in *Proceeding of Science*, vol. 36, (eprint: arXiv:1909.08750), p. 791, SISSA Medialab, July 2019. [Cit. on pages 102, 124, 150, and 167]

[182] A. A. Compagnino, T. Mineo, M. C. Maccarone, *et al.*, “The ASTRI-Horn telescope: Comparison with the auxiliary UVscope measurements as a feasible diagnostic and calibration tool,” *In preparation*, p. 20. [Cit. on page 107]

[183] G. Bonnoli, *Very High Energy Emission from Blazars Interpreted through Simultaneous Multiwavelength Observations*. PhD thesis, UNIVERSITA‘ DEGLI STUDI DI SIENA, Dipartimento di Fisica, Dec. 2010. [Cit. on page 108]

[184] D. J. Fegan, “Gamma/hadron separation at TeV energies,” *Journal of Physics G: Nuclear and Particle Physics*, vol. 23, pp. 1013–1060, Sept. 1997. [Cit. on page 108]

[185] L. Lindegren, U. Lammers, U. Bastian, *et al.*, "Gaia Data Release 1: Astrometry: One billion positions, two million proper motions and parallaxes," *Astronomy & Astrophysics*, vol. 595, p. A4, Nov. 2016. [Cit. on page 128]

[186] L. Lindegren, J. Hernández, A. Bombrun, *et al.*, "Gaia Data Release 2 - The astrometric solution," *Astronomy & Astrophysics*, vol. 616, p. A2, Aug. 2018. [Cit. on page 128]

[187] D. Barghini, D. Gardiol, A. Carbognani, and S. Mancuso, "Astrometric calibration for all-sky cameras revisited," *Astronomy & Astrophysics*, vol. 626, p. A105, June 2019. [Cit. on page 128]

[188] E. Bertin and S. Arnouts, "SExtractor: Software for source extraction.," *Astronomy and Astrophysics Supplement Series*, vol. 117, pp. 393–404, June 1996. [Cit. on page 129]

[189] E. Bertin, M. Schefer, N. Apostolakos, *et al.*, "The SourceXtractor++ Software," vol. 527, p. 461, Jan. 2020. [Cit. on page 129]

[190] D. Lang, D. W. Hogg, K. Mierle, M. Blanton, and S. Roweis, "Astrometry.net: Blind Astrometric Calibration of Arbitrary Astronomical Images," *The Astronomical Journal*, vol. 139, pp. 1782–1800, May 2010. [Cit. on page 129]

[191] W. M. Smart, W. M. Smart, and R. M. Green, *Textbook on Spherical Astronomy*. Cambridge University Press, July 1977. [Cit. on page 130]

[192] A. V. Filippenko, "The importance of atmospheric differential refraction in spectrophotometry," *Publications of the Astronomical Society of the Pacific*, vol. 94, p. 715, Aug. 1982. [Cit. on page 131]

[193] W. A. Hiltner, *Astronomical Techniques*. Chicago: University Press, 1962. [Cit. on page 131]

[194] P. Van De Kamp, *Principles of Astrometry*. San Francisco: Freeman, Jan. 1967. [Cit. on pages 134 and 135]

[195] C. A. Murray, *Vectorial Astrometry*. Jan. 1983. [Cit. on page 135]

[196] S. Newcomb, *A Compendium of Spherical Astronomy with Its Applications to the Determination and Reduction of Positions of the Fixed Stars*. Macmillan, 1906. [Cit. on page 137]

[197] G. Rodeghiero, C. Arcidiacono, J.-U. Pott, *et al.*, “Performance and limitations of using ELT and MCAO for 50 uas astrometry,” in *Ground-Based and Airborne Instrumentation for Astronomy VIII*, vol. 11447, p. 114471Z, International Society for Optics and Photonics, Dec. 2020. [Cit. on page 150]

[198] S. Iovenitti, G. Sironi, E. Giro, *et al.*, “Assessment of the Cherenkov camera alignment through Variance images for the ASTRI telescope,” *Experimental Astronomy*, Nov. 2021. [Cit. on pages 150, 167, and 253]

[199] S. Iovenitti, G. Sironi, A. Segreto, O. Catalano, and T. Mineo, “Effective pointing of the ASTRI-Horn telescope using the Cherenkov camera with the Variance method,” in *Proceedings of 37th International Cosmic Ray Conference — PoS(ICRC2021)*, vol. 395, p. 837, SISSA Medialab, July 2021. [Cit. on pages 150 and 254]

[200] S. Iovenitti, ““Star coverage”, a simple tool to schedule an observation when FOV rotation matters,” in *Proceedings of 37th International Cosmic Ray Conference — PoS(ICRC2021)*, vol. 395, p. 735, SISSA Medialab, July 2021. [Cit. on pages 153 and 253]

[201] M. Wenger, F. Ochsenbein, D. Egret, *et al.*, “The SIMBAD astronomical database. The CDS reference database for astronomical objects,” *Astronomy and Astrophysics Supplement, v.143, p.9-22*, vol. 143, p. 9, Apr. 2000. [Cit. on pages 153 and 173]

[202] B. Everitt, S. Landau, M. Leese, and D. Stahl, *Cluster Analysis*. Wiley Series in Probability and Statistics, Wiley, fifth ed., Feb. 2011. [Cit. on page 156]

[203] F. Russo, “Database query tool manual.” June 2020. [Cit. on page 172]

[204] D. G. Monet, S. E. Levine, B. Canzian, *et al.*, “The USNO-B Catalog,” *The Astronomical Journal*, vol. 125, pp. 984–993, Feb. 2003. [Cit. on page 173]

[205] F. Ochsenbein, P. Bauer, and J. Marcout, “The VizieR database of astronomical catalogues,” *Astronomy and Astrophysics Supplement Series*, vol. 143, pp. 23–32, Apr. 2000. [Cit. on page 173]

[206] M. a. C. Perryman, L. Lindegren, J. Kovalevsky, *et al.*, "The Hipparcos Catalogue.," *Astronomy and Astrophysics, Vol. 500, p. 501-504 (2009)*, vol. 500, p. 501, July 1997. [Cit. on page 173]

[207] D. W. Hogg and D. Lang, "Telescopes don't make catalogues!," *EAS Publications Series*, vol. 45, pp. 351–358, 2010. [Cit. on page 173]

[208] L. Lindegren, U. Lammers, D. Hobbs, *et al.*, "The astrometric core solution for the Gaia mission. Overview of models, algorithms, and software implementation," *Astronomy & Astrophysics*, vol. 538, p. 47, Feb. 2012. [Cit. on page 174]

[209] L. Lindegren and D. Dravins, "The fundamental definition of "radial velocity"," *Astronomy and Astrophysics*, vol. 401, pp. 1185–1201, Apr. 2003. [Cit. on page 174]

[210] J. Watson and S. Flis, "CHEC Camera: Pointing calibration," 2020, 29 January. [Cit. on page 174]

[211] N. La Palombara, G. Sironi, E. Giro, *et al.*, "Mirror production for the Cherenkov telescopes of the ASTRI Mini-Array and of the MST project for the Cherenkov Telescope Array," *Journal of Astronomical Telescopes, Instruments, and Systems*, 2022. [Cit. on pages 204 and 253]

[212] W. B. Landsman, "The IDL Astronomy User's Library," in *ASP Conference Series*, vol. 77, p. 437, R.A. Shaw, H.E. Payne, and J.J.E. Hayes, 1995. [Cit. on page 207]

[213] C. B. Markwardt, "Non-linear Least-squares Fitting in IDL with MPFIT," in *Proceeding of ADASS*, vol. 411 of *Astronomical Society of the Pacific Conference Series*, p. 251, 2009. [Cit. on page 207]

[214] D. W. Marquardt, "An Algorithm for Least-Squares Estimation of Nonlinear Parameters," *Journal of the Society for Industrial and Applied Mathematics*, vol. 11, no. 2, pp. 431–441, 1963. [Cit. on page 207]

[215] K. Levenberg, "A method for the solution of certain non-linear problems in least squares," *Quarterly of Applied Mathematics*, vol. 2, no. 2, pp. 164–168, 1944. [Cit. on page 207]

[216] J. J. Moré, "The Levenberg-Marquardt algorithm: Implementation and theory," in *Numerical Analysis* (G. A. Watson, ed.), Lecture Notes in Mathematics, (Berlin, Heidelberg), pp. 105–116, Springer, 1978. [Cit. on page 207]

[217] T. Mineo, M. C. Maccarone, O. Catalano, *et al.*, "Calibration Plan for the Cherenkov Telescopes," Technical Report ASTRI-INAF-PLA-2600-001, INAF-PLA, Apr. 2021. [Cit. on page 253]

[218] V. Conforti, A. Costa, M. Fiori, *et al.*, "Online Observation Quality System Use Cases," Technical Report ASTRI-INAF-SPE-9100-003, INAF-SPE, Apr. 2021. [Cit. on page 253]

[219] S. Iovenitti, C. Righi, S. Orsenigo, and R. Sgarro, "Astrophotography as an effective tool for Outreach and Education: IACTs in exposition," in *Proceedings of 37th International Cosmic Ray Conference — PoS(ICRC2021)*, vol. 395, p. 1380, SISSA Medialab, July 2021. [Cit. on page 254]

[220] S. Iovenitti and L. Perri, "HOW TO (DIS-)ASSEMBLE A PLANETARY SYSTEM," *Submitted to CAP proceedings*, p. 2, 2021. [Cit. on page 254]

[221] S. Iovenitti and G. Sironi, "Starfield astrometry with the Cherenkov camera of ASTRI-Horn," *In preparation*, p. 18, Nov. 2021. [Cit. on page 254]

[222] S. Iovenitti, G. Sironi, T. Mineo, *et al.*, "New pointing calibration technique using star signals in the ASTRI Cherenkov camera and the Variance method," in *SPIE Conference Proceedings*, 2022. [Cit. on page 254]

Sitography

[223] Apple | Keynote.
https://www.apple.com/it/keynote/.

[224] ASTRI | DATA GETAWAY.
http://astriweb.oa-roma.inaf.it/.

[225] ASTRI | Home page.
http://www.astri.inaf.it/.

[226] ASTRI | Instagram account.
instagram.com/astrigamma.

[227] ASTRI | P.I. email address.
mailto:giovanni.pareschi@inaf.it.

[228] Astrometric solution of frame 218 in run 1597.
https://nova.astrometry.net/user_images/4589702.

[229] Astrometry.net.
https://astrometry.net/.

[230] CAP 2021 | Talk about outreach.
https://youtu.be/t8FsglAhQrE.

[231] Cartes du Ciel (skychart).
https://www.ap-i.net/skychart//it/start.

[232] Cassiopeia A SNR.
https://chandra.harvard.edu/photo/2009/casa/.

[233] Celestial mechanics by J. Tatum.
https://tinyurl.com/CELESTIALMECHANICS.

[234] Cern Archive | A bubble chamber.
https://tinyurl.com/CERNBUBBLECHAMBER.

[235] CORSIKA | Home.
https://www.iap.kit.edu/corsika/index.php.

[236] CTA | Crab detection animation.
https://tinyurl.com/CTALST1CRAB.

[237] CTA | Technology.
cta-observatory.org/project/technology/.

[238] DropBox | Home.
https://www.dropbox.com/.

[239] EIE Group s.r.l.
https://www.eie.it/.

[240] ESO | Home.
https://www.eso.org/public/.

[241] Gamma Ray Binaries.
astromev.in2p3.fr/?q=aboutus/gamma-ray-binaries.

[242] Google Script programming language.
https://www.google.com/script/start/.

[243] Google Spreadsheet API Python.
developers.google.com/sheets/api.

[244] Hamamatsu.
https://www.hamamatsu.com/jp/en/index.html.

[245] HAWC | Home.
https://www.hawc-observatory.org/.

[246] HEGRA | Home.
https://www.mpi-hd.mpg.de/hfm/HEGRA/HEGRA.html.

[247] H.E.S.S. | Home.
https://www.mpi-hd.mpg.de/hfm/HESS/.

[248] ICRC 2021 | Flash-talk about StarCoverage.
https://tinyurl.com/ICRC2021STARCOVERAGE.

[249] ICRC 2021 | Flash-talk about the Camera Alignment.
https://tinyurl.com/ICRC2021CAMALIGNMENT.

[250] ICRC 2021 | Talk about Astro-photography.
https://tinyurl.com/ICRC2021OUTREACH.

[251] IDL | Astronomy Library.
idlastro.gsfc.nasa.gov.

[252] IDL | ATV source code.
http://www.physics.uci.edu/~barth/atv.

[253] IDL | Home.
l3harrisgeospatial.com/docs/using_idl_home.html.

[254] IDL | MPFIT Routines.
https://cow.physics.wisc.edu/~craigm/idl/.

[255] INAF | Home.
http://www.inaf.it/it.

[256] INAF | OAS Bologna.
https://www.oas.inaf.it/it/.

[257] LHAASO Webpage.
http://english.ihep.cas.cn/lhaaso/.

[258] MAGIC - The MAGIC Telescope Web Server on La Palma.
http://www.magic.iac.es/.

[259] MAGIC | Home.
https://magic.mpp.mpg.de/.

[260] Mostra Scientifica | Audio-guide.
guida.mostrascientifica.it.

[261] Mostra Scientifica | Home.
mostrascientifica.it.

[262] Mostra scientifica | Overview.
l.infn.it/overviewmostra.

[263] MySQL database.
https://www.mysql.com/it/.

[264] NASA | FITS Support Office.
https://fits.gsfc.nasa.gov/.

[265] NED | NASA/IPAC Extragalactic Database.
https://ned.ipac.caltech.edu.

[266] Omega Micro.
http://omega.in2p3.fr.

[267] PhysicalPub | Home.
https://www.physical.pub/.

[268] Python | Home page.
http://www.python.org.

[269] Python | PyCharm IDE.
https://www.jetbrains.com/pycharm/.

[270] Simbad | Home.
http://simbad.u-strasbg.fr/simbad/.

[271] Stellarium.
https://stellarium.org/it/.

[272] Symphonic concert "Beethoven and black holes".
https://streaming.laverdi.org/it/video/play/4.

[273] TeVCat, an Online Gamma-Ray Catalog.
http://tevcat.uchicago.edu/.

[274] The TeGeV Catalogue from SSDC.
https://www.ssdc.asi.it/tgevcat/#start_page.

[275] Transforming Measured to Standard Coordinates.
https://tinyurl.com/STDCOORDS.

[276] UNIMI | Physics department.
http://www.fisica.unimi.it/ecm/home.

[277] VAR logbook on Google Spreadsheet.
`https://tinyurl.com/VARLOGBOOK`.

[278] Veritas | Home.
`https://veritas.sao.arizona.edu/`.

[279] VizieR | Home.
`https://vizier.cds.unistra.fr/viz-bin/VizieR`.

[280] WEEROC.
`https://www.weeroc.com/`.

[281] William Hanlon's Web Page.
`https://www.physics.utah.edu/~whanlon/`.

[282] Xilinx ArtiX.
`xilinx.com/products/silicon-devices/fpga.html`.

List of Figures

List of Tables

List of code listings

We decided to report very few code listings in this document. The reason is that we are interested in astrophysics, much more than in programming. However, it should be noticed that we spent most of our time writing code, probably for the same reason.

List of publications related to my doctoral project

These publications are based on or include a large part of my doctoral work. In the following list there are no technical reports or collaboration articles into which I was involved [e.g. 141, 140, 217, 218], but only those works where I made a decisive contribution. I have not used or discussed these publications to obtain my previous academic degrees.

1. *"Assessment of the Cherenkov camera alignment through Variance images for the ASTRI telescope"*, Iovenitti S., Sironi G., Giro E., Segreto A., Catalano O. and Capalbi M. – Peer-reviewed article on the journal "Experimental Astronomy" [198].

2. *"Mirror production for the Cherenkov telescopes of the ASTRI Mini-Array and of the MST project for the Cherenkov Telescope Array"*, La Palombara N., Sironi G., Giro E., Scuderi S., Canestrari R., Iovenitti S., *et al.* – Peer-reviewed article on the Journal of Astronomical Telescopes, Instruments, and Systems (accepted for publication) [211].

3. *"Star coverage, a simple tool to schedule an observation when FOV rotation matters"*, Iovenitti S. – Proceedings of the International Cosmic Ray Conference 2021 (poster on page 255) [*flash-talk video,* 248] [200].

4. *"Effective pointing of the ASTRI-Horn telescope using the Cherenkov camera with the Variance method"*, Iovenitti S., Sironi G., Segreto A., Catalano O. and Mineo T. – Proceedings of the International Cosmic Ray Conference 2021 (poster on page 256) [*flash-talk video,* 249] [199].

5. [Outreach] *"Astro-photography as an effective tool for Outreach and Education: IACTs in exposition"*, Iovenitti S., Righi C., Orsenigo S., Sgarro R. – Proceedings of the International Cosmic Ray Conference 2021 (poster on page 257) [*talk video,* 250] [219].

6. [Outreach] *"How to (dis-)assemble a planetary system (turning a video game into an educational game)"*, Iovenitti S., Perri L. – Proceedings of the conference "Communicating Astronomy with the Public" 2021 [*talk video,* 230] [220].

7. [In preparation] *"Starfield astrometry with the Cherenkov camera of ASTRI-Horn"*, Iovenitti S., Sironi G. – written for the submission to a peer-reviewed journal [221].

In January 2022 we submitted a proposal for an oral presentation entitled “New pointing calibration technique using star signals in the ASTRI Cherenkov camera and the Variance method” [222] to the international conference: SPIE Astronomical Telescopes + Instrumentation 2022 (Observatory Operations: Strategies, Processes, and Systems IX).
In the following pages we report the web-posters presented at the ICRC online in 2021.

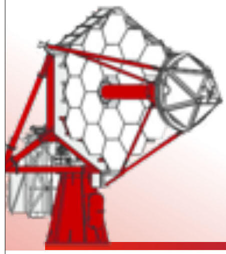

STAR COVERAGE

A simple tool to schedule an observation when FOV rotation matters

Simone Iovenitti *(Università degli Studi di Milano / INAF - Osservatorio astronomico di Brera)*
ICRC 2021 - 37th International Cosmic Ray Conference
12 - 23 July 2021, Berlin.
simone.iovenitti@inaf.it

THE ROTATION OF THE FIELD OF VIEW (FOV)

Every alt-azimuthal telescope presents the effect of field-of-view rotation during observation in tracking mode. This is due to the evolution of the **parallactic angle**, i.e. the one between the zenith and the NCP with the vertex in the pointing direction, as represented in figure 1.

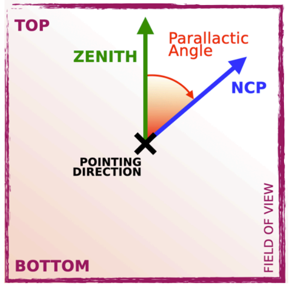

Fig.1: Schematic drawing of the parallactic angle.

REAL LIFE USE CASES

The FOV rotation can be exploited for **different purposes:** astrometric calibration, optical alignment of the camera (figure 2), retrieving of an effective camera efficiency map. These techniques are particularly interesting in Cherenkov astronomy, where detectors are usually not able to image the star field with fine angular resolution, but long exposures (figure 3) can still provide diagnostic images (Poster 826).

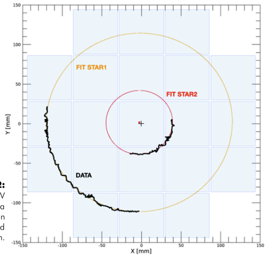

Fig.2: Analysis of the FOV rotation: there is a misalignment between the camera center and the pointing direction.

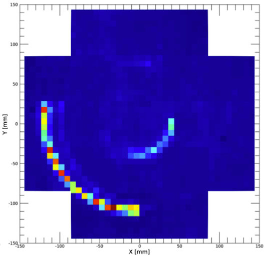

Fig.3: Real data from ASTRI-Horn, taken with the "Variance" method (3h 49m 27s).
Star1 : HIP 47908
Star2 : HIP 46750

NEED FOR SW TOOL: The evolution of the parallactic angle depends on the pointing coordinates: if the source is not circumpolar then rotation is not even complete! We need a handy software to simulate the FOV.

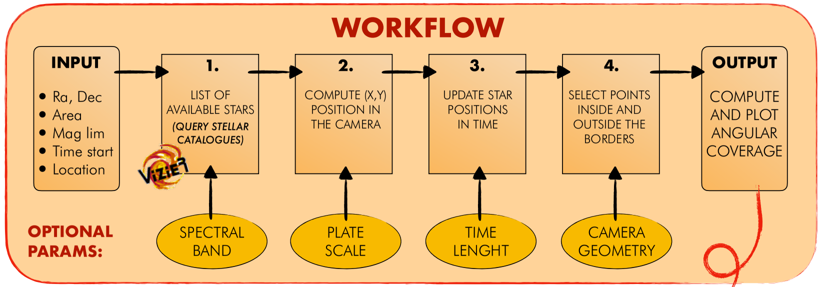

WORKFLOW

INPUT
- Ra, Dec
- Area
- Mag lim
- Time start
- Location

1. LIST OF AVAILABLE STARS *(QUERY STELLAR CATALOGUES)*

2. COMPUTE (X,Y) POSITION IN THE CAMERA

3. UPDATE STAR POSITIONS IN TIME

4. SELECT POINTS INSIDE AND OUTSIDE THE BORDERS

OUTPUT COMPUTE AND PLOT ANGULAR COVERAGE

OPTIONAL PARAMS: SPECTRAL BAND; PLATE SCALE; TIME LENGHT; CAMERA GEOMETRY

OPTIONAL CHEKS:
- ✓ field minimum altitude
- ✓ avoid sunset and sunrise
- ✓ distance of Moon, planets and ISS from the field

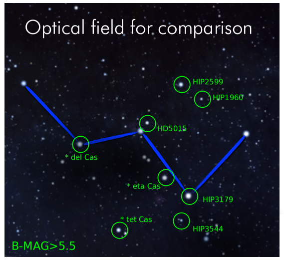

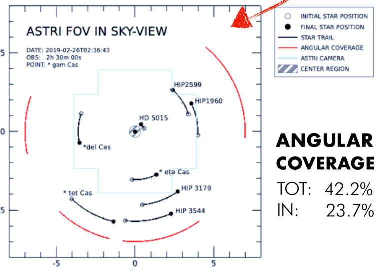

ANGULAR COVERAGE
TOT: 42.2%
IN: 23.7%

This sw will help the **ASTRI MINIARRAY** in scheduling the observing runs for the calibration: to choose the best duration and pointing strategy.

Coded in IDL
Source on Git-Lab
https://www.ict.inaf.it/gitlab/users/simone.iovenitti/projects

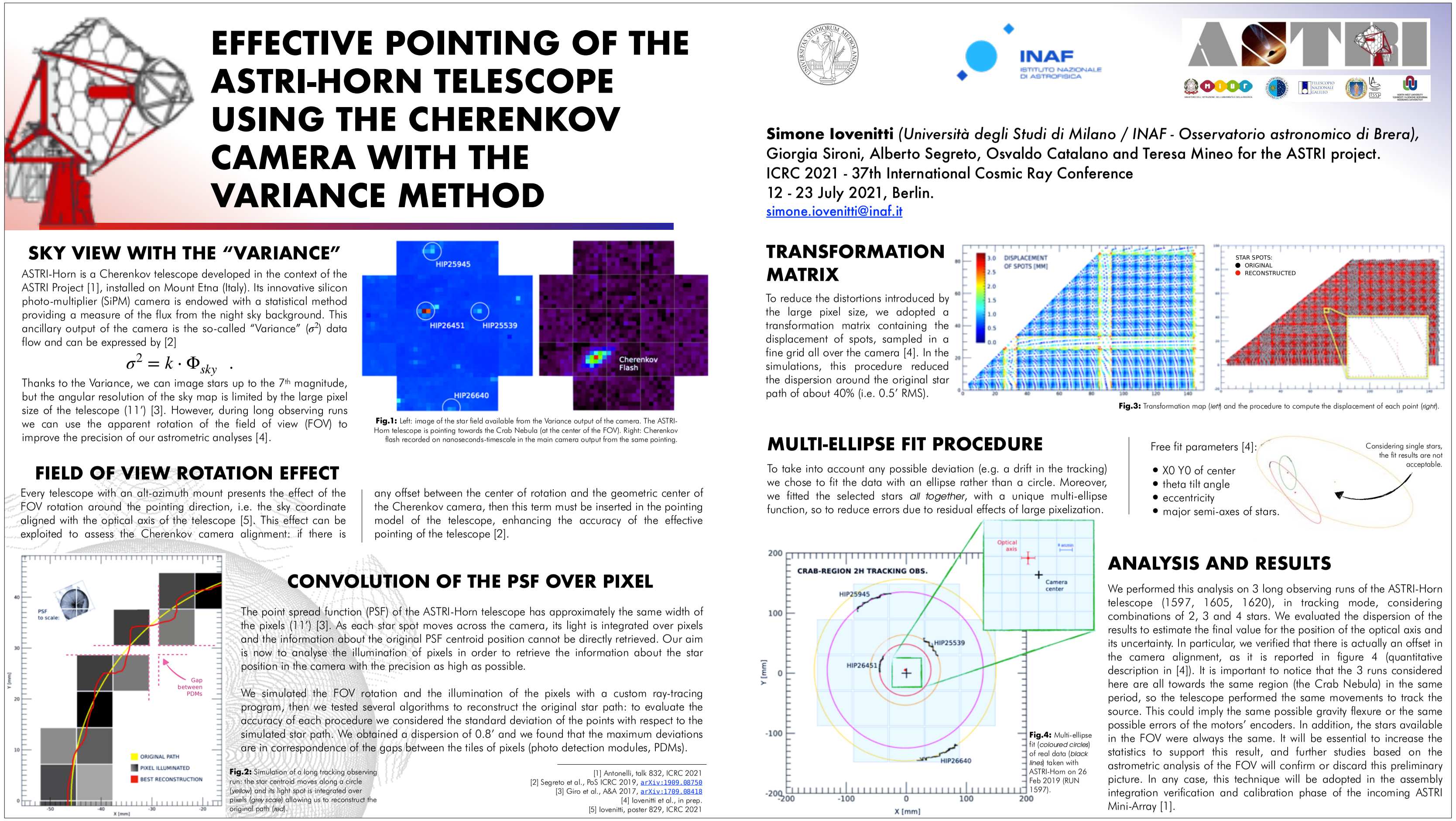

EFFECTIVE POINTING OF THE ASTRI-HORN TELESCOPE USING THE CHERENKOV CAMERA WITH THE VARIANCE METHOD

Simone Iovenitti (*Università degli Studi di Milano / INAF - Osservatorio astronomico di Brera*),
Giorgia Sironi, Alberto Segreto, Osvaldo Catalano and Teresa Mineo for the ASTRI project.
ICRC 2021 - 37th International Cosmic Ray Conference
12 - 23 July 2021, Berlin.
simone.iovenitti@inaf.it

SKY VIEW WITH THE "VARIANCE"

ASTRI-Horn is a Cherenkov telescope developed in the context of the ASTRI Project [1], installed on Mount Etna (Italy). Its innovative silicon photo-multiplier (SiPM) camera is endowed with a statistical method providing a measure of the flux from the night sky background. This ancillary output of the camera is the so-called "Variance" (σ^2) data flow and can be expressed by [2]

$$\sigma^2 = k \cdot \Phi_{sky} \quad .$$

Thanks to the Variance, we can image stars up to the 7th magnitude, but the angular resolution of the sky map is limited by the large pixel size of the telescope (11′) [3]. However, during long observing runs we can use the apparent rotation of the field of view (FOV) to improve the precision of our astrometric analyses [4].

Fig.1: Left: image of the star field available from the Variance output of the camera. The ASTRI-Horn telescope is pointing towards the Crab Nebula (at the center of the FOV). Right: Cherenkov flash recorded on nanoseconds-timescale in the main camera output from the same pointing.

FIELD OF VIEW ROTATION EFFECT

Every telescope with an alt-azimuth mount presents the effect of the FOV rotation around the pointing direction, i.e. the sky coordinate aligned with the optical axis of the telescope [5]. This effect can be exploited to assess the Cherenkov camera alignment: if there is any offset between the center of rotation and the geometric center of the Cherenkov camera, then this term must be inserted in the pointing model of the telescope, enhancing the accuracy of the effective pointing of the telescope [2].

CONVOLUTION OF THE PSF OVER PIXEL

The point spread function (PSF) of the ASTRI-Horn telescope has approximately the same width of the pixels (11′) [3]. As each star spot moves across the camera, its light is integrated over pixels and the information about the original PSF centroid position cannot be directly retrieved. Our aim is now to analyse the illumination of pixels in order to retrieve the information about the star position in the camera with the precision as high as possible.

We simulated the FOV rotation and the illumination of the pixels with a custom ray-tracing program, then we tested several algorithms to reconstruct the original star path: to evaluate the accuracy of each procedure we considered the standard deviation of the points with respect to the simulated star path. We obtained a dispersion of 0.8′ and we found that the maximum deviations are in correspondence of the gaps between the tiles of pixels (photo detection modules, PDMs).

Fig.2: Simulation of a long tracking observing run: the star centroid moves along a circle (*yellow*) and its light spot is integrated over pixels (*grey scale*) allowing us to reconstruct the original path (*red*).

[1] Antonelli, talk 832, ICRC 2021
[2] Segreto et al., PoS ICRC 2019, arXiv:1909.08750
[3] Giro et al., A&A 2017, arXiv:1709.08418
[4] Iovenitti et al., in prep.
[5] Iovenitti, poster 829, ICRC 2021

TRANSFORMATION MATRIX

To reduce the distortions introduced by the large pixel size, we adopted a transformation matrix containing the displacement of spots, sampled in a fine grid all over the camera [4]. In the simulations, this procedure reduced the dispersion around the original star path of about 40% (i.e. 0.5′ RMS).

Fig.3: Transformation map (*left*) and the procedure to compute the displacement of each point (*right*).

MULTI-ELLIPSE FIT PROCEDURE

To take into account any possible deviation (e.g. a drift in the tracking) we chose to fit the data with an ellipse rather than a circle. Moreover, we fitted the selected stars *all together*, with a unique multi-ellipse function, so to reduce errors due to residual effects of large pixelization.

Free fit parameters [4]:

- X0 Y0 of center
- theta tilt angle
- eccentricity
- major semi-axes of stars.

Considering single stars, the fit results are not acceptable.

Fig.4: Multi-ellipse fit (*coloured circles*) of real data (*black lines*) taken with ASTRI-Horn on 26 Feb 2019 (RUN 1597).

ANALYSIS AND RESULTS

We performed this analysis on 3 long observing runs of the ASTRI-Horn telescope (1597, 1605, 1620), in tracking mode, considering combinations of 2, 3 and 4 stars. We evaluated the dispersion of the results to estimate the final value for the position of the optical axis and its uncertainty. In particular, we verified that there is actually an offset in the camera alignment, as it is reported in figure 4 (quantitative description in [4]). It is important to notice that the 3 runs considered here are all towards the same region (the Crab Nebula) in the same period, so the telescope performed the same movements to track the source. This could imply the same possible gravity flexure or the same possible errors of the motors' encoders. In addition, the stars available in the FOV were always the same. It will be essential to increase the statistics to support this result, and further studies based on the astrometric analysis of the FOV will confirm or discard this preliminary picture. In any case, this technique will be adopted in the assembly integration verification and calibration phase of the incoming ASTRI Mini-Array [1].

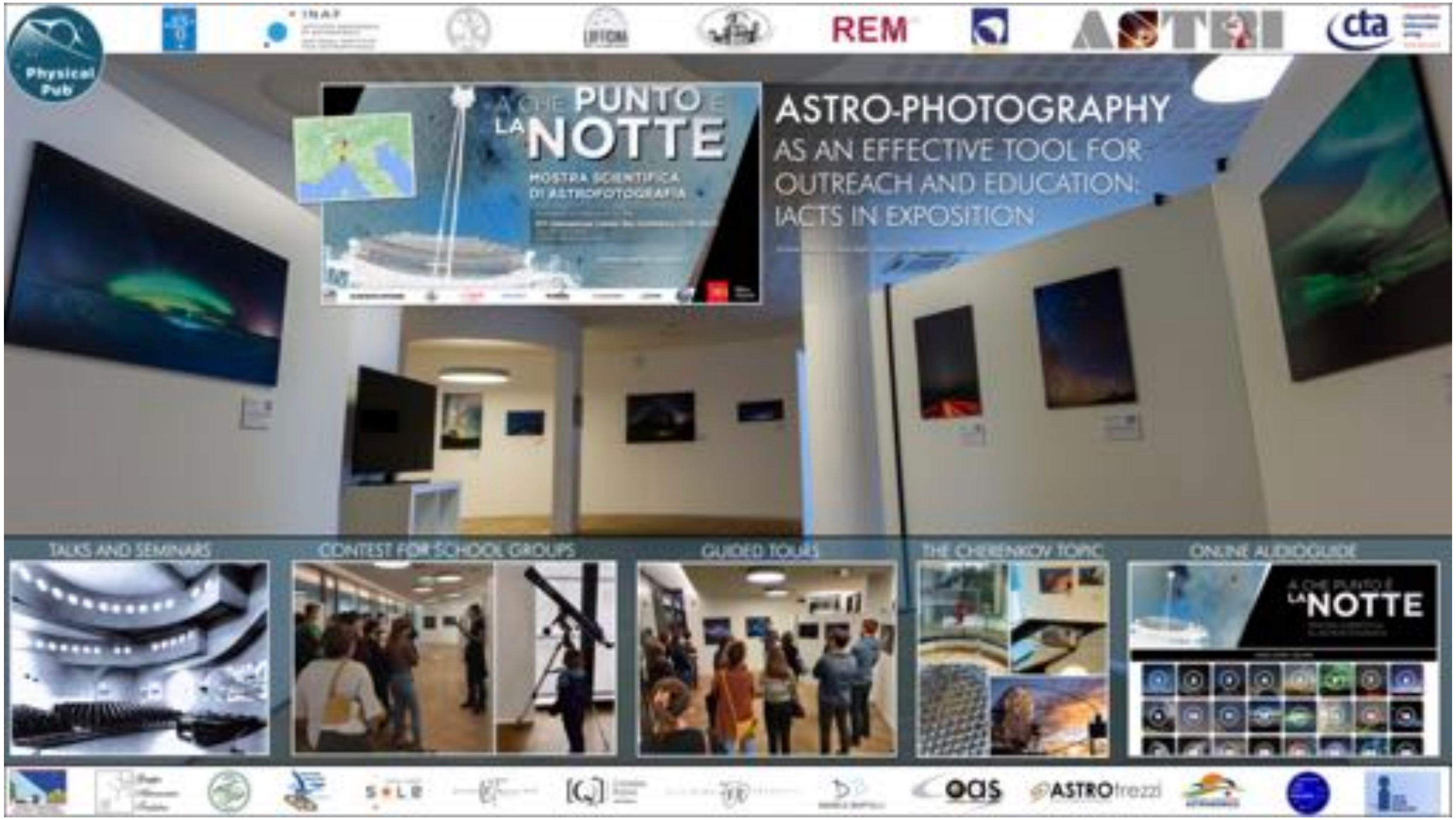

ASTRO-PHOTOGRAPHY
AS AN EFFECTIVE TOOL FOR
OUTREACH AND EDUCATION:
IACTS IN EXPOSITION

Acknowledgments

This is a very short version of the Acknowledgments chapter, that I decided to insert only in the printed copies of this thesis, using the Italian language.

At the end of this work it is important to remark that it would have been impossible to carry out, without the help and the guidance of Giorgia Sironi and Giovanni Pareschi. Moreover, I would like to thank also other INAF researchers, who appreciated my work and contributed with important discussions and suggestions: Enrico, Milvia, Teresa, Osvaldo, and Pierluca.

Of course, a fundamental contribution came indirectly from people, places and activities that enriched my life in the PhD period: my family, friends, the Physical Pub association, the beautiful Merate observatory, ski-alpinism, sailing experiences, and my guitar.

Finally, there is undoubtedly one person in particular who played a key role in my decision to remain in the research field. Thank you, Chiara.

Made with LaTeX
and a MacBook Pro .